# Effect of Soft Ground Tunneling-Induced Displacements on Railway Embankments

Hongyu Su

A Thesis

In

The Department

of

Building, Civil, and Environment Engineering

Presented in Partial Fulfillment of the Requirements

for the Degree of Master of Applied Science (Civil Engineering) at

Concordia University

Montréal, Québec, Canada

November 2020

# CONCORDIA UNIVERSITY

**School of Graduate Studies**

This is to certify that the thesis prepared

By: Hongyu Su

Entitled: Effect of Soft Ground Tunneling-Induced Displacements on Railway Embankments

and submitted in partial fulfilment of the requirements for the degree of

**Master of Applied Science (Civil Engineering)**

complies with regulations of the University and meets the accepted standards with respect to originality and quality.

Signed by the final Examining Committee:

_____ Chair

*Dr. Biao Li*

_____ Examiner

*Dr. Ali Dolatabadi*

_____ Examiner

*Dr. Biao Li*

_____ Supervisor

*Dr. Attila Michael Zsaki*

Approved by _____

*Dr. Michelle Nokken*, Graduate Program Director

November 25 2020 _____

*Dr. Mourad Debbabi*, Dean of Faculty

# ABSTRACT

Effect of Soft Ground Tunneling-Induced Displacements on Railway Embankments

Hongyu Su

With the rapid development of urban infrastructure, certain transportation lines, utilities and pipelines are needed to be excavated under operating railway lines. When a tunnel under a railway is excavated, it will inevitably cause disturbance to the track structures, and the disturbance could influence the safety of railway operations. Consequently, the alleviation of ground surface displacement is of great significance to ensure the safety of both railway operations and tunnel construction. This thesis is a fundamental study of the surface displacements due to the construction of both shallow (near-surface) and deep (away from the surface) tunnels. The analysis of displacement along the surface of railway embankments is performed via two-dimensional finite element modeling. The freight train operating speed, tunnel diameter and tunnel depth are the three key factors that affect the surface displacement. The results illustrate that a 3 m diameter tunnel at depths greater than 3 m or a 4 m diameter tunnel at any depth greater than 16 m can be constructed beneath an existing railway without significantly affecting the safety of railway operations by considering subsidence control standards. Thus, this thesis contributes to determination of the maximum displacement of railway embankments induced by tunnel excavation as a function of various factors considered. Also, the findings of this thesis can help to guide future tunnel design and displacement control measures for excavations under operating freight railway lines.

# ACKNOWLEDGEMENT

First and foremost, I would like to express my sincere gratitude to my supervisor, Dr. Attila Michael Zsaki, for providing me the opportunity to fulfill my study aim. His professional and inspired guidance helped me finish my research project.

I also want to record my deepest appreciation to my parents, who always love me unselfishly and support me consistently and encourage me through many difficult times. My gratitude also extends to my family members, friends, who helped me with their encouragement and company.

Besides, I am grateful for the financial support that was provided by Dr. Attila Michael Zsaki through ENCS/GCS FRS fund to successfully complete my research.

# Table of Contents

**List of Tables** ..... **vii**
**List of Figures** ..... **ix**
**List of Symbols** ..... **xiii**
**Chapter 1 Introduction** ..... **1**
1.1 Motivation ..... 1
1.2 Objectives ..... 2
1.3 Method of Analysis ..... 2
1.4 Summary of Findings and Contribution ..... 3
**Chapter 2 Literature Review** ..... **4**
2.1 Empirical Methods for Prediction of Ground Movement Induced by Tunneling ..... 4
2.2 Numerical Methods for Prediction of Ground Movement Induced by Tunneling ..... 6
2.2.1 Typical Numerical Methods in Geotechnical Engineering ..... 6
2.2.2 Numerical Methods in Tunneling ..... 7
2.3 Railway Embankment and Track Loadings ..... 12
2.3.1 Railway Embankment – Track Structure ..... 12
2.3.2 Track Forces Transmitted to Railway Track Foundation ..... 14
2.4 Load Transfer Mechanism ..... 17
2.5 Key Parameters of the Model ..... 20
2.5.1 Railway System ..... 21
2.5.2 Natural Ground Material Properties ..... 26
2.5.3 Tunnel ..... 26
2.6 FEM Methodology ..... 29
2.7 Convergence Criteria ..... 32
2.8 Constitutive Models for Soils ..... 33
2.8.1 Elastic Model ..... 33
2.8.2 Elasto-Plastic Model ..... 35
**Chapter 3 Generation of FEM Models Representing Tunneling Under Railways** ..... **38**
3.1 Process of Establishing a Model ..... 38
3.1.1 Railway System Geometry and Model Geometry ..... 38
3.1.2 Loading Conditions Due to Trains ..... 41
3.1.3 Material Properties of the Ground ..... 46
3.1.4 Mesh Convergence Study ..... 47
3.1.5 Boundary Conditions in the FEM Model ..... 51
3.1.6 Parametrized Models in the Simulation ..... 52
3.2 Verification of Numerical Modelling ..... 53
3.2.1 Comparison of Numerical Models and Analytical Methods for Elastic Materials ..... 53

3.2.2 Comparison of the Results of Numerical and Analytical Methods for Elasto-Plastic Materials ..... 59
**Chapter 4 Discussion of FEM Modeling Results of Tunneling-induced Displacements on Railway Embankments ..... 68**
4.1 Scenario 1 – The Influence of Train Operation Speed on the Ballast Surface Vertical Displacement ($S_v$) ..... 68
4.2 Scenario 2 - Tunnel Excavation Under an Operating Rail Line – Influence of Train Speed on the Vertical Surface Displacement ($S_v$) ..... 73
4.2.1 Excavation of D = 3 m Tunnel Located at Various Depths Subjected to Train Loading ..... 73
4.2.2 Excavation of D = 14 m Tunnel Located at Various Depths Subjected to Train Loading ..... 78
4.2.3 Vertical Displacement of the Ballast Surface at the Tunnel's Central Axis ($S_{vp-c}$) ..... 86
4.3 Scenario 3 - Influence of Tunnel Depth (H) on the Vertical Surface Displacement along the Ground Surface ..... 90
4.3.1 Model with D = 3 m - Relating Tunnel Depth's Influence on $S_v$ ..... 90
4.3.2 Model with D = 14 m - Relating Tunnel Depth's Influence on $S_v$ ..... 93
4.3.3 Allowable Maximum Displacement to Ensure Railway Operation Safety ..... 98
4.4 Scenario 3 - Influence of Tunnel Diameter (D) to the Vertical Surface Displacement ..... 99
4.5 Summary ..... 101
**Chapter 5 Conclusion and Recommendations ..... 103**
5.1 Thesis Summary ..... 103
5.2 Conclusion ..... 103
5.3 Limitations ..... 104
5.4 Future Work ..... 105
**References ..... 106**
**Appendix A: Soil Properties ..... 111**
**Appendix B: Displacement Distribution, $S_{vt-max}$, $R_{Svt-max}$ (%) for Models from D = 4 m to D = 13 m, Referring to Scenario 3 ..... 115**
**Appendix C: Train Loadings Distribution in the Models ..... 123**

# List of Tables

Table 2.1 Commonly used equations for determining effective length of sleepers (Sadeghi 2012) .....20
Table 2.2 Typical heavy axle loads of freight cars around the world (Li et al. 2016).....21
Table 2.3 Number of axles and weight per axle of several rolling stock types (Esveld 2001) .....21
Table 2.4 Dimensions for locomotives and freight cars (Dick et al. 2011).....22
Table 2.5 Rail gauge values (Selig and Waters 1994).....22
Table 2.6 Maximum speeds for different railway lines (Esveld 2001) .....23
Table 2.7 Typical tie dimensions (Selig and Waters 1994) .....23
Table 2.8 Material properties of ballast, subballast (Profillidis 2014).....25
Table 2.9 Range of elastic moduli for crushed stone (Pavement Interactive n.d.).....25
Table 2.10 Material properties of railway embankment (Xu et al. 2010) .....25
Table 2.11 Material properties of railway embankments (Li et al. 2016) .....25
Table 2.12 Material properties ranges of ballast and subballast (Li et al. 2016).....25
Table 2.13 The credible range of soil functional parameters .....26
Table 2.14 Relation between overburden depth and external dimension of a tunnel.....27
Table 2.15 Properties of tunnel lining (Xie et al., 2016).....28
Table 2.16 The parameters of the supporting system (Large Pipe-shed) (Zhao and Qi 2014).....28
Table 2.17 Comparison between mechanical parameters of original and reinforced soils (Zhou et al. 2002).....28
Table 2.18 Properties of tunnel lining (Gong and Zhou 2008) .....28
Table 3.1 Key parameters for chosen locomotive and freight car.....41
Table 3.2 Contact pressure between sleepers and the ballast surface for locomotive.....42
Table 3.3 Contact pressure between sleepers and the ballast surface for a freight car .....43
Table 3.4 Natural ground properties.....46
Table 3.5 Substructure component properties .....46
Table 3.6 Tunnel liner properties (Gong and Zhou 2008).....46
Table 3.7 Different number of elements and nodes corresponding to the maximum vertical displacement of the ballast surface induced by tunnel excavation ($S_{vt\text{-}max}$) and the displacement discrepancy for the sample model D = 14 m, H = 114 m, $V_4$ = 120 km/h .....47
Table 3.8 Relative number of mesh elements and nodes of each model.....49
Table 3.9 Elastic material parameters and in-situ field stress ($P_1$, $P_2$).....54
Table 3.10 Error in RS2 analysis relative to analytical solution for elastic material. .....59
Table 3.11 Elasto-plastic material parameters, in-situ field stress ($P0$) and internal pressure ($Pi$) .....59
Table 3.12 Error in RS2 analysis relative to analytical solution for both associated (dilatancy = friction angle) and non-associated (dilatancy = 0) flow cases .....67

Table 4.1 Average and maximum difference (%) between $S_{vv}$ and $S_{vp}$ when D = 3 m under four train speed conditions ..... 76
Table 4.2 Average and maximum difference (%) between $S_{vv}$ and $S_{vp}$ when D = 14 m under four train speed conditions ..... 81
Table 4.3 Average and maximum relative difference of $S_{vt}$ along the ground surface (%) ..... 95
Table 4.4 $S_{vt\text{-}max}$ (mm) for allowable tunnel construction without reinforcement underneath railways, $V_1$ = 0 km/h ..... 98
Table 4.5 The relative difference of $S_{vt\text{-}max}$ changes when tunnel diameter is increased in 1m increments ..... 100
Table 4.6 The relative difference of $S_{vt\text{-}max}$ changes from tunnel D = 3 m to other tunnel diameters ..... 101

# List of Figures

Figure 1.1. Collapsed sinkhole beneath the existing surface rail tracks and buckled railway tracks (Shani and TunnelTalk 2017). ..... 1
Figure 1.2. Concrete backfills the collapsed tunnel (Shani and TunnelTalk 2017)..... 2
Figure 2.1. Transverse ground surface settlement trough in Peck formulation (Xie et al. 2016). ... 4
Figure 2.2. The gap method for modeling tunnel excavation (Potts and Zdravković 2001). ..... 8
Figure 2.3. Convergence-confinement method (Potts and Zdravković 2001). ..... 9
Figure 2.4. (a) Volume loss method; (b) Modeling excavation of solid element (Karakus 2007). .. 9
Figure 2.5. Progressive softening method (Potts and Zdravković 2001). ..... 10
Figure 2.6. Deformation modes for a shallow tunnel cavity according to Whittle et al. (2001).... 10
Figure 2.7. CR-live loading for heavy haul railway (Zhang et al. 2014). ..... 12
Figure 2.8. (a) Cross-section of slab rail track (Indraratna et al. 2011, Esveld 2001)..... 13
Figure 2.8. (b) Cross-section of ballasted rail track (Indraratna et al. 2011). ..... 13
Figure 2.9. Ballasted track structure components (Selig and Waters 1994)..... 13
Figure 2.10. Schematic illustration of axles and bogies and record of pressure under the sleeper due to the passage of a freight train (Sun et al. 2015; Indraratna et al. 2010). ..... 15
Figure 2.11. Various sources of impact loading in rail track (Indraratna et al. 2011). ..... 16
Figure 2.12. Typical wheel load distribution in a track (Indraratna et al. 2011). ..... 17
Figure 2.13. Rail seat load determination (Zhang et al. 2016), where Q is the wheel loading; s is crosstie spacing. ..... 18
Figure 2.14. Estimated of maximum distribution factor for a single sleeper, AREMA (2010). .... 18
Figure 2.15. Wheel load distribution along successive sleepers (Profillidis 2014). ..... 19
Figure 2.16. Rail seat load distribution (Ministry of Railway of the People's Republic of China 2016), where $Pd$ is the dynamic wheel load. ..... 19
Figure 2.17. Effective length of a sleeper support at rail seat (Sadeghi 2012). ..... 20
Figure 2.18. Typical dimension for a railcar (Dick et al. 2011). ..... 22
Figure 2.19. Geometrical characteristics of timber sleepers in standard gauge tracks (Profillidis, ..... 24
Figure 2.20. Size categories for 7-inch and 6-inch crossties (AREMA 2010)..... 24
Figure 2.21. (a) Two cell rectangular tunnel; (b) Circular tunnel; (c) Horseshoe and Curvilinear (Oval) tunnel (Hung et al. 2010). ..... 29
Figure 2.22. Typical two-dimensional finite elements (Potts and Zdravković 1999). ..... 30
Figure 2.23. The non-linear response of a spring to applied load (Rocscience Inc. 2019). ..... 32
Figure 2.24. General state of stress (Budhu 2010). ..... 34
Figure 2.25. (a) Rigid plastic model; (b) elastic-ideal plastic model, (Li 2004). ..... 35
Figure 2.26. Mohr circle defining the conditions at failure (Pietruszczak 2010)..... 36
Figure 2.27. Mohr-Coulomb criterion in the principal stress space (Pietruszczak 2010). ..... 37
Figure 3.1. Railway embankment components with their dimensions. ..... 39

Figure 3.2. Typical model geometry with dimensions. ....39
Figure 3.3. Model geometry for a D = 14m, H = 112m tunnel excavation with 120 km/h train speed loading. ....40
Figure 3.4. Stress distribution for model with D = 14 m, H = 112 m, with 120 km/h train speed loading. ....40
Figure 3.5. Distribution of average contact pressure between sleeper and ballast (locomotive). ..44
Figure 3.6. Distribution of average contact pressure between sleeper and ballast (freight car). ...45
Figure 3.7. Critical mesh elements effect on the maximum vertical displacement at the ballast surface induced by tunnel excavation ($S_{vt\text{-}max}$) for the numerical models, and the corresponding displacement discrepancy. ....48
Figure 3.8. Model with loading and boundary conditions for the case of a tunnel diameter ....52
Figure 3.9. Sketch indicating the position of tunnel's central axis, and H and D parameters....53
Figure 3.10. Configuration of RS2 model for the verification example. ....54
Figure 3.11. Parameters for Kirsch equation (Jaeger and Cook 1976). ....55
Figure 3.12. Comparison of radial stress distributions along the x-axis from the tunnel center to the designated point....56
Figure 3.13. Comparison of tangential stress distributions along the x-axis from the tunnel center to the designated point....56
Figure 3.14. Comparison of radial displacement distributions along the x-axis from the tunnel center to the designated point. ....57
Figure 3.15. Contours of radial stress from RS2 analysis. ....57
Figure 3.16. Contours of tangential stress from RS2 analysis. ....58
Figure 3.17. Contours of radial displacement from RS2 analysis. ....58
Figure 3.18. Comparison of radial stress distributions along the x-axis from the tunnel center to the designated point for ($\psi$ = 0 °) case. ....61
Figure 3.19. Comparison of tangential stress distributions along the x-axis from the tunnel center to the designated point for ($\psi$ = 0 °) case. ....61
Figure 3.20. Comparison of radial displacement distributions along the x-axis from the tunnel center to the designated point for ($\psi$ = 0 °) case. ....62
Figure 3.21. Contours of radial stress from RS2 for ($\psi$ = 0 °) case. ....62
Figure 3.22. Contours of tangential stress from RS2 for ($\psi$ = 0 °) case. ....63
Figure 3.23. Contours of radial displacement from RS for ($\psi$ = 0 °) case. ....63
Figure 3.24. Comparison of radial stress distributions along the x-axis from the tunnel center to the designated point for ($\psi$ = 30 °) case. ....64
Figure 3.25. Comparison of tangential stress distributions along the x-axis from the tunnel center to the designated point for ($\psi$ = 30 °) case. ....64
Figure 3.26. Comparison of radial displacement distributions along the x-axis from the tunnel center to the designated point for ($\psi$ = 30 °) case. ....65
Figure 3.27. Contours of radial stress from RS2 for ($\psi$ = 30 °) case. ....65
Figure 3.28. Contours of tangential stress from RS2 for ($\psi$ = 30 °) case. ....66

Figure 3.29. Contours of radial displacement from RS for ($\psi$ = 30 °) case.....66
Figure 3.30. Contours of yield and plastic zone from RS2 for ($\psi$ = 30 °) case. .....66
Figure 4.1. Load distribution from freight train in simulation models. .....69
Figure 4.2. Vertical ground displacement along the ballast surface caused by trainload ($S_{vv}$) with train speeds of 0, 40, 80, 120 km/h. .....70
Figure 4.3. (a) Vertical displacement contour for the model with $V_1$ = 0 km/h train loading. .....71
Figure 4.3. (b) Vertical displacement contour for the model with $V_2$ = 40 km/h train loading. .....71
Figure 4.3. (c) Vertical displacement contour for the model with $V_3$ = 80 km/h train loading. .....72
Figure 4.3. (d) Vertical displacement contour for the model with $V_4$ = 120 km/h train loading. ....72
Figure 4.4. Maximum vertical displacement along the ballast surface caused by trainload ($S_{vv\text{-}max}$) for the four train speeds considered (0,40,80,120 km/h). .....73
Figure 4.5. (a) Symmetrical displacement distribution for model D = 3 m excavation with operating train ($V_1$ = 0 km/h).....74
Figure 4.5. (b) Symmetrical displacement distribution for model D = 3 m excavation with operating train ($V_2$ = 40 km/h).....74
Figure 4.5. (c) Symmetrical displacement distribution for model D = 3 m excavation with operating train ($V_3$ = 80 km/h).....75
Figure 4.5. (d) Symmetrical displacement distribution for model D = 3 m excavation with operating train ($V_4$ = 120 km/h).....75
Figure 4.6. Vertical displacement contour for model with D = 3 m, H = 3 m, $V_4$ = 120 km/h. .....77
Figure 4.7. Vertical displacement contour for model with D = 3 m, H = 24 m, $V_4$ = 120 km/h. ...77
Figure 4.8. (a) Symmetrical displacement distribution for model D = 14 m excavation with stationary train ($V_1$ = 0 km/h).....78
Figure 4.8. (b) Symmetrical displacement distribution for model D = 14 m excavation with stationary train ($V_2$ = 40 km/h).....79
Figure 4.8. (c) Symmetrical displacement distribution for model D = 14 m excavation with stationary train ($V_3$ = 80 km/h).....79
Figure 4.8. (d) Symmetrical displacement distribution for model D = 14 m excavation with stationary train ($V_4$ = 120 km/h).....80
Figure 4.9. (a) Vertical displacement contour for model with D = 14 m, H = 14 m, $V_1$ = 0 km/h. 81
Figure 4.9. (b) Vertical displacement contour for model with D = 14 m, H = 14 m, $V_2$ = 40 km/h. .....82
Figure 4.9. (c) Vertical displacement contour for model with D = 14 m, H = 14 m, $V_3$ = 80 km/h. .....82
Figure 4.9. (d) Vertical displacement contour for model with D = 14 m, H = 14 m, $V_4$ = 120 km/h. .....83
Figure 4.10. (a) Vertical displacement contour for model with D = 14 m, H = 112 m, $V_1$ = 0 km/h. .....83
Figure 4.10. (b) Vertical displacement contour for model with D = 14 m, H = 112 m, $V_2$ = 40 km/h. .....84

Figure 4.10. (c) Vertical displacement contour for model with D = 14 m, H = 112 m, $V_3$ = 80 km/h. ..... 84
Figure 4.10. (d) Vertical displacement contour for model with D = 14 m, H = 112 m, $V_3$ = 80 km/h. ..... 85
Figure 4.11. (a) Vertical displacement of the ballast surface at tunnel's central axis ($S_{vp\text{-}c}$), $V_1$ = 0 km/h. ..... 86
Figure 4.11. (b) Vertical displacement of the ballast surface at tunnel's central axis ($S_{vp\text{-}c}$), $V_2$ = 40 km/h. ..... 87
Figure 4.11. (c) Vertical displacement of the ballast surface at tunnel's central axis ($S_{vp\text{-}c}$), $V_3$ = 80 km/h. ..... 87
Figure 4.11. (d) Vertical displacement of the ballast surface at tunnel's central axis ($S_{vp\text{-}c}$), $V_4$ = 120 km/h. ..... 88
Figure 4.12 The relative difference between $V_1$ = 0 km/h models to $V_2$ = 40 km/h on the difference between $S_{vv\text{-}c}$ and $S_{vp\text{-}c}$. ..... 88
Figure 4.13 The relative difference between $V_1$ = 0 km/h models to $V_3$ = 80 km/h on the ..... 89
Figure 4.14 The relative difference between $V_1$ = 0 km/h models to $V_4$ = 120 km/h on the difference between $S_{vv\text{-}c}$ and $S_{vp\text{-}c}$. ..... 89
Figure 4.15. Displacement distribution along ballast surface for model D = 3 m, $V_1$ = 0 km/h. ... 91
Figure 4.16. Tunnel depth (H) influence on $S_{vt\text{-}max}$, for four train speed conditions, D = 3 m. ..... 92
Figure 4.17. Tunnel depth (H) influence on $S_{vt\text{-}max}$ relative difference, for four train speed conditions, D = 3 m. ..... 92
Figure 4.18. Displacement distribution along ballast surface, D = 14 m, $V_1$ = 0 km/h. ..... 93
Figure 4.19. Tunnel depth (H) influence on $S_{vt\text{-}max}$, for four train speed conditions, D = 14 m. ..... 94
Figure 4.20. Tunnel depth (H) influence on $S_{vt\text{-}max}$ relative difference for four train speeds, D = 14 m. ..... 94
Figure 4.21. Maximum vertical displacement at the ballast surface, D = 3 m to D = 14 m. ..... 99
Figure 4.22. H/D ratio related to tunnel diameter influence on $S_{vt\text{-}max}$. ..... 100

# List of Symbols

| | | |
|---|---|---|
| $a$ | = | tunnel radius (m) |
| $c$ | = | cohesion (kPa) |
| $D$ | = | tunnel diameter (m) |
| $DF$ | = | distribution factor (%) |
| $E$ | = | Young's modulus (kPa) or (MPa) |
| $G$ | = | compressive (shear) modulus (kPa) or (MPa) |
| $h$ | = | average thickness of soil layer (m) |
| $H$ | = | tunnel depth (m) |
| i | = | trough width parameter |
| $I_1$ | = | first stress invariant |
| $IF$ | = | dynamic (impact) factor (%) |
| $l$ | = | liner thickness (m) |
| $J_2$ | = | second deviator stress invariant |
| $K$ | = | non-linear stiffness of spring (kN/m) |
| $K_s$ | = | coefficient of settlement trough width |
| $K_p$ | = | passive earth pressure coefficient |
| $L_o$ | = | overall length of railcar measured over the pulling face of the coupler (m) or (inch) |
| $P$ | = | applied load to a spring (kN) |
| $P_0,\ P_1, P_2$ | = | in-situ field stress (kPa) |
| $P_i$ | = | internal stress (kPa) |
| $P_s$ | = | static wheel loading (kN) or (lb) |
| $R_0$ | = | yield zone radius (m) |
| $R_{(S_{vt-max})}$ | = | relative difference in $S_{vt-max}$ |
| $S_I$ | = | inboard axle spacing, distance between the inside axles of a railcar (m) or (inch) |
| $S_o$ | = | outboard axle spacing, distance between the outside axles of a railcar (m) or (inch) |
| $S_{max}$ | = | vertical maximum ground surface settlement (m) or (mm) |
| $S_x$ | = | ground surface settlement (m) or (mm) |
| $S_T$ | = | track axle spacing, distance between the adjacent axles of a truck (m) or (inch) |
| $S_{vv}$ | = | vertical displacement along the ballast surface induced by train loading only (mm) |
| $S_{vp}$ | = | vertical displacement along the ballast surface generated by tunnel excavation with train loading (mm) |
| $S_{vt}$ | = | vertical displacement along the ballast surface caused by tunneling without the effect of the train loading only (mm) |
| $S_{vv-max}$ | = | maximum vertical displacement along the ballast surface induced by train loading only (mm) |
| $S_{vp-max}$ | = | maximum vertical displacement along the ballast surface generated by tunnel excavation with train loading (mm) |

| | | |
|---|---|---|
| $S_{vt-max}$ | = | maximum vertical displacement along the ballast surface caused by tunneling without the effect of the train loading only (mm) |
| $t$ | = | time duration of loading pulse (sec) |
| $U$ | = | displacement of a spring (mm) |
| $V$ | = | train operation speed (km/h) or (mile/h) |
| $V_l$ | = | volume loss ratio (%) |
| $V_s$ | = | ground surface settlement volume ($m^3$) |
| $w$ | = | weight of track substructure per unit weight area ($kg/m^2$) |
| x | = | horizontal distance from the tunnel center (m) |
| $z$ | = | depth of track substructure (m) |
| $\beta$ | = | stiffness reduction factor |
| $\gamma$ | = | bulk unit weight ($kN/m^3$) |
| $\gamma_{ij}$ | = | shear strain (m/m) |
| $\varepsilon$ | = | strain (m/m) |
| $\theta$ | = | Lode angle (◦) |
| $\lambda$ | = | proportion of unloading |
| $\lambda_d$ | = | design value of $\lambda$ |
| $u_r$ | = | radial displacement (m) or (mm) |
| $v$ | = | Poisson's ratio |
| $\rho$ | = | density ($kg/m^3$) |
| $\sigma$ | = | normal stress (kPa) |
| $\sigma_r$ | = | radial stress (kPa) |
| $\sigma_y$ | = | yielding stress (kPa) |
| $\sigma_\theta$ | = | tangential stress (kPa) |
| $\tau$ | = | shear strength (kPa) |
| $\varphi$ | = | friction angle (◦) |
| $\psi$ | = | dilation angle (◦) |
| $\{\sigma_0\}$ | = | initial soil stress (kPa) |
| $\{\Delta d_E\}$ | = | vector of incremental element nodal displacements (mm) |
| $\{\Delta d_G\}$ | = | vector of all incremental nodal displacements (mm) |
| $\{F_0\}$ | = | equivalent nodal forces on the tunnel boundary (N) or (kN) |
| $[K_E]$ | = | element stiffness matrix |
| $[K_G]$ | = | global stiffness matrix |
| $\{\Delta R_E\}$ | = | vector of incremental element nodal forces (N) or (kN) |
| $\{\Delta R_G\}$ | = | vector of all incremental element nodal forces (N) or (kN) |

# Chapter 1 Introduction

## 1.1 Motivation

With the rapid development of urban infrastructure, a great number of transportation lines and pipelines are needed to be constructed via tunneling, under existing and operating railway lines. These excavations will disturb the original stress field within the railway foundations, then could lead to an inevitable deformation of ground surface and railway embankment. Under these circumstances, the safety of existing railway operations should be a top priority. There has been a considerable amount of research done to predict ground surface displacement induced by tunneling. However, comparatively, tunneling under an existing railway was rarely discussed in this context. Any surface settlement of railway embankments can lead to deformation and misalignment of the rail that can easily lead to derailment of trains. Thus, the ground surface displacement is influenced by a set of factors, which are the train operation speed, tunnel diameter and depth. The effect of these on the displacement of railway embankments at the ballast level is the topic of this thesis.

To illustrate the type of failure can occur, a recent railway incident can be introduced by Shani and TunnelTalk (2017). A tunnel boring machine (TBM) was driven underneath a main freight and passenger railway line at Rastatt in Germany. Ground freezing collars were installed to prevent ground deformation during construction period. However, a 500 mm subsidence failure occurred beneath the railway tracks and led to buckled rails, as seen in Figure 1.1. The reason for this subsidence was found to be the displacement of the liner segments behind the tunneling face, leading to water break through the construction field and ground surface. This incident resulted in altering routes of 370 trains per day to avoid the collapsed area. The area was closed for about two months. Also, a TBM costing 18 million euros was buried because of the backfill concrete, see Figure 1.2.


Figure 1.1. Collapsed sinkhole beneath the existing surface rail tracks and buckled railway tracks (Shani and TunnelTalk 2017).

Figure 1.2. Concrete backfills the collapsed tunnel (Shani and TunnelTalk 2017).

## 1.2 Objectives

This research aims to determine the effect of train speed, tunnel diameter and its depth on the ground surface displacement through two-dimensional modeling. A parametric study will be performed in this research. The vertical displacement along the ballast surface under different conditions is going to be obtained from modeling results. The relationship between the train speed and the maximum ground surface deformation is going to be investigated. Besides, this research will study the maximum displacement under the impact of both train operation and tunnel excavation, and the maximum displacement induced by the tunnel excavation without the train operation effect. It is expected to investigate how tunnel diameter and tunnel depth changes affect the ground surface displacement. In relation to the subsidence control standard, this research will provide the allowable tunnel construction information.

## 1.3 Method of Analysis

Although there can be a great variety of situations under which an excavation is made under an existing railway line, this thesis will adopt some assumptions that are set up to represent the majority of cases that are considered in the models:

- Only a straight section of a railway will be considered.
- The environmental factors like temperature and wind will be neglected.
- Lateral and longitudinal track forces will not be considered.
- Friction between rail and wheel will be ignored.

The modeling will be carried out using a two-dimensional finite element method (FEM), representing a section along the rail line, under the rails. The tunneling will occur perpendicular to the direction of the rails. From a thorough literature review (Chapter 2), key parameters will be compiled to build representative models. Before establishing these models, a mesh convergence study and model verification will be performed to validate the accuracy of FEM models and analysis (Chapter 3). Afterward, a unit thickness railway embankment, overlaying a clay ground will be simulated. Train loading under different operation speeds will be exerted on the model's upper boundary to simulate the moving trains. Subsequently, tunnels with different diameters, excavated at various depths based on the chosen tunnel depth-diameter ratio (H/D) will generated in the models. There will be a total of three scenarios that comprise a parametric study of the influence parameters (Chapter 4). Scenario 1 studies the ground surface displacement caused solely by moving trains. Scenario 2 incorporates the effect of tunnel excavation in addition of moving trains; thus, the tunnel excavation is the only difference between Scenario 1 and 2. While as a baseline, Scenario 3 only examines the influence of tunnel excavation on the ground surface displacement.

## 1.4 Summary of Findings and Contribution

According to the previous outline, the findings are briefly summarized below:

- The relationship of the maximum ground surface displacement and operation train speed is linear in the absence of tunneling.
- Shallow depth tunnels with a low depth-diameter ratio (H/D) generate significant ground surface displacement as compared to deeply-buried tunnels.
- Only a certain H/D combination of tunnels can be constructed beneath the existing railway within the subsidence control standard (10mm).
- A one-meter increase of tunnel diameter for a small, shallow tunnels affects ground surface displacement considerably more than a large shallow tunnel.
- A large tunnel diameter generates more ground vertical displacement than a small tunnel.

Upon analyzing data from the model results, this thesis contributes to our understanding of railway embankment deformations due to tunneling that can help with future tunnel design and displacement control under operating railways lines.

# Chapter 2 Literature Review

The main objective of this thesis is to investigate the effect of tunneling in clayey ground under in-use railway tracks, which are subjected to dynamic loading from passing locomotives pulling a string of freight cars. In order to ensure the safety of operating railways during the tunnel construction period and beyond, the deformation induced by tunneling must be in an acceptable range. Hence, this chapter will review the ground movement prediction using empirical and numerical methods during tunneling, and the dynamic ground response induced by passing trains. Furthermore, the related study of relevant parameters will be reviewed as well. Also, FEM is a widely used numerical method to simulate tunnel excavation. Thus, the salient features and methodology of FEM will be introduced in this chapter as well.

## 2.1 Empirical Methods for Prediction of Ground Movement Induced by Tunneling

Many empirical methods have been developed to predict the ground surface movement induced by tunneling in soil in the last forty years, such as Knothe (1957); Peck (1969); Clough and Schmidt (1981); O'Reilly and New (1982); Rankin (1988); Mair et al. (1993), etc. Most of them were deducted from considerable field measurement data. Nevertheless, the most commonly used empirical expression in engineering practice was developed by Peck (1969). It assumed that a Gaussian distribution curve can describe the transverse ground surface settlement trough, as shown in Figure 2.1.

The formulation by Peck (1969) is expressed as follows:

$$S_x = S_{max}\exp\left(-\frac{x^2}{2i^2}\right) \tag{2.1}$$

where $S_x$ is the ground surface settlement (mm) or (m) at a horizontal distance x (m) from the tunnel center; $S_{max}$ is the maximum vertical ground surface settlement (mm) or (m); i is the trough width parameter, which is the distance from tunnel center to the inflection point.

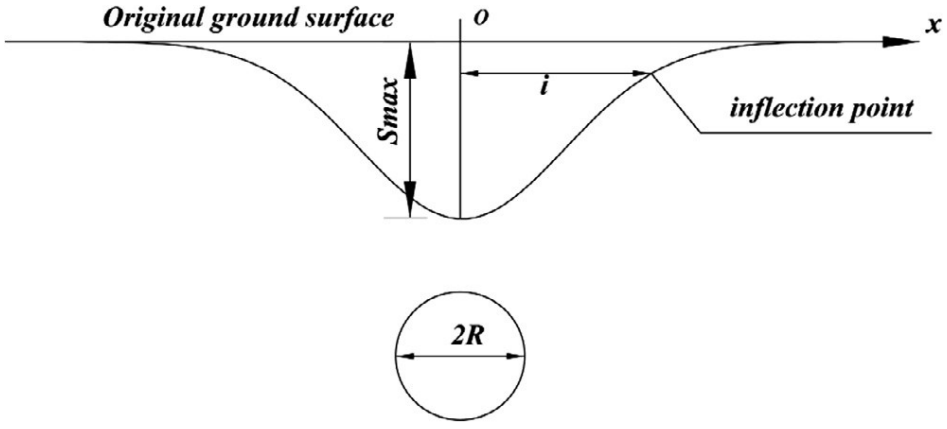


Figure 2.1. Transverse ground surface settlement trough in Peck formulation (Xie et al. 2016).

The trough width parameter i is used to define the cross-sectional width of settlement. There are other formulations that are derived by different researchers, as follows:

a) i is related to soil property friction angle $\varphi$ and tunnel depth $H$, was proposed by Knothe (1957), where $\varphi$ is the friction angle of soil:

$$\mathrm{i} = \frac{H}{\sqrt{2\pi}\tan(45^\circ - {}^{\varphi}/_{2})} \tag{2.2}$$

b) i is decided by the tunnel diameter D and depth $H$, proposed by Peck (1969) as:

$$\mathrm{i} = 0.5\left(\frac{H}{\mathrm{D}}\right)^{1-n} * \mathrm{H}, n = 0.8\sim1.0 \tag{2.3}$$

c) i is determined by the tunnel radius $a$ and depth $H$, was provided by Clough and Schmidt (1981):

$$\mathrm{i} = \mathrm{a}(\frac{H}{2R})^{0.8} \tag{2.4}$$

d) i relies only on the tunnel depth H, proposed by O'Reilly and New (1982), for cohesive soils:

$$\mathrm{i} = 0.43z_0 + 1.1 \tag{2.5}$$

e) i is obtained by the tunnel depth $H$ and coefficient of settlement trough width $\mathrm{K}_s$, proposed by Rankin (1988):

$$\mathrm{i} = \mathrm{K}_s H \tag{2.6}$$

where $\mathrm{K}_s$, is taken as 0.5 for practical purposes.

To characterize the maximum ground surface settlement induced by tunneling, the volume loss ratio ($V_l$) is established as an important parameter (Mair et al. 1993). Volume loss value for most cases of soft ground tunneling is normally around or below 1 % when the ground is treated well (Mair 2008). The parameter $V_l$ amounts to:

$$V_l = \frac{4V_s}{\pi D^2} \tag{2.7}$$

where $V_s$ is the ground surface settlement volume as Equation (2.8) shows and $D$ is the excavated tunnel diameter

$$V_s = \sqrt{2\pi} * i * S_{max} = 2.5i * S_{max} \tag{2.8}$$

Combining Equation (2.1) and Equation (2.8), the $\mathrm{S}_{max}$ is expressed as Equation (2.9):

$$S_{max} \approx \frac{V_s}{2.5i} = \frac{\frac{V_l \pi D^2}{4}}{2.5i} = \frac{0.314 V_l D^2}{i} \tag{2.9}$$

The magnitude and shape of a surface settlement curve are only decided by the volume loss ratio $V_l$ and the trough width parameter i when tunnel diameter D is known (Xie et al. 2016).

Empirical methods that are used to predict the ground settlement induced by tunneling are relatively simple and commonly used in practice, especially in the early stage of a design. Based on well-known construction conditions, the results that are provided by the empirical methods could be reasonable and trustworthy.

However, empirical methods rely on existing projects, in which it is difficult to generalize all field construction situations for different tunnel geometries, ground conditions, construction techniques, etc. (Loganathan and Poulos 1998). Besides, the empirical methods can only be applied to relatively simple tunneling conditions. Potts and Zdravković (2001) stated that empirical methods usually use uncoupled elastic solutions; however, the realistic tunneling problem is coupled with many influence parameters. Xie et al. (2016) indicated that the empirical methods are not appropriate to predict the ground surface settlement for large tunnel (diameter larger than 10 meters) projects.

With the development of computer technology, numerical analysis is more widely used in the current engineering field to conduct stress-strain analysis using relevant geotechnical properties and construction schemes (Potts and Zdravković 2001). Therefore, the use of empirical methods is preferred to be combined with numerical methods. For instance, empirical methods can often be used to verify the rationality of the results obtained from numerical methods.

## 2.2 Numerical Methods for Prediction of Ground Movement Induced by Tunneling

In this section, some typical numerical methods will be briefly introduced. Also, the reason to choose the FEM in this thesis will be outlined. The main part of this section is used to discuss the applicability of FEM analysis in tunnel excavation in the past decades. Thus, some methods and results of model assembly using numerical methods will be studied.

### 2.2.1 Typical Numerical Methods in Geotechnical Engineering

Four typical numerical methods are widely used in geotechnical engineering (Maidl et al. 2014):

- Finite Difference Method (FDM)
- Discrete Element Method (DEM)
- Boundary Element Method (BEM)
- Finite Element Method (FEM)

The finite difference method was mainly used in geotechnical engineering before the development of the FEM (Desai and Christian 1977). This method has difficulty in applying to non-linear boundaries; thus, it is not widely used in tunneling (Maidl et al. 2014). The discrete element method is designed to resolve the contact situations for the assemblage of irregular particles, like crushed stones, gravel (Munjiza 2004). In the boundary element method, only the boundaries of the simulation area will be discretized instead of the entire model (Maidl et al. 2014). Therefore, BEM is less computationally expensive at the cost of only capable of simulating elastic material behavior.

The FEM was first presented by Clough (1960). It is a method in which a continuum is discretized into small finite elements. The FEM assumes that displacement at any point within the element can be obtained from the displacement at the nodes through interpolation functions (Bobet 2010). Moreover, both plastic and time-dependent behavior of ground and tunnel support can be simulated by FEM (Maidl et al. 2014). Thus, the FEM is a well-established method for modeling of tunneling. The methodology of FEM will be introduced in Section 2.6.

Chapman et al. (2010) proposed that FEM and FDM are most adopted for modeling tunnel projects in continua, such as soils. For modeling in discontinua like rocks, both BEM and DEM are suitable.

### 2.2.2 Numerical Methods in Tunneling

There have been a number of numerical analysis cases in two-dimensions and three-dimensions conducted to assess tunneling-induced ground movement (Rowe et al. 1983; Lee and Rowe 1990; Swoboda 1979; Swoboda et al. 1994; Panet and Guenot 1982; Whittle et al. 2001; Potts and Zdravković 2001; Karakus and Fowell 2005; Gong and Zhou 2008; Gong et al. 2012; Chakeri and Ünver 2014; Zhao and Qi 2014; Zhang et al. 2014; Bian et al. 2016; Xie et al. 2016; Ieronymaki et al. 2017).

The gap parameter method was proposed by Rowe et al. (1983). It was applied in a plane strain elasto-plastic finite element program to estimate the ground deformation induced by the tunneling machine installation of a lined tunnel in soft clay ground. It also helped to perform a parametric study for the parameters influencing the ground surface displacement, such as soil properties, grouting pressure etc. A gap parameter, as shown in Figure 2.2, is the void between actual tunnel diameter and the outer diameter of tunneling machine; it is also the predefined distance between the tunnel crown and the initial ground position before tunnel construction in a finite element mesh. This method incorporates the tunnel construction process into the finite element method. However, the predefined gap parameter in the simulation procedure is essential but hard to be precisely determined by tunnel boring machine and lining characteristics, workmanship quality, and soil type. Rowe et al. (1983) used a drained condition but did not provide a hydraulic situation. It stated that the results obtained from ground surface displacement under the drained condition contain both short-term and long-term deformation.

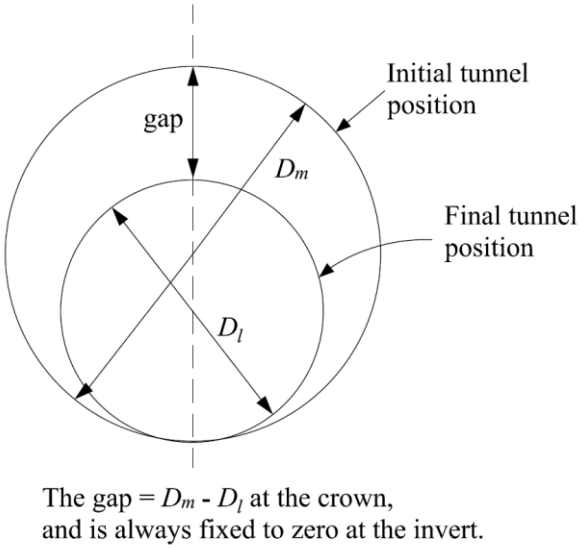


Figure 2.2. The gap method for modeling tunnel excavation (Potts and Zdravković 2001).

The gap parameter method was supported by Lee and Rowe (1990). In their article, a three-dimensional elasto-plastic finite element technique was used to study the stress pattern and ground surface displacement of the surrounding soil in an undrained condition with no lining and, in another case, with a complete lining of the shallow tunnel. Tunneling at shallow depth could lead to displacement, which occurs at or near the ground surface that may induce damage to overlying utilities and buildings. Moreover, the locations and the features of the displacement occurred were studied.

Panet and Guenot (1982) proposed the convergence-confinement method, which is an approach to simulate stress relief of the process between excavation and liner installation at tunnel face, as shown in Figure 2.3. In this method, the unloading of initial soil stresses $\{\sigma_0\}$ by the factor $(1-\lambda)$ is applied at the nodes on the excavation boundaries before liner is installed, where $\lambda$ is gradually increasing from 0 to 1 (Potts and Zdravković 2001). The liner stress is indicated by a prescribed value of $\lambda_d$ to express the liner installation.

Potts and Zdravković (2001) introduced the volume loss control method. Like the convergence-confinement method, volume loss is prescribed on the completion of excavation, replaces the proportion of unloading (Potts and Zdravković 2001; Karakus 2007), see Figure 2.4. $\{F_0\}$, the equivalent nodal forces on the tunnel boundary, represents the pressure exerted by the soil to be excavated. The number of increments $n$ divides the forces to $\{\Delta F\}$, which is applied to the excavation boundary. The equal but opposite $-\{\Delta F\}$ is then exerted at the same boundary for each increment of excavation and after liner installation. The volume loss can be monitored at each increment. When the desired volume loss is reached, the tunnel liner is installed.

Swoboda (1979) and Swoboda et al. (1994) developed a method called progressive softening method for modeling the New Austrian Tunnel Method (NATM) tunneling. The soil stiffness (elasticity modulus) within the tunnel excavation face is softened by multiplying a reduction factor $\beta$ (Potts and Zdravković 2001), as shown in Figure 2.5.

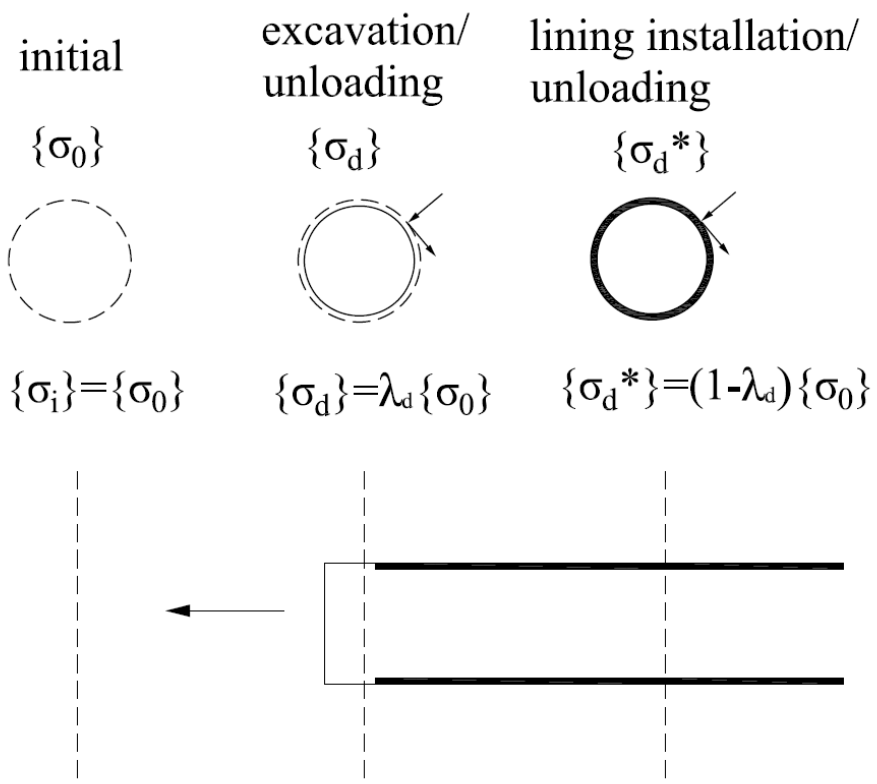


Figure 2.3. Convergence-confinement method (Potts and Zdravković 2001).

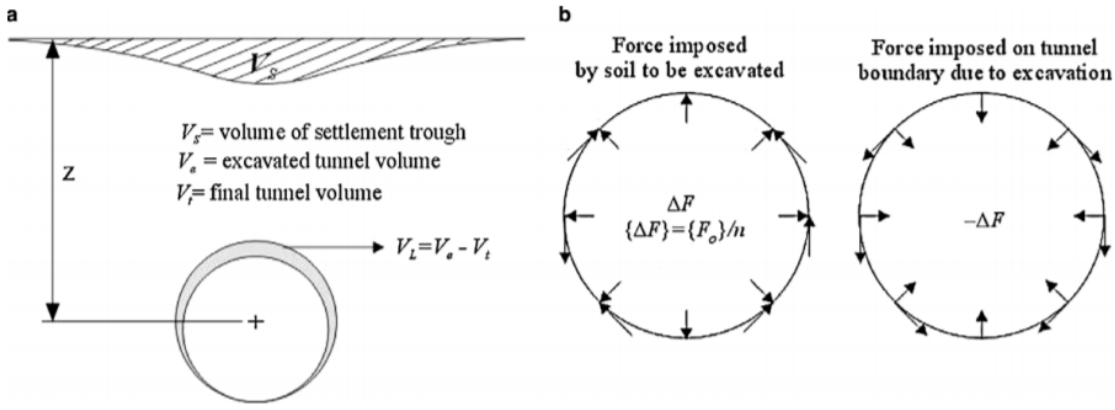


Figure 2.4. (a) Volume loss method; (b) Modeling excavation of solid element (Karakus 2007).

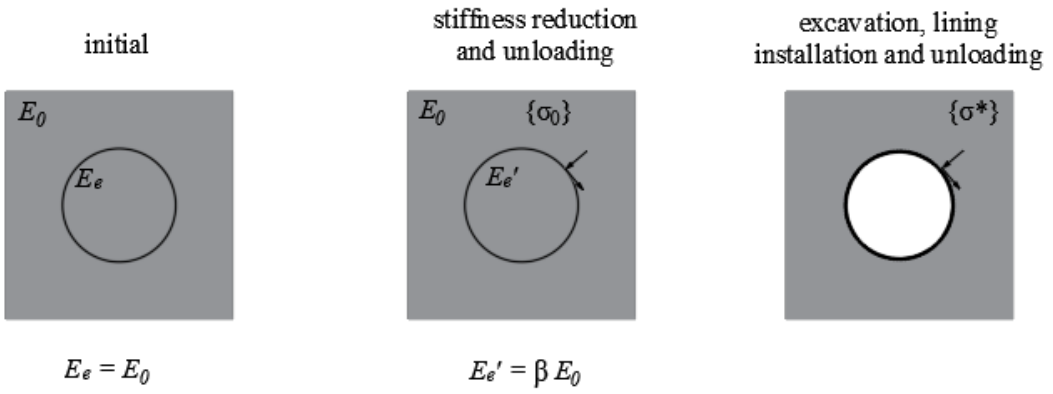


Figure 2.5. Progressive softening method (Potts and Zdravković 2001).

Whittle et al. (2001) combined the analytical method (as shown in Figure 2.6) with numerical modeling to predict ground deformation due to shallow tunneling in non-linear, inelastic soft soils. However, the results only offer a primary understanding of the role of non-linear inelastic soil behavior; also, the three independent cavity deformation parameters are based on the simplified assumption of linear material behavior.

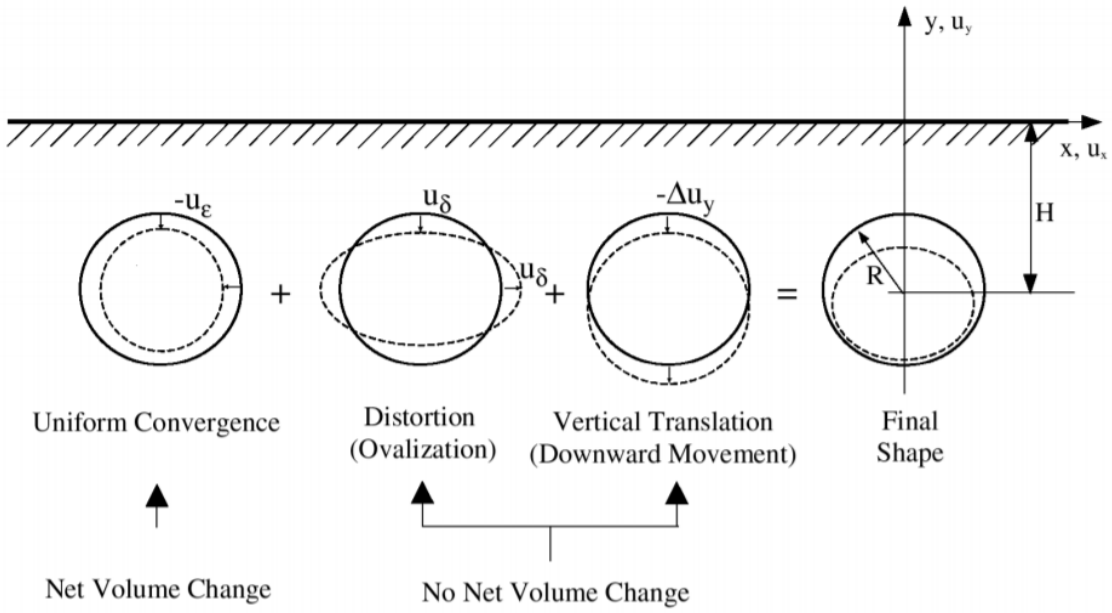


Figure 2.6. Deformation modes for a shallow tunnel cavity according to Whittle et al. (2001).

Similar to Whittle et al. (2001), Ieronymaki et al. (2017) adopted a two-dimensional FEM to simulate twin tunnel construction by Earth Pressure Balance (EPB) machines in London clay. The massive database of laboratory results of London clay was used to calibrate the simulation results of ground movement with different soil models (Mohr-Coulomb and MIT-S1). In addition, the analytical cavity parameters of ground movement were optimized by numerical analysis.

Bian et al. (2016) evaluated the Shanghai soft clay response to shield tunneling for both in short-term and long-term time frame by two-dimensional FEM. The stress reduction method was used to simulate the effect of tunnel excavation. Gong et al. (2012) took a large diameter metro tunnel project to study the influence of EPB shield tunneling on ground deformation. The model was simulated using a three-dimensional FEM. The results provided three main phases of ground deformation, which included before shielding arriving, shield arriving, and backfill grouting. The percentage of total ground deformation of the three phases was 32 %, 45 %, and 23 %, respectively.

The tunnel construction-induced ground movement not only affects the ground surface structure but also influences the existing substructure in the ground. Zhao and Qi (2014) investigated the effects of a new tunnel excavated underneath an existing tunnel. The three-dimensional FEM and analytical equations were taken to determine the subsurface displacement and volume loss under two situations, with and without the large pipe-shed (LPS) ground stabilization system. The results proved that the excavation of the new tunnel could lead to a significant upward movement at the bottom of the burial existing tunnel without the LPS system.

The finite difference method (FDM) is also a useful tool to obtain a detailed and precise result of the prediction of ground deformation due to tunneling. Chakeri and Ünver (2014) incorporated a three-dimensional FDM analysis to the analytical solutions to obtain a new equation for determining the ground displacement. The actual data of existing tunnel projects verified the accuracy of the new equation. Their paper also investigated the percentage of tunnel and soil parameters effects on the maximum surface settlement.

Another three-dimensional FDM model was established to simulate a large diameter EPB shield tunnel in Shanghai by Xie et al. (2016). Field data was taken to validate the numerical analysis results. Also, both field data and numerical results illustrated that the grouting pressure and quality determine the surface displacement rather than the supporting pressure at the working face in order to guarantee the safety of the tunnel construction process. Besides, the empirical method (Peck 1969) and field observation provided that the ground volume loss should be controlled within 0.2 % to keep ground surface displacement within 10 mm.

None of the above numerical analyses involved the tunneling under an existing railway, which the next two journal articles specifically target.

Gong and Zhou (2008) chose a site of Shanghai metro, which was shielding driven under the Hu-Ning railway line. In order to ensure the railway operation has no disturbance due to tunnel construction, a three-dimensional FEM model was established to investigate the effect of tunnel advancement. The maximum ground surface displacement was 23 mm as the tunnel advanced, which kept increasing with tunnel excavation. The locomotive-track dynamic coupling model was chosen to simulate the train loading by using the derail coefficient and the rate of wheel load reduction.

A model using a shield tunnel, driven under an existing railway line, was established by Zhang et al. (2014) through a two-dimensional FEM. To simulate the existing railway, the dynamic freight train load (simulated by CR-live loading) was converted to uniform load and concentrated load by the impact factor in their model. The length of sleepers (crossties) and the train speed are two crucial parameters in their railway simulation. Figure 2.7 shows the trainload model in their

simulation. This trainload model is generally used in the calculation of passing train loading on the bridges, according to UIC (2006). However, it could be adopted to the underground excavations as well. The heaviest train loadings would be exerted on the area above the excavations.

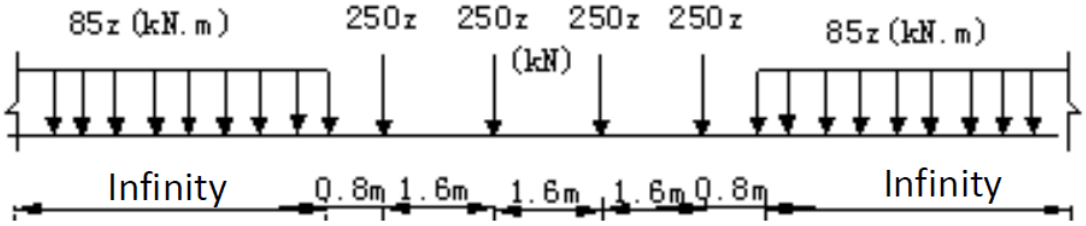


Figure 2.7. CR-live loading for heavy haul railway (Zhang et al. 2014).

The ground subsidence control standard states that the ground surface deformation caused by tunneling should be less than 10 mm to ensure the safety of railway operation (Zhang et al. 2014).

## 2.3 Railway Embankment and Track Loadings

How to express the loadings induced by passing trains in modeling is always a complex issue. The environment concerns, which influence the railway operation, are difficult to simulate. Therefore, it is essential to approximate the train loading calculation method with a reasonable model. In this section, the components of railway embankment will be discussed. In addition, three types of loadings on the track foundation will also be introduced.

### 2.3.1 Railway Embankment – Track Structure

The railway track structure is aimed to ensure the safety and economy of train operation (Selig and Waters 1994). Two types of railway tracks are commonly used, ballasted track and slab track, as shown in Figure 2.8 (a) and (b) (Indraratna et al. 2011; Esveld 2001). Indraratna et al. (2011) indicated that the slab railway tracks are the better options for high-speed and high-intensity traffic lines, providing fewer maintenance and durable service life. However, the principal limitation is the high initial construction cost, which limits the widespread use of slab tracks, making the ballasted tracks still prevalent in many parts of the world.

Ballasted railway tracks are considerably more economical than slab tracks. They are also the most used and practical type of railway structure in North America; and they are easy to design, construct and maintain (Li et al. 2016). Furthermore, the materials can be obtained from domestic sources (timber) (Indraratna et al. 2011). Nevertheless, the high frequency of maintenance can interrupt the rail traffic due to the degradation and fouling of ballast. In this thesis, a ballasted railway track is selected to represent a typical North American railway system.

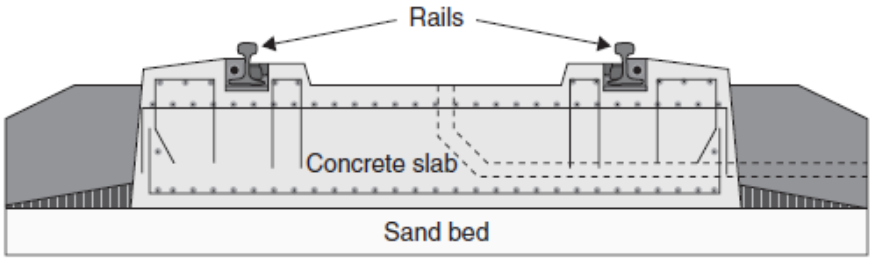


Figure 2.8. (a) Cross-section of slab rail track (Indraratna et al. 2011, Esveld 2001).

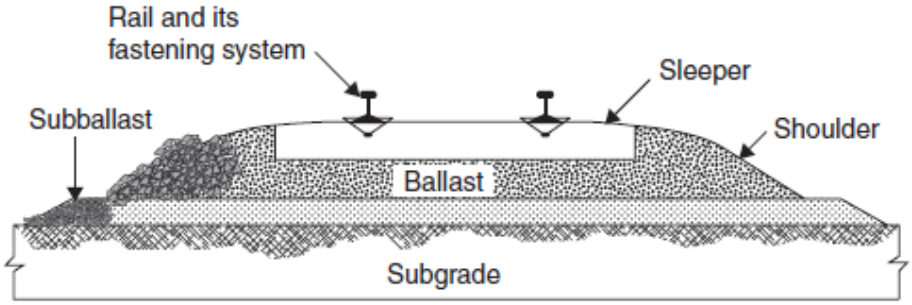


Figure 2.8. (b) Cross-section of ballasted rail track (Indraratna et al. 2011).

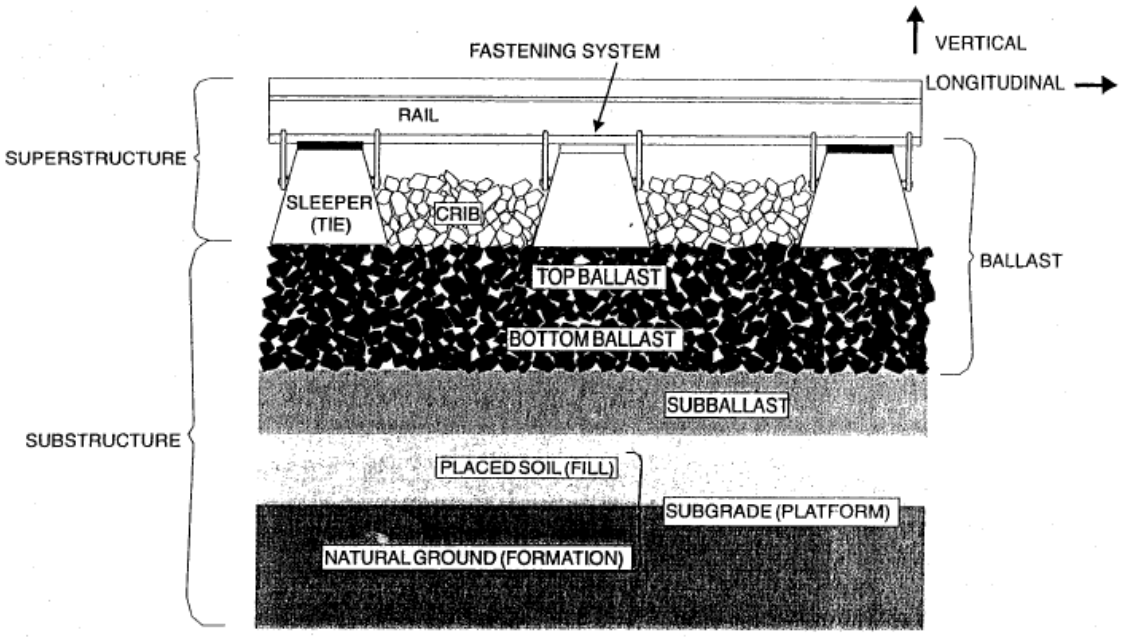


Figure 2.9. Ballasted track structure components (Selig and Waters 1994).

Figure 2.9 illustrates key elements of a typical ballasted railway embankment in the longitudinal direction, which can be classified as superstructure and substructure (Selig and Waters 1994). The superstructure contains the rail, fastening system and sleepers (crossties). The substructure is comprised of ballast, subballast and subgrade. Subgrade contains a layer of soil fill and natural ground. The interface between sleepers and ballast separates superstructure and substructure. In this thesis, this surface is adopted to distribute the train loadings.

Indraratna et al. (2011) summarized the key advantage and purpose of the ballast and subballast. Ballast is a layer assembled from coarse geomaterials, which provides a stable and uniform load-bearing platform for the superstructure. Subballast prevents the migration of ballast materials into the subgrade, it also prevents the relocation of fine particles in the subgrade and water flow into ballast.

### 2.3.2 Track Forces Transmitted to Railway Track Foundation

Three types of track loading can be transmitted to the railway track foundation, namely static, cyclic and dynamic loading (Li et al. 2016). Static loading depends on the train weight and the weight of track and subgrade. The train weight on track foundation is transferred from the point loads at contact points of wheel and rail. The track weight contains rail weight and sleeper (crosstie) weight. The size of rail and cross-section decides rail weight, which can vary from 45 to 75 kg/m (Li et al. 2016). Crosstie weight is based on the type of material and size of the tie. For a typical timber tie, it weighs about 110 kg; while a classic concrete tie weighs 360 kg. Unit weight of each material from track substructure and the depth can determine the weight of track substructure, which is given by Equation (2.10) below (Li et al. 2016):

$$w = \gamma * z \tag{2.10}$$

where $w$ is the weight of track substructure per unit weight area (kg/m$^2$); $\gamma$ is the unit weight of material (kg/m$^3$); $z$ is the depth (m).

According to Li et al. (2016), cyclic loading is produced repeatedly on a railway track while a train operates over it. Cyclic loading can be specified with several elements, such as shape, duration, the magnitude of loading pulse, time interval between consecutive pulses, and the total number of loading pulses. The factors, including axle spacing, truck spacing, and depth of track structure, determine both the interaction of adjacent wheel loads within the track structure and the influence of track responses from adjacent wheel loads. The duration of loading pulse can be calculated by Equation (2.11):

$$t = \frac{L}{V} \tag{2.11}$$

where $t$ is the time duration of loading pulse; $V$ is the train speed; $L$ is the influence length of an axle load or adjacent axle loads for a given depth of ballast or subgrade.

Sun et al. (2015) studied the deformation and degradation mechanisms of railway ballast under high-frequency cyclic loading. Figure 2.10 illustrates that multiple axles of a typical freight train

conduct independent load cycles which indicates that the shorter axle spacing can generate the maximum frequency. The frequency of cyclic loading is expressed in Equation (2.12):

$$f = \frac{V}{L} \tag{2.12}$$

Where $V$ is the train speed; $L$ is the length of adjacent axle loads.

In Sun et al.'s study (2015), the results showed that high frequency loading results in excessive permanent deformation, and it can negatively impact the track performance by generating particle degradation.

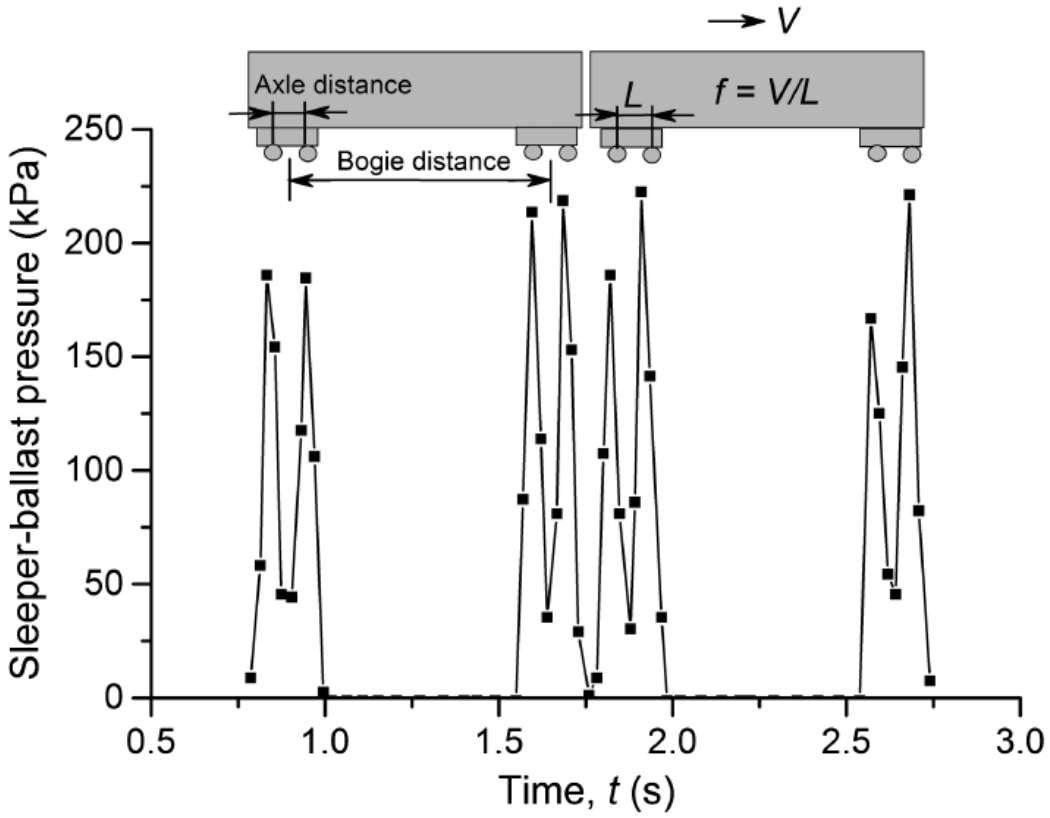


Figure 2.10. Schematic illustration of axles and bogies and record of pressure under the sleeper due to the passage of a freight train (Sun et al. 2015; Indraratna et al. 2010).

Dynamic loading, also called impact loading, can be characterized into short duration forces and long duration forces (Li et al. 2016). The short duration forces are caused by the discontinuities of wheel or rail in a limited track length, which lead to a short duration pulse. The types of discontinuities in wheel and rail are illustrated in Figure 2.11. The main source of long duration forces is due to track geometry irregularities.

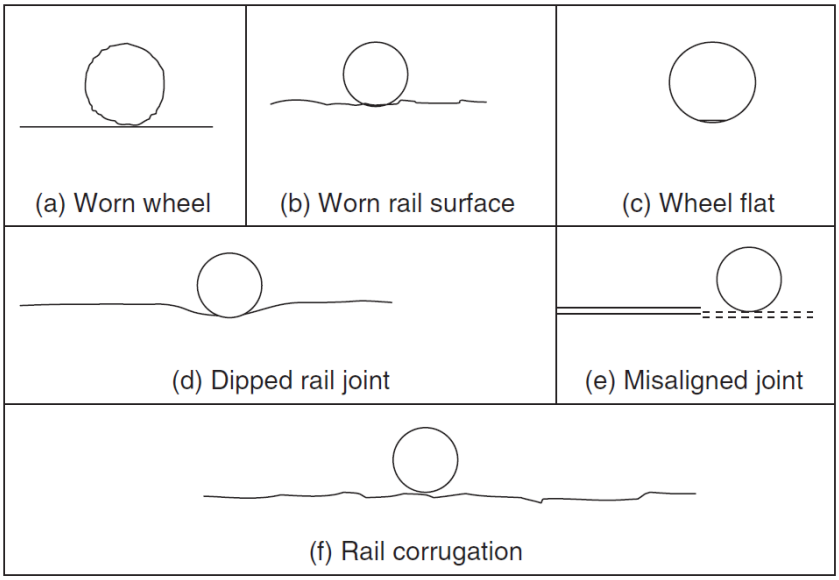


Figure 2.11. Various sources of impact loading in rail track (Indraratna et al. 2011).

Jeffs and Tew (1991) stated some principal aspects that affect the magnitude of dynamic loading, such as train speed, static wheel load and wheel diameter, train weight, and properties of ballast and subballast, etc. Dynamic loading induced by passing trains is a complicated issue to simulate in a model. A commonly used method to determine dynamic loading is increasing static wheel load by a dynamic (impact) factor to estimate the dynamic effect of wheel and rail irregularities (Indraratna et al. 2011; Li et al. 2016). The equation was given as:

$$P_d = \alpha * P_s \tag{2.13}$$

where $P_d$ is the dynamic wheel load (kN); $P_s$ is the static wheel load (kN); $\alpha$ is the dynamic (impact) load factor. Indraratna et al. (2011) indicated that the static load of one wheel should be half of the per axle load.

There are many empirical equations to define the impact factor for the track. Two typical expressions are introduced. AREMA (2012) recommends an equation for calculating dynamic load factor for freight trains only, as shown in Equation (2.14).

$$\alpha = 1 + \frac{0.0052V}{D} \tag{2.14}$$

where $V$ is the train speed (km/h); $D$ is the wheel diameter (m).

While, the Ministry of Railway of the People's Republic of China (2016) provides the equation to obtain the dynamic factor, given as:

$$\alpha = 1 + 0.004V \tag{2.15}$$

where $V$ is the train speed (km/h).

## 2.4 Load Transfer Mechanism

After listing the possible types of track forces, the load transfer mechanism is investigated. The basic transfer process is from track force to sleepers, ballast, subballast and subgrade, as shown in Figure 2.12. As mentioned before, the interface between sleepers and ballast separates the substructure and superstructure. When considering load transfer from running trains to the substructure, this interface is adopted to distribute the train loadings in the simulation models in the thesis. Sadeghi and Barati (2010) concluded that the current practical load transfer mechanism is from vertical static wheel load through the rail, which distributes rail seat loads to certain number of sleepers.

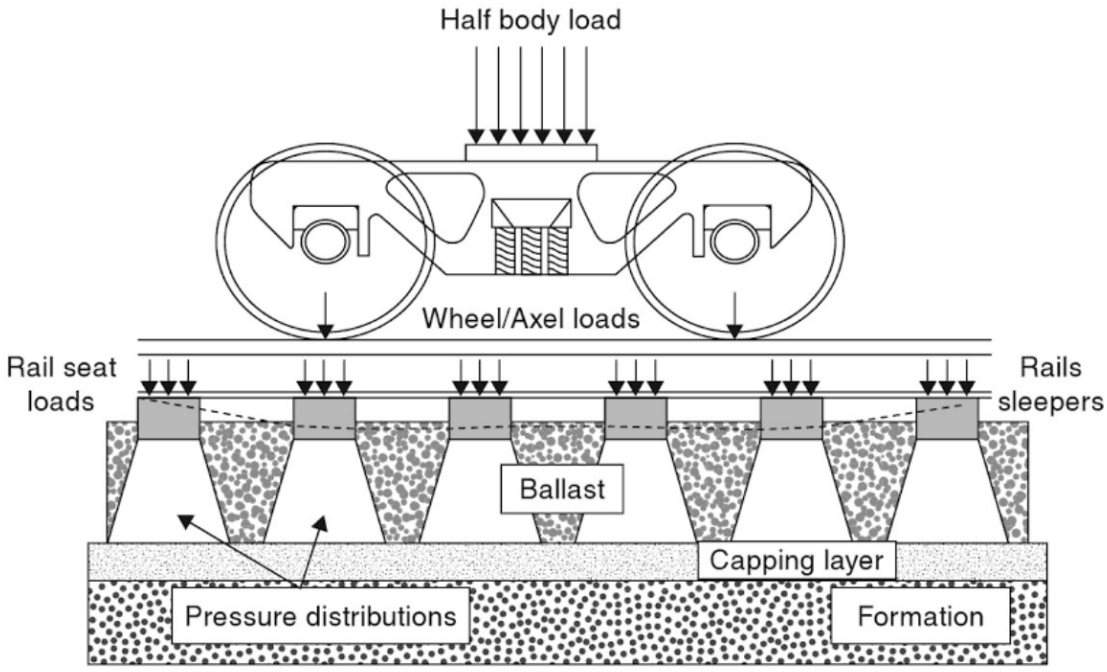


Figure 2.12. Typical wheel load distribution in a track (Indraratna et al. 2011).

Rail seat loads vary with different sleepers located away from the application of the load. The maximum rail seat load is 50 % of wheel load on the sleeper directly under the wheel; the neighboring sleepers support another 25 % (Zhang et al. 2016), as shown in Figure 2.13. Therefore, only three sleepers are affected by one-wheel load. AREMA (2010) suggests determining the maximum rail seat load by the approximate percentage of wheel load distribution factor for an individual sleeper by crosstie spacing, as seen in Figure 2.14. However, Profillidis (2014) proposed to consider the rail seat load distribution along successive sleepers, which involves five sleepers by the influence of one-wheel load, as shown in Figure 2.15: a) 40 % of wheel load to the sleeper directly under; b) 23 % for the first neighboring sleepers; and c) 7 % for second neighboring sleepers. Similarly, Ministry of Railway of the People's Republic of China (2016) indicated that the distribution factor for five sleepers is 0.1: 0.2: 0.4: 0.2: 0.1 to calculate the loading at sleeper-ballast interface exerted by dynamic loadings, as illustrated in Figure 2.16.

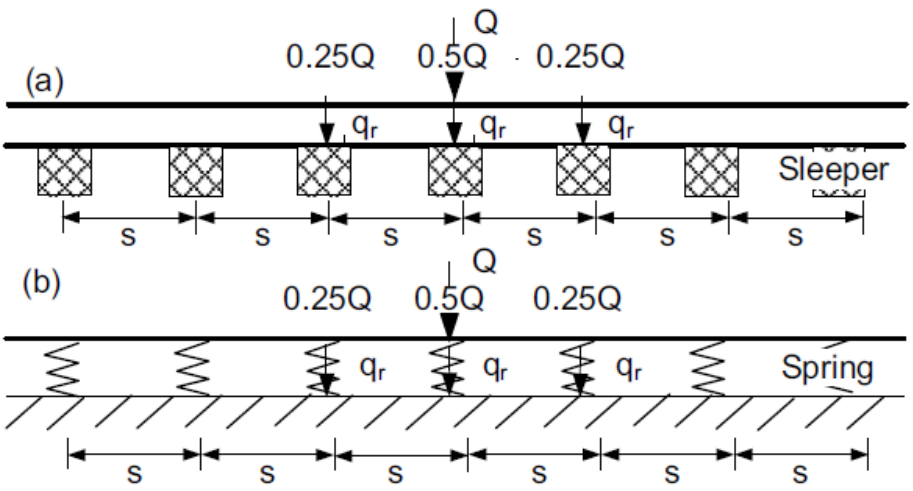


Figure 2.13. Rail seat load determination (Zhang et al. 2016), where Q is the wheel loading; s is crosstie spacing.

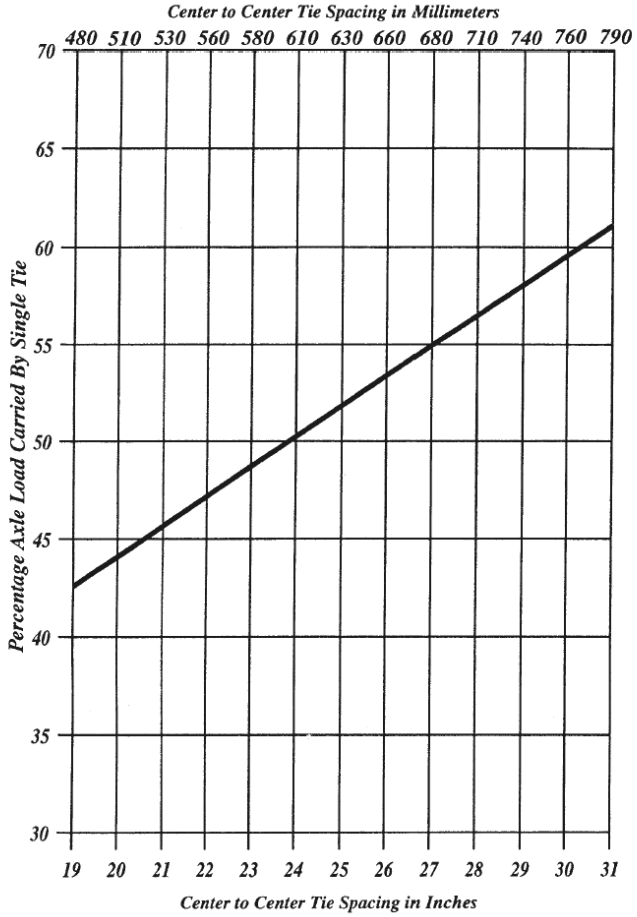


Figure 2.14. Estimated of maximum distribution factor for a single sleeper, AREMA (2010).

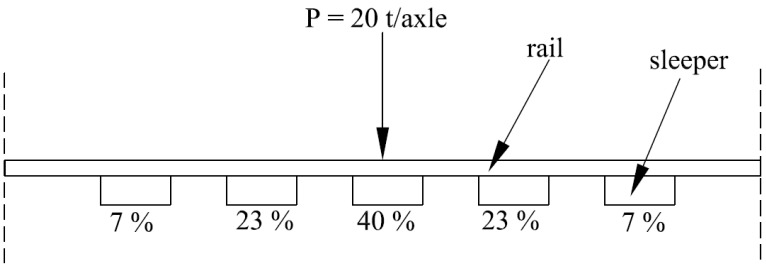


Figure 2.15. Wheel load distribution along successive sleepers (Profillidis 2014).

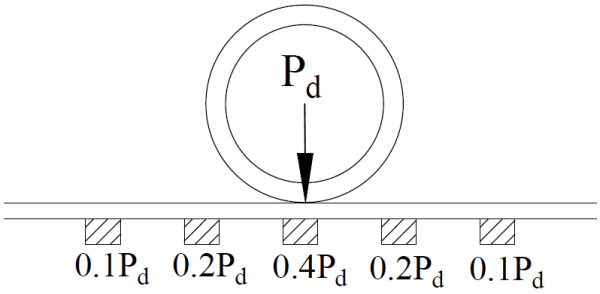


Figure 2.16. Rail seat load distribution (Ministry of Railway of the People's Republic of China 2016), where $P_d$ is the dynamic wheel load.

The average contact pressure (also called average ballast pressure), is treated as external loads in model simulation. AREMA (2010) provided an equation to calculate the average ballast pressure at the interface between sleepers (ties) and ballast. The equation is given as:

$$ABP = [2 * P_s(1 + IF) * DF]/A \tag{2.16}$$

where $P_s$ is the static wheel loading (lb); $IF$ is the impact factor in percentage; $DF$ is the distribution factor in percentage; $ABP$ is average ballast pressure at base of tie (psi); $A$ is the area of contact face ($in^2$), equal to width of sleeper times length ($l$) of sleeper; the equation to determine $IF$ is:

$$IF = \frac{33V}{100D} \tag{2.17}$$

where $V$ is the train speed (mile/h); $D$ is the wheel diameter (inch).

Some methods used the effective length of a sleeper instead of the true length of a sleeper. For the effective length of a sleeper, a few methods are illustrated in Table 2.1, which was summarized by Sadeghi (2012).

Table 2.1 Commonly used equations for determining effective length of sleepers (Sadeghi 2012)

| Developer | Equations |
|---|---|
| Scharamm (Doyle 1980) | $L = \frac{l-g}{2}$ |
| Clarke (Doyle 1980) | $L = l/3$ |
| Australian Standard (2002) | $L = l - g$ |

Note: $l$ is the total length of sleeper; $L$ is the effective length of sleeper; $g$ is the distance between the rail head center and edge of the sleeper, as shown in Figure 2.17.

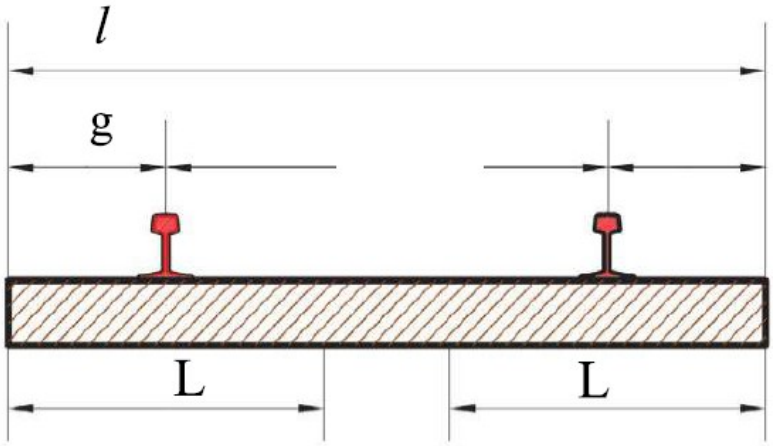


Figure 2.17. Effective length of a sleeper support at rail seat (Sadeghi 2012).

To be noted that, in two-dimensional simulations, the software will assume a one-meter default thickness for the model. Thus, the length of sleeper will be 1m for calculating the average contact pressure exerted in the models.

## 2.5 Key Parameters of the Model

Models in this thesis are created to investigate the surface deformation of the railway embankment overlaying a homogeneous clay soil mass under which a tunnel excavation occurs while the railway is in operation. To present a reliable model, some key parameters need to be set within a reasonable range or as specific values. The three crucial components in the models are the railway system, natural ground, and tunnel. Therefore, this section will discuss each parameter properties for each component.

### 2.5.1 Railway System

(a) Freight Trains

Freight trains contain a locomotive and number of freight cars. In order to estimate train loadings, a train weight and related axle load is required. Also, the train dimensions are important to determine the train loading locations along a longitudinal section. Wheel diameter is a variable parameter for different freight car types. The representative wheel diameter is 920 mm (Johansson 2006). Each parameter is introduced as follows: Table 2.2 summarizes the typical axle load of freight cars around the world. Table 2.3 provides the nominal axle loads applied to the track.

Table 2.2 Typical heavy axle loads of freight cars around the world (Li et al. 2016)

| Country | Axle load (Tonnes) |
|---|---|
| United States and Canada | 33 |
| Australia | 33-35 |
| South Africa | 26-30 |
| Brazil | 27.5-32.5 |
| Sweden | 30 |
| China | 25-27 |

Table 2.3 Number of axles and weight per axle of several rolling stock types (Esveld 2001)

| Car types | Number of axles | Empty (kN) | Loaded (kN) |
|---|---|---|---|
| Trams | 4 | 50 | 70 |
| Light rail | 4 | 80 | 100 |
| Passenger coach | 4 | 100 | 120 |
| Passenger motor coach | 4 | 150 | 170 |
| Locomotive | 4 or 6 | 215 | - |
| Freight wagon | 2 | 120 | 225 |
| Heavy haul (USA, Australia) | 2 | 120 | 250-350 |

Each type of freight car and locomotive has its own dimension. As an example, Figure 2.18 and Table 2.4 illustrate the dimensions of freight cars along the longitudinal direction.

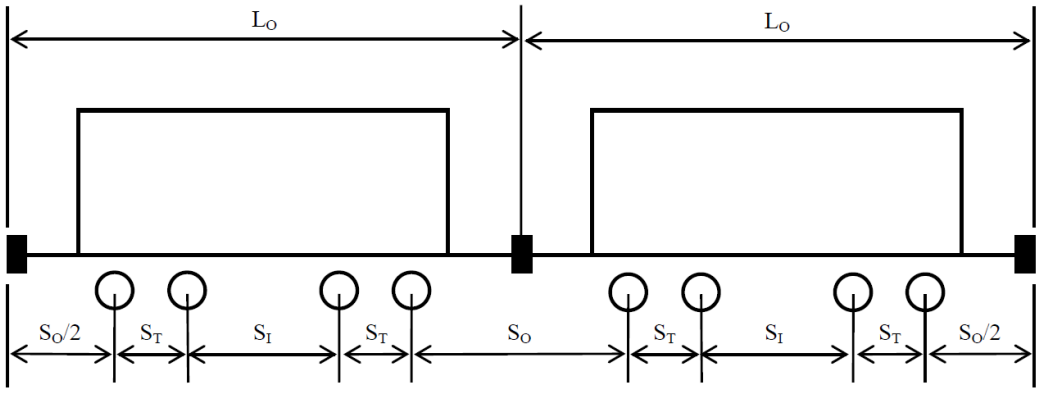


$L_O$ - Overall length of railcar measured over the pulling face of the coupler
$S_I$ - Inboard Axle Spacing, the distance between the inside axles of the railcar
$S_O$ - Outboard Axle Spacing, the distance between the outside axles of the railcar
$S_T$ - Truck Axle Spacing, the distance between the adjacent axles of a truck.

Figure 2.18. Typical dimension for a railcar (Dick et al. 2011).

Table 2.4 Dimensions for locomotives and freight cars (Dick et al. 2011)

| Type | $L_o$ (inches) | $S_o$ (inches) | $S_I$ (inches) | $S_T$ (inches) |
|---|---|---|---|---|
| Six axles Locomotive | 74 | 11.89 | 34.79 | 6.83 |
| Four axles | | | | |
| Sand/Cement Hopper | 41.96 | 6.71 | 23.58 | 5.83 |
| Coal | 53.08 | 6.75 | 34.67 | 5.83 |
| Long Hopper | 69.00 | 6.71 | 50.63 | 5.83 |
| TOFC | 94.67 | 22.83 | 60.17 | 5.83 |

Rail gauge is the spacing between the middle lines of rails (Selig and Waters 1994). Different regions have different design for rail gauge, as displayed in Table 2.5. The most common value is 1.435 m.

Table 2.5 Rail gauge values (Selig and Waters 1994)

| Location | Gauge (mm) | Gauge (in.) |
|---|---|---|
| North America | 1435 | 56.5 |
| Europe | 1435-1668 | 56.5-65.7 |
| South Africa | 1065 | 41.9 |
| Australia | 1524-1676 | 42-63 |
| China | 1435 | 56.5 |

(b) Train Speed

As shown in Table 2.6, the maximum freight train speed is 120 km/h (75 miles/h). Usually, the train speed during the tunnel construction should be controlled to be below 120 km/h (Zhang et al. 2014). Thus, the most unfavorable situation of train loading is when train speed is 120 km/h. As a note, zero train speed means the train is stationary.

Table 2.6 Maximum speeds for different railway lines (Esveld 2001)

| Type of railway lines | Passenger trains | Freight trains |
|---|---|---|
| Branch lines | / | 30-40 km/h |
| Secondary lines | 80-120 km/h | 60-80 km/h |
| Main lines | 160-200 km/h | 100-120 km/h |
| High speed lines | 250-300 km/h | / |

(c) Sleeper (Crosstie) Dimensions

Sleepers (crossties) normally can be made of timber, concrete and steel. Wooden materials are easier to obtain than concrete and steel ties. Also, steel ties are considerably expensive than timber ties. The concrete ties perform well on resisting movement, but the fracturing problem can become serious under the high cyclic and impact loads from heavy haul freight trains (Indraratna et al. 2011).

For timber ties, being the most popular type, the standard dimension for heavy axle load freight trains in North America is 0.152 m or 0.178 m in height, 2.59 m in length and 0.229 m in width. The tie spacing, the spacing between crosstie centers, in this case, takes the typical value of 0.495 m (19.5 inches) (Selig and Waters 1994). Some typical tie dimensions are illustrated in Table 2.7. Also, cross-sectional dimensions of crossties are illustrated in Figure 2.19 and Figure 2.20.

Table 2.7 Typical tie dimensions (Selig and Waters 1994)

| Location | Material | Width (mm) | Length (mm) | Spacing (mm) |
|---|---|---|---|---|
| Australia | Wood | 210-260 | 2000-2743 | 610-760 |
| | Concrete | / | / | 600-685 |
| China | Wood | 190-220 | 2500 | 543-568 |
| | Concrete | 240-290 | 2500 | 568 |
| Europe | Wood | 250 | 2600 | 630-700 |
| | Concrete | 250-300 | 2300-2600 | 692 |
| North America | Wood | 229 | 2590 | 495 |
| | Concrete | 286 | 2629 | 610 |
| South Africa | Wood | 250 | 2100 | 700 |
| | Concrete | 203-254 | 2057 | 700 |
| | | 230-300 | 2200 | 600 |

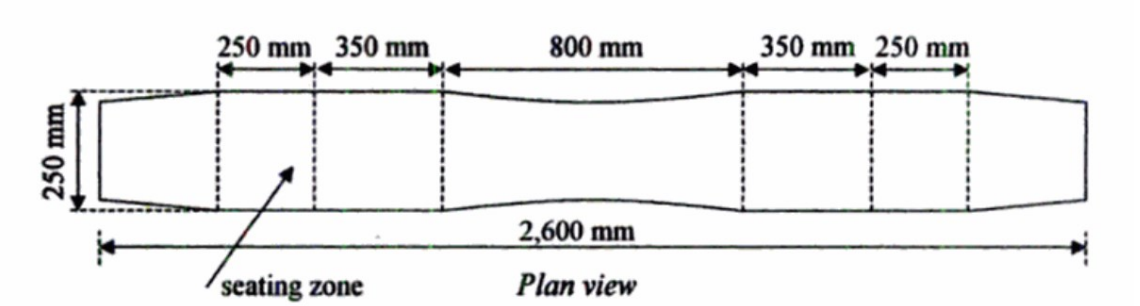


Figure 2.19. Geometrical characteristics of timber sleepers in standard gauge tracks (Profillidis 2014).

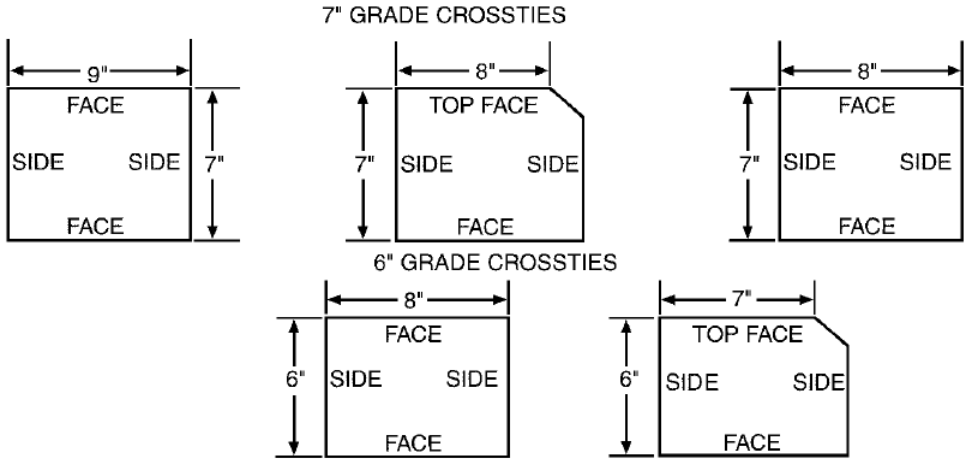


Figure 2.20. Size categories for 7-inch and 6-inch crossties (AREMA 2010).

(d) Substructure Component Material Properties

As discussed before, the substructure of railway embankment is comprised of ballast, subballast and subgrade. According to the suggestion of AREMA (2010), the minimum depth of ballast is required to be 12 inches (300 mm) for standard rail gauge. The total depth of ballast and subballast is needed to satisfy the minimum value of 24 inches (600 mm). Different countries and railway organizations have various requirements for embankment materials. In general, ballast materials are chosen from locally available geomaterials, which must be angular, uniformly graded, strong, and durable to support train loads and resist harsh environmental conditions (Indraratna et al. 2011). Nominal ballast size is 60 mm. Some hard rocks are alternative, such as granite, quartzite, and carbonate rocks (AREMA 2010). Subballast shall be granular materials; aggregates include crushed stone, natural or crushed gravels, natural or manufactured sands, crushed slag, or a homogeneous mixture of these materials. Table 2.8 to Table 2.12 show some typical material properties of ballast and subballast.

Table 2.8 Material properties of ballast, subballast (Profillidis 2014)

| Material | Elasticity modulus (MPa) | Poisson's ratio | Cohesion (kPa) | Friction angle (◦) |
|---|---|---|---|---|
| Ballast | 127.49 | 0.2 | 0.00 | 45 |
| Gravel subballast | 196.13 | 0.3 | 0.00 | 35 |

Table 2.9 Range of elastic moduli for crushed stone (Pavement Interactive n.d.)

| Name | Elastic modulus (MPa) |
|---|---|
| Crushed stone | 150-300 |

Table 2.10 Material properties of railway embankment (Xu et al. 2010)

| Name | Thickness (m) | Friction Angle (°) | Cohesion (kPa) | Unit weight ($kN/m^3$) | Poisson's ratio | Young's modulus (MPa) |
|---|---|---|---|---|---|---|
| Graded gravel | 0.40 | 60.00 | 0.00 | 19.6 | 0.15 | 119.99 |
| AB-group soil | 0.1 | 30.00 | 20.00 | 19.6 | 0.15 | 60.00 |
| Filled soil | 0.1 | 30.00 | 15.00 | 19.13 | 0.2 | 15.00 |
| Gravel subcrust | 0.40 | 60.00 | 0.00 | 19.6 | 0.15 | 119.99 |

Table 2.11 Material properties of railway embankments (Li et al. 2016)

| Name | Density ($Mg/m^3$) | Poisson's ratio | Modulus (MPa) | Thickness (m) |
|---|---|---|---|---|
| Ballast | 1.76 | 0.3 | 276 | 0.3 |
| Subballast | 1.92 | 0.35 | 138 | 0.15 |
| Subgrade | 1.92 | 0.35 | 41 | infinite |

Table 2.12 Material properties ranges of ballast and subballast (Li et al. 2016)

| Name | Resilient modulus (MPa) | Poisson's ratio | Friction angle (°) |
|---|---|---|---|
| Ballast | 140-550 | 0.3 | 40-55 |
| Subballast | 55-105 | 0.3-0.4 | 25-40 |

### 2.5.2 Natural Ground Material Properties

In this thesis, the ground is defined as a soft soil because it is susceptible to deformation induced by the tunnel construction. Moreover, the soil experiences surface displacement due to tunnel construction and train operation, thus elastic and plastic deformation will be experienced. Ground conditions could determine the behavior of soil when the external loads are applied. There are many actual projects of tunnel construction in soft ground, providing ample information about soil conditions, which will be introduced as follows. Based on the ground soil properties summarized in Appendix A, the functional parameters' ranges of soft ground soil are defined in Table 2.13.

The unit weight is a basic parameter of soil. In a traditional Mohr-Coulomb constitutive model, the internal friction angle and cohesion determine the shear strength of a soil mass. The Young's modulus and Poisson's ratio are two parameters that describe the elastic deformation of a soil material. These key parameters express the property of a soil.

Table 2.13 The credible range of soil functional parameters

| Name | $\gamma$ (kN/m$^3$) | $v$ | $\varphi$ (°) | $c$ (kPa) | $E$ (MPa) |
|---|---|---|---|---|---|
| Mucky clay | 16.8-17.1 | 0.35-0.35 | 9.0-10.0 | 14.0-15.0 | / |
| Clay | 16.5 | 0.35 | 14.0 | 20.0 | 20.0 |
| Silty clay | 17.7-19.4 | 0.28-0.38 | 13.5-30.0 | 14.0-18.0 | 5.27-25.0 |
| Hard clay | 17.2 | 0.40 | 20.0 | 25.0 | 28.0 |
| Clay-silt | 19.0 | 0.35 | 27.0 | 40.0 | 30.0 |
| Sandy silt | 18.2 | 0.24 | 30.3 | 3 | 45.0 |
| Dense sand | 19.0 | / | 35.0 | / | 24.0 |
| Very dense sand | 19.5 | / | 35.0 | / | 30.0 |

Note: $\gamma$ unit weight, $v$ Poisson's ratio, $\varphi$ internal friction angle, $c$ cohesion, $E$ Young's modulus, $e$ void ratio, $K_0$ lateral earth pressure coefficient at rest. (Xie et al. 2014; Zhang et al. 2014; Chakeri and Ünver 2014; Ercelebi et al. 2011; Ocak 2014; Zhao and Qi 2014; Huo et al. 2011; Xiao and Zhang 2011; Zhang et al. 2005; Cao and Wei 2008).

### 2.5.3 Tunnel

There are some key geometric properties of tunnels that can affect the ground surface deformation, such as tunnel diameter, tunnel depth, etc. (Zhou et al. 2017). The following information in this section provides reasonable ranges of tunnel diameter and depth obtained from existing tunnel projects. In addition, some typical tunnel support parameters and tunnel shapes are introduced as well.

(a) Dimension of a Tunnel

According to reported engineering cases in recent years, typical tunnel geometries can be summarized as follows. Generally, based on the data found in literature, tunnel dimension ranges from 2.47 m to 14.27 m in diameter. Considering the influence of tunnel excavation depth on ground surface displacement, this thesis focuses on both shallow and deep tunnels. Based on the

data, the typical range of overburden depth can be defined as 9 m - 35 m. In addition, overburden depth/tunnel dimension (H/D) is identified as an important parameter, which helps to design a tunnel. Typical values are shown in Table 2.14.

Table 2.14 Relation between overburden depth and external dimension of a tunnel

| No. | Name of tunnel | Overburden depth (m) | External dimension (m) | Depth/Diameter (H/D) |
|---|---|---|---|---|
| 1 | Yingbin San Road Tunnel | 14 | 14.27 | 0.98 |
| 2 | Power cable tunnel | 12 | 6.6 | 0.33 |
| 3 | Istanbul Metro Line | 9.7-16 | 6.3-6.54 | 1.54-2.45 |
| 4 | Tehran Metro Line 7 | 20.8 | 8.85 | 2.35 |
| 5 | Shenyang Metro Line 2 | 15 | 5 | 3 |
| 6 | New Jiuyanshan Tunnel | 22 | 13.8 | 1.59 |
| 7 | Suzhou Metro Tunnel | 12.4 | 6.2 | 2 |
| 8 | Binhai Mass Transit | 22 | 6.2 | 3.55 |
| 9 | Tunnel A | 20 | 6.34 | 3.15 |
| 10 | Shanghai Metro Line 11 | 9.0-11.08 | 6.2 | 1.45-1.79 |
| 11 | Heathrow Express Trail Tunnel, UK | 19 | 8.5 | 2.24 |
| 12 | Thunder Bay Tunnel, Canada | 10.7 | 2.47 | 4.33 |
| 13 | Barcelona Subway Network Extension Tunnel, Barcelona | 10.0 | 8.0 | 1.25 |
| 14 | Bangkok Sewer Tunnel, Thailand | 18.5 | 2.66 | 6.95 |
| 15 | Crossrail Project Tunnel, UK | 35 | 7.1 | 4.93 |

Note: References displayed in order.: Xie et al. (2016); Zhang et al. (2014); Ercelebi et al. (2011) and Ocak (2014); Chakeri and Ünver (2014); Yang et al. (2009); Zhao and Qi (2014); Huo et al. (2011); Xiao and Zhang (2011); Zhang et al. (2005); Cao and Wei (2008) and Gong and Zhou (2008) and Lv and Zhou (2007); Loganathan and Poulos (1998) and Deane and Bassett (1995); Loganathan and Poulos (1998) and Lee et al. (1992) and Palmer and Belshaw (1980); Loganathan and Poulos (1998) and Ledesma and Romero (1997) and Phienwej (1997); Loganathan and Poulos (1998) and Ramasamy (1992); Ieronymaki et al. (2017).

Later on, in the research, the importance of H/D will be studied to establish a relationship between overburden depth and the outer dimension of a tunnel and how the two parameters influence the magnitude of ground surface deformation.

(b) Tunnel Support and Reinforcement Measures

For construction of tunnel structures in a soft ground, it should generally be the intention to preserve the load-bearing capacity of the surrounding area. Reinforcement of soil is mainly used to control deformation in an acceptable scale. According to existing projects, lining and grouting are two main measures that are normally used.

Lining, as a preliminary tunnel support method, helps resist the excavation from collapsing. Also, grouting is an efficient and crucial reinforcement measure to avoid or control ground subsidence in a tunnel construction area (Maidl et al. 2014). Zhang et al. (2014) simulated a tunnel lining

structure as an elastic uniform-rigidity ring and modeled the grouting reinforcement by increasing compression modulus of soil to 15 MPa. Table 2.15 to Table 2.18 summarize some other lining and grouting parameters from real tunnel construction projects.

Table 2.15 Properties of tunnel lining (Xie et al., 2016)

| Tunnel lining | Thickness (m) | Density (kg/m$^3$) | Young's modulus (MPa) | Poisson's ratio |
|---|---|---|---|---|
| Value | 0.6 | 2,500 | 28,800 | 0.167 |

Table 2.16 The parameters of the supporting system (Large Pipe-shed) (Zhao and Qi 2014)

| Properties | Bulk modulus (MPa) | Shear modulus (MPa) | Bulk density (kg/m$^3$) | Friction angle (°) | Cohesion (MPa) |
|---|---|---|---|---|---|
| Value | 600 | 210 | 2,350 | 40 | 0.250 |

Table 2.17 Comparison between mechanical parameters of original and reinforced soils (Zhou et al. 2002)

| Soil | Unit weight (kN/m$^3$) | Young's modulus (MPa) | Cohesion (kPa) | Friction angle (°) |
|---|---|---|---|---|
| Original | 18.3 | 3.74 | 13.4 | 20.2 |
| Grouted | 19.1 | 5.41 | 18.7 | 26.4 |
| Enhanced rate (%) | / | 45 | 40 | 30 |

Table 2.18 Properties of tunnel lining (Gong and Zhou 2008)

| Properties | Thickness (m) | Young's modulus (GPa) | Unit weight (kN/m$^3$) | Poisson's ratio |
|---|---|---|---|---|
| Value | 0.35 | 30 | 24 | 0.3 |

(c) Tunnel Shape

Hung et al. (2010) introduced some classical tunnel shapes, as shown in Figure 2.21. The selection of tunnel shape mostly depends on the tunneling method and ground conditions. The circular tunnel is normally constructed by tunnel boring machines in soils. Thus, the circular tunnel shape is chosen to simulate this in the models considered in the thesis.

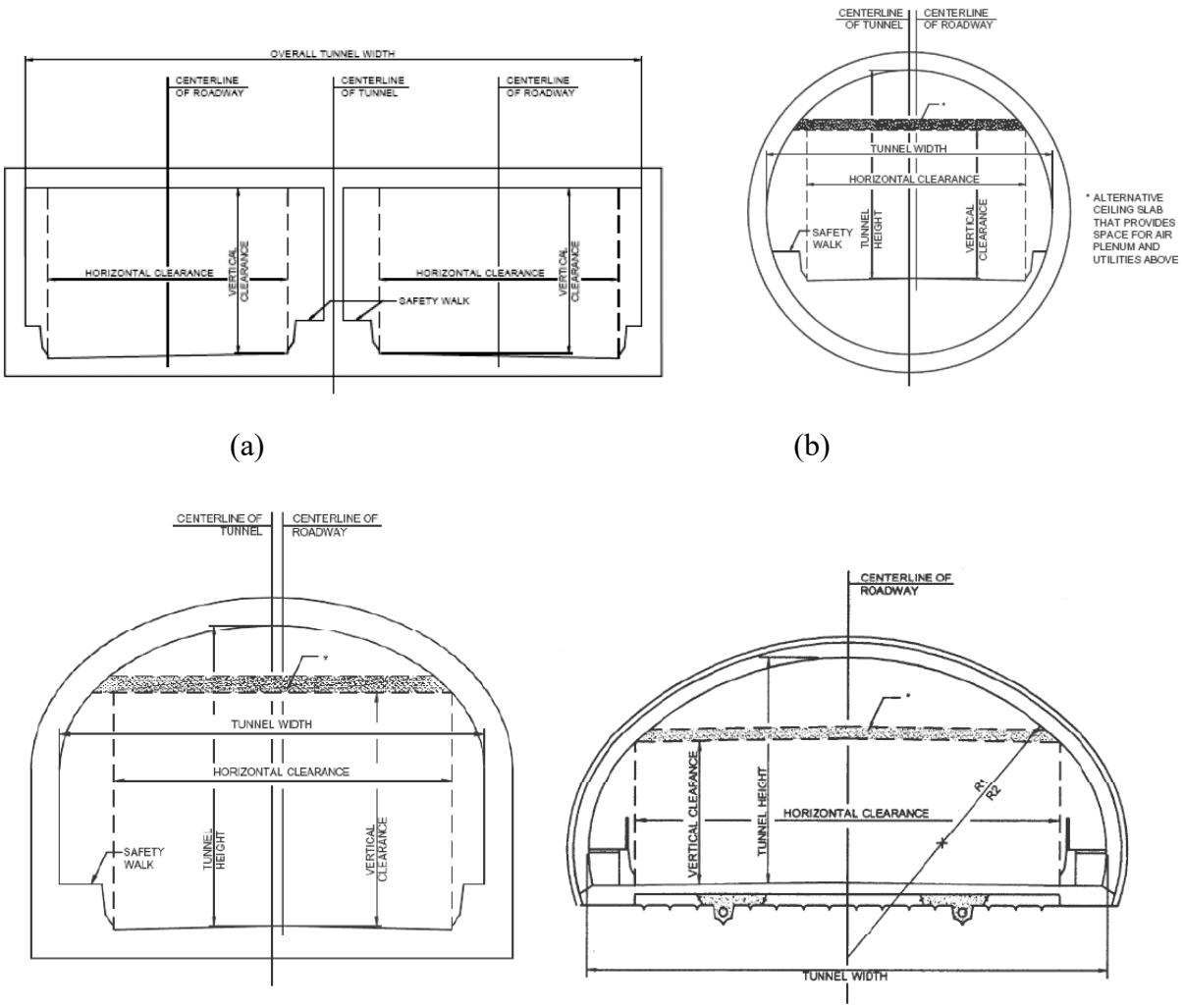


Figure 2.21. (a) Two cell rectangular tunnel; (b) Circular tunnel; (c) Horseshoe and Curvilinear Oval) tunnel (Hung et al. 2010).

## 2.6 FEM Methodology

The FEM is based on the representation of a body or a structure by an assemblage of subdivisions called finite elements (Potts and Zdravković 1999). These elements are connected at nodes. Displacement functions are chosen to approximate the variation of displacements over each finite element. Polynomial functions are commonly employed to approximate these displacements. Equilibrium equations for each element are obtained by means of the principle of minimum potential energy. These equations are formulated for the entire body by combining the equations for the individual elements so that the continuity of displacements is preserved at the nodes. The

resulting equations are solved satisfying the boundary conditions to obtain the unknown displacements. The entire procedure of the FEM involves six steps, as introduced by Potts and Zdravković (1999).

(a) Element Discretization

Element discretization is a process, which divides a geometry of the problem into many small parts, in terms of finite elements, in a certain domain. Nodes connect each element and form the element boundary. Thus, these finite elements assemble an equivalent mesh, which represents the geometry of a problem. In two-dimensional finite element analysis, triangular and quadrilateral elements are normally used (Figure 2.22).

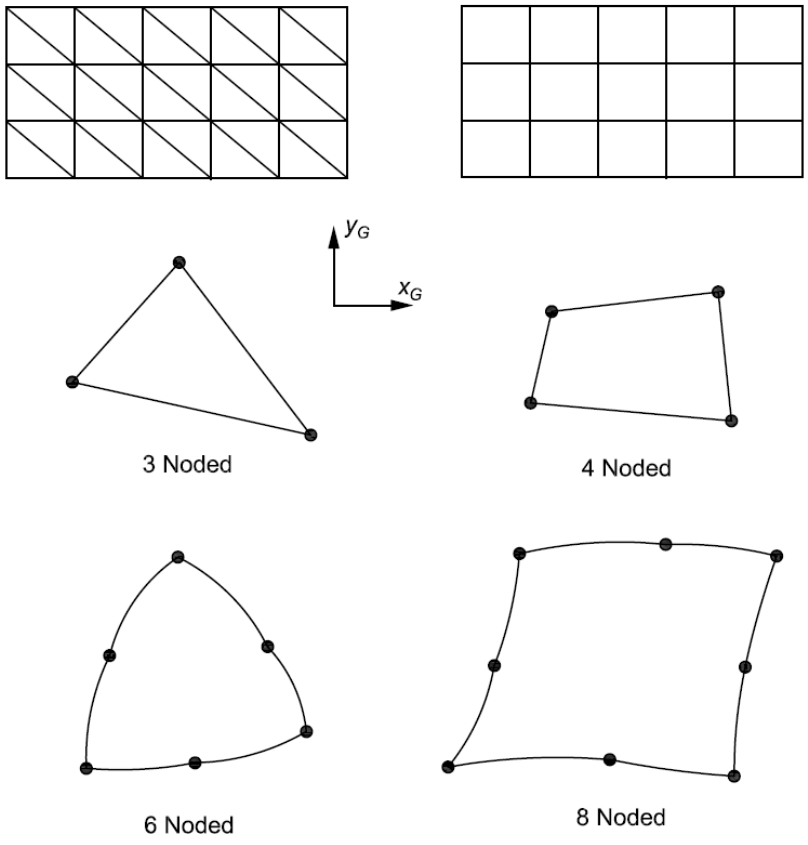


Figure 2.22. Typical two-dimensional finite elements (Potts and Zdravković 1999).

The fine mesh of small elements is required to bring in accurate results. To refine the mesh elements, mid-side nodes between nodes in an element boundary will be added. At the same time, thin elements should be avoided because they can lead to large errors in the solution. Normally, the ratio between the longest and shortest sides of an element should be smaller than 5:1 for quadrilateral elements. Triangle shaped elements are commonly adopted for excavations in two-dimensional model simulations.

(b) Primary Variable Approximation (Displacement Approximation)

The primary unknown quantity in displacement-based FEM is the displacement field, which varies over the model domain. In two-dimensional plane strain situations, the two global displacements $u$ and $v$ characterize the displacement field in $x$ and $y$ coordinate directions, respectively. The approximation is to assume a simple polynomial form for the displacement components of each element. Then, the displacement components, as variations, are expressed in terms of their values at the nodes. For some elements with curved sides, the interpolation functions can express the element displacement and element geometry.

(c) Element Equations

Element equations govern the deformational behavior of each element. Those equations can be derived by using variational principles (e.g. Minimum potential energy):

$$[K_E]\{\Delta d_E\} = \{\Delta R_E\} \tag{2.18}$$

where $[K_E]$ is the element stiffness matrix; $\{\Delta d_E\}$ is the vector of incremental element nodal displacements; $\{\Delta R_E\}$ is the vector of incremental element nodal forces.

(d) Global Equations

Combining the separate equations of each element to assemble the global equations, which provides a stiffness relation for the entire system. The equations can be formed as:

$$[K_G]\{\Delta d_G\} = \{\Delta R_G\} \tag{2.19}$$

where $[K_G]$ is the global stiffness matrix; $\{\Delta d_G\}$ is the vector of all incremental nodal displacements; $\{\Delta R_G\}$ is the vector of all incremental element nodal forces.

(e) Boundary Conditions

Applying boundary conditions, which are defined by load and displacement conditions, help to set up the global system. Loading conditions, such as line loads, surcharge pressure and body force, affect $\{\Delta R_G\}$. Displacement boundary conditions affect $\{\Delta d_G\}$. For two-dimensional plane strain problems, the prescribed displacement must be defined for nodes in $x$ and $y$ coordinate directions.

(f) Solution of Global Equations

A great number of simultaneous equations will be formed after establishing the global stiffness matrix and adding boundary conditions. The solution of the equations gives values to nodal displacements $\{\Delta d_G\}$ as primary computation quantities. Afterward, stresses and strains as secondary quantities can be evaluated.

## 2.7 Convergence Criteria

The convergence of finite element analysis is a complex issue. The software used in this thesis (RS2) uses a non-linear spring subjected to a single force to explain the finite element solution process, the convergence criteria and the iteration stopping criterion (Rocscience Inc. 2019). The relationship between the applied load $P$ and the displacement $U$ is shown as:

$$KU = P \tag{2.20}$$

where $K$ is the non-linear stiffness of spring; it is also a function of displacement, $K = K(U)$. Finite element analysis curve in Figure 2.23 represents the response of spring to applied loads.

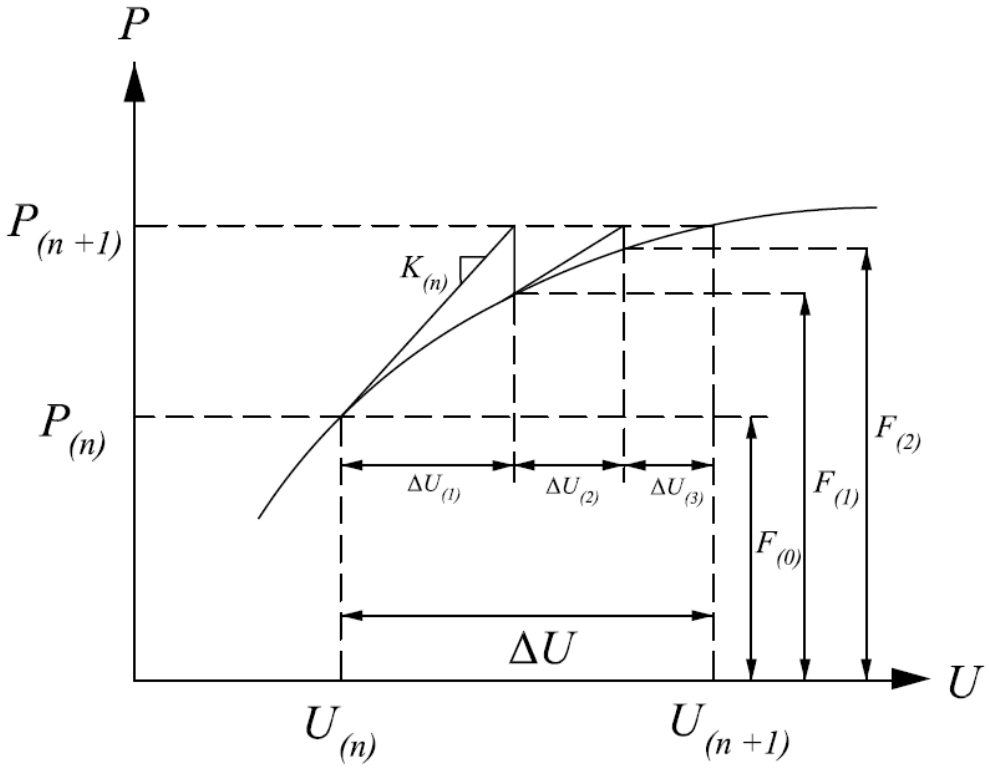


Figure 2.23. The non-linear response of a spring to applied load (Rocscience Inc. 2019).

According to Figure 2.23, the process of finite element solution can be explained as follows. Assuming the solution for displacement $U_{(n)}$ is known after $P_{(n)}$ load is applied to the spring. Before the new load applied to the spring, the internal force or resisting force of the spring is $F_{(0)}$, which is in equilibrium with $P_{(n)}$. The displacement increment $\Delta U$ is subjected to the new applied load $P_{(n+1)}$. The key is to update displacement $U_{(n+1)}$ to approach the real solution. The first iteration starts from calculating the tangent stiffness of spring $K_{(0)}$, at the origin point $(U_{(n)}, P_{(n)})$ of the curve. Then, the linear part of the line of $K_{(0)}$ intersects $P_{(n+1)}$. At this point, the

displacement increment $\Delta U_1$ from the first iteration can be determined. Thus, the current displacement is updated to $U_{(n+1)=}U_{(n)} + \Delta U_1$; and a new internal force $F_{(1)}$ is obtained in the spring. The load imbalance or force error at this stage is $P_{(n+1)} - F_{(1)}$, which is large as displayed in Figure 2.23. The purpose of all iterations in FEM analysis is to reduce the load imbalance to zero. The next iteration to calculate $K_{(1)}$ begins at the new displacement $U_{(n+1)}$ and applies the same $P_{(n+1)}$. According to the previous procedure, it can obtain the displacement increment $\Delta U_2$. Therefore, the current displacement is $U_{(n+1)=}U_{(n)} + \Delta U_1 + \Delta U_2$; and the new internal force $F_{(2)}$ can also be determined. The value of $P_{(n+1)} - F_{(2)}$ in this iteration is much smaller than the previous one. As the iteration process continues, the load imbalance and the displacement increment are both getting smaller and approaching zero. To avoid unnecessary iterations, a stopping criterion can help to reduce the processing time when the results are adequately close to the real solution.

The RS2 program will check two conditions at the same time; absolute energy and absolute force criterions. The Equation (2.21) and (2.22) for the two criterions are shown as follow, respectively:

$$\left|\frac{\Delta U_{(i)}^T (P_{(n+1)} - F_{(i)})}{\Delta U_{(0)}^T (P_{(n)} - F_{(0)})}\right| < (specified\ energy\ tolerance) \tag{2.21}$$

$$\left|\frac{(P_{(n+1)} - F_{(i)})}{(P_{(n+1)})}\right| < (specified\ \ tolerance) \tag{2.22}$$

where $i = 0,1,2$ ...n is the iteration number.

The absolute energy criterion means the iteration can stop when the current displacement increment is sufficiently smaller than the initial displacement. On the other hand, the absolute force criterion only considers the load imbalance. When the current load imbalance becomes a small fraction of the current load level, the iteration can stop.

## 2.8 Constitutive Models for Soils

This section provides the background information of constitutive models, which describes the physical behavior of these materials. Both elastic models (Hooke's law) and elasto-plastic models (Mohr-Coulomb) will be introduced.

### 2.8.1 Elastic Model

Hooke's law correlates stresses and strains for a linear, isotropic, elastic soil (Budhu 2010). For a general state of stress (Figure 2.24), elastic stress-strain constitutive equation (Equation (2.23)) of Hooke's law is as follow:

$$\begin{Bmatrix} \varepsilon_x \\ \varepsilon_y \\ \varepsilon_z \\ \gamma_{xy} \\ \gamma_{yz} \\ \gamma_{zx} \end{Bmatrix} = \frac{1}{E} \begin{bmatrix} 1 & -v & -v & 0 & 0 & 0 \\ -v & 1 & -v & 0 & 0 & 0 \\ -v & -v & 1 & 0 & 0 & 0 \\ 0 & 0 & 0 & 2(1+v) & 0 & 0 \\ 0 & 0 & 0 & 0 & 2(1+v) & 0 \\ 0 & 0 & 0 & 0 & 0 & 2(1+v) \end{bmatrix} \begin{Bmatrix} \sigma_x \\ \sigma_y \\ \sigma_z \\ \tau_{xy} \\ \tau_{yz} \\ \tau_{zx} \end{Bmatrix} \quad (2.23)$$

where $E$ is the elastic or (Young's) modulus; $v$ is Poisson's ratio; $\varepsilon_x$, $\varepsilon_y$ and $\varepsilon_z$ are axial strains in X, Y and Z directions; $\sigma_x$, $\sigma_y$ and $\sigma_z$ are normal stresses acting on the planes normal to the X, Y and Z axes; $\gamma_{xy}$, $\gamma_{yz}$ and $\gamma_{zx}$ are shear strains, and $\tau_{xy}$, $\tau_{yz}$ and $\tau_{zx}$ are shear stresses in XY, YZ and ZX planes, respectively.

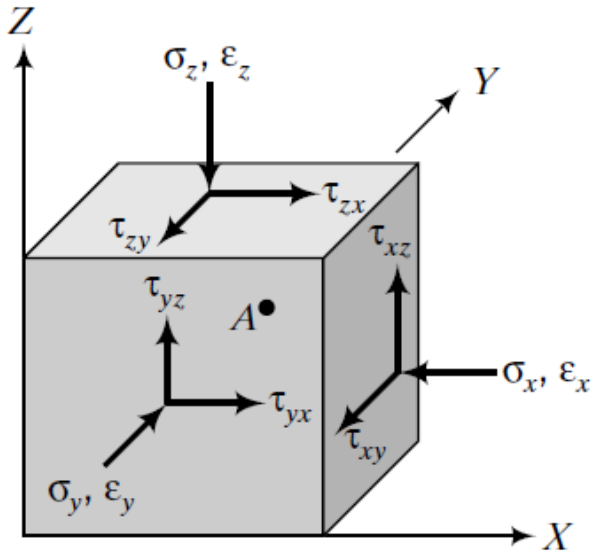


Figure 2.24. General state of stress (Budhu 2010).

There are three elastic parameters: Young's modulus, Poisson's ratio and shear modulus. Normally, only two of these parameters are needed to solve problems when handling linear, isotropic soils. For instance, shear modulus can be determined from Young's modulus and Poisson's ratio by Equation (2.24).

$$G = \frac{E}{2(1+v)} \quad (2.24)$$

Hooke's law is a basic elastic theory in the engineering field. The equation terms are simple to be determined by constant parameters. But it is too simplified for use in the high stress and strain condition. Therefore, non-linear stress-strain elastic constitutive models were proposed, such as Duncan-Chang elastic model, Cauchy elastic model, Green elastic model (hyper-elastic theory), hypo-elasticity model, etc. (Li 2004).

2.8.2 Elasto-Plastic Model

Various elasto-plastic models were proposed to express the soil behavior, the classic models such as Tresca, Von Mises, Mohr-Coulomb and Drucker-Prager; and advanced elasto-plastic models such as Lade-Duncan, Cam-clay and Matsuoka-Nakai, were developed as well (Li 2004). Since the advanced models require site-specific parameters from laboratory data, only the classic models are applied in this research.

The classic elasto-plastic models were developed according to elasto-plastic theories, which contain rigid plastic theory and ideal plastic theory; their stress-strain relationships are as shown in Figure 2.25. The rigid plastic theory does not account for the soil deformation before reaching yielding stress ($\sigma_y$); the strain of soil reaches plastic deformation, which can be determined from the boundary conditions once yield stress is reached (Figure 2.25 (a)). The ideal plastic model has two stages of the stress-strain relationship. The first one is a linear elastic stress-strain relationship before stress reaching $\sigma_y$. Once yielding occurs, it becomes the ideal plastic deformation as the second stage. Therefore, the strain is approaching infinity or being determined by boundary condition (Figure 2.25 (b)) (Li 2004). The elastic-ideal plastic model is widely used in classic models. The most used model is the Mohr-Coulomb model. Thus, this material model is chosen in this research due to the general availability of tabulated material properties, as shown in a previous section.

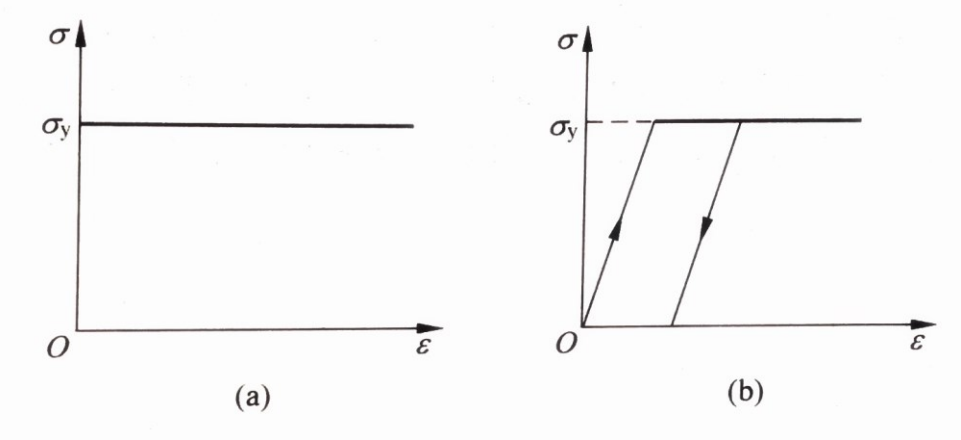


Figure 2.25. (a) Rigid plastic model; (b) elastic-ideal plastic model (Li 2004).

The strength of material indicates the stress condition when failure occurs. Strength theory can also be used to express the material failure criterion (Li 2004). Coulomb proposed the equation to define the linear relationship between shear strength and normal stress on a plane (Pietruszczak 2010), as follows:

$$\tau = f(\sigma) \tag{2.25}$$

$$\tau = c - \sigma \tan \varphi \tag{2.26}$$

where $\tau$ is shear strength; $c$ is cohesion; $\sigma$ is normal stress; $\varphi$ is internal friction angle. The failure on a plane occurs while $\tau$ and $\sigma$ reach a certain critical combination.

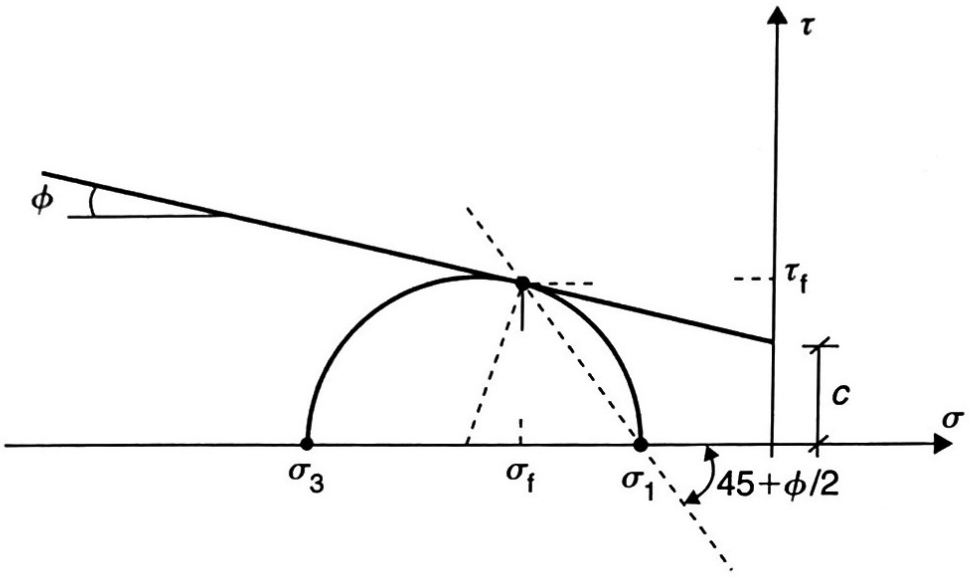


Figure 2.26. Mohr circle defining the conditions at failure (Pietruszczak 2010).

The Mohr circle representation combines Equation (2.26) that can formulate a general mathematical criterion (Pietruszczak 2010). The failure occurs when the circle becomes tangential to the Coulomb envelope (Figure 2.26). The state of shear stress and normal stress at failure satisfies Equations (2.27) and (2.28):

$$\tau = \frac{1}{2}(\sigma_1 - \sigma_3)\cos\varphi \tag{2.27}$$

$$\sigma = \frac{1}{2}(\sigma_1 + \sigma_3) + \frac{1}{2}(\sigma_1 - \sigma_3)\sin\varphi \tag{2.28}$$

Combining Equation (2.26) with Equation (2.27) and (2.28), Mohr-Coulomb failure criterion can be adopted as the yield function corresponding to the convention of principal stresses $\sigma_1 > \sigma_2 > \sigma_3$:

$$F = \frac{1}{2}(\sigma_1 - \sigma_3) + \frac{1}{2}(\sigma_1 + \sigma_3)\sin\varphi - c\cos\varphi = 0 \tag{2.29}$$

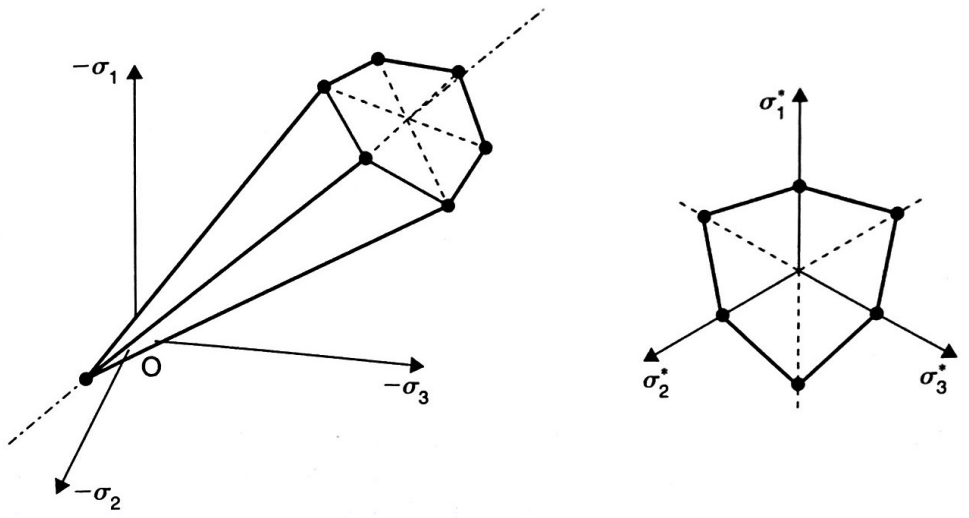


Figure 2.27. Mohr-Coulomb criterion in the principal stress space (Pietruszczak 2010).

An irregular hexagonal pyramid in three-dimensional principal stress space can be defined by the set of six equations of the type as Equation (2.29) in geometrical terms (Pietruszczak 2010), as shown in Figure 2.27. The cross-section in the octahedral plane is represented by an irregular hexagon. For an isotropic material, the Mohr-Coulomb yield surface is expressed as Equation (2.30) in terms of stress invariants (Owen et al. 1980; Li 2004).

$$F = \frac{I_1}{3}\sin\varphi + \sqrt{J_2}\left[\cos\theta - \frac{1}{\sqrt{3}}\sin\theta\sin\varphi\right] - c\cos\varphi = 0 \tag{2.30}$$

where:

$I_1$ is the first stress invariant, $I_1 = \sigma_1 + \sigma_2 + \sigma_3$;
$\varphi$ is the internal friction angle;
$J_2$ is the second deviator stress invariant, $J_2 = \frac{1}{6}[(\sigma_1 - \sigma_2)^2 + (\sigma_2 - \sigma_3)^2 + (\sigma_3 - \sigma_1)^2]$;
$\theta$ is the Lode angle, ranges from $-30^\circ$ to $30^\circ$ if defines $\sigma_1 \geq \sigma_2 \geq \sigma_3$;
$c$ is the cohesion.

# Chapter 3 Generation of FEM Models Representing Tunneling Under Railways

In this chapter, the generation of two-dimensional FEM models will be discussed based on the literature review presented in the preceding chapter. The model geometry, which includes the substructure of the track system and natural ground, will be investigated in Section 3.1. Section 3.1.2 determines the loads due to trains. Materials for natural ground, tunnel lining and individual layers for the substructure of the track system will be presented in Section 3.1.3. Section 3.1.4 introduces boundary conditions that will be used in the models. To ensure the quality and adequacy of the FEM models, an important mesh convergence study will be discussed in Section 3.1.5. While, model verifications will be performed to compare results between the FEM solutions and the analytical methods of Jaeger and Cook (1976) and Salencon (1969), which is discussed in Section 3.2.

## 3.1 Process of Establishing a Model

In this section, the process of establishing a model will be discussed. Starting from determining the model geometry, a sufficient size soil domain needs to be modeled. In addition, applying accurate trainload is vital to the analysis. The actual trainload for different train speeds and the distribution along the boundaries of the model for both a locomotive and a freight train that will be used in RS2 will also be discussed, corresponding to the material presented in the literature review.

### 3.1.1 Railway System Geometry and Model Geometry

The geometry of a typical railway embankment is shown in Figure 3.1, representing a longitudinal section along the tracks. It is one meter high in total, which obeys the minimum value suggested by AREMA (2010). There are two systems that comprise the track structure. One is named superstructure that contains the rails, fastening system and sleepers (crossties). Another is called substructure, which has three components: ballast, subballast and subgrade. The natural ground is taken as the foundation of the entire track structure, as shown in Figure 3.2. To be noted that, the rail track, the fastening system and the sleepers are not included in the RS2 model because their behavior is not the aim of this thesis, rather it is assumed that the equivalent loading at the sleeper-ballast interface will be applied.

To model an adequate amount of soil by avoiding stress reflection at the boundaries, the rule adopted is to take the geometry to be at least 10D*10D, where D is the tunnel diameter. Considering all scenarios and to reduce the amount of model re-generation, it was decided that all models are to be taken the same external size, which is 140*140m, corresponding to the largest tunnel diameter of D = 14 m. In addition, a ratio of tunnel overburden depth to tunnel diameter (H/D), which is a crucial parameter to decide the tunnel excavated depth; so it will be set up with different values from 1 to 8 with increments of 1, to represent the typical range of tunnels, as discussed in the preceding chapter. Moreover, the tunnel diameter from the minimum value of 3 m to the maximum value of 14 m will be used in the simulations based on real projects, as reviewed in Chapter 2.

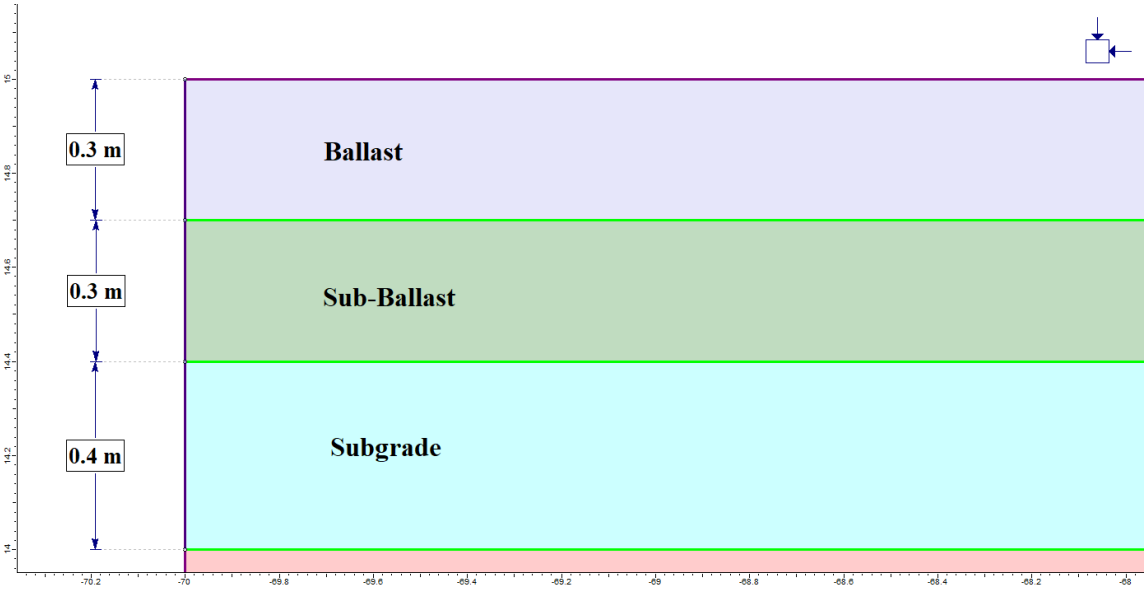


Figure 3.1. Railway embankment components with their dimensions.

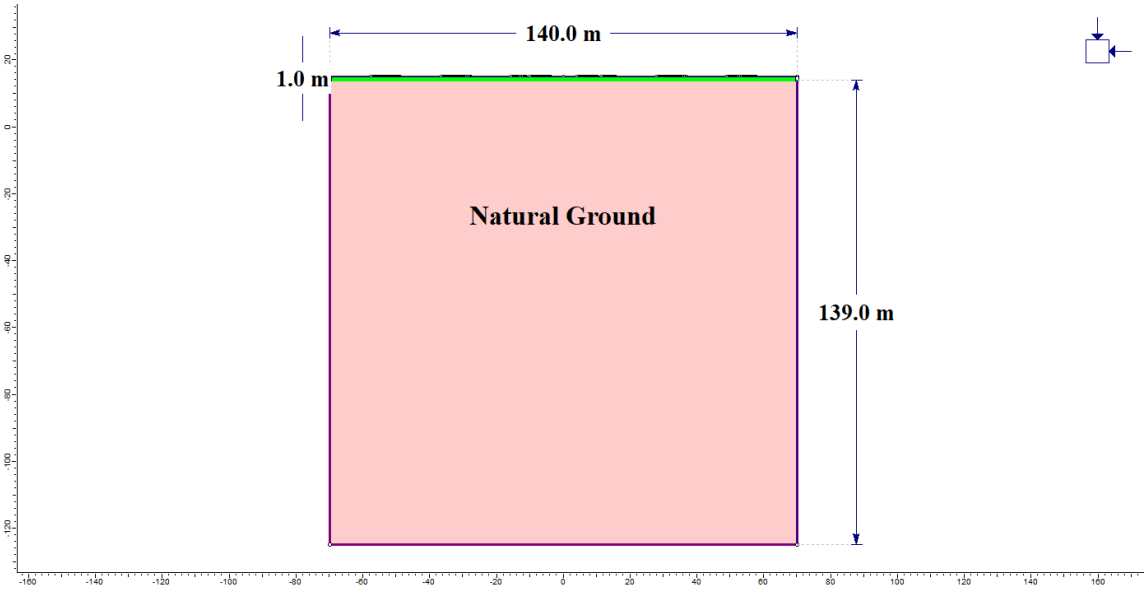


Figure 3.2. Typical model geometry with dimensions.

In order to verify that the model's geometry extent is reasonable for all the models in this thesis, an example situation will be considered. For the case when tunnel diameter is 14 m, the largest overburden depth could reach 112 m, and the largest boundary dimension in the vertical direction is 140 m for all models, as shown in Figure 3.3. In this case, the distance from the lower crown of the tunnel to the lower boundary of the model will be 20 m, which is 1.4 times the tunnel diameter. According to the data interpreted from RS2 shown in Figure 3.4, the stress distribution near the

lower boundary maintains a uniform stress level at 2600 kPa, signifying that the excavation does not cause reflection at the lower (closest) boundary. The details of train loadings distribution (referring to Figure 3.3 and 3.4) for the half model on the top boundary are illustrated in Appendix C by separate figures.

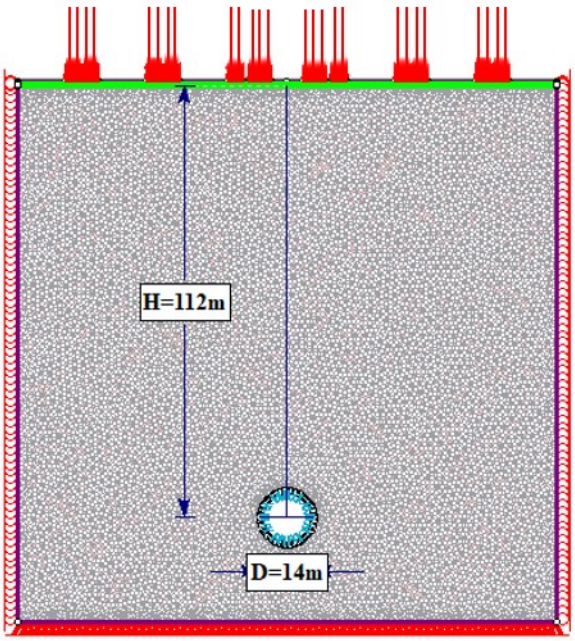


Figure 3.3. Model geometry for a D = 14m, H = 112m tunnel excavation with 120 km/h train speed loading.

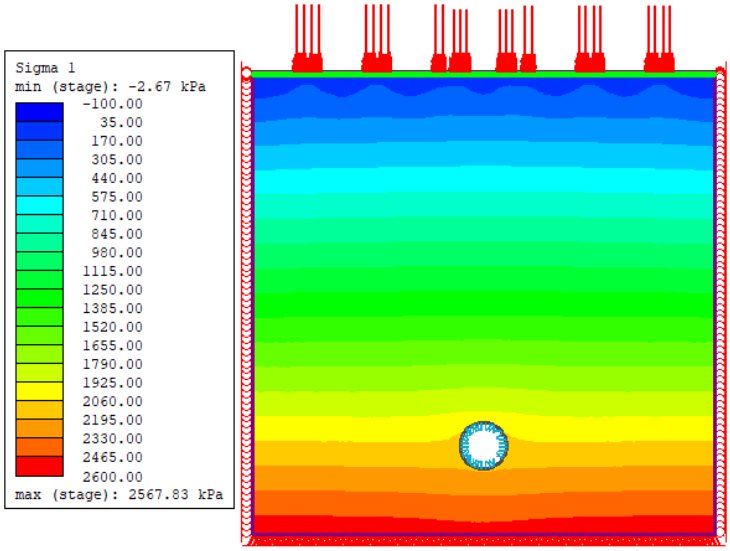


Figure 3.4. Stress distribution for model with D = 14 m, H = 112 m, with 120 km/h train speed loading.

### 3.1.2 Loading Conditions Due to Trains

The load transfer mechanism from a passing train is discussed in this section. The trainload transfer from moving trains to the subgrade is a complex process. In order to simplify the computation procedure in this thesis, several assumptions are established before processing the trainload transfer mechanism.

Thus, only a straight section of a railway track will be considered in the simulation. Moreover, the friction between rail and wheel will be ignored. In addition, the temperature and other environmental factors will be neglected in this case; therefore, there are neither lateral forces nor longitudinal forces caused by them will be considered. Vertical loads are from the operation of a train, which either are in a stationary condition or with a steady running speed, will be used in the trainload calculation.
The load transformation is made from wheel to rail then to the contact area between the sleepers' (or crossties') bottom and the ballast surface. The train operation direction is designed to be along the model's top boundary, at a right angle to the tunneling direction. Therefore, the trainload distribution is along the longitudinal direction.

In this thesis, the most often used locomotive and freight car in Canada are chosen to be used in the simulations. Their parameters are shown in Table 3.1.

Table 3.1 Key parameters for chosen locomotive and freight car

| | Locomotive | Freight car |
|---|---|---|
| Type | GE C44-9W | Greenbrier 6250 covered hopper |
| Weight (kg) | 192,800 | 127,728 |
| Weight (kN) | 1,891.37 | 1,272.62 |
| Length (m) | 22.3 | 20.67 |
| Wheel diameter (m) | 1.07 | 0.91 |
| Axles number per car | 6 | 4 |
| Axle load per wheel (kN) | 157.61 | 159.08 |
| Axle center to center distance (m) | 2 | 1.78 |
| Bogie center to center distance (m) | 14 | 16.5 |

The method that AREMA (2010) provided to calculate the contact pressure between the sleepers and the ballast surface can be found in the literature review chapter. The process of load transfer is from axle load to wheel load, then to rail seat to contact pressure at the sleepers.

According to the previous information, the contact pressure between tie-ballast for the locomotive and the freight car will be shown in Table 3.2 and Table 3.3, respectively. In order to adopt metric units, which will be used in RS2, imperial units will be all transferred for the final value of the contact pressure of the tie-ballast area.

In this thesis, the tie width, according to the typical wooden type that is used in North America, was chosen as 0.23 m. Similarly, the tie spacing was set to be 0.5 m. For 2D simulations, the thickness of the model is one meter, which means the actual tie bottom area is the area of tie width and model thickness. In addition, the tie spacing decides the wheel load distribution factor (AREMA 2010), which was discussed in Chapter 2, which is 43 % in this case. However, AREMA (2010) only provides the maximum distribution factor for one single sleeper, that cannot be adopted to all the sleepers along the longitudinal direction. Profillidis (2014) and Ministry of Railway of the People's Republic of China (2016) stated that one wheel could affect five ties underneath it. For calculation convenience and acquiring reasonable results, therefore, the tie directly under the wheel carries the maximum rail seat load, which is given DF as 0.4. For the adjacent ties, the DF is given as 0.2 for the first tie and 0.1 for the second tie on either side.

Table 3.2 Contact pressure between sleepers and the ballast surface for locomotive

| Parameters | | Values | | | |
|---|---|---|---|---|---|
| Train speed (km/h) | | $V_1 = 0$ | $V_2 = 40$ | $V_3 = 80$ | $V_4 = 120$ |
| Train speed (miles/h) | | $V_1 = 0$ | $V_2 = 25$ | $V_3 = 50$ | $V_4 = 75$ |
| Impact factor | | 0 | 0.196 | 0.393 | 0.589 |
| Impact factor in percent | | 0 % | 19.6 % | 39.3 % | 58.9 % |
| Wheel load (kN)/(lb) | | 157.61/35432 | | | |
| Contact area ($m^2$) | | 0.23 | | | |
| | | Contact pressure (kPa) | | | |
| Distributed factor (DF) | 0.1 | 68.70 | 82.17 | 95.65 | 435.65 |
| | 0.2 | 136.96 | 163.91 | 190.87 | 217.83 |
| | 0.4 | 273.91 | 327.83 | 381.74 | 435.65 |

Table 3.3 Contact pressure between sleepers and the ballast surface for a freight car

| Parameters | | Values | | | |
|---|---|---|---|---|---|
| Train speed (km/h) | | $V_1 = 0$ | $V_2 = 40$ | $V_3 = 80$ | $V_4 = 120$ |
| Train speed (miles/h) | | $V_1 = 0$ | $V_2 = 25$ | $V_3 = 50$ | $V_4 = 75$ |
| Impact factor | | 0 | 0.229 | 0.458 | 0.688 |
| Impact factor in percent | | 0 % | 22.9 % | 45.8 % | 68.8 % |
| Wheel load (kN)/(lb) | | 159.08/35763 | | | |
| Contact area ($m^2$) | | 0.23 | | | |
| | | Contact pressure (kPa) | | | |
| Distributed factor (DF) | 0.1 | 69.13 | 85.22 | 100.87 | 116.96 |
| | 0.2 | 138.26 | 170.0 | 201.74 | 233.48 |
| | 0.4 | 276.52 | 340.0 | 403.48 | 466.96 |

Figure 3.5 and Figure 3.6 correspond to the locomotive and freight car trainload distribution along the ballast surface, respectively. Also, the axle distance, total length, and bogie (truck) center to center distance for both locomotive and freight car are illustrated in the figures. The total length of the locomotive and the freight car contains the length of the pulling sections at each side. In the worst-case scenario, the locomotive is at the center of the model so that the heaviest component of the train is located just above the tunnel excavation. There are two adjacent freight cars connected to the locomotive on each side for all models. In addition, there is a bogie of a freight car that is also connected to the outer car on each side. This setting can simulate the train operation over the whole ground surface. The outboard axle spacing between the outside axles of the locomotive and the freight car is 3.4 m. The axle spacing between two adjacent freight cars is 2.4 m. The details of train loadings distribution for the half model on the top boundary under different train speed conditions are illustrated in Appendix C by separate figures.

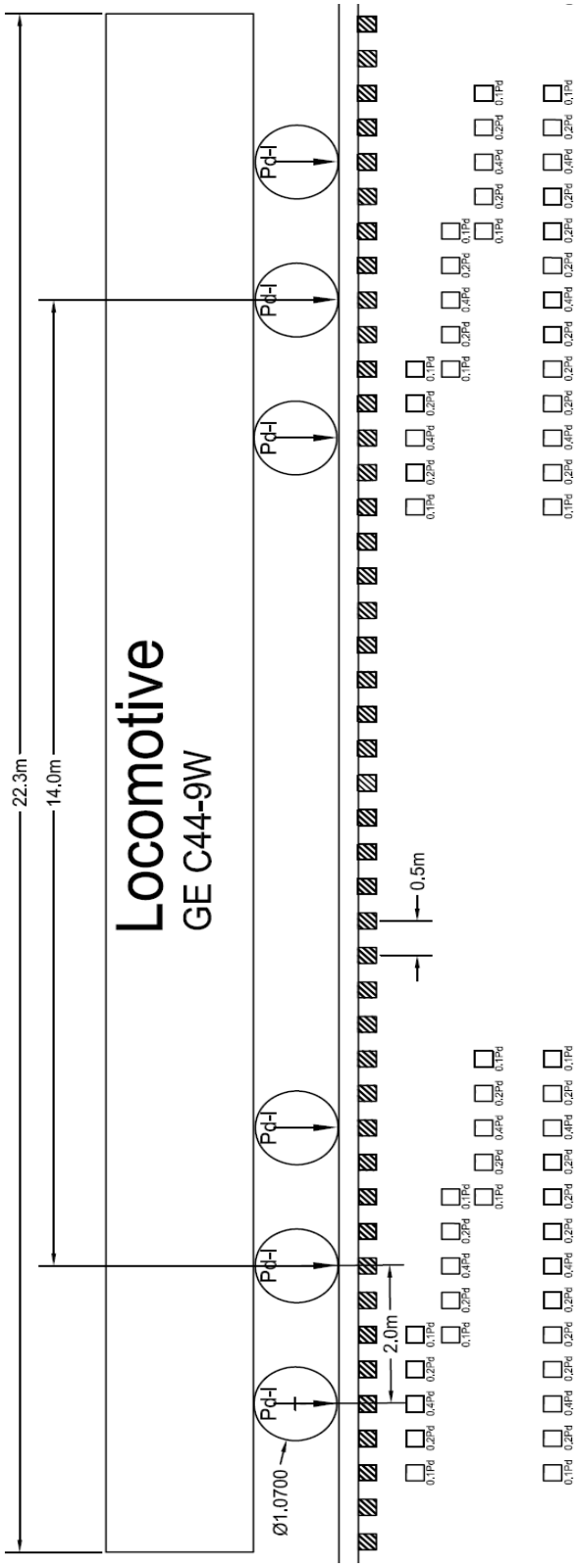


Figure 3.5. Distribution of average contact pressure between sleeper and ballast (locomotive).

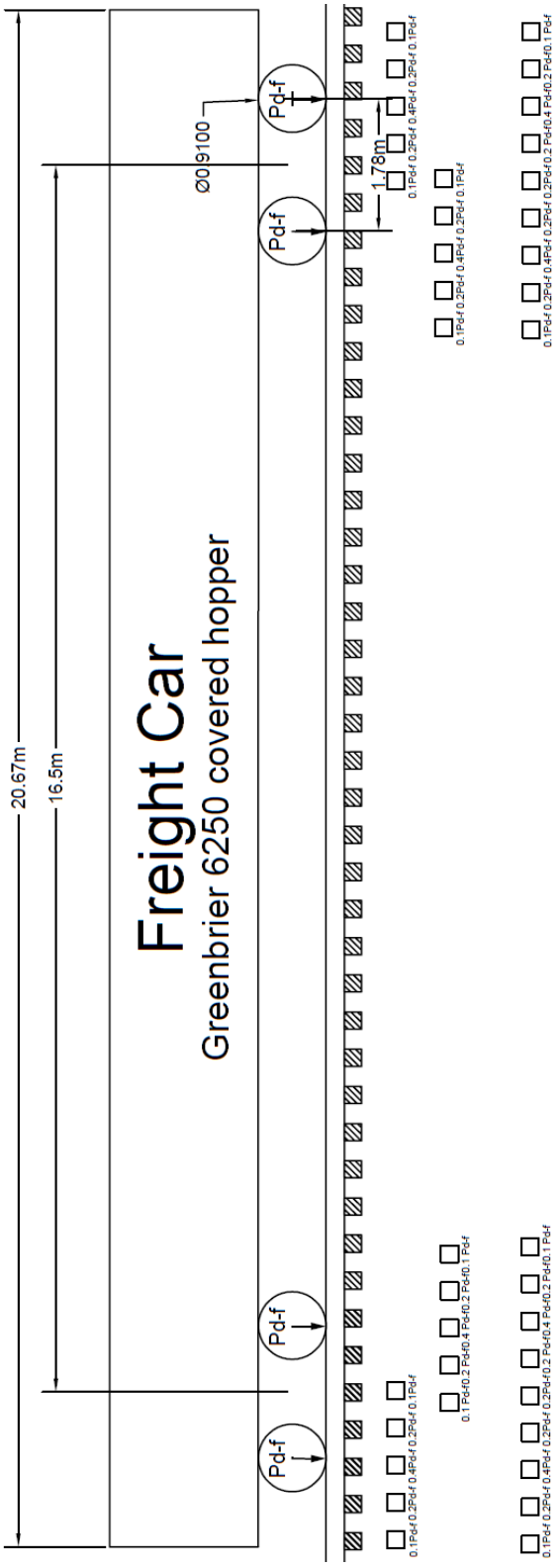


Figure 3.6. Distribution of average contact pressure between sleeper and ballast (freight car).

### 3.1.3 Material Properties of the Ground

The primary ground material is soft silty clay, which is the main body of soft ground; the properties are summarized in Table 3.4. The parameters collected are from real engineering projects, in which tunnels are excavated, and the average published value will be used in the models. All parameters from the real engineering projects were presented in Chapter 2 and in Appendix A.

Table 3.4 Natural ground properties

| Name | Material | $\gamma\ (kN/m^3)$ | $c$ (kPa) | $\varphi$ (°) | $v$ | $E$ (kPa) |
|---|---|---|---|---|---|---|
| Natural ground | Silty clay | 18 | 16 | 22 | 0.3 | 15,000 |

Note: $\gamma$ is unit weight; $c$ is cohesion; $\varphi$ is friction angle; $v$ is Poisson's ratio; E is Young's modulus.

The substructure of the railway system has three components, which are overlying the natural ground. The properties of each component used in the models are shown in Table 3.5. The railway tracks are perpendicular to the tunnel excavation direction; therefore, the substructure of the track system looks like three thin layers in the two-dimensional model.

Table 3.5 Substructure component properties

| Name | Material | $h\ (m)$ | $\varphi$ (°) | $c$ (kPa) | $\gamma\ (kN/m^3)$ | $v$ | $E$ (kPa) |
|---|---|---|---|---|---|---|---|
| Ballast | Crushed Stone | 0.3 | 48 | 0 | 21.2 | 0.3 | 225,000 |
| Sub-ballast | Gravel | 0.3 | 33 | 0 | 18.9 | 0.15 | 138,000 |
| Subgrade (placed fill soil) | Hard clay | 0.4 | 30 | 15 | 21 | 0.3 | 65,000 |

Note: h is the thickness of each material; $\varphi$ is friction angle; $c$ is cohesion; $\gamma$ is unit weight; $v$ is Poisson's ratio; E is Young's modulus.

A liner, used as preliminary support of the tunnel, is a crucial support structure that could reduce the possibility of ground surface displacement. The liner properties used are shown in Table 3.6, representing a typical tunnel liner. The tunnel liner properties are the same for all models for reducing the possible number of variables in the model.

Table 3.6 Tunnel liner properties (Gong and Zhou 2008)

| Name | $l\ (m)$ | $v$ | $E$ (kPa) | $\gamma\ (kN/m^3)$ |
|---|---|---|---|---|
| Tunnel liner | 0.35 | 0.3 | 30,000,000 | 24 |

Note: $l$ is the thickness of liner; $v$ is Poisson's ratio; E is Young's modulus; $\gamma$ is the unit weight.

All materials of the substructure of track system (railway embankment) and natural ground are elasto-plastic materials; thus, the failure criteria are both set as Mohr-Coulomb. The liner is set as an elastic material. In addition, all soil materials are in a drained condition.

### 3.1.4 Mesh Convergence Study

To investigate the appropriate mesh element density, a mesh convergence study is imperative. This convergence study is used to compare how the mesh and discretization density influences the results' accuracy. How to choose a suitable element shape and to add more active nodes of an element is also the reason that could affect the ensuing quality of analysis results. When the discretization density is increased, the number of elements and nodes also increases. However, in general, the software could compute more accurate and reliable results.

In this thesis, triangular elements with six nodes produce a good graded mesh for most models, especially for the excavation problem, using what is known as a quadtree nodal insertion technique, which was chosen for the FEM generation. The graded mesh type will automatically generate fine mesh around any boundaries in the model, then decreases the discretization density with the distance further away from the boundaries. For this mesh type, the density of discretization of external and material boundaries is determined by the gradation factor in conjunction with the default number of nodes on the excavation boundary. The tunnel excavation boundary is established by setting up 80 segments to produce a finely discretized circle. Therefore, the default number of nodes on the excavation boundary is going to be 80 as well. The gradation factor is the ratio of the average length of discretization on excavation boundaries to the length of discretization on the external boundaries, at the maximum distance from the excavation boundaries. Since the number of nodes on the excavation boundary is constant, the gradation factor is a function that enables the increase of mesh density. Because of the nature of the discretization process, the gradation factor should be considered an approximate number. In this study, the gradation factor was chosen as: 0.01, 0.02, 0.05, 0.08, 0.1, 0.15, 0.2, 0.25, 0.3, 0.35, 0.4, 0.5. To be noted that, very narrow material layers are more often to generate ill-formed and thus problematic elements. In order to solve this problem in the models, the advanced mesh regions are manually selected to refine mesh elements for the ballast, sub-ballast and subgrade with 0.5-meter element length. Different mesh settings and discretization densities have been generated in this model to compare how they affect the ground surface vertical displacement, which could be presented by the displacement discrepancy (%). The stable displacement ($S_{vt\text{-}max}$), which was obtained for the models with high mesh density, was 20.3 mm; therefore, the equation used for comparison is:

$$Displacement_{discrepancy} = \frac{Displacement - 20.3}{20.3} \tag{3.1}$$

Table 3.7 Different number of elements and nodes corresponding to the maximum vertical displacement of the ballast surface induced by tunnel excavation ($S_{vt\text{-}max}$) and the displacement discrepancy for the sample model D = 14 m, H = 114 m, $V_4$ = 120 km/h

| Number of nodes | Number of elements | $S_{vt\text{-}max}$ (mm) | Displacement discrepancy (%) |
|---|---|---|---|
| 2471 | 1067 | 18.9 | 6.9 |
| 9583 | 4539 | 19.4 | 4.4 |
| 10366 | 4920 | 20.4 | -0.5 |
| 11330 | 5476 | 20.3 | 0.0 |
| 14793 | 7068 | 20.3 | 0.0 |

Table 3.7 Different number of elements and nodes corresponding to the maximum vertical displacement of the ballast surface induced by tunnel excavation ($S_{vt\text{-}max}$) and the displacement discrepancy for the sample model D = 14 m, H = 114 m, $V_4$ = 120 km/h – Continued

| Number of nodes | Number of elements | $S_{vt\text{-}max}$ (mm) | Displacement discrepancy (%) |
|---|---|---|---|
| 15198 | 7256 | 20.3 | 0.0 |
| 26059 | 12566 | 20.3 | 0.0 |
| 26779 | 12987 | 20.3 | 0.0 |
| 27639 | 13391 | 20.3 | 0.0 |
| 28318 | 13708 | 20.3 | 0.0 |
| 28931 | 13993 | 20.3 | 0.0 |
| 72544 | 35808 | 20.3 | 0.0 |
| 73558 | 36278 | 20.3 | 0.0 |

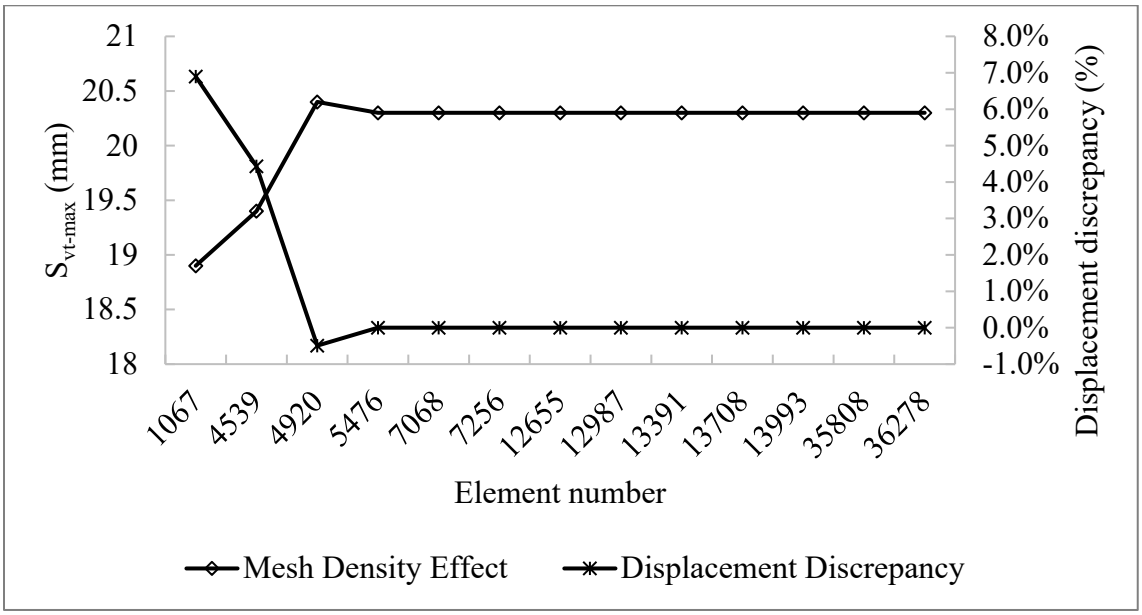


Figure 3.7. Critical mesh elements effect on the maximum vertical displacement at the ballast surface induced by tunnel excavation ($S_{vt\text{-}max}$) for the numerical models, and the corresponding displacement discrepancy.

In Table 3.7 and Figure 3.7, the convergence occurs at 5476 mesh elements, corresponding to a 0 % displacement discrepancy. On the other hand, the displacement discrepancy reaches 6.9 % for a coarse mesh without advanced mesh refinement, which contains 1067 mesh elements. In general, the displacement discrepancy decreases with the increasing element density. When the number of mesh elements is equal or larger than 5476, stabilized results can be achieved. Thus, the number of mesh elements should be larger than 5476 for most models. In order the express the relationship between mesh element number and each critical dimension (tunnel diameter), Table 3.8 summarized the number of mesh elements and nodes for each model in this research.

Table 3.8 Relative number of mesh elements and nodes of each model

| Tunnel diameter (m) | Tunnel depth (m) | Number of mesh element | Number of nodes |
|---|---|---|---|
| 3 | 3 | 40637 | 82276 |
| | 6 | 40104 | 81189 |
| | 9 | 39444 | 79847 |
| | 12 | 38859 | 78662 |
| | 15 | 38375 | 77684 |
| | 18 | 37989 | 76896 |
| | 21 | 37730 | 76367 |
| | 24 | 37568 | 76033 |
| 4 | 4 | 15144 | 31083 |
| | 8 | 12974 | 26589 |
| | 12 | 14192 | 29151 |
| | 16 | 13997 | 28748 |
| | 20 | 13705 | 28152 |
| | 24 | 13438 | 27607 |
| | 28 | 13388 | 27499 |
| | 32 | 13157 | 27022 |
| 5 | 5 | 13433 | 27546 |
| | 10 | 13221 | 27112 |
| | 15 | 13013 | 26678 |
| | 20 | 12744 | 26133 |
| | 25 | 12536 | 25703 |
| | 30 | 12495 | 25608 |
| | 35 | 12354 | 25317 |
| | 40 | 12088 | 24773 |
| 6 | 6 | 12698 | 26003 |
| | 12 | 12434 | 25461 |
| | 18 | 12253 | 25084 |
| | 24 | 12097 | 24762 |
| | 30 | 11892 | 24337 |
| | 36 | 11706 | 23953 |
| | 42 | 11425 | 23384 |
| | 48 | 11158 | 22837 |
| 7 | 7 | 11983 | 24518 |
| | 14 | 11849 | 24234 |
| | 21 | 11542 | 23609 |
| | 28 | 11448 | 23409 |
| | 35 | 11015 | 22530 |
| | 42 | 13030 | 26605 |
| | 49 | 10509 | 21498 |
| | 56 | 12700 | 25915 |

Table 3.8 Relative number of mesh elements and nodes of each model – Continued

| Tunnel diameter (m) | Tunnel depth (m) | Number of mesh element | Number of nodes |
|---|---|---|---|
| 8 | 8 | 12756 | 26153 |
| | 16 | 12060 | 24833 |
| | 24 | 11169 | 22822 |
| | 32 | 10734 | 21941 |
| | 40 | 15268 | 31359 |
| | 48 | 12477 | 25710 |
| | 56 | 10824 | 22377 |
| | 64 | 14672 | 30021 |
| 9 | 9 | 18582 | 38081 |
| | 18 | 13122 | 26973 |
| | 27 | 12850 | 26429 |
| | 36 | 13716 | 28187 |
| | 45 | 12257 | 25068 |
| | 54 | 9710 | 20067 |
| | 63 | 9024 | 18691 |
| | 72 | 12921 | 26446 |
| 10 | 10 | 17120 | 35069 |
| | 20 | 15634 | 32089 |
| | 30 | 13874 | 28507 |
| | 40 | 13370 | 27431 |
| | 50 | 15758 | 32301 |
| | 60 | 15076 | 30899 |
| | 70 | 13820 | 28235 |
| | 80 | 12559 | 25696 |
| 11 | 11 | 13090 | 26801 |
| | 22 | 12762 | 26127 |
| | 33 | 12552 | 25687 |
| | 44 | 13168 | 26965 |
| | 55 | 15140 | 31007 |
| | 66 | 13944 | 28457 |
| | 77 | 14102 | 28787 |
| | 88 | 14278 | 29161 |
| 12 | 12 | 15286 | 31247 |
| | 24 | 13148 | 26961 |
| | 36 | 16282 | 33185 |
| | 48 | 12352 | 25423 |
| | 60 | 13322 | 27233 |
| | 72 | 13644 | 27833 |
| | 84 | 13360 | 27375 |
| | 96 | 14112 | 28827 |

Table 3.8 Relative number of mesh elements and nodes of each model – Continued

| Tunnel diameter (m) | Tunnel depth (m) | Number of mesh element | Number of nodes |
|---|---|---|---|
| 13 | 13 | 18110 | 37029 |
| | 26 | 12786 | 26267 |
| | 39 | 15350 | 31429 |
| | 52 | 12946 | 26535 |
| | 65 | 14604 | 29809 |
| | 78 | 14508 | 29619 |
| | 91 | 9739 | 20156 |
| | 104 | 17086 | 35195 |
| 14 | 14 | 13000 | 26679 |
| | 28 | 13452 | 27533 |
| | 42 | 14234 | 29181 |
| | 56 | 12496 | 25603 |
| | 70 | 11988 | 24547 |
| | 84 | 14584 | 29905 |
| | 98 | 12632 | 25815 |
| | 112 | 13672 | 28007 |

The tunnel diameter in the models is the variable to determine the mesh density on the excavation boundary and ground surface. The tunnel excavation boundary is established by setting up 80 segments. For the small tunnels, the length of each segment is relatively shorter than the large tunnels. Therefore, the mesh element size is relatively small around the tunnel, which leads to an increase in mesh density around the excavations. Besides, the length of discretization on the external boundaries is determined by the length of discretization on the excavation boundaries. The small tunnels have a short length of discretization on the excavation boundary, which results in a short length of discretization and an increase of mesh density on the external boundaries.

### 3.1.5 Boundary Conditions in the FEM Model

There are three types of boundary conditions used in the models. The left and right side of the model boundary has a restraint in the horizontal (x) direction to prevent lateral movement. While in the vertical direction, because the ballast surface displacement induced by tunneling and trainload in a vertical direction will be much higher than the horizontal direction, the nodes will be free to move, essentially creating a roller-type support. The bottom boundary will be restrained in both horizontal and vertical directions, creating a pinned support. The top boundary will be free of any restraint, which allows all the nodes along the boundary to move in any direction. Figure 3.8 illustrates the complete model for a tunnel diameter D = 14 m, tunnel depth H = 114 m, train speed of 120 km/h. The details of train loadings ($V_4$ = 120 km/h) distribution for the half model on the top boundary are displayed in Appendix C. For all other models, the boundary conditions remain the same throughout the entire simulation sequence.

The initial element loading for all materials is a field stress and body force, which means the initial element is in equilibrium under the material's own body force and state of initial stress. The field stress type is gravity by using the actual ground surface, which is the top boundary in this case. This setting in essence defines that the initial stress is equal to the gravity force of the materials to balance the material body force.

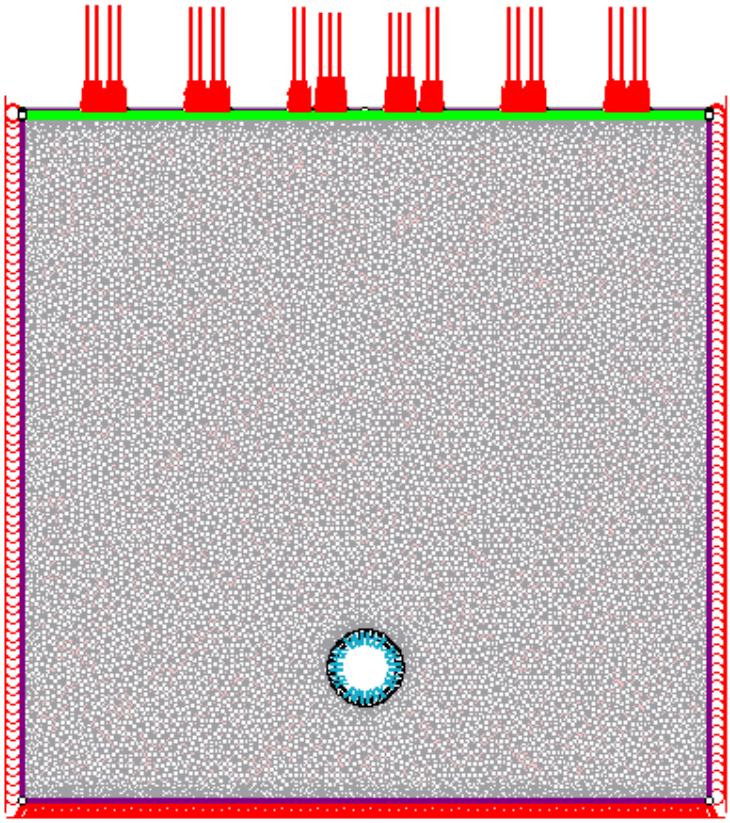

Figure 3.8. Model with loading and boundary conditions for the case of a tunnel diameter D = 14 m, tunnel depth H = 114 m, train speed of 120 km/h.

### 3.1.6 Parametrized Models in the Simulation

All FEM models were generated as a function of the overburden ratio of H/D parameter, where H is the tunnel depth, and D is the tunnel diameter. This ratio helps to determine the tunnel depths for each tunnel diameter. As an illustration, the tunnel's central axis and the position of tunnel depth and diameter is shown in Figure 3.9. The range of H/D is from 1 to 8, with increments of 1, as discussed before. With the increase of H/D at constant D, the tunnel is buried at a larger depth. As a result, for each tunnel diameter, there are eight different depths, respectively. Based on the literature review in Chapter 2, the range of the tunnel diameters selected in this thesis is 3 m to 14 m with an increment of 1 m. While, the train speed is selected to be 0 km/h, 40 km/h, 80 km/h and 120 km/h, with increments of 40 km/h. A stationary situation of a freight train is represented when

train speed is 0 km/h; while the maximum allowable operation speed for a freight train is 120 km/h. Corresponding to Section 3.1.2, the contact pressure between sleepers and ballast surface for locomotive and freight cars is exerted on the ground surface. There are 96 models for each trainload condition, and 384 models in total.

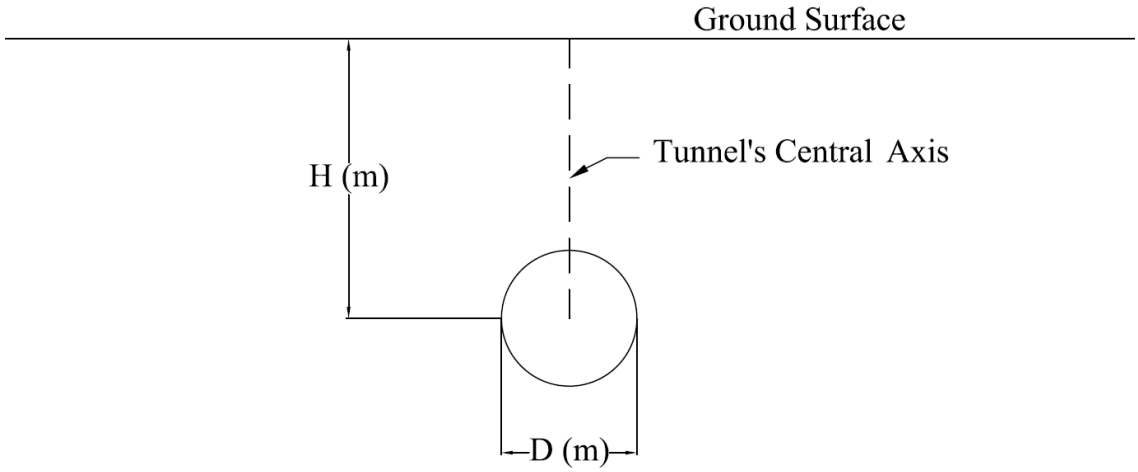


Figure 3.9. Sketch indicating the position of tunnel's central axis, and H and D parameters.

The ground surface in the simulation represents the surface of the ballast. Tunnel depth is accounted for from the tunnel center to the ground surface. The tunnel diameter is the outer diameter of the circle; the liner is installed within the outer diameter. The tunnel's central axis is the axis that crosses the upper crown of the tunnel.

## 3.2 Verification of Numerical Modelling

In numerical modeling, a verification of the basic modeling assumptions is needed to be done before starting any detailed model analysis. In this section, sample models are established to compare their results with the analytical solutions for elastic and elasto-plastic materials, respectively. The classical Kirsch equations (Jaeger and Cook 1976) can predict radial and tangential stress and displacement fields for a cylindrical excavation in an elastic medium subjected to a hydrostatic compressive stress field. Similarly, for a cylindrical excavation in an elasto-plastic material under the same stress field, Salencon (1969) established equations for solving radial and tangential stress and displacement in both elastic and plastic fields.

### 3.2.1 Comparison of Numerical Models and Analytical Methods for Elastic Materials

The selected excavation is a typical tunnel geometry, common to transportation tunnels, water conveyance tunnels and similar. The geometry is of a circular shape, using the plane strain 2D assumptions, it is equivalent to an infinitely long cylindrical tunnel with a diameter of 6 m,

excavated in an isotropic, ideal elastic material. In RS2, the excavation boundary was assembled from 80 segments. Hydrostatic compressive field stress was applied to represent the in-situ stresses. The tunnel radius was assumed to be small enough relative to the tunnel length that plane strain conditions are appropriate (RS2 User Manual 2019). Figure 3.10 illustrates the configuration of the resulting RS2 model. The external boundary in the model is an equilateral quadrilateral, which is fixed (pinned) on each side to represent an infinite plane. The mesh type was chosen to be a 6-noded graded mesh with 8744 mesh elements. This mesh density is proven as a converged mesh by a mesh convergence study. The study had tested the number of mesh elements from 936 to 33088. The total displacement at tunnel crown is a stabilized value of 10.73 mm when the number of elements reaches 8744. The external boundary was set to be 60 m away from the tunnel center. Table 3.9 summarizes material parameters and the in-situ field stress.

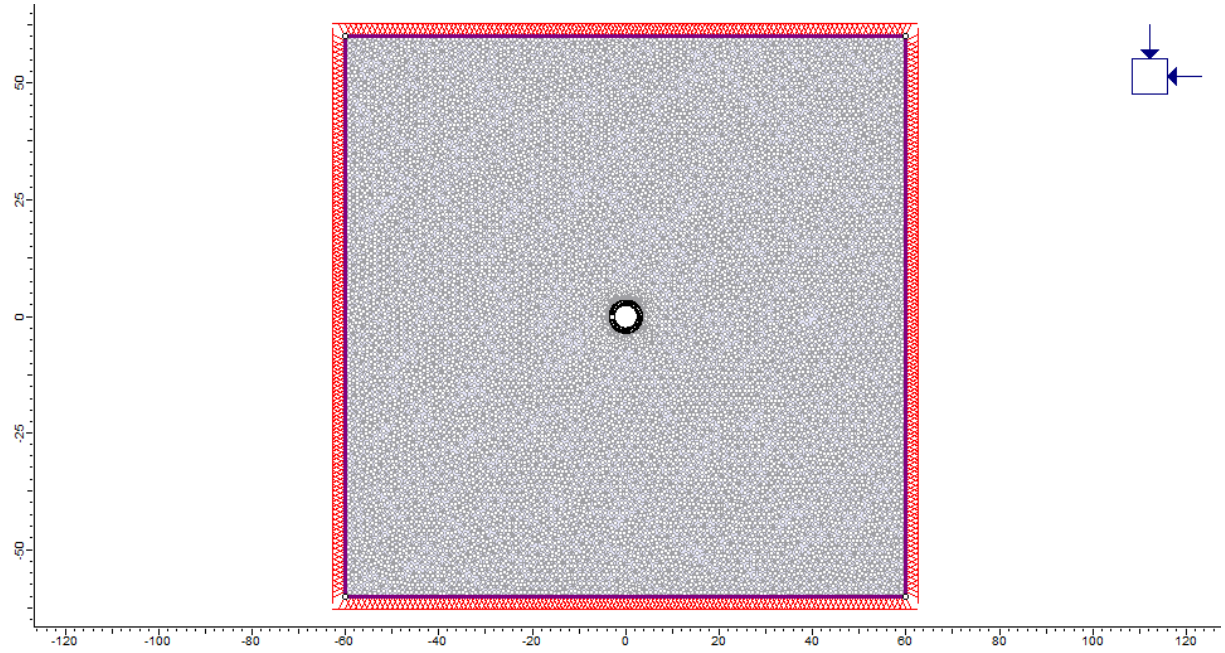


Figure 3.10. Configuration of RS2 model for the verification example.

Table 3.9 Elastic material parameters and in-situ field stress ($P_1$, $P_2$)

| Parameter | Value |
|---|---|
| $E$ (MPa) | 10,000 |
| $v$ | 0.2 |
| $\varphi$ (°) | 35 |
| $c$ (MPa) | 10.5 |
| $\gamma$ $(^{MN}/_{m^3})$ | 0.027 |
| $P_1, P_2$ (MPa) | 30 |

Note: E is Young's modulus; $v$ is Poisson's ratio; $\varphi$ is friction angle; $c$ is cohesion; $\gamma$ is the unit weight.

The analytical solution, Kirsch equations (Jaeger and Cook 1976), uses polar coordinates $(r, \theta)$ where $r$ is the distance from the tunnel center to the examined point, $\theta$ is the angle from tunnel spring line to the point. The setup for the Kirsch equation is displayed in Figure 3.11. The equations for determining the radial and tangential stress and radial displacement are as follows:

$$\sigma_r = \frac{P_1 + P_2}{2}\left(1 - \frac{a^2}{r^2}\right) + \frac{P_1 - P_2}{2}\left[1 - \frac{4a^2}{r^2} + \frac{3a^4}{r^4}\right]\cos 2\theta \tag{3.2}$$

$$\sigma_\theta = \frac{P_1 + P_2}{2}\left(1 + \frac{a^2}{r^2}\right) - \frac{P_1 - P_2}{2}\left[1 + \frac{3a^4}{r^4}\right]\cos 2\theta \tag{3.3}$$

$$u_r = \frac{P_1 + P_2}{4G}\frac{a^2}{r} + \frac{P_1 - P_2}{4G}\left[4(1 - v) - \frac{a^2}{r^2}\right]\cos 2\theta \tag{3.4}$$

where, $\sigma_r$ and $\sigma_\theta$ represent the radial and tangential stress, and $u_r$ is the radial displacement, $a$ is the radius of a tunnel, G is the compressive modulus, which is obtained from Equation 3.5.

$$G = \frac{E}{2(1 + v)} \tag{3.5}$$

where $E$ is the Young's Modulus, and $v$ is the Poisson's ratio.

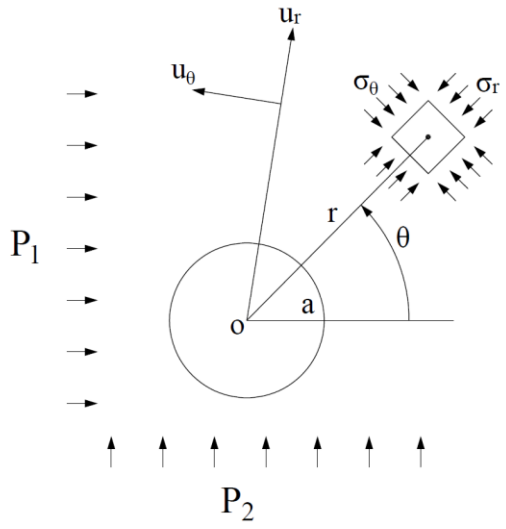


Figure 3.11. Parameters for Kirsch equation (Jaeger and Cook 1976).

For any point, the radial and tangential stresses and radial displacements are calculated along the x-axis from the tunnel center to the point. In this case, the $r$ is set to be 18 m, which is three times the tunnel diameter. The comparison between analytical results and RS2 results is shown in Figure 3.12, Figure 3.13 and Figure 3.14, respectively. The contours from RS2 are also shown in Figure 3.15, Figure 3.16 and Figure 3.17 for radial and tangential stress and radial displacement, respectively. Table 3.10 presents the error in RS2 analysis relative to analytical solution for this elastic material.

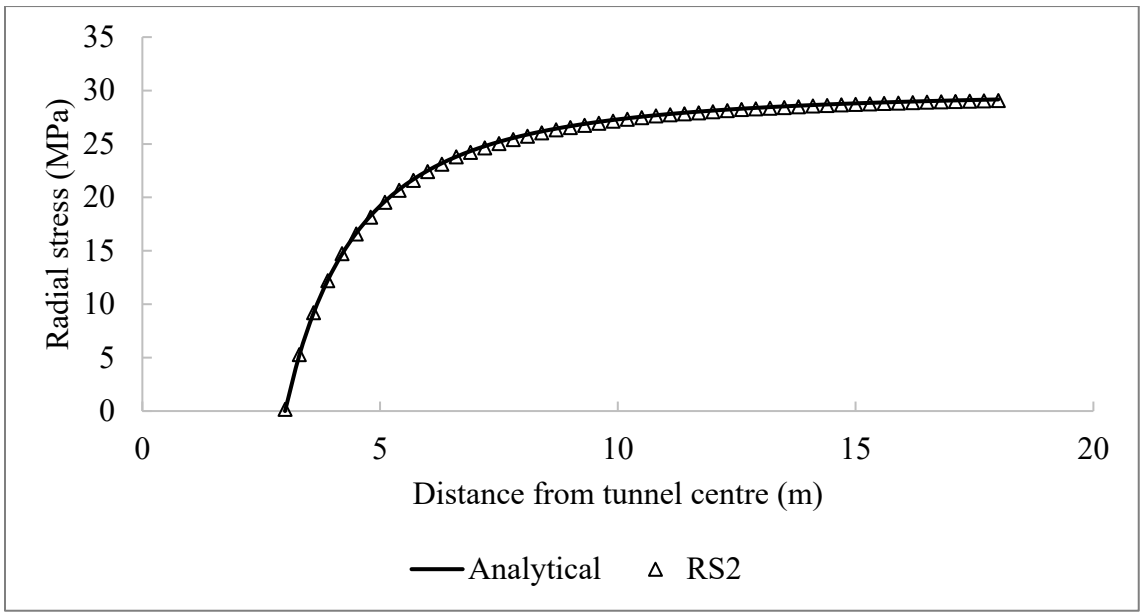


Figure 3.12. Comparison of radial stress distributions along the x-axis from the tunnel center to the designated point.

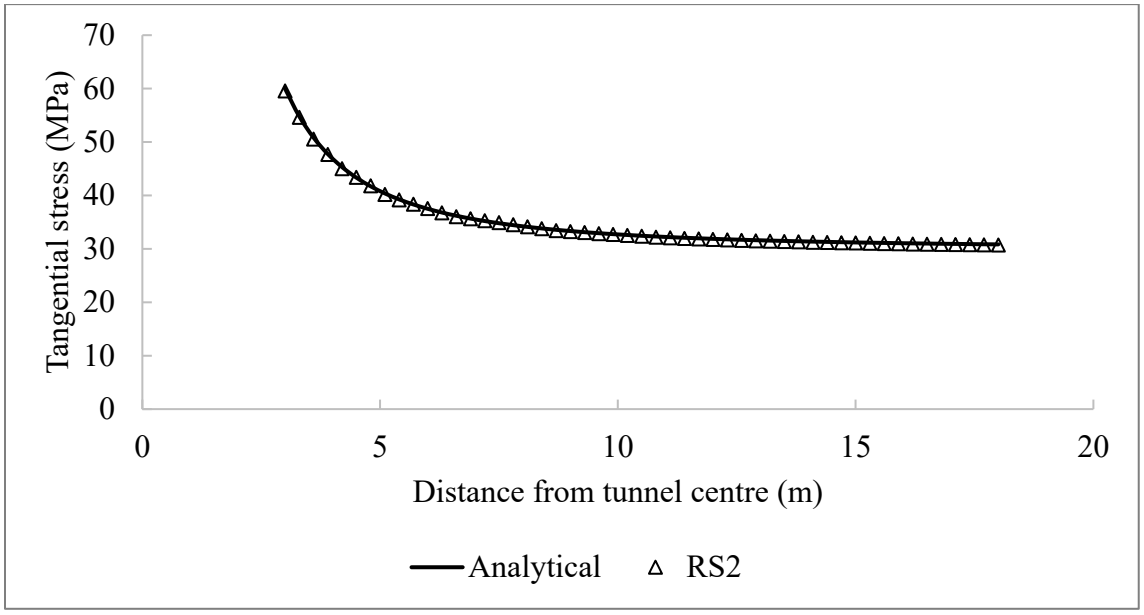


Figure 3.13. Comparison of tangential stress distributions along the x-axis from the tunnel center to the designated point.

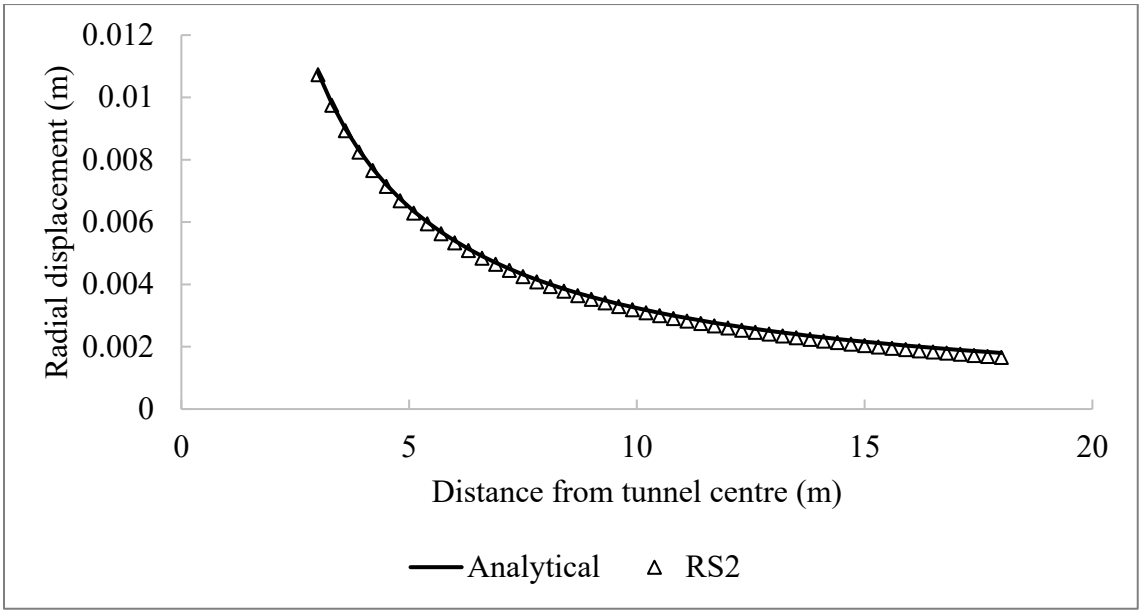


Figure 3.14. Comparison of radial displacement distributions along the x-axis from the tunnel center to the designated point.

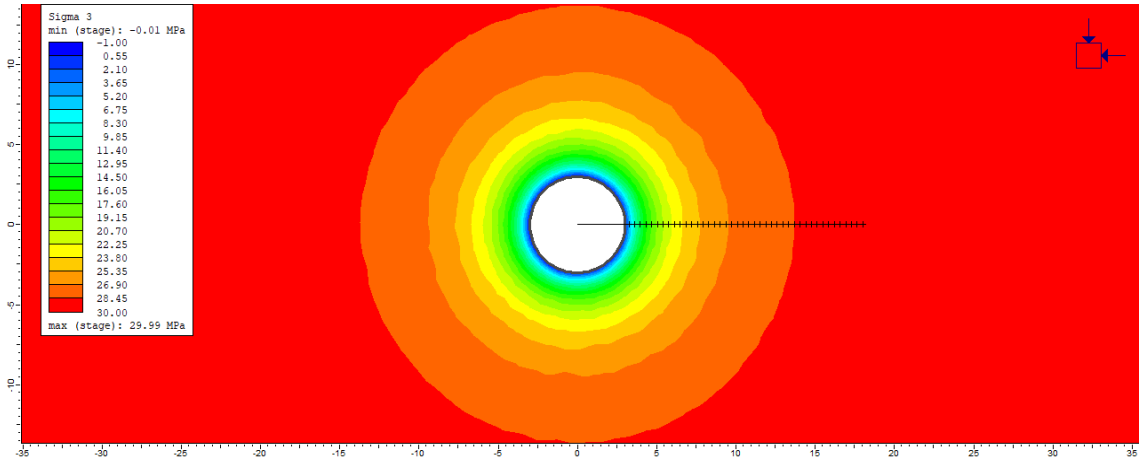


Figure 3.15. Contours of radial stress from RS2 analysis.

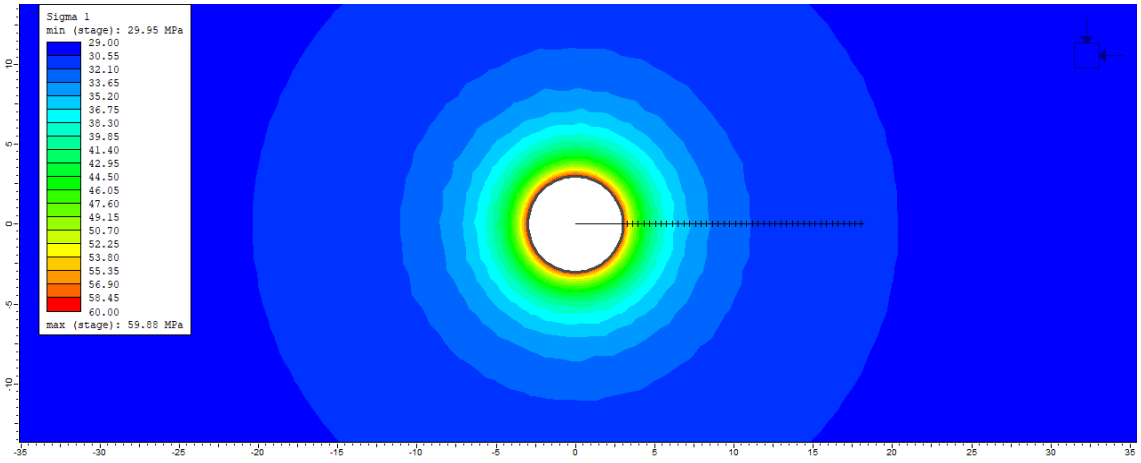


Figure 3.16. Contours of tangential stress from RS2 analysis.

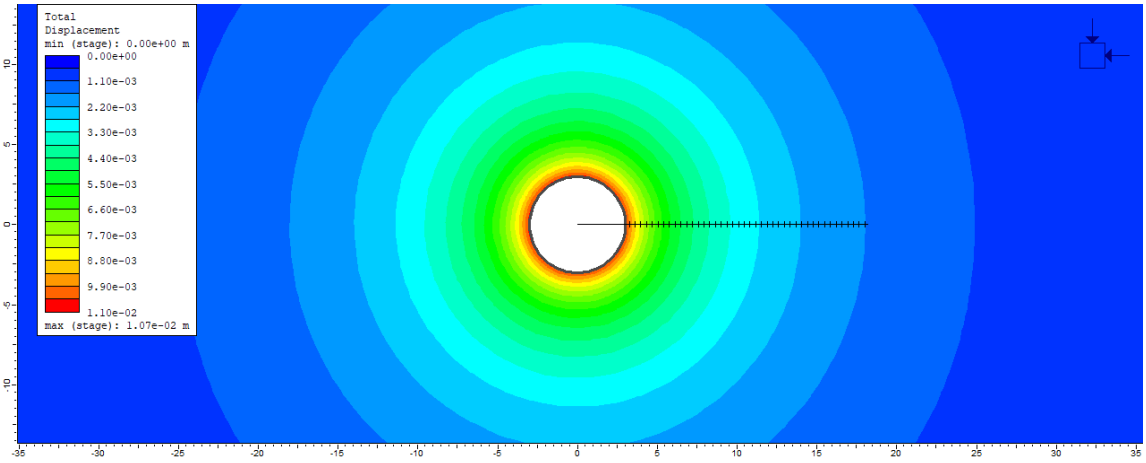


Figure 3.17. Contours of radial displacement from RS2 analysis.

Through this comparison between the analytical method and RS2 simulation, the stress analysis is converged for the tunnel excavation in elastic material. Table 3.10 summarizes the error of RS2 analysis compared to the analytical method. The average errors for radial and tangential stress are less than 1 %. While, the maximum stress error is 1.3 % and 0.7 %, respectively, the location is at the tunnel boundary for both. It proves that the RS2 solution provides a reliable result for stress analysis for elastic materials. On the other hand, the maximum radial displacement error value is 8.0 %, which is located at $r$ = 18 m along the x-axis from the tunnel center. Although the displacement analysis in RS2 has a relatively larger error than stress analysis, the exact difference is between the analytical method and RS2 solution is 0.1 mm, which is a limited difference.

Table 3.10 Error in RS2 analysis relative to analytical solution for elastic material.

| | Average | Maximum |
|---|---|---|
| Radial stress | 0.4 % | 1.3 % |
| Tangential stress | 0.3 % | 0.7 % |
| Displacement | 3.4 % | 8.0 % |

### 3.2.2 Comparison of the Results of Numerical and Analytical Methods for Elasto-Plastic Materials

Using the same test case of a circular tunnel representing a cylindrical tunnel excavated in an elasto-plastic material, the process is more complex than the elastic problem. The medium surrounding the excavation undergoes yielding and failure according to the Mohr-Coulomb failure criterion. Two cases were tested, one using an associated (dilatancy = friction angle) and another using a non-associated (dilatancy = 0) flow. The basic model setting is as same as the model established in Section 3.2.1. The plastic material parameters are shown in Table 3.11.

Table 3.11 Elasto-plastic material parameters, in-situ field stress ($P_0$) and internal pressure ($P_i$)

| Parameter | Value |
|---|---|
| $E$ (MPa) | 10,000 |
| $v$ | 0.2 |
| $\varphi$ (°) | 35 |
| $c$ (MPa) | 10.5 |
| $\gamma$ ($^{MN}/_{m^3}$) | 0.027 |
| $P_0$ (MPa) | 30 |
| $P_i$ (MPa) | 0 |
| G (MPa) | 4166.667 |
| $\psi$ (°) | 0 °, 30 ° |

Note: E is Young's modulus; $v$ is Poisson's ratio; $\varphi$ is friction angle; $c$ is cohesion; $\gamma$ is unit weight; G is compressive modulus; $\psi$ is dilation angle.

The analytical method divided the solution into two sets: elastic zone and a plastic zone. According to Salencon (1969), the yield zone radius $R_0$ is given by:

$$R_0 = a\left(\frac{2}{K_p+1}\frac{P_0+\frac{q}{K_{p-1}}}{P_i+\frac{q}{K_{p-1}}}\right)^{1/(K_p-1)} \tag{3.6}$$

where

$$K_p = \frac{1+\sin\varphi}{1-\sin\varphi} \tag{3.7}$$

$$q = 2c\tan(45+\varphi/2) \tag{3.8}$$

According to the parameters shown in Table 3.11, the yield zone radius is equal to 5.205 m, which is measured from the tunnel center. $K_p$ is the passive earth pressure coefficient, which is determined by the material friction angle, which was equal to 3. The uniaxial compressive strength $q$, which is related to the Mohr-Coulomb strength parameters, was 11.95 MPa.

The radial stress at the elasto-plastic interface is:

$$\sigma_{re} = \frac{1}{K_p+1}(2P_0 - q) \tag{3.9}$$

In radial coordinates $(r,\theta)$, stresses and radial displacement in the elastic zone are given by:

$$\sigma_r = P_0 - (P_0 - \sigma_{re})(\frac{R_0}{r})^2 \tag{3.10}$$

$$\sigma_\theta = P_0 + (P_0 - \sigma_{re})(\frac{R_0}{r})^2 \tag{3.11}$$

$$u_r = \frac{{R_0}^2}{2G}\left(P_0 - \frac{2P_0 - q}{K_p+1}\right)\frac{1}{r} \tag{3.12}$$

While the stresses and radial displacement in the plastic zone are:

$$\sigma_r = -\frac{q}{K_p-1} + (P_i + \frac{q}{K_p-1})(\frac{r}{a})^{(K_p-1)} \tag{3.13}$$

$$\sigma_\theta = -\frac{q}{K_p-1} + K_p(P_i + \frac{q}{K_p-1})(\frac{r}{a})^{(K_p-1)} \tag{3.14}$$

$$\begin{aligned} u_r = \frac{r}{2G}\Bigg[&(2v-1)\left(P_0 + \frac{q}{K_p-1}\right) \\ &+ \frac{(1-v)({K_p}^2-1)}{K_p+K_{ps}}\left(P_i + \frac{q}{K_p-1}\right)\left(\frac{R_0}{a}\right)^{(K_p-1)}\left(\frac{R_0}{r}\right)^{(K_{ps}+1)} \\ &+ \left(\frac{(1-v)(K_pK_{ps}+1)}{K_p+K_{ps}} - v\right)(P_i + \frac{q}{K_p-1})\left(\frac{r}{a}\right)^{(K_p-1)}\Bigg] \end{aligned} \tag{3.15}$$

where

$$K_{ps} = \frac{1+\sin\psi}{1-\sin\psi} \tag{3.16}$$

For dilatancy = 0 ($\psi = 0$ °), the comparison between the analytical method and RS2 for radial and tangential stress and radial displacement is shown in Figure 3.18, Figure 3.19 and Figure 3.20. The contours of stresses and displacements obtained from RS2 are illustrated in Figure 3.21, Figure 3.22 and Figure 3.23. In Table 3.12, the error in RS2 analysis relative to analytical solution for both associated (dilatancy = friction angle) and non-associated (dilatancy = 0) flow cases is shown.

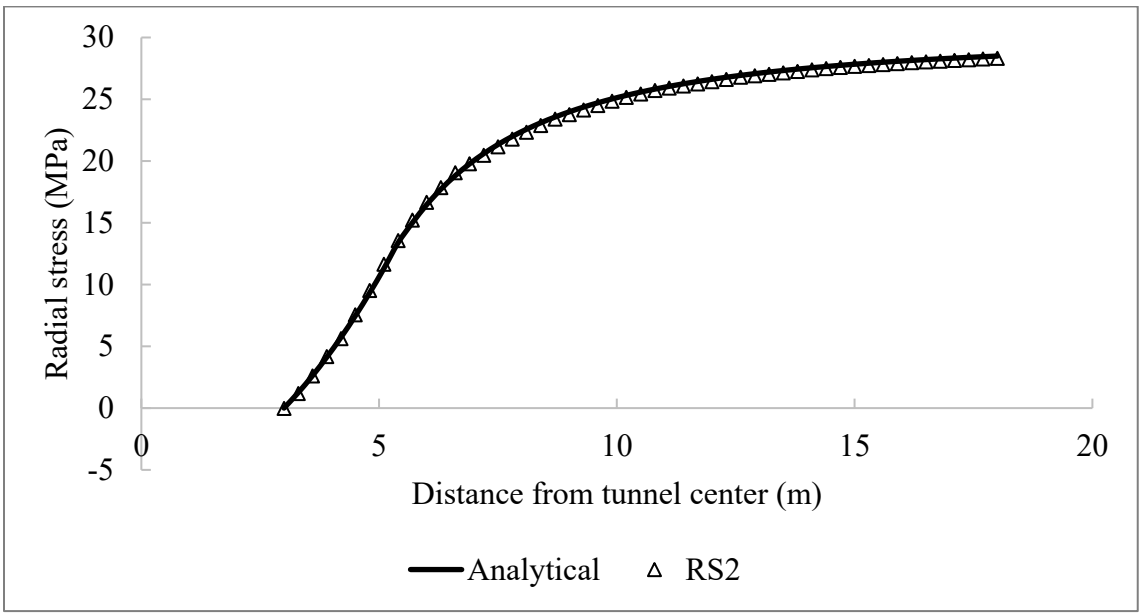


Figure 3.18. Comparison of radial stress distributions along the x-axis from the tunnel center to the designated point for ($\psi$ = 0 °) case.

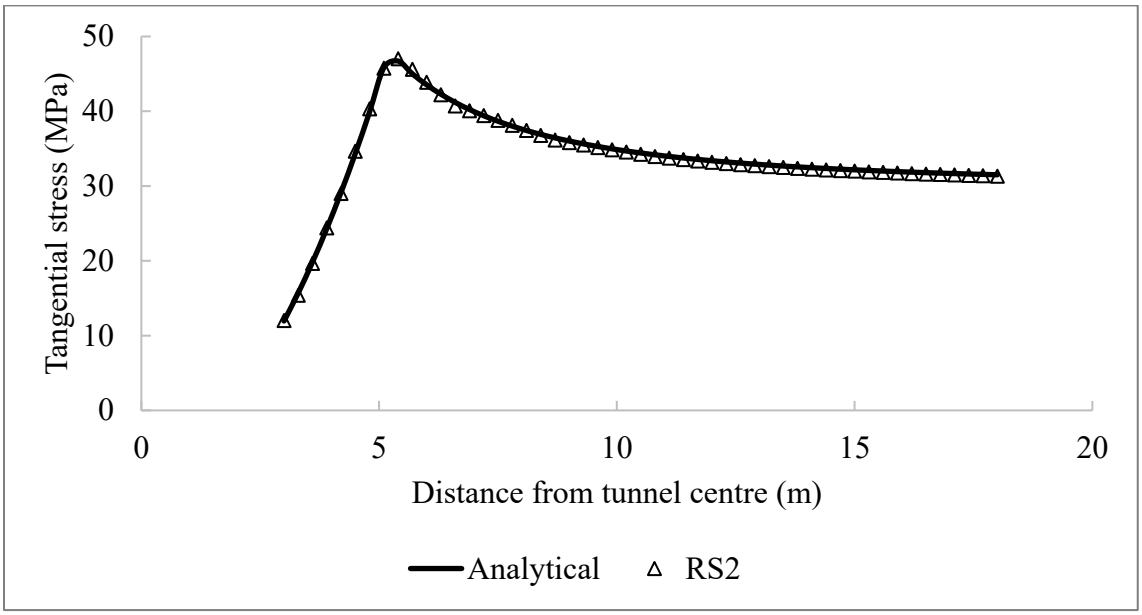


Figure 3.19. Comparison of tangential stress distributions along the x-axis from the tunnel center to the designated point for ($\psi$ = 0 °) case.

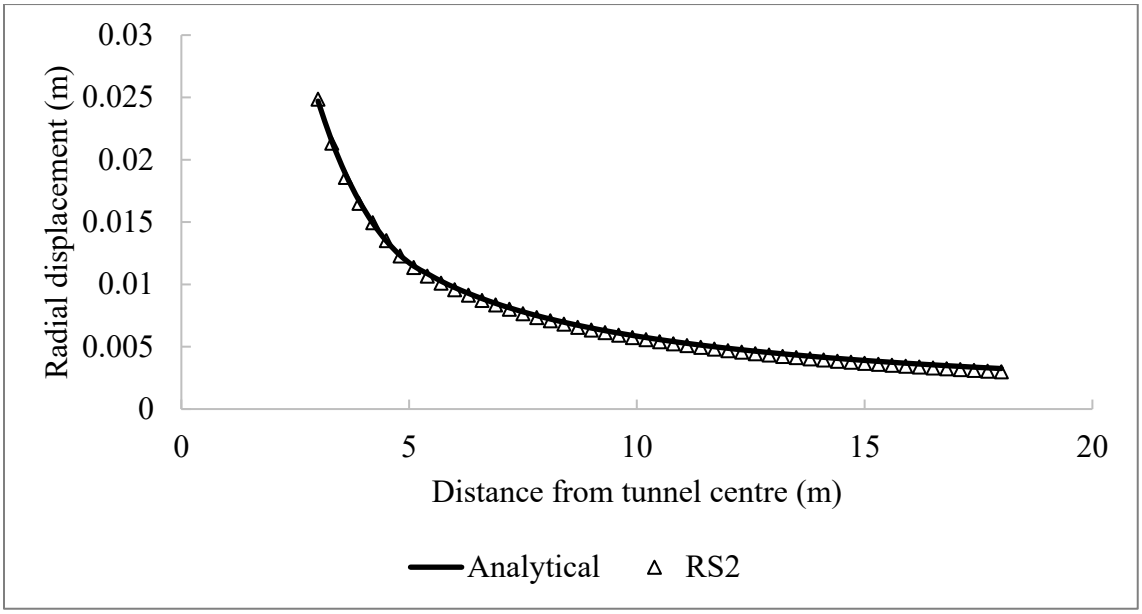


Figure 3.20. Comparison of radial displacement distributions along the x-axis from the tunnel center to the designated point for ($\psi$ = 0 °) case.

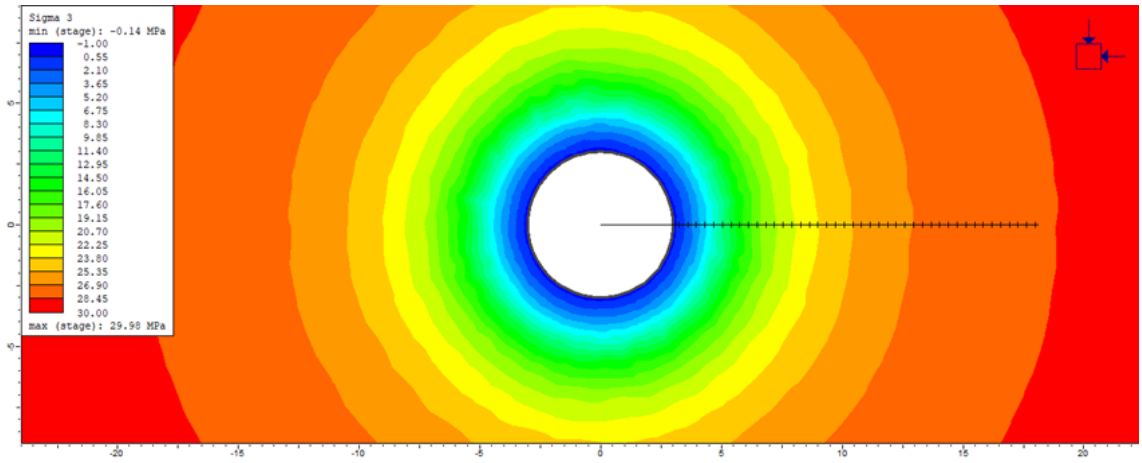


Figure 3.21. Contours of radial stress from RS2 for ($\psi$ = 0 °) case.

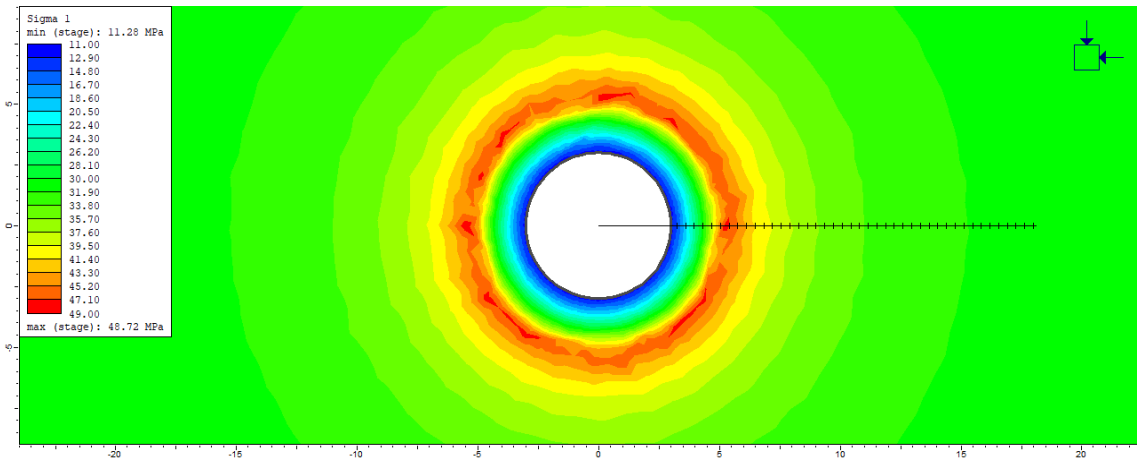


Figure 3.22. Contours of tangential stress from RS2 for ($\psi$ = 0 °) case.

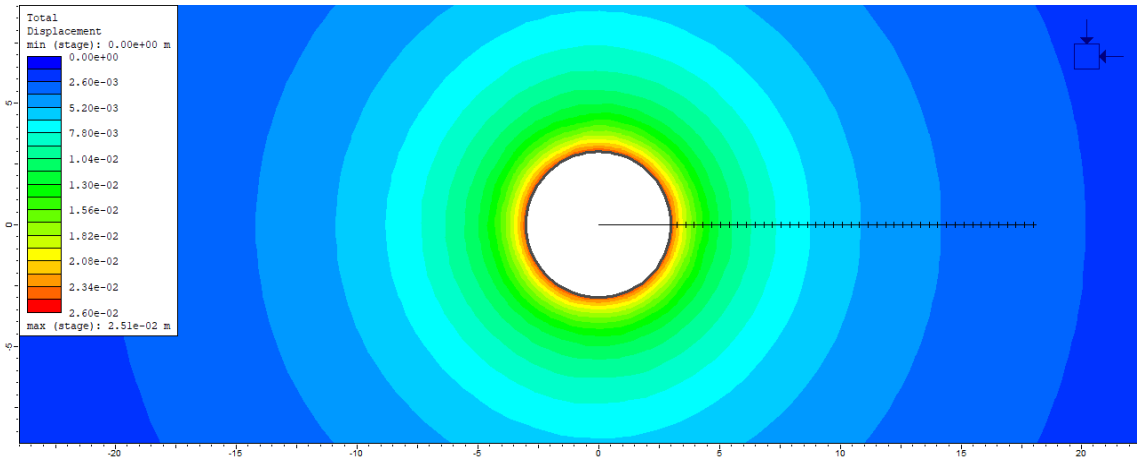


Figure 3.23. Contours of radial displacement from RS for ($\psi$ = 0 °) case.

For dilatancy = friction angle ($\psi = 30$ °), the comparison between the analytical method and RS2 for radial and tangential stress and radial displacement is shown in Figure 3.24, Figure 3.25 and Figure 3.26. The contours of stresses and displacements from RS2 are shown in Figure 3.27, Figure 3.28 and Figure 3.29. Also, the yield zone around the tunnel will be shown in Figure 3.30.

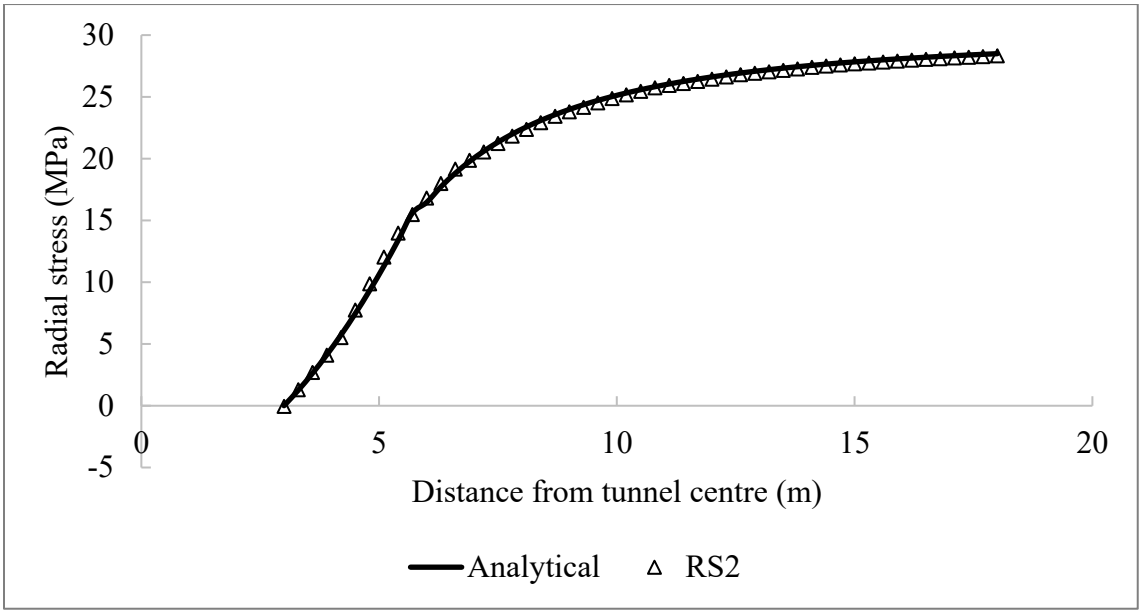


Figure 3.24. Comparison of radial stress distributions along the x-axis from the tunnel center to the designated point for ($\psi$ = 30 °) case.

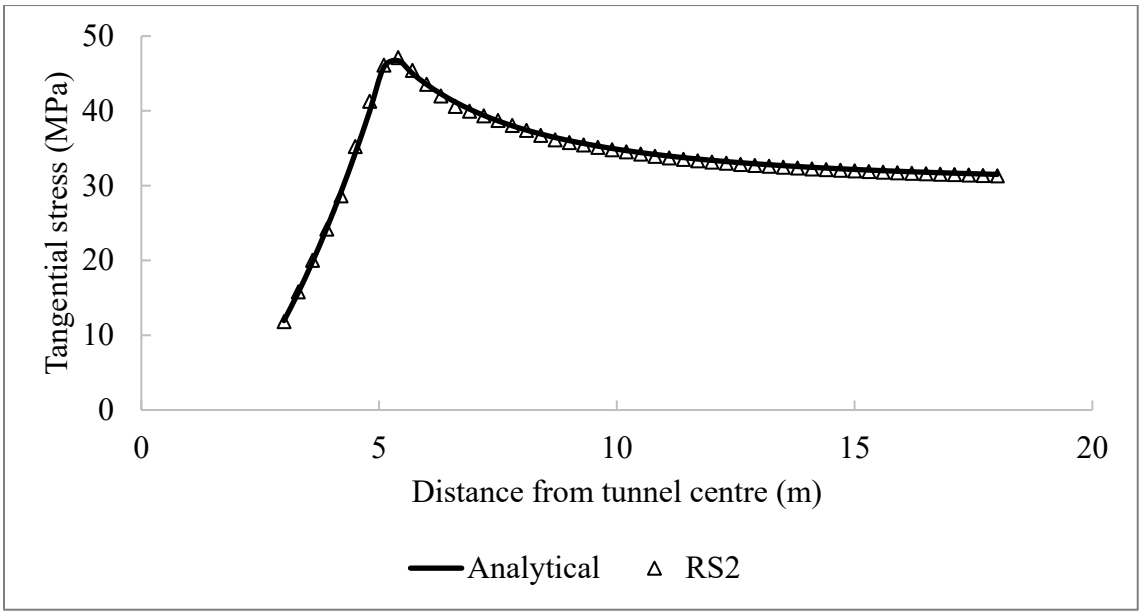


Figure 3.25. Comparison of tangential stress distributions along the x-axis from the tunnel center to the designated point for ($\psi$ = 30 °) case.

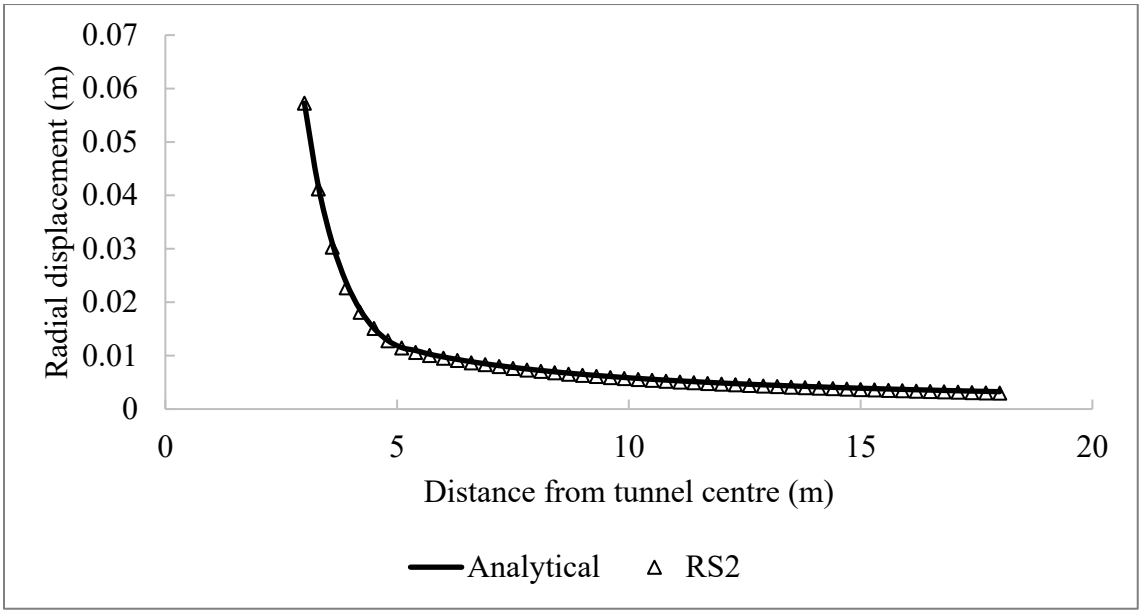


Figure 3.26. Comparison of radial displacement distributions along the x-axis from the tunnel center to the designated point for ($\psi$ = 30 °) case.

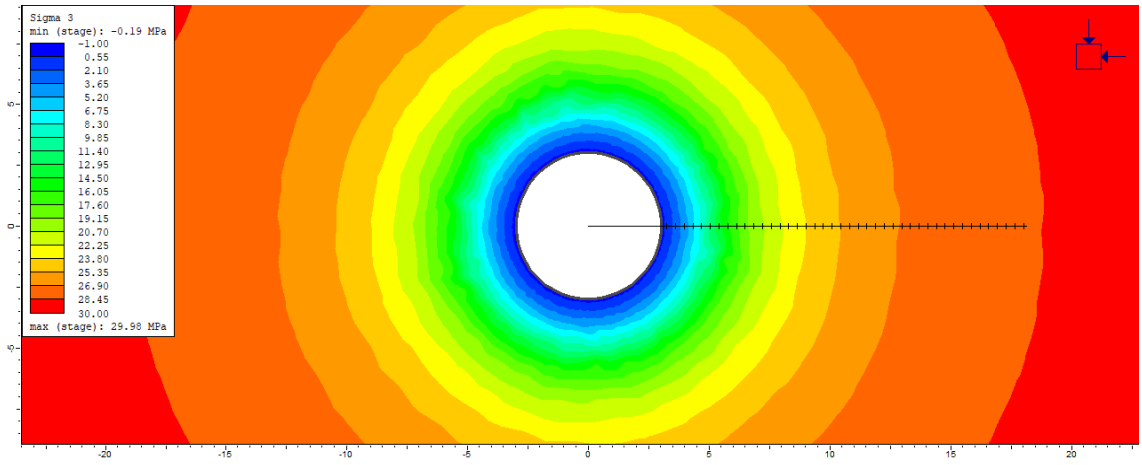


Figure 3.27. Contours of radial stress from RS2 for ($\psi$ = 30 °) case.

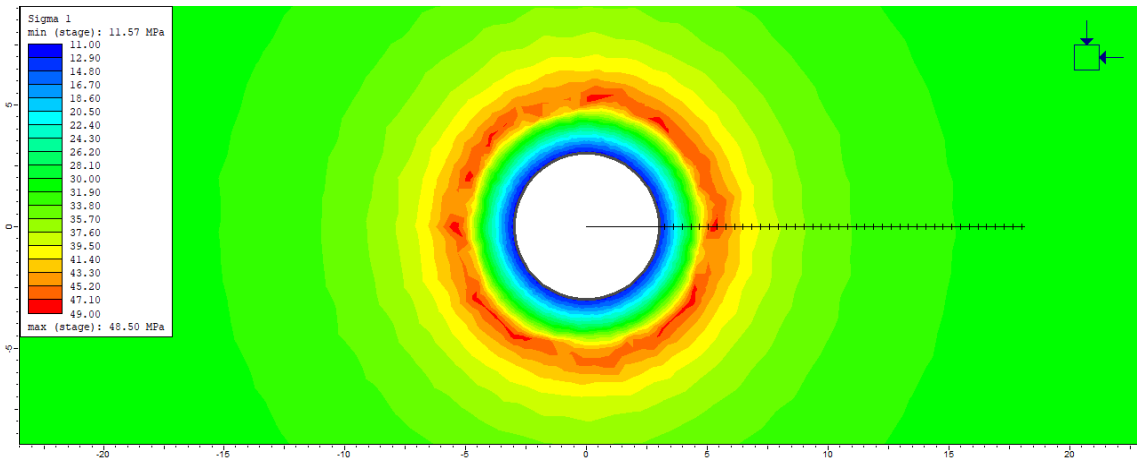


Figure 3.28. Contours of tangential stress from RS2 for ($\psi$ = 30 °) case.

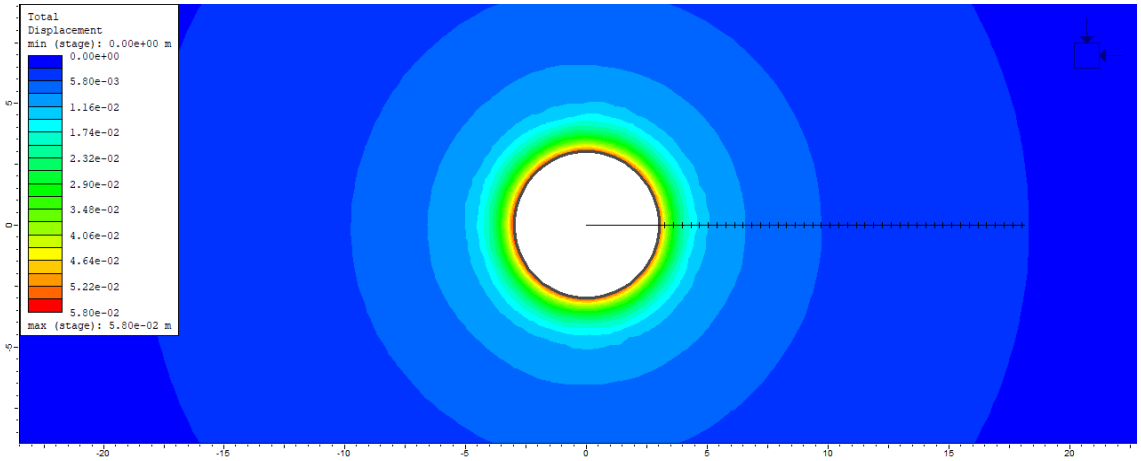


Figure 3.29. Contours of radial displacement from RS for ($\psi$ = 30 °) case.

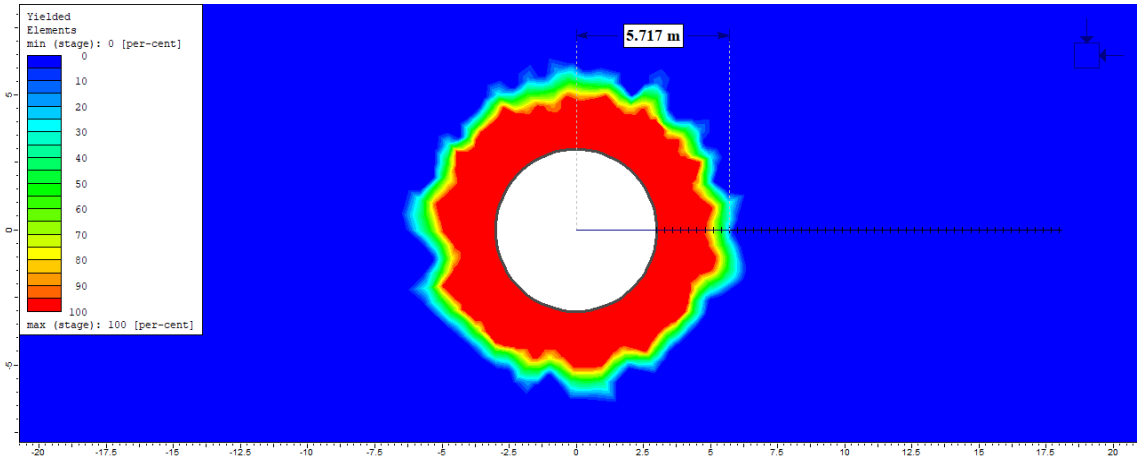


Figure 3.30. Contours of yield and plastic zone from RS2 for ($\psi$ = 30 °) case.

The RS2 error analysis results are displayed in Table 3.12. The location of the maximum error in RS2 stresses analysis for both $\psi = 0\,^\circ$ and $\psi = 30\,^\circ$ cases is at the tunnel boundary. On the other hand, the maximum error for displacement analysis for the two instances occurs at $r$ = 18 m along the x-axis from the tunnel center. The average errors are less than 5 % for both cases in RS2 stresses and displacement analysis. The Yielded Elements contouring in Figure 3.30 helps to describe the degree of yielding surrounding the excavations. The degree of yielding (also called as perfect yielding) at each node is expressed as a percent, which can be given by the rate of the number of yielded elements by the total number of elements attached to a node (RS2 User Manual 2019). Therefore, the large degree of yielding is in the most critical area (red zone in Figure 3.30) surrounds the tunnel; and it decreases with the increase of distance away from the tunnel center. In addition, the plastic zone radius from the analytical method is 5.025 m. This value is 5.717 m from the RS2 solution, as shown in Figure 3.30, which is larger than the analytical result by 0.692 m. Combining results from Figures 3.18 to 3.30, it proves that RS2 can provide reliable results for a cylindrical tunnel excavated in a Mohr-Coulomb material.

Table 3.12 Error in RS2 analysis relative to analytical solution for both associated (dilatancy = friction angle) and non-associated (dilatancy = 0) flow cases

| / | $\psi = 0\,^\circ$ | | $\psi = 30\,^\circ$ | |
|---|---|---|---|---|
| | Average | Maximum | Average | Maximum |
| Radial stress | 1.0 % | 7.0 % | 1.2 % | 6.4 % |
| Tangential stress | 0.6 % | 2.0 % | 0.7 % | 3.4 % |
| Displacement | 3.7 % | 8.3 % | 4.3 % | 8.8 % |

# Chapter 4 Discussion of FEM Modeling Results of Tunneling-induced Displacements on Railway Embankments

Based on the preceding discussion of creating FEM models using RS2, in this chapter, the results obtained from solving the models will be discussed. Certain key factors that affect the ground surface displacement, such as tunnel diameter, tunnel depth, and train operating speed, will also be analyzed in the discussion and interpretation of results. The influence of key parameters will be determined by adopting the vertical displacement along the ballast surface as a measure of influence since it directly affects the safety of train operations. There are three scenarios to be discussed in this chapter. In the first scenario, the influence of train operation on ground deformation will be considered by itself. In addition to the first scenario, the second scenario considers the effect of tunneling with different tunnel diameters at various depths. In order to investigate the ground surface displacement induced by tunnel excavation without the effect of the train operation, the third scenario is established as well. This scenario focuses on how the tunnel depth (H) parameter and tunnel diameter (D) parameter impact the vertical surface deformation. To be noted, the ballast surface in the FEM models is treated as the ground surface.

## 4.1 Scenario 1 – The Influence of Train Operation Speed on the Ballast Surface Vertical Displacement ($S_v$)

This scenario is to observe the effect of train speed through the simulation of railway operation induced trainloads applied on the ballast surface. Therefore, the influence of different train speeds on the vertical displacement along the ballast surface ($S_{vv}$) will be investigated. Figure 4.1 illustrates the train loading distribution along the longitudinal direction of the railway. The displacement distributions caused by the four train speeds considered (0, 40, 80, 120 km/h) are shown in Figure 4.2. Also, the location of maximum deformation is indicated in Figure 4.2.

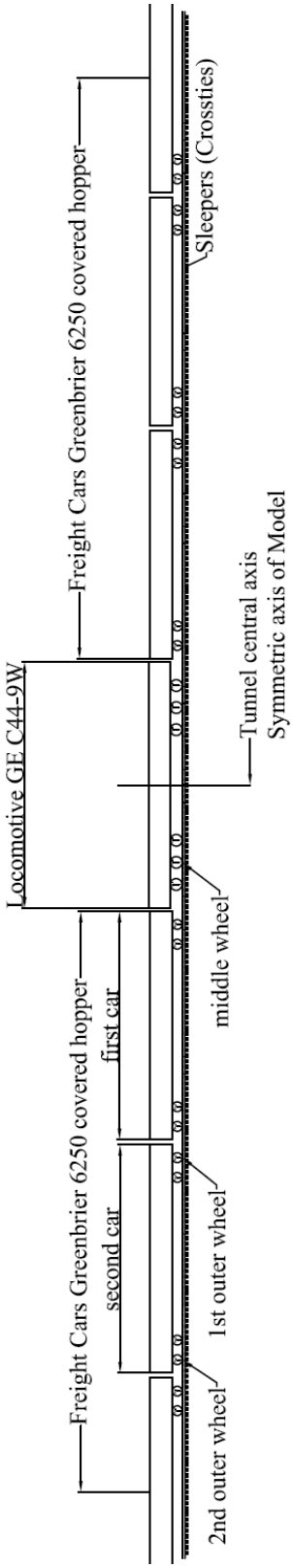


Figure 4.1 Load distribution from freight train in simulation models.

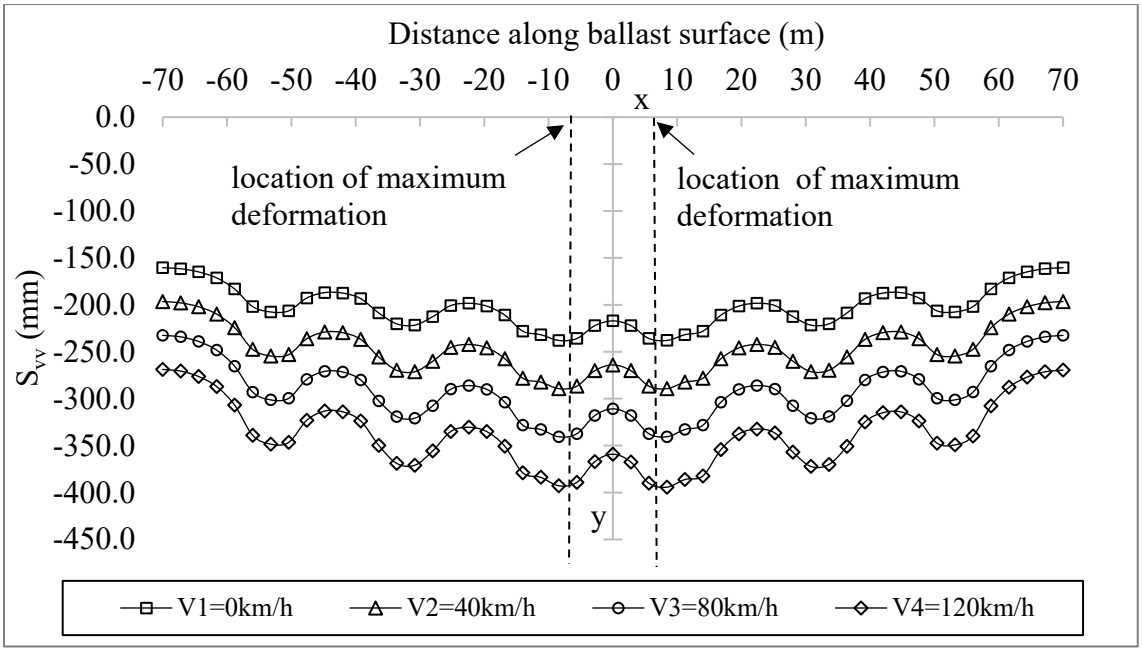


Figure 4.2.Vertical ground displacement along the ballast surface caused by trainload ($S_{vv}$) with train speeds of 0, 40, 80, 120 km/h.

Corresponding to the results shown in Figure 4.2, the trainload can generate large deformations in the clay ground. All curves of displacement are symmetric about the central axis, and the curved shape of $S_{vv}$ along the ballast surface follows the position where the locomotive and freight train axle loads are applied. The maximum values of $S_{vv}$ occur at x = -7 m and x = 7 m, which are the positions of the sleeper under the middle wheel of a locomotive bogie, referring to the positions in Figure 4.1. The vertical displacement contour at four different train speeds is illustrated in Figure 4.3 (a) to 4.3 (d). The value of the maximum vertical displacement at the ballast surface is shown in Figure 4.4.

From Figure 4.3 (a) to 4.3 (d), it can be observed that the ground moves downward with the increasing trainload; the applied trainloads compress the silty clay ground. The shape of displacement along the ballast surface does not change when the load magnitude rises; only the values increase. The details of train loadings distribution for the half model on the top boundary under different train loading conditions are shown in Appendix C.

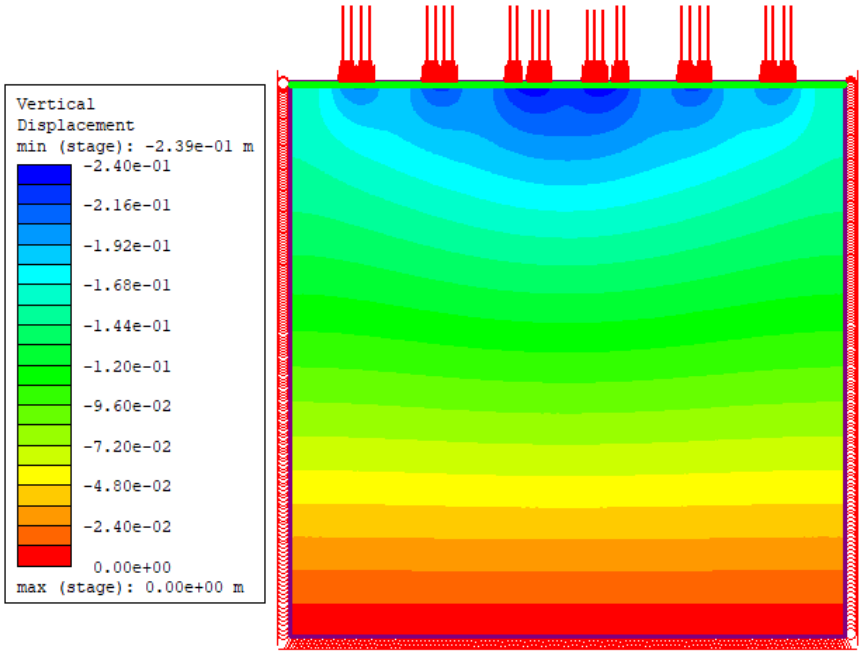


Figure 4.3. (a) Vertical displacement contour for the model with $V_1 = 0$ km/h train loading.

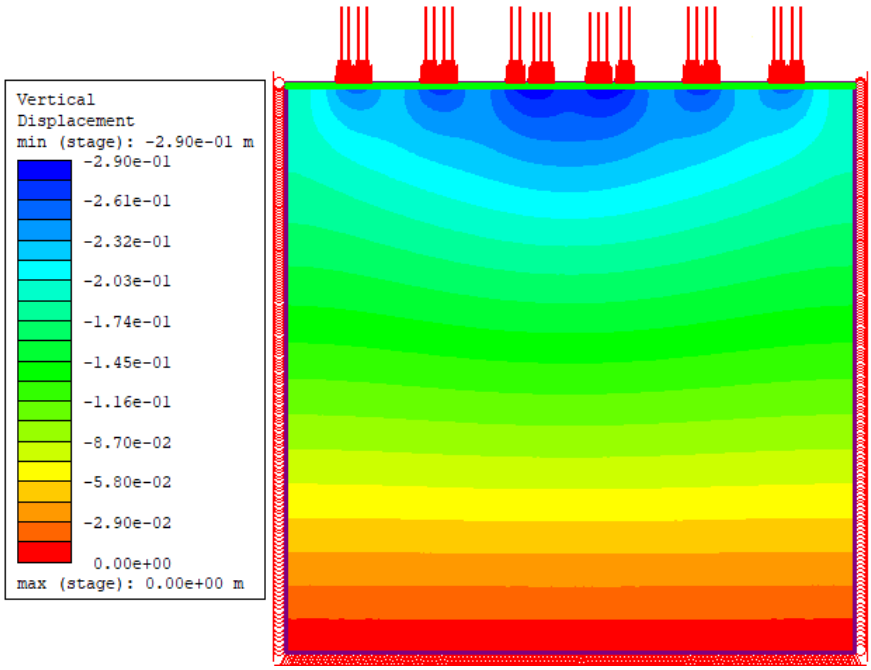


Figure 4.3. (b) Vertical displacement contour for the model with $V_2 = 40$ km/h train loading.

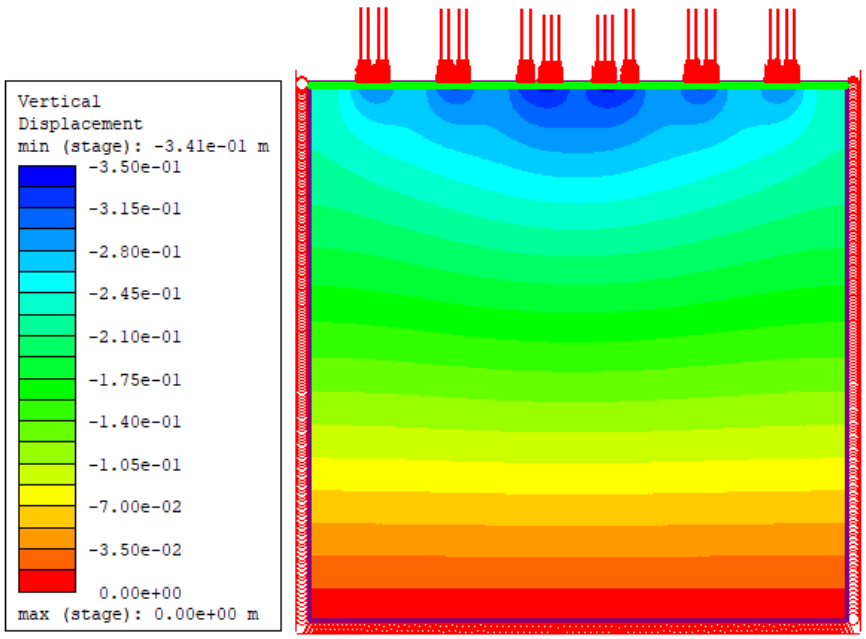


Figure 4.3. (c) Vertical displacement contour for the model with $V_3$ = 80 km/h train loading.

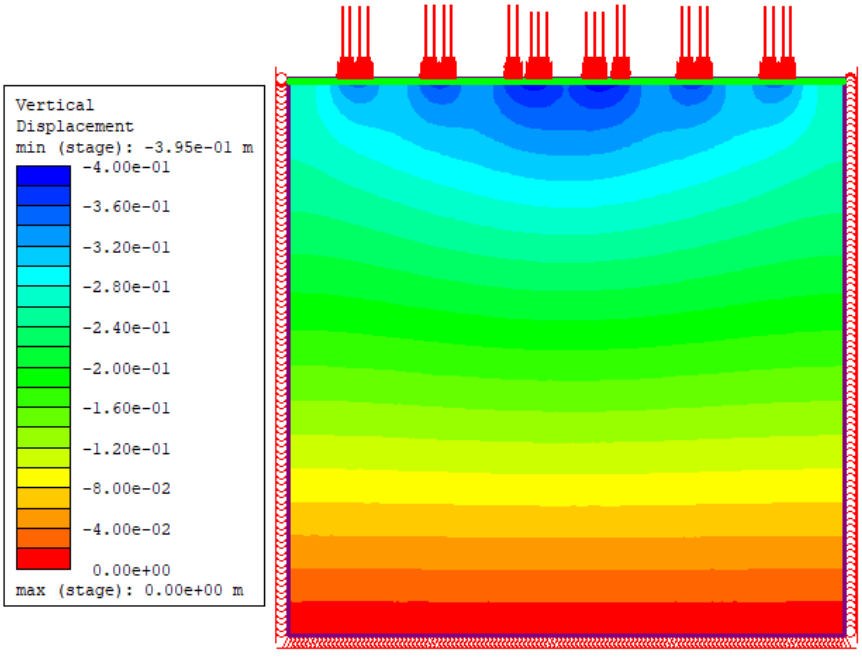


Figure 4.3. (d) Vertical displacement contour for the model with $V_4$ = 120 km/h train loading.

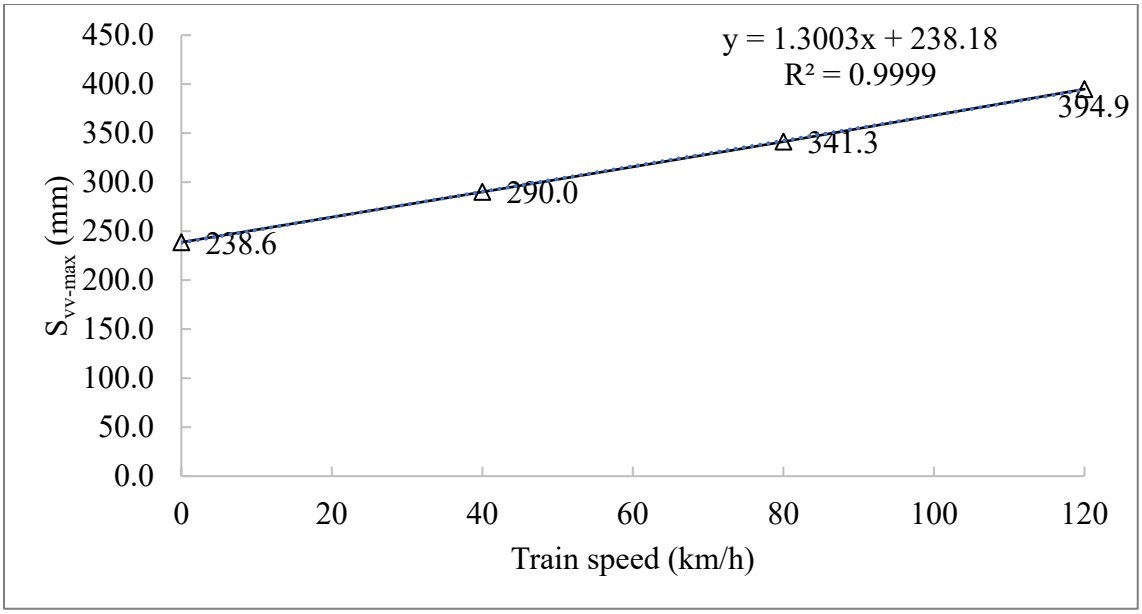


Figure 4.4. Maximum vertical displacement along the ballast surface caused by trainload ($S_{vv\text{-}max}$) for the four train speeds considered (0,40,80,120 km/h).

Figure 4.4 shows the values of $S_{vv\text{-}max}$ for the four train speeds considered. The results appear to follow a linear trend. The line is a very close fit to the data ($R^2 = 0.999$); accordingly, the $S_{vv\text{-}max}$ induced by train operation at a certain speed between (0 to 120 km/h) can be predicted using the equation shown in the figure.

## 4.2 Scenario 2 - Tunnel Excavation Under an Operating Rail Line – Influence of Train Speed on the Vertical Surface Displacement ($S_v$)

In this scenario, the vertical displacement along the ballast surface ($S_{vp}$) induced by simultaneous train operation and tunnel excavation is presented. In Sections 4.2.1 and 4.2.2, the minimum (D = 3 m) and maximum (D = 14 m) tunnel diameters, respectively, are chosen as examples to interpret the data. As expected, the tunnel excavation has the greatest influence on the area directly above the tunnel. The vertical displacement of the ballast surface at the tunnel's central axis ($S_{vp\text{-}c}$) will be examined in Section 4.2.3.

### 4.2.1 Excavation of D = 3 m Tunnel Located at Various Depths Subjected to Train Loading

From Figure 4.5 (a) to 4.5 (d), the vertical displacement distribution of excavation for model D = 3 m at multiple depths while the train is in operation with train speeds 0, 40, 80 and 120 km/h are displayed, respectively. Since the data is symmetrical from the y-axis, results for only half of the model are plotted in Figure 4.5 (a) to (d).

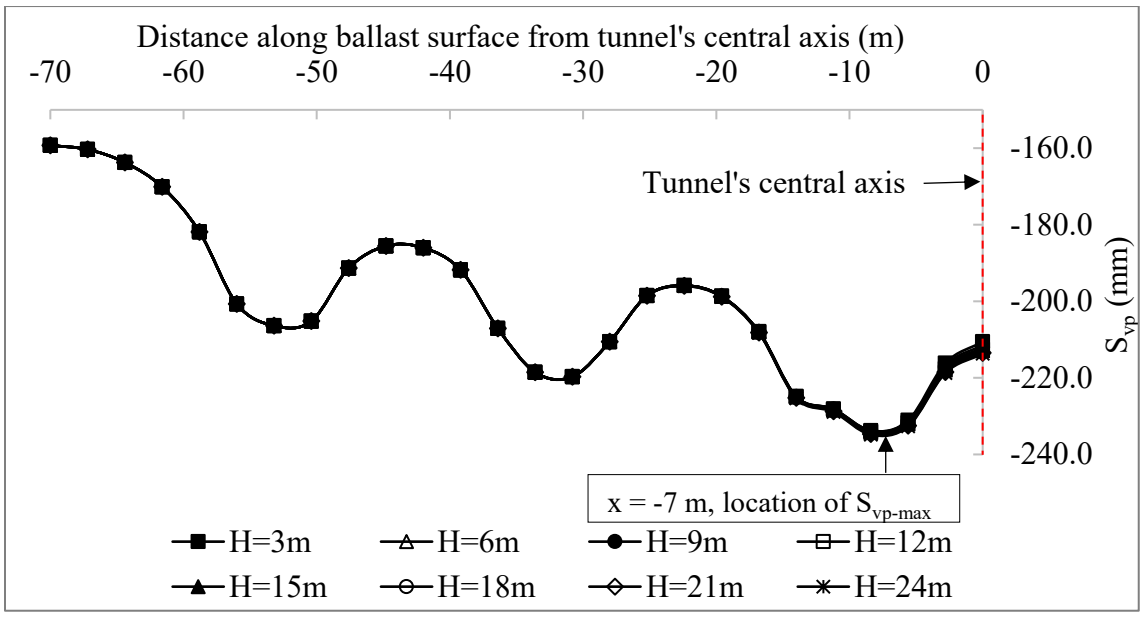


Figure 4.5. (a) Symmetrical displacement distribution for model D = 3 m excavation with operating train ($V_1$ = 0 km/h).

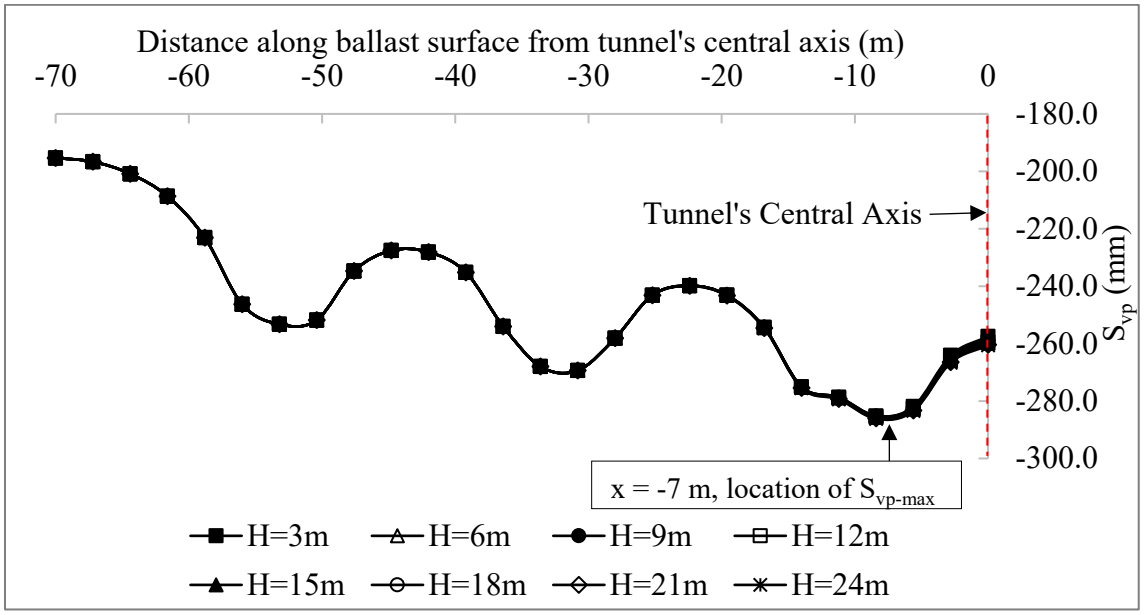


Figure 4.5. (b) Symmetrical displacement distribution for model D = 3 m excavation with operating train ($V_2$ = 40 km/h).

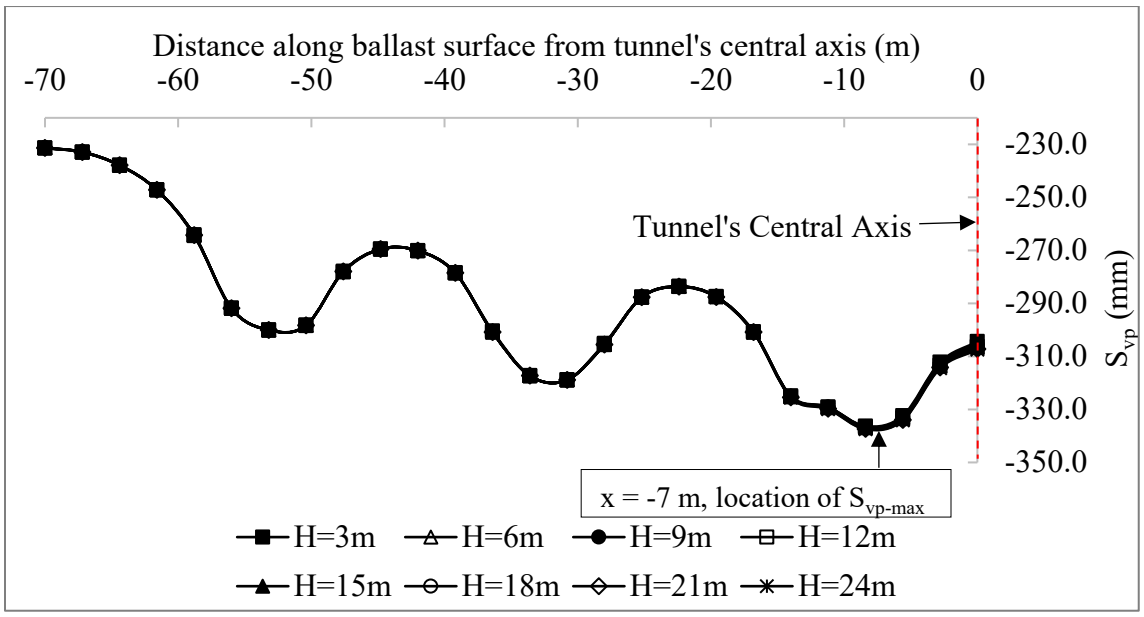


Figure 4.5. (c) Symmetrical displacement distribution for model D = 3 m excavation with operating train ($V_3$ = 80 km/h).

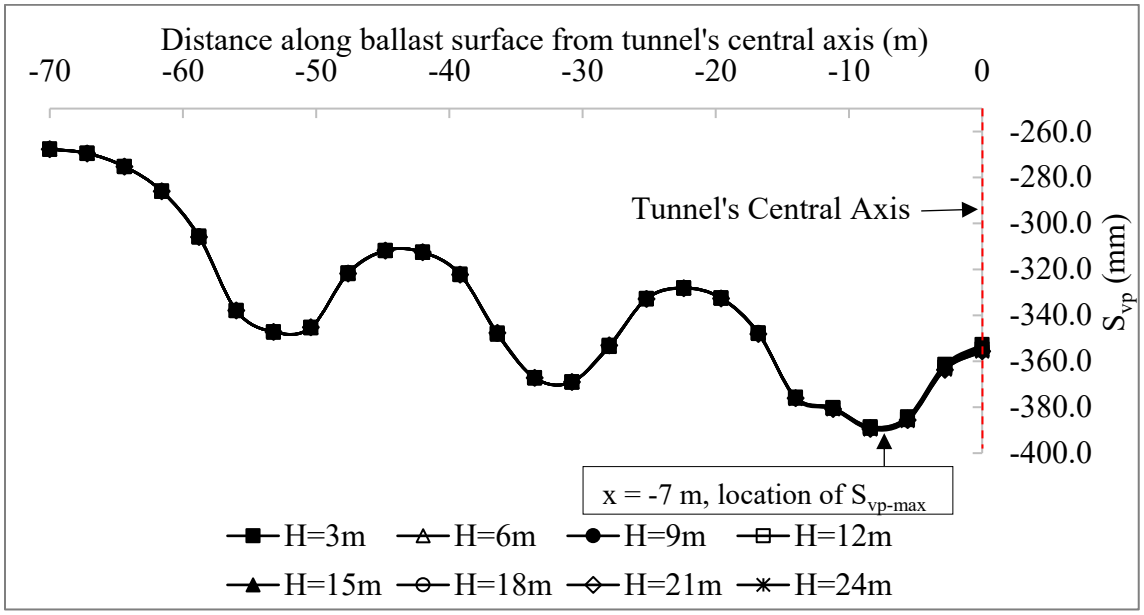


Figure 4.5. (d) Symmetrical displacement distribution for model D = 3 m excavation with operating train ($V_4$ = 120 km/h).

Corresponding to Figure 4.5 (a) to 4.5 (d), the $S_{vp}$ distributions for the model with tunnel diameter of 3 m under the four train loadings follow the same shape but increasing magnitude as the train speed increases. All curves more or less overlap with each other. The maximum value is in the same position at x = -7 m, as shown in the figures, referring to Figure 4.1, which has been discussed in Section 4.1. Based on the displacement scales from the figures, the tunnel excavation for model D = 3 m under train operation has an insignificant influence on the ground surface deformation in comparison to the case with the train loading only. The average and maximum difference (%) between $S_{vv}$ and $S_{vp}$ for D = 3 m under different train speed conditions are illustrated in Table 4.1. The location of the maximum difference is at the tunnel's central axis. Both average and maximum differences decrease when the train speed increases from 0 km/h to 120 km/h. Also, when the tunnel deepens, the average and maximum differences decline. Figure 4.6 displays the vertical displacement contour for tunnel D = 3 m at depth H = 3 m with $V_4$ = 120 km/h train loading. Figure 4.7 illustrates the same tunnel diameter at depth H = 24 m with the same train speed.

Table 4.1 Average and maximum difference (%) between $S_{vv}$ and $S_{vp}$ when D = 3 m under four train speed conditions

| / | Average difference (%) | | | | Maximum difference (%) | | | |
|---|---|---|---|---|---|---|---|---|
| H (m) | $V_1$=0 km/h | $V_2$=40 km/h | $V_3$=80 km/h | $V_4$=120 km/h | $V_1$=0 km/h | $V_2$=40 km/h | $V_3$=80 km/h | $V_4$=120 km/h |
| 3 | 1.1 | 0.9 | 0.8 | 0.7 | 3.0 | 2.5 | 2.1 | 1.8 |
| 6 | 1.1 | 0.9 | 0.8 | 0.6 | 2.6 | 2.1 | 1.8 | 1.5 |
| 9 | 1.1 | 0.9 | 0.7 | 0.6 | 2.3 | 1.9 | 1.6 | 1.4 |
| 12 | 1.0 | 0.9 | 0.7 | 0.6 | 2.1 | 1.7 | 1.4 | 1.3 |
| 15 | 1.0 | 0.8 | 0.7 | 0.6 | 1.9 | 1.6 | 1.4 | 1.2 |
| 18 | 1.0 | 0.8 | 0.7 | 0.6 | 1.8 | 1.5 | 1.2 | 1.1 |
| 21 | 1.0 | 0.8 | 0.7 | 0.6 | 1.7 | 1.4 | 1.2 | 1.0 |
| 24 | 0.9 | 0.8 | 0.7 | 0.6 | 1.6 | 1.3 | 1.1 | 0.9 |

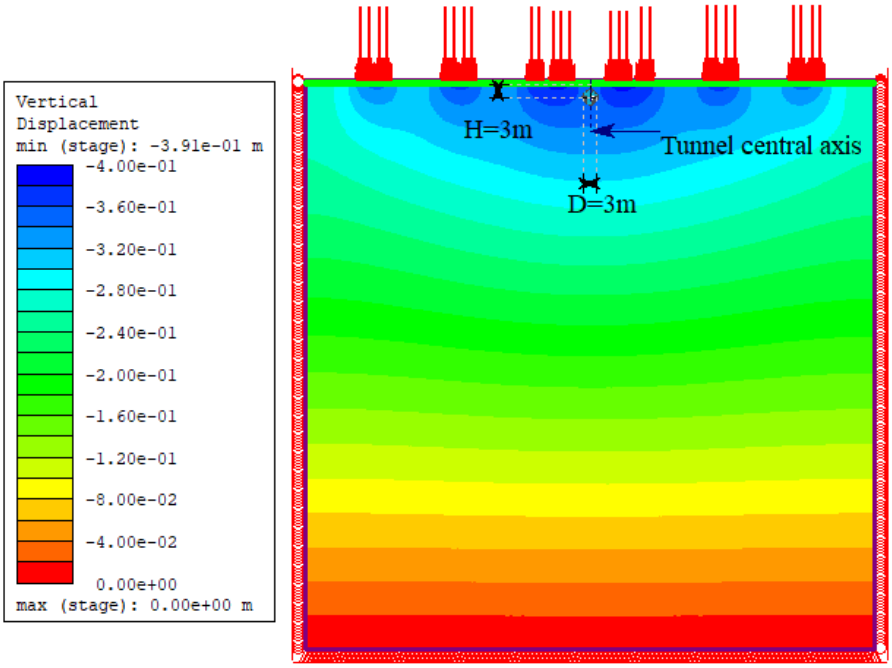


Figure 4.6. Vertical displacement contour for model with D = 3 m, H = 3 m, $V_4$ = 120 km/h.

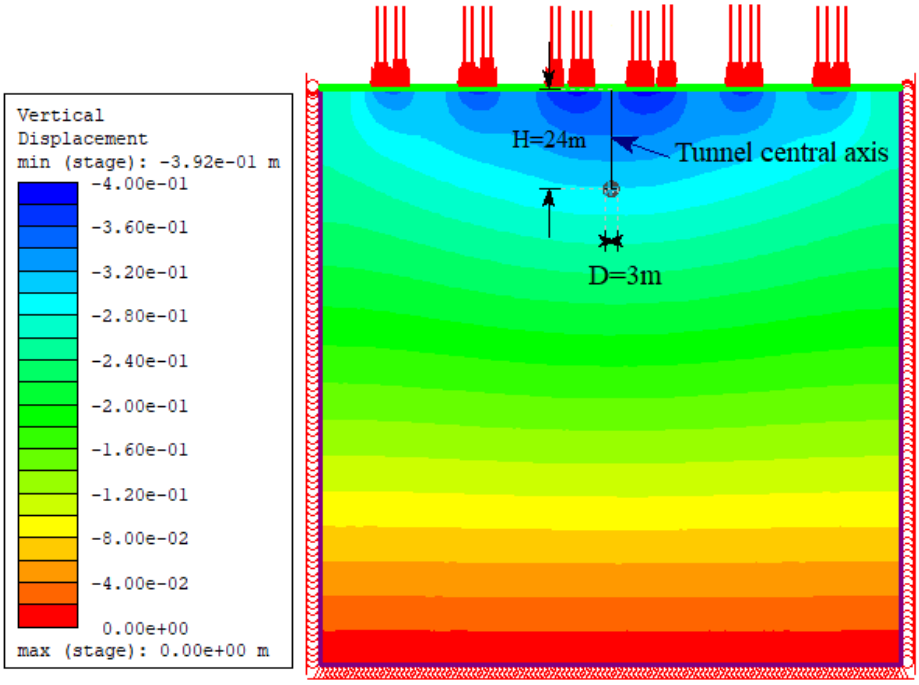


Figure 4.7. Vertical displacement contour for model with D = 3 m, H = 24 m, $V_4$ = 120 km/h.

The vertical displacement contours in Figure 4.6 and Figure 4.7 indicate that the displacement patterns still follow the applied trainloads' magnitude; it is the same as the previous observation. The most critical locations are still under the locomotive bogie. Comparing Figure 4.6 with Figure 4.3 (d), there is a 4 mm difference between $S_{vv\text{-}max}$ and $S_{vp\text{-}max}$ as shown in the contour labels, which is induced by the tunnel excavation (D = 3 m, H = 3 m, $V_4$ = 120 km/h). When the tunnel is excavated at depth H = 24 m with $V_4$ = 120 km/h condition, the difference between $S_{vv\text{-}max}$ and $S_{vp\text{-}max}$ is 3 mm, as seen in comparing Figure 4.7 to Figure 4.3 (d). In addition, these comparisons also prove that the D = 3 m tunnel excavation at various depths has a relatively small impact on the ground surface deformation. The details of train loadings distributions for the half model on the top boundary of models under train speed $V_4$ = 120 km/h are shown in Appendix C.

### 4.2.2 Excavation of D = 14 m Tunnel Located at Various Depths Subjected to Train Loading

Figure 4.8 (a) to 4.8 (d), shows the vertical displacement distribution for the model with D = 14 m at multiple depths while the train is in operation with train speeds of 0, 40, 80 and 120 km/h, respectively. The locations of $S_{vp\text{-}max}$ at different tunnel depths are also illustrated in Figures 4.8 (a) to 4.8 (d).

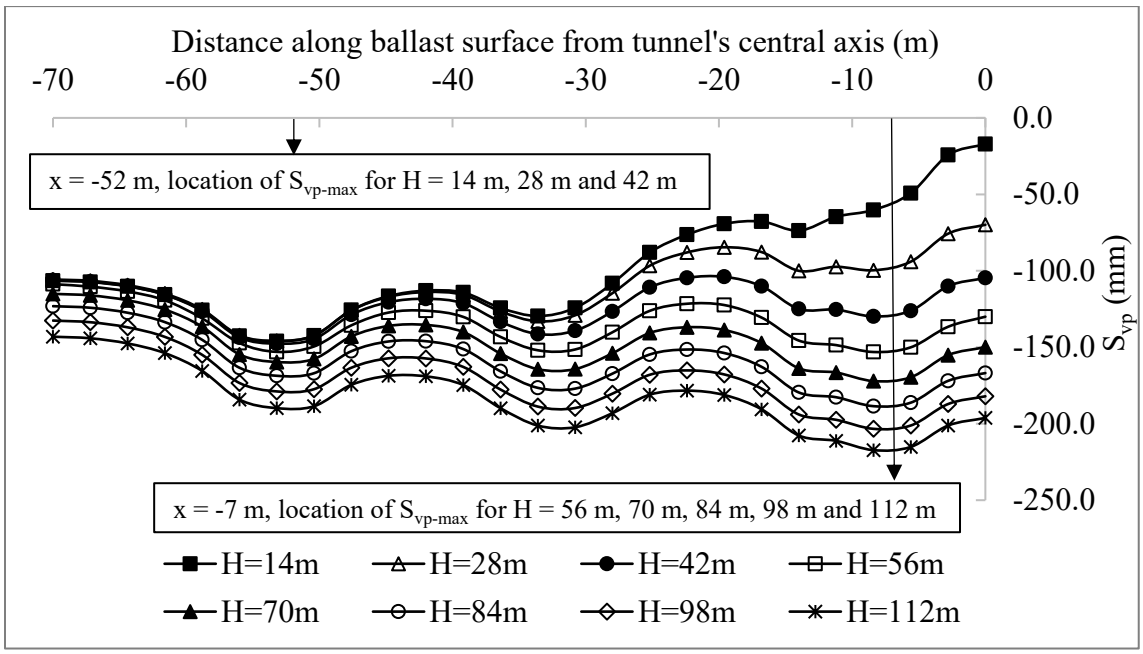


Figure 4.8. (a) Symmetrical displacement distribution for model D = 14 m excavation with stationary train ($V_1$ = 0 km/h).

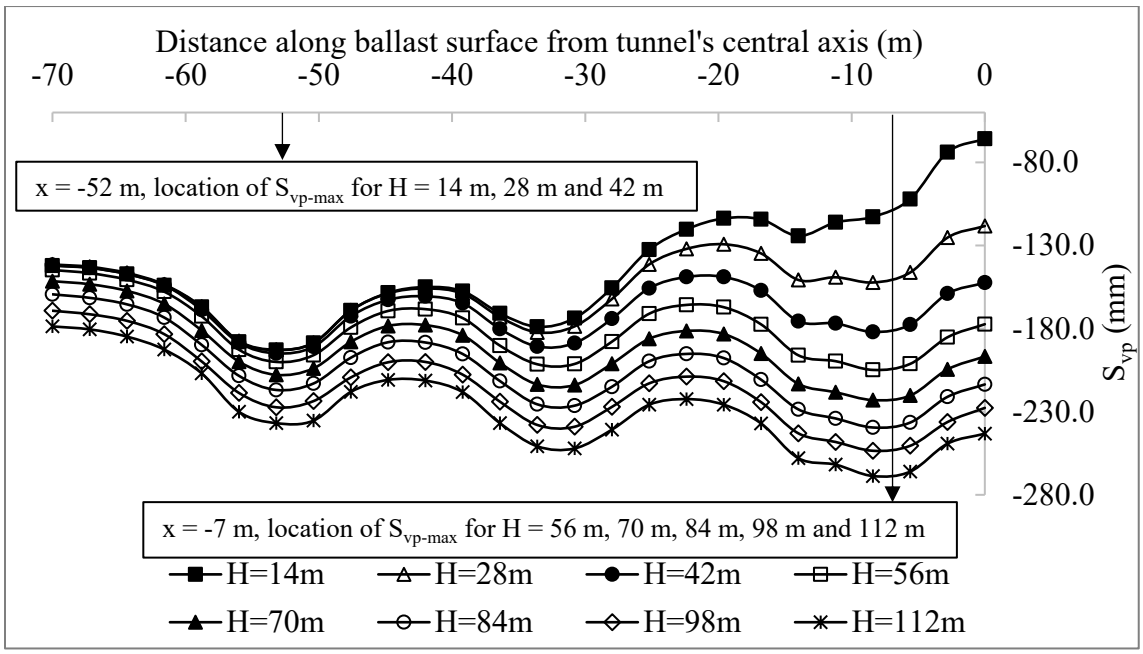


Figure 4.8. (b) Symmetrical displacement distribution for model D = 14 m excavation with operating train ($V_2$ = 40 km/h).

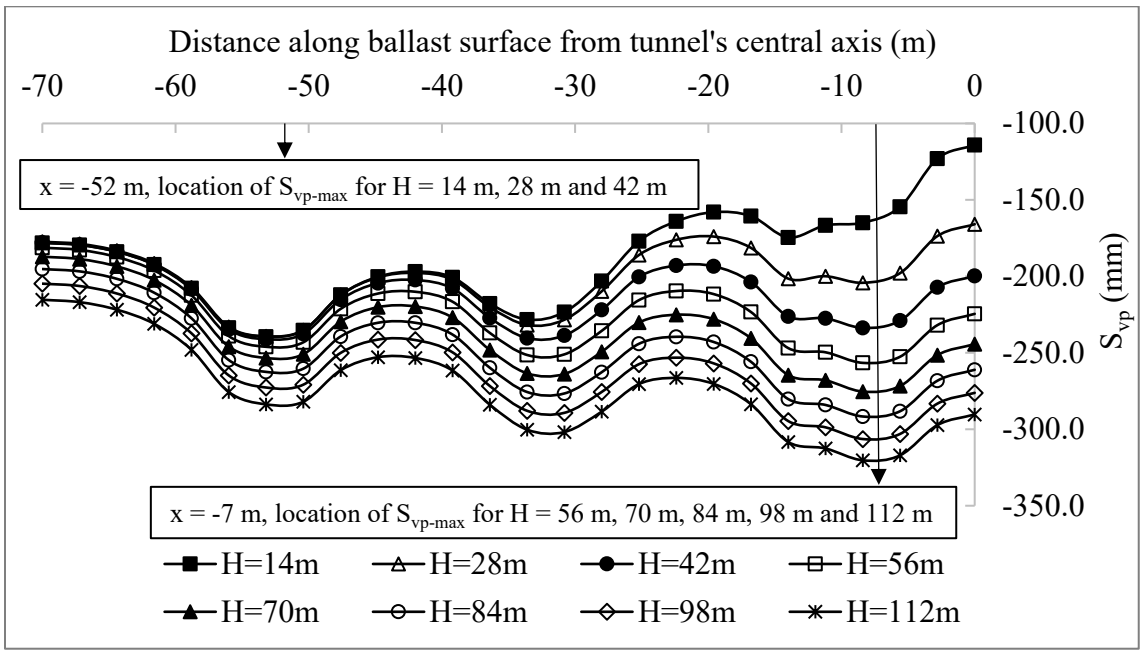


Figure 4.8. (c) Symmetrical displacement distribution for model D = 14 m excavation with operating train ($V_3$ = 80 km/h).

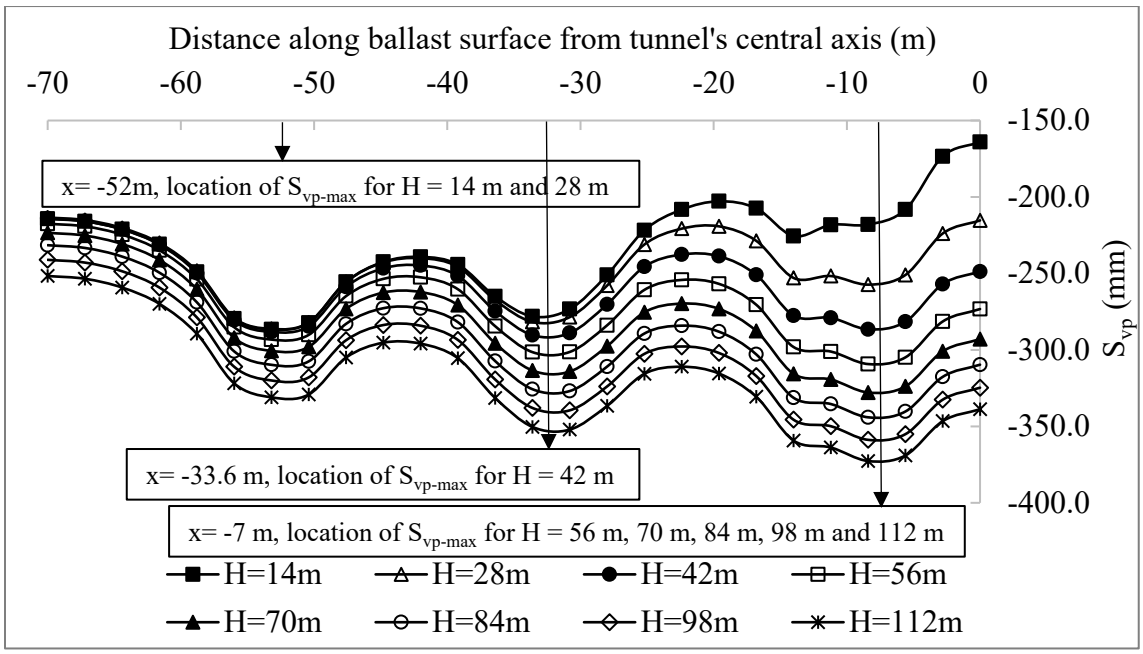


Figure 4.8. (d) Symmetrical displacement distribution for model D = 14 m excavation with operating train ($V_4$ = 120 km/h).

Figure 4.8 (a) to 4.8 (d) reveals that the displacement magnitudes at every depth for model D = 14 m have more distinguishable difference than those for model D = 3 m. That is because the increase of tunnel diameter from 3 m to 14 m leads to deeper tunnel overburden depth when the H/D ratio is the same. Moreover, the growing tunnel diameter results in a more significant deformation. For each train speed condition, the average and maximum difference (%) between $S_{vv}$ and $S_{vp}$ for D =14 m are illustrated in Table 4.2. The location of the maximum difference varies with different tunnel depths and train speeds. For model H = 14 m, 28 m, 42 m and 56 m, this location is at the tunnel's central axis under all four train speeds; for model H = 70 m, the central axis is the location of maximum difference only when train speed is 40 and 80 km/h. This location horizontally shifts to be 19.6 m from the tunnel's central axis for model H = 84 m under all four train speeds, and model H = 70 m at 0 and 120 km/h. For model H = 98 m and 112 m under all four train speeds, this location is 70 m away from the tunnel's central axis, which is at the top boundary edge. More details about the influence of tunnel depth will be discussed in Section 4.3.

As discussed for the D = 3 m cases, the trainload induced maximum displacement occurs at the position under the middle wheel of a locomotive bogie. For the excavation of tunnel D = 14 m under different train operation speeds, the locations of maximum displacement vary with different tunnel depths, as illustrated in Figure 4.1 and Figure 4.8 (a) to (d). When train speed is 0, 40, 80 km/h, the $S_{vp-max}$ for H = 14 m, 28 m and 42 m, is located at x = -52 m, where it is directly under the second freight car's second outer wheel. The location of the $S_{vp-max}$ is under the middle wheel of a bogie for a locomotive when the tunnel is excavated at depth 56 m, 70 m, 84 m, 98 m and 112 m. However, when the train speed is 120 km/h, the location of $S_{vp-max}$ for tunnel depth 42 m is under the second freight car's first outer wheel; the location of $S_{vp-max}$ remains the same as the other train speed operation conditions for other tunnel depths.

Table 4.2 Average and maximum difference (%) between $S_{vv}$ and $S_{vp}$ when D = 14 m under four train speed conditions

| / | Average difference (%) | | | | Maximum difference (%) | | | |
|---|---|---|---|---|---|---|---|---|
| H (m) | $V_1$=0 km/h | $V_2$=40 km/h | $V_3$=80 km/h | $V_4$=120 km/h | $V_1$=0 km/h | $V_2$=40 km/h | $V_3$=80 km/h | $V_4$=120 km/h |
| 14 | 50.3 | 41.1 | 34.8 | 30.1 | 92.1 | 75.1 | 63.3 | 54.3 |
| 28 | 44.8 | 36.6 | 31.0 | 26.7 | 67.8 | 55.2 | 46.6 | 40.1 |
| 42 | 39.2 | 31.9 | 27.0 | 23.3 | 51.8 | 42.3 | 35.7 | 30.7 |
| 56 | 33.3 | 27.2 | 23.0 | 19.9 | 40.1 | 32.8 | 27.8 | 23.9 |
| 70 | 27.5 | 22.3 | 19.0 | 16.4 | 31.1 | 25.5 | 21.4 | 18.5 |
| 84 | 21.6 | 17.5 | 14.8 | 12.8 | 23.6 | 19.6 | 16.3 | 14.0 |
| 98 | 15.5 | 12.5 | 10.7 | 9.2 | 17.4 | 13.9 | 11.9 | 10.3 |
| 112 | 9.5 | 7.7 | 6.5 | 5.5 | 10.8 | 9.1 | 7.4 | 6.4 |

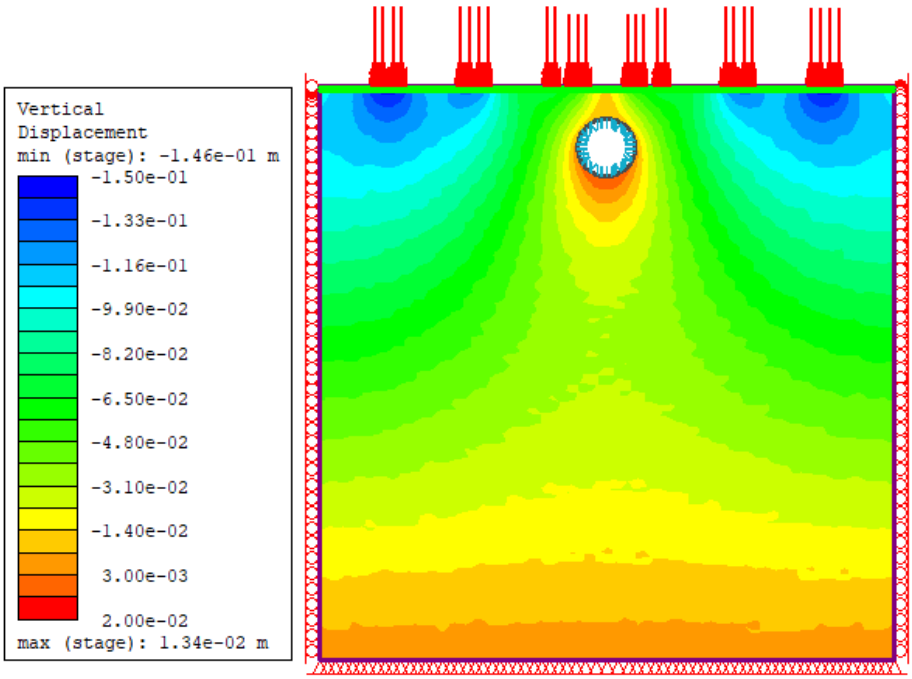


Figure 4.9. (a) Vertical displacement contour for model with D = 14 m, H = 14 m, $V_1$ = 0 km/h.

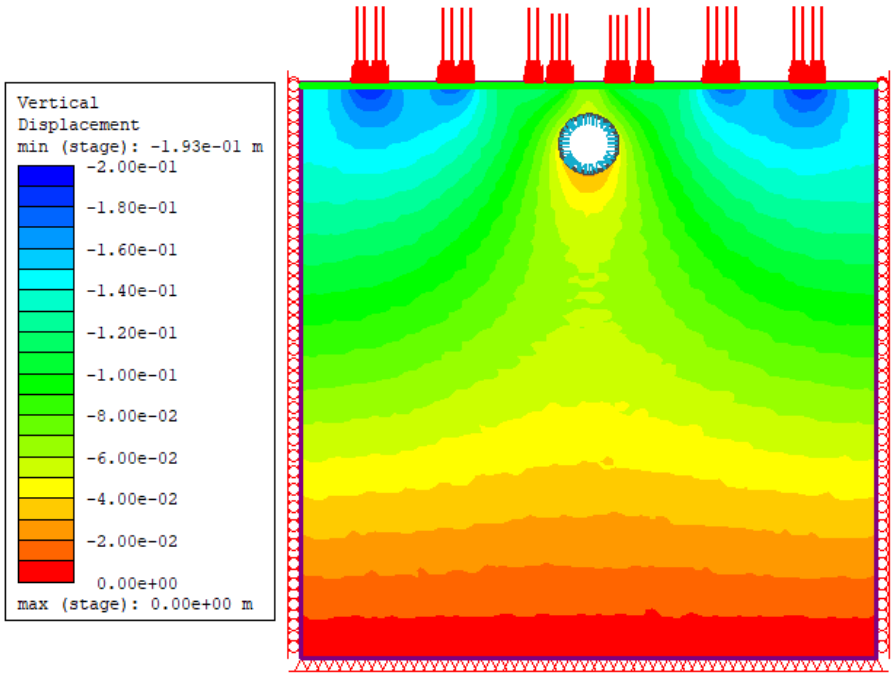


Figure 4.9. (b) Vertical displacement contour for model with D = 14 m, H = 14 m, $V_2$ = 40 km/h.

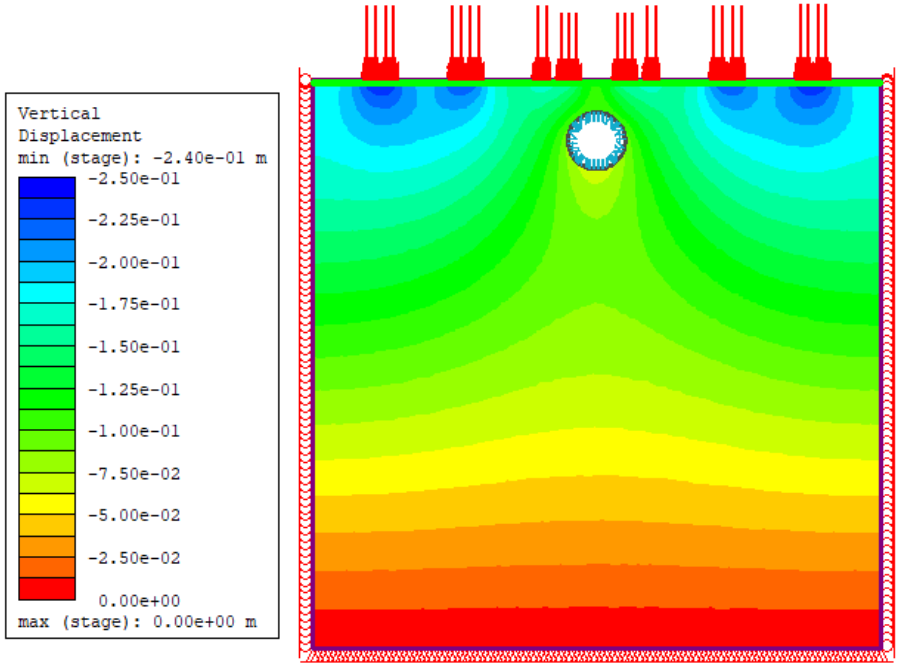


Figure 4.9. (c) Vertical displacement contour for model with D = 14 m, H = 14 m, $V_3$ = 80 km/h.

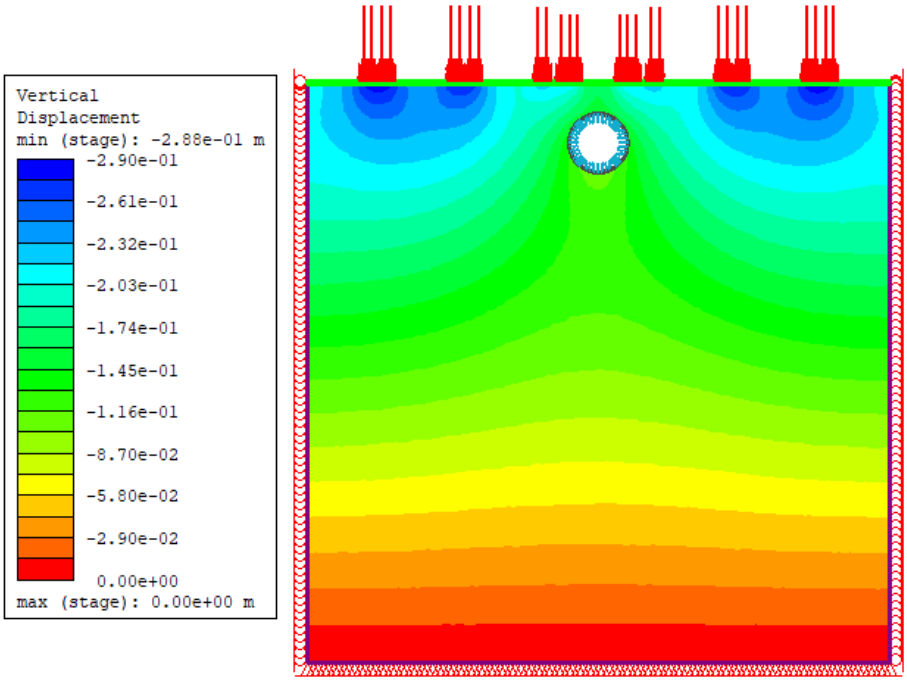


Figure 4.9. (d) Vertical displacement contour for model with D = 14 m, H = 14 m, $V_4$ = 120 km/h.

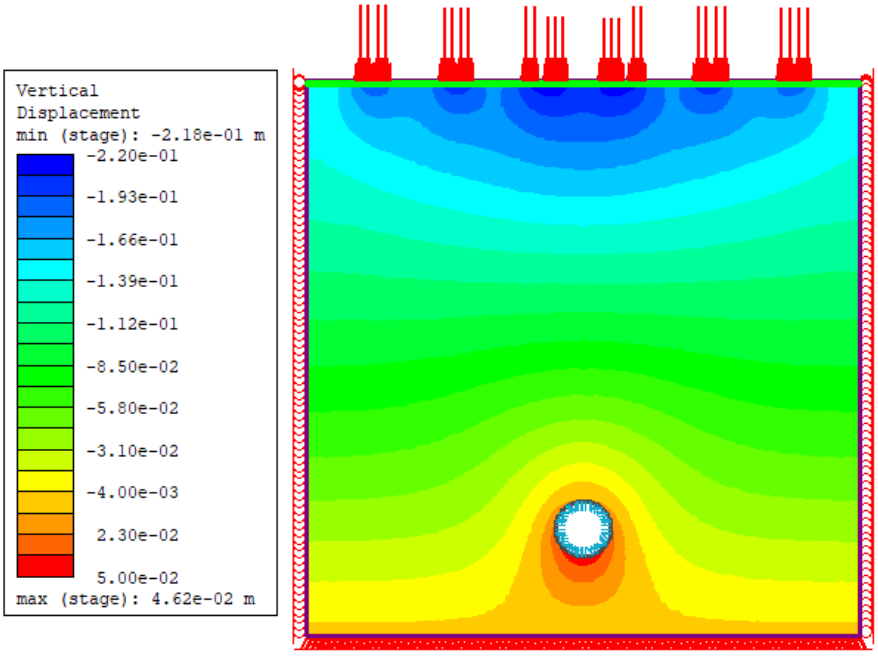


Figure 4.10. (a) Vertical displacement contour for model with D = 14 m, H = 112 m, $V_1$ = 0 km/h.

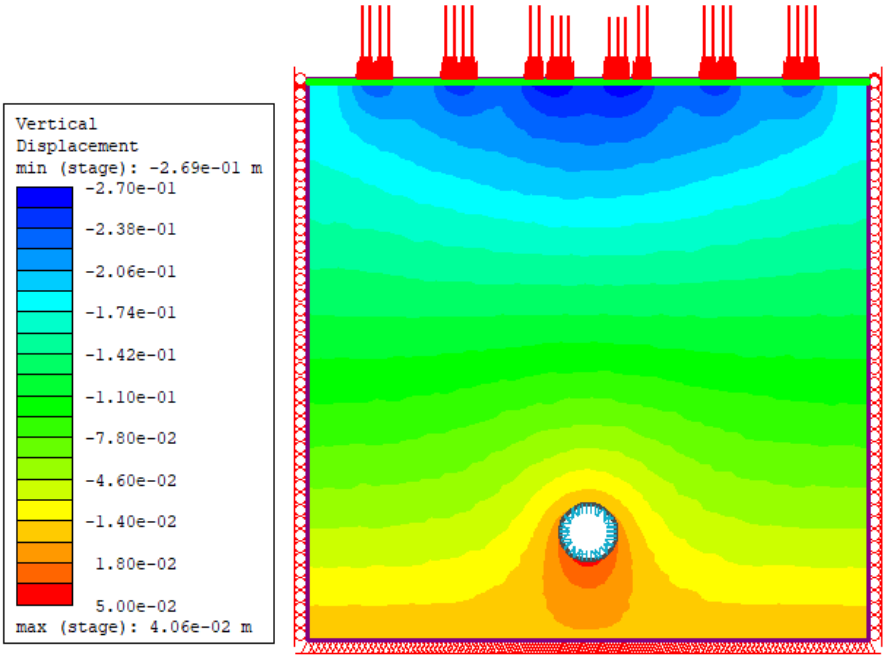


Figure 4.10. (b) Vertical displacement contour for model with D = 14 m, H = 112 m, $V_2$ = 40 km/h.

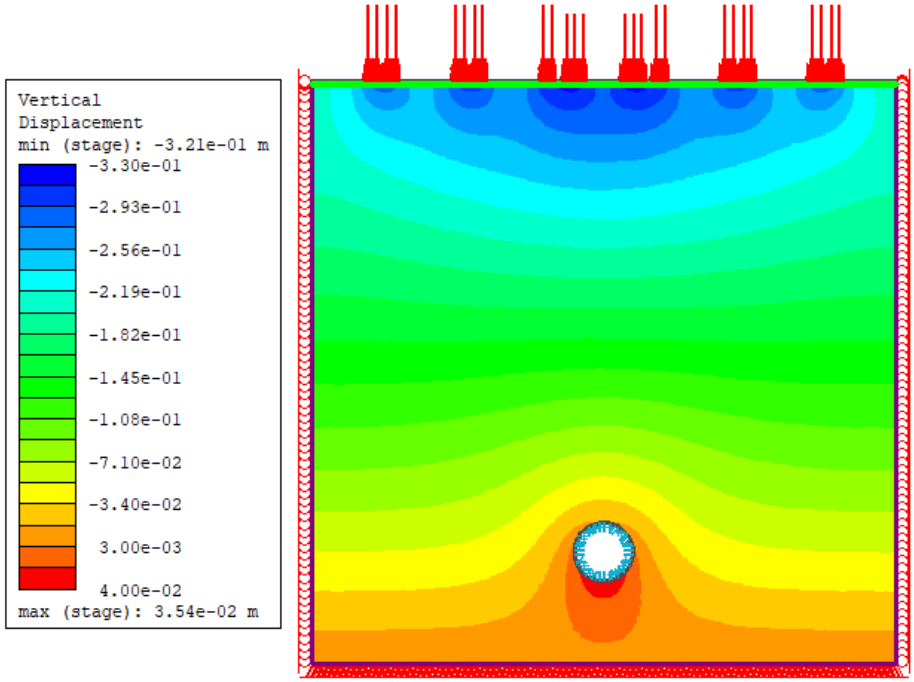


Figure 4.10. (c) Vertical displacement contour for model with D = 14 m, H = 112 m, $V_3$ = 80 km/h.

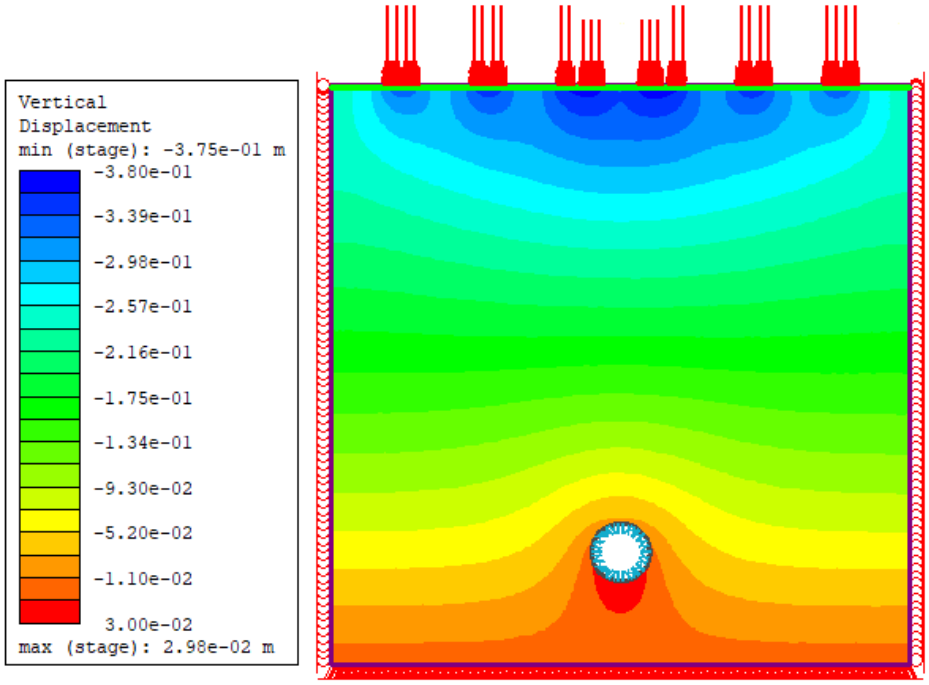


Figure 4.10. (d) Vertical displacement contour for model with D = 14 m, H = 112 m, $V_4$ = 120 km/h.

Figure 4.9 (a) to 4.9 (d) and Figure 4.10 (a) to (d) illustrate the vertical displacement contour for models with D = 14 m under four train speeds conditions at H = 14 m and H = 112 m, respectively. The details of train loadings distributions for the half model on the top boundary of models under various train speed conditions are shown in Appendix C. In Figure 4.9 (a), the contour label shows that positive values of $S_{vp}$ are at the tunnel bottom, which indicates the upward soil movement at the tunnel bottom. But the same tunnel under other train speed conditions does not exhibit the upward movement at the tunnel bottom. In Figure 4.10 (a) to 4.10 (d), the upward soil movement at the tunnel bottom has also appeared. But the upward movement value decreases with the increase in train speed. Larger trainloads result in stronger resistance on upward movement. When a tunnel with D = 14 m is excavated at tunnel depth of 112 m, it is close to the fixed bottom boundary, which does not move in any direction. In addition, the tunnel liner is set to have no solid deformation; the soil is only moving around the tunnel. Thus, the soil at the tunnel bottom will move upward while the train loadings are compressing the ground.

In order to explain the above, in Section 3.1.5, it has been introduced that the initial stress is in equilibrium with the body force. Tunnel excavation removes a certain amount of soil, which leads to a reduction of the body force. Therefore, the tunnel excavation causes an upward expanding behavior (in essence de-stressing) of the ground. In this case, the expanding behavior is with the effect of the proceeding trainload, which means the tunnel excavation induced upward displacement can offset part of the deformation caused by trainloads.

4.2.3 Vertical Displacement of the Ballast Surface at the Tunnel's Central Axis ($S_{vp-c}$)

In Section 4.1, the features of ground displacement distribution and the trend caused by train operation have been discussed. Also, Sections 4.2.1 and 4.2.2 present the results of tunnel excavation under existing railway operation inducing surface displacement for the minimum (D = 3 m) and maximum (D = 14 m) tunnel diameter, respectively. According to the previous observation, tunnel excavation disturbs the ground and causes most of the vertical surface displacement changes in the area above the tunnel. Therefore, in this section, the vertical displacement of the ballast surface at the tunnel's central axis ($S_{vp-c}$) for all the models will be shown, in reference to Figure 3.9. Also, the results from this section will be used in Section 4.3 and 4.4.

In Figure 4.11 (a) to 4.11 (d), the dashed lines represent the value of vertical displacement induced by the different train loadings at the center of the ballast surface ($S_{vv-c}$). Thus, the $S_{vv-c}$ is the reference datum, which helps to determine the influence on ground surface displacement generated by other parameters. The only effect of increasing train speed is to generate a larger displacement. But the difference between $S_{vv-c}$ and $S_{vp-c}$ is in a limited range under various train speed conditions since the tunnel excavation is the only variable. Figure 4.12 illustrates the relative difference of ($S_{vv-c}$ - $S_{vp-c}$) between train speed $V_1$ = 0 km/h and $V_2$ = 40 km/h, at different H and D. Figure 4.13 and Figure 4.14 are analogous to Figure 4.12, except that the comparison is made between $V_1$ = 0 km/h versus $V_3$ = 80 km/h and $V_4$ = 120 km/h, respectively. Such relative difference increases with train speed. Therefore, the maximum relative difference on the difference between $S_{vv-c}$ and $S_{vp-c}$ appears when train speed is $V_4$ = 120 km/h, as 2.6 %. The influence of tunnel depth and diameter will be discussed in Sections 4.3 and 4.4. Figure 4.11 (a) to 4.11 (d) shows that when the tunnel diameter is increased from D = 3 m to D = 14 m, $S_{vp-c}$ decreases at a faster rate as the ratio of H/D increases. The difference in $S_{vp-c}$ decreases among different tunnel diameters.

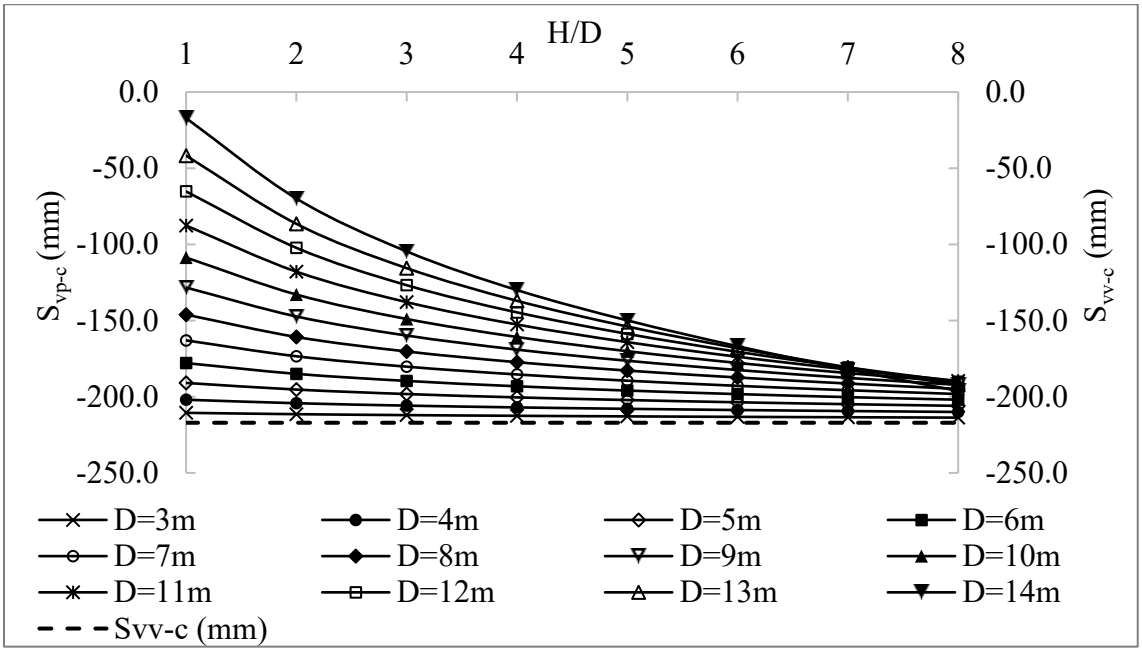


Figure 4.11. (a) Vertical displacement of the ballast surface at tunnel's central axis ($S_{vp-c}$), $V_1$ = 0 km/h.

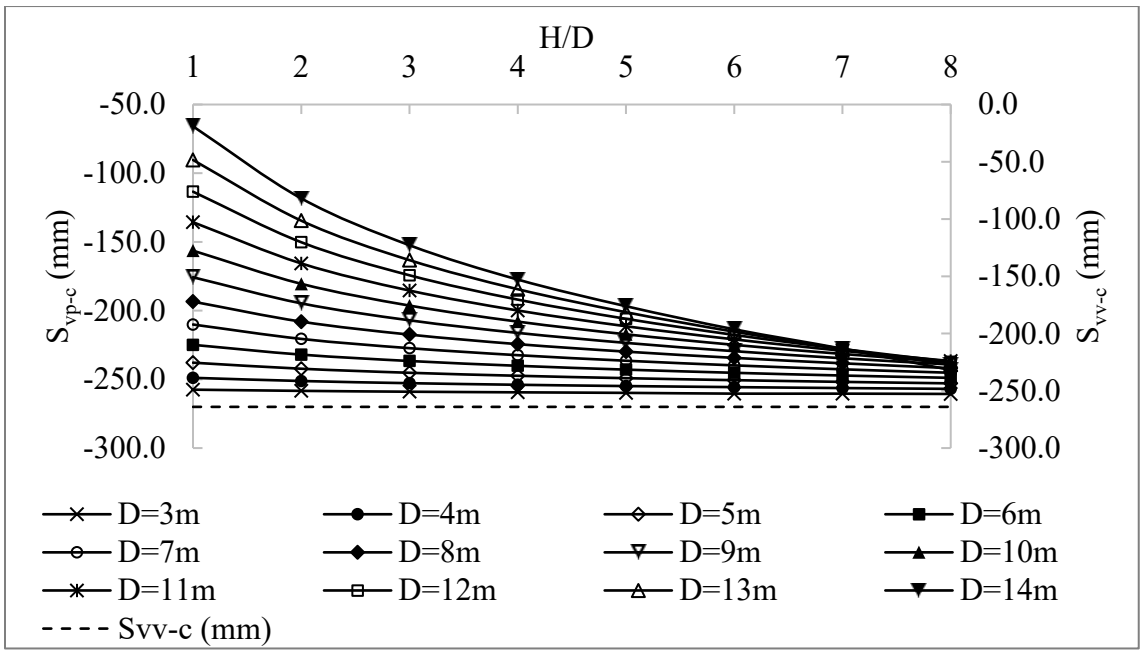


Figure 4.11. (b) Vertical displacement of the ballast surface at tunnel's central axis ($S_{vp-c}$), $V_2$ = 40 km/h.

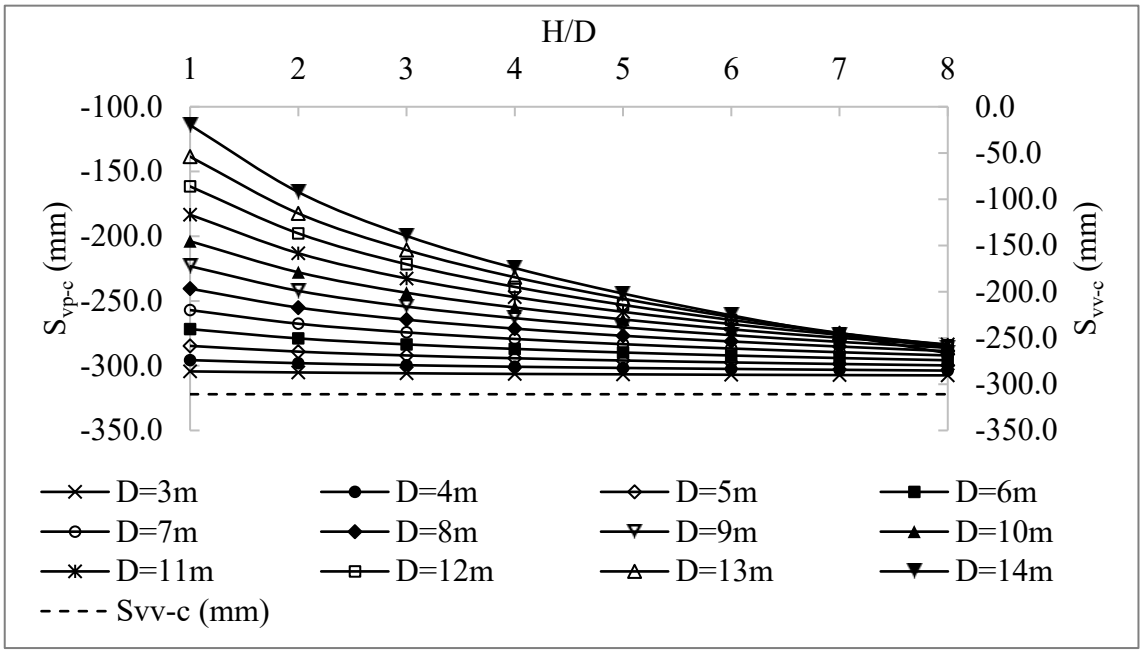


Figure 4.11. (c) Vertical displacement of the ballast surface at tunnel's central axis ($S_{vp-c}$), $V_3$ = 80 km/h.

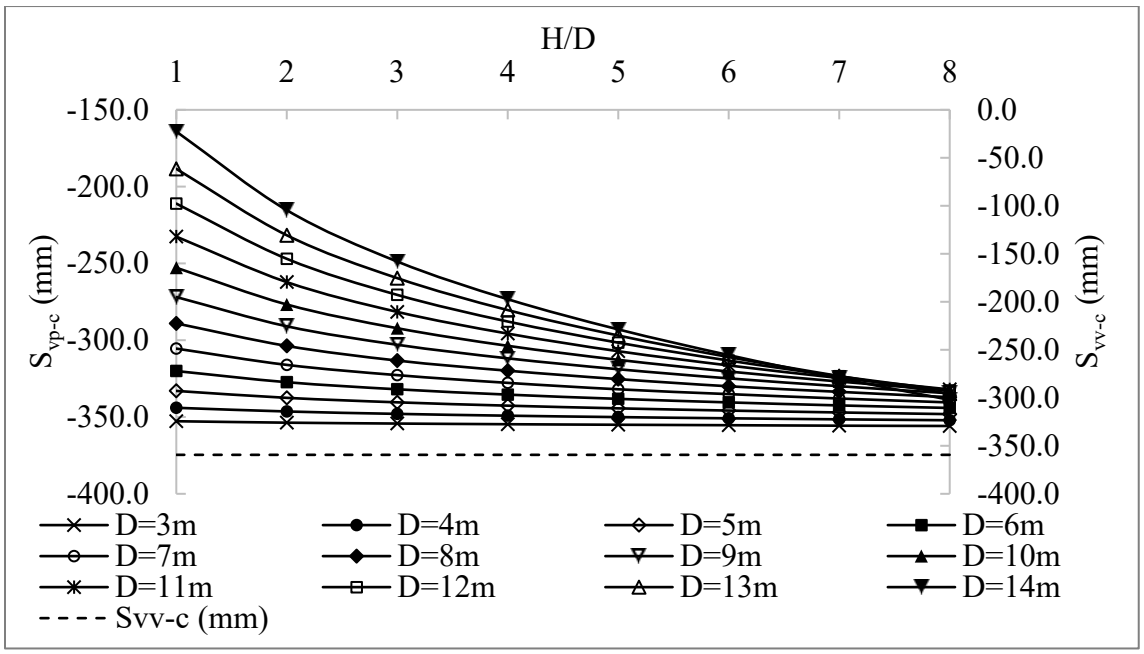


Figure 4.11. (d) Vertical displacement of the ballast surface at tunnel's central axis ($S_{vp\text{-}c}$), $V_4$ = 120 km/h.

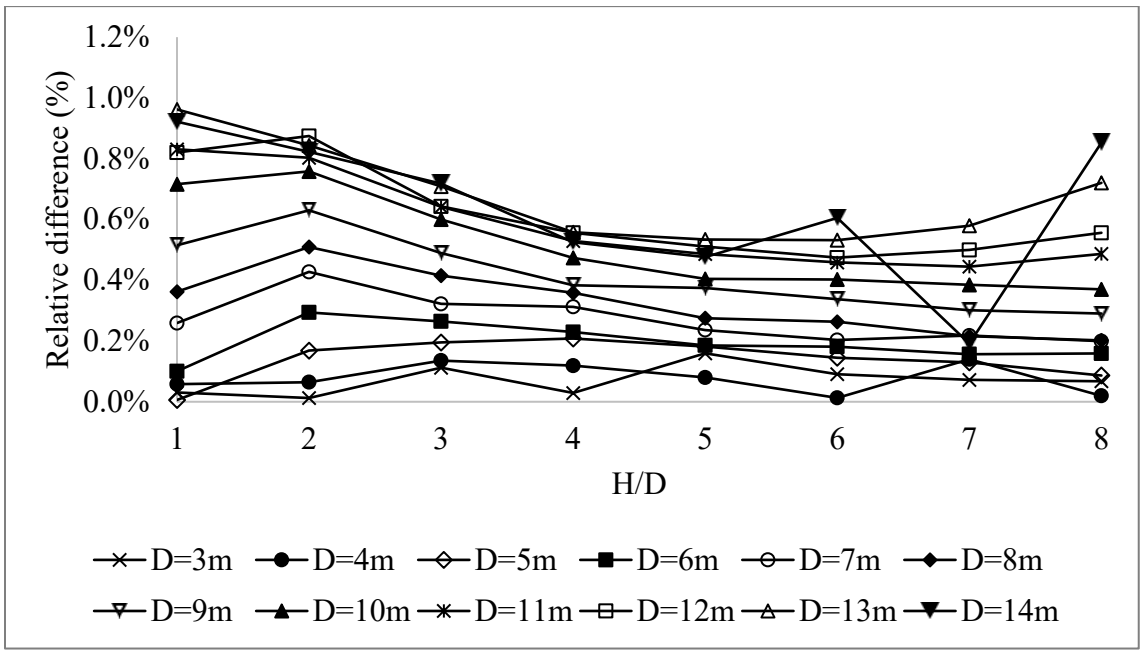


Figure 4.12 The relative difference between $V_1$ = 0 km/h models to $V_2$ = 40 km/h on the difference between $S_{vv\text{-}c}$ and $S_{vp\text{-}c}$.

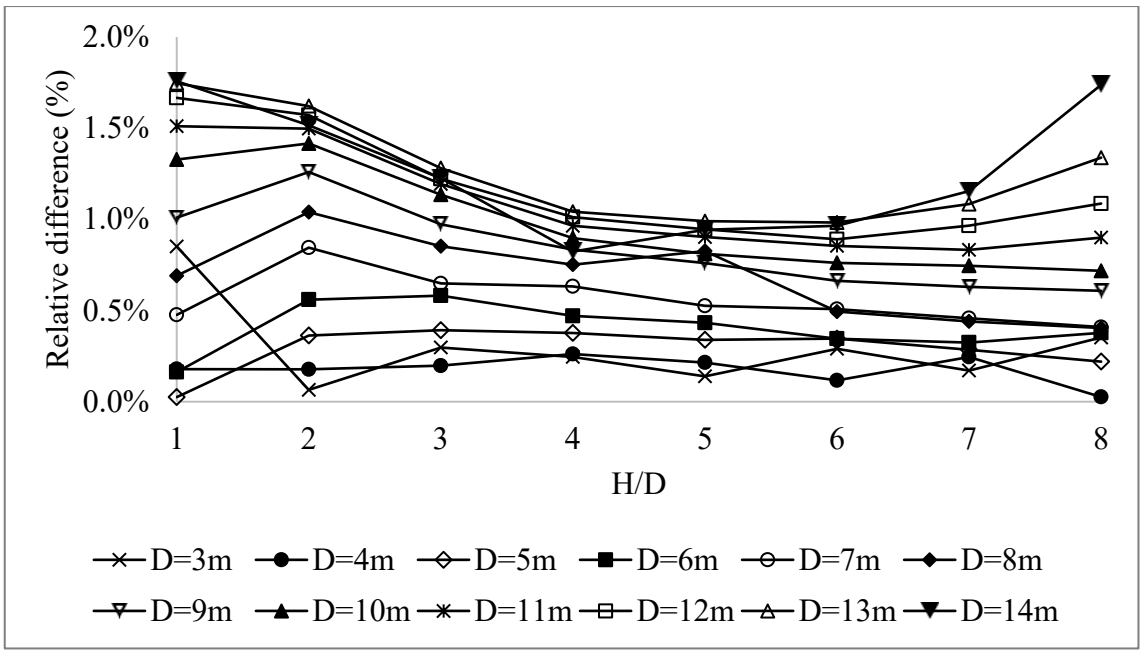


Figure 4.13 The relative difference between $V_1$ = 0 km/h models to $V_3$ = 80 km/h on the difference between $S_{vv\text{-}c}$ and $S_{vp\text{-}c}$.

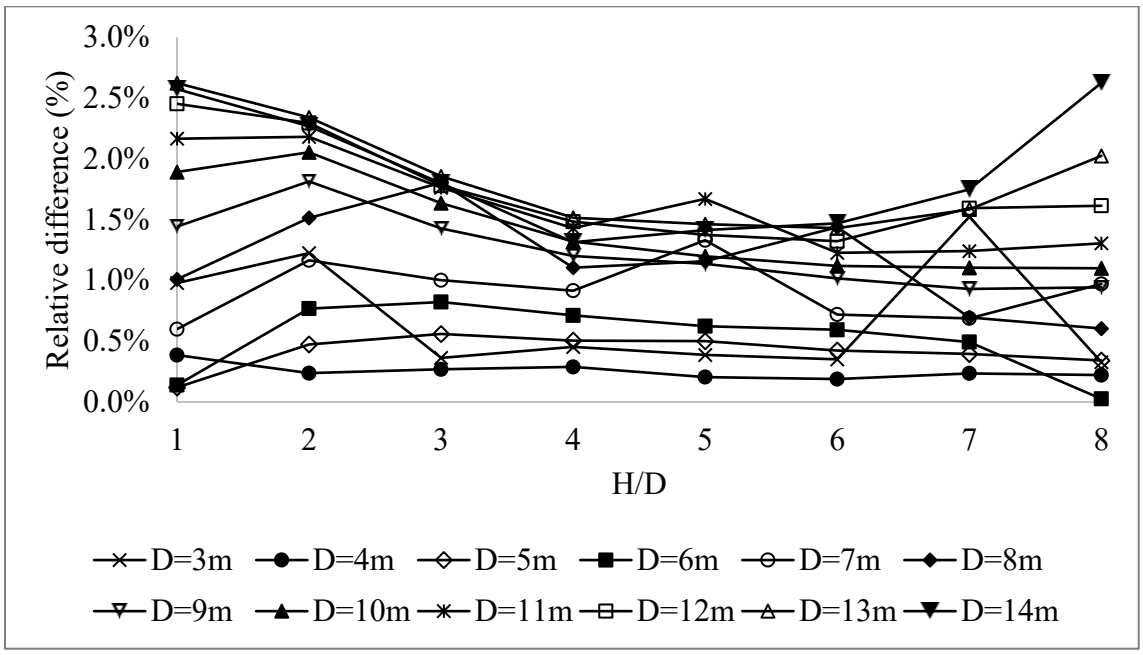


Figure 4.14 The relative difference between $V_1$ = 0 km/h models to $V_4$ = 120 km/h on the difference between $S_{vv\text{-}c}$ and $S_{vp\text{-}c}$.

## 4.3 Scenario 3 - Influence of Tunnel Depth (H) on the Vertical Surface Displacement along the Ground Surface

As discussed in the previous section, the tunnel excavation is the only difference between the train operation scenario and the simultaneous tunnel excavation and train operation. Therefore, the displacement induced by tunnel excavation could be obtained from $S_{vp}$ and $S_{vv}$. The equation is shown as:

$$S_{vt} = S_{vv} - S_{vp} \tag{4.1}$$

where $S_{vt}$ is the vertical displacement along the ballast surface caused by tunneling without the effect of the train loading (mm); $S_{vv}$ is the vertical displacement along the ballast surface induced by train loadings only (mm); and $S_{vp}$ is the vertical displacement along the ballast surface generated by tunnel excavation with train loading in the models (mm).

With the aim of investigating the influence of tunnel excavation depth (H) for different tunnel diameters on the maximum vertical displacement along the ballast surface, for each tunnel diameter (D), the maximum value of $S_{vt}$ under various H will be compared to the $S_{vt\text{-}max}$ at the shallowest H, which results in the largest vertical displacement. Models from D = 3 m and D = 14 m are used as examples in Section 4.3.1 and 4.3.2, respectively. Other diameters' results will be shown in Appendix B.

The relative difference ($S_{vt\text{-}max}$) in $S_{vt\text{-}max}$ under various tunnel depths is defined as:

$$R_{(S_{vt-max})} = \frac{S_{vt-max-a} - S_{vt-max-b}}{S_{vt-max-a}} \tag{4.2}$$

where $R_{(S_{vt-max})}$ is the relative difference in $S_{vt\text{-}max}$; $a$ isthe $S_{vt-max}$ at shallowest depth; $b$ is the $S_{vt-max}$ for other depths.

### 4.3.1 Model with D = 3 m - Relating Tunnel Depth's Influence on $S_v$

The vertical displacement along the ballast surface induced by tunneling only ($S_{vt}$) corresponding to various tunnel depth for tunnel D = 3 m will be investigated. In Figure 4.15, the vertical displacement distribution along the ballast surface produced by tunneling $S_{vt}$ (mm) at different tunnel depths (H) for D = 3 m is shown. The x-axis represents the distance along the ballast surface. The $S_{vt}$ value is represented by the y-axis, which also represents the tunnel's central axis. The location of the tunnel's central axis is displayed in Figure 3.9. Therefore, the curves are symmetric with respect to the y-axis.

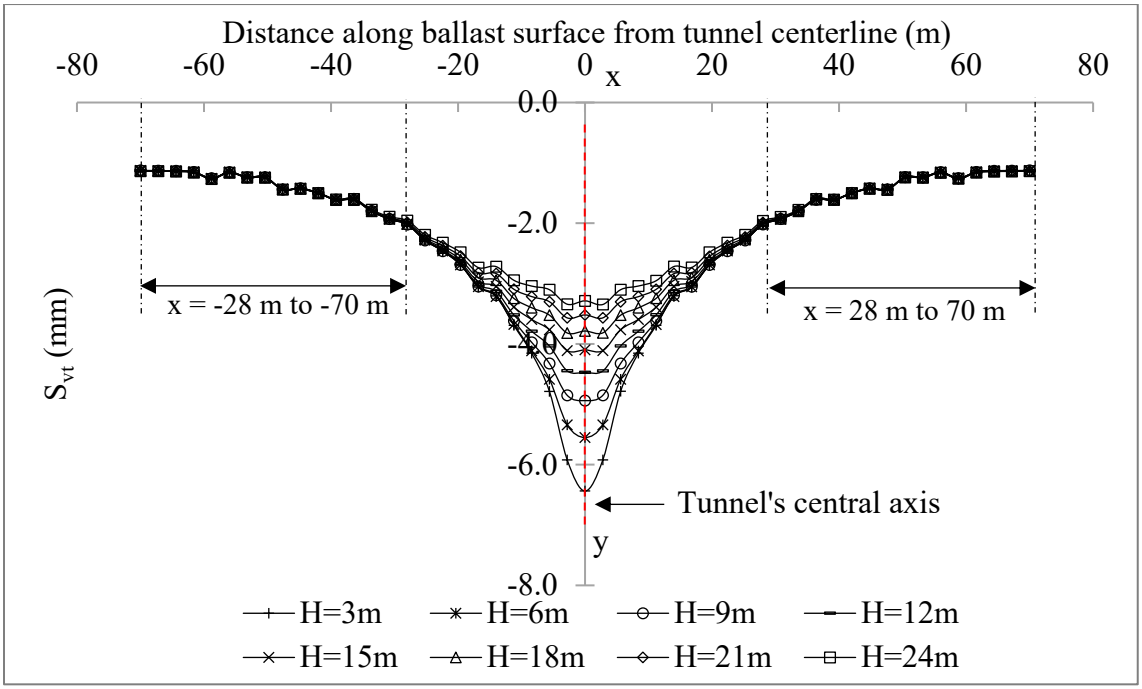


Figure 4.15. Displacement distribution along ballast surface for model D = 3 m, $V_1$ = 0 km/h.

Corresponding to the results in Figure 4.15, the displacement distribution follows the similar shape of a Gaussian curve. In the intervals from 28 m to 70 m or from -28 m to -70 m, $S_{vt}$ for different tunnel depths overlap each other for D = 3 m, which is not the case for the larger D, as shown in Figure 4.15. The distance from x = 28 m to the tunnel's central axis is equal to 9 times of tunnel diameter. Between x = -28 m to x = 28 m, the $S_{vt}$ curves for various tunnel depths no longer overlap. The maximum vertical displacement along the ballast surface caused by tunneling ($S_{vt\text{-}max}$) is located at the tunnel's central axis. In Figure 4.16, the $S_{vt\text{-}max}$ for each tunnel depth is shown. Figure 4.17 displays the relative difference in $S_{vt\text{-}max}$ from H = 3 m to other tunnel depths.

Figure 4.16 and Figure 4.17 express that the shallowest tunnel depth (H/D = 1) excavation disturbs the railway embankment the most since the $S_{vt\text{-}max}$ is the maximum among all tunnel depths for the model with D = 3 m. The maximum displacement of the ballast surface induced by tunneling under trainload ($V_1$ = 0 km/h) is reduced by the increasing of tunnel depth. The maximum value difference between the shallowest tunnel (H = 3 m) and the deepest tunnel (H = 24 m) is 3.1 mm, which corresponds to a -49.0 % relative difference in $S_{vt\text{-}max}$. This means that a displacement reduction rate is 49.0 % as the tunnel depth increases from 3 m to 24 m.

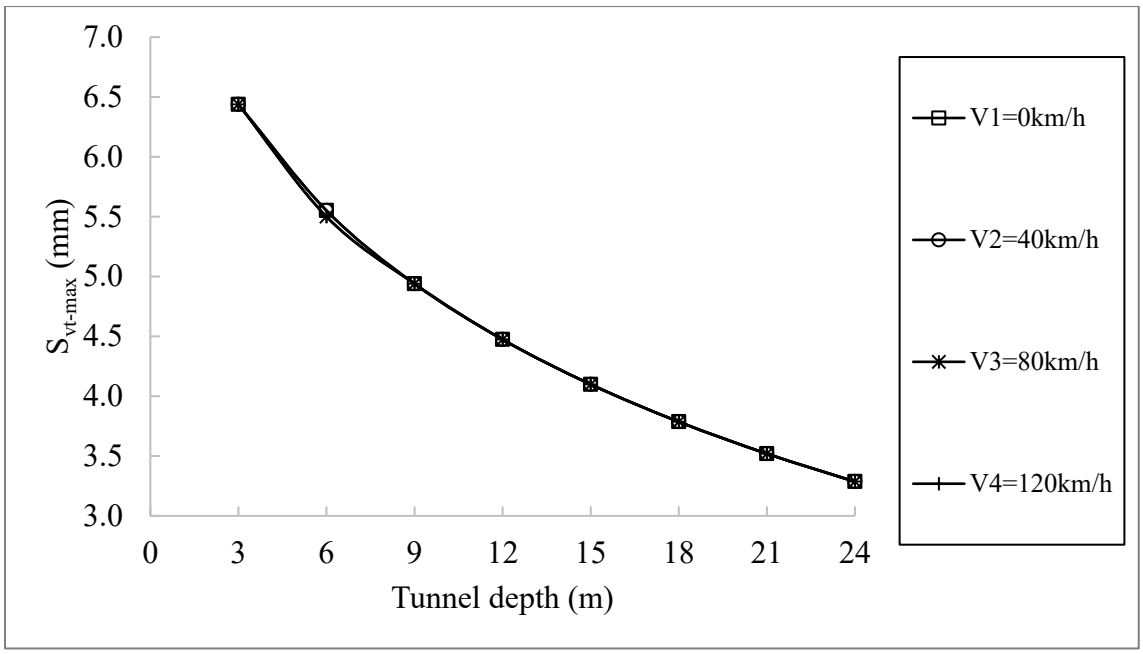


Figure 4.16. Tunnel depth (H) influence on $S_{vt\text{-}max}$, for four train speed conditions, D = 3 m.

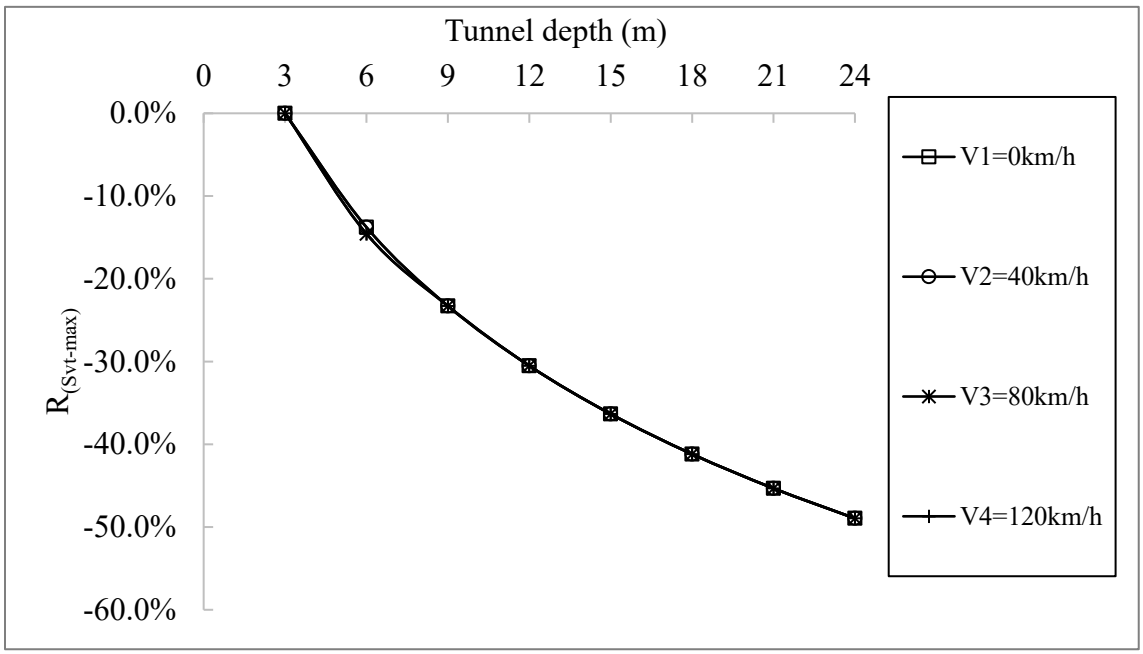


Figure 4.17. Tunnel depth (H) influence on $S_{vt\text{-}max}$ relative difference, for four train speed conditions, D = 3 m.

4.3.2 Model with D = 14 m - Relating Tunnel Depth's Influence on $S_v$

For large tunnel diameters like D = 14 m, the maximum vertical displacement induced by tunneling only ($S_{vt\text{-}max}$) under train loading ($V_1$ = 0 km/h) along the ballast surface occurs at the tunnel's central axis, as shown in Figure 4.18. The same phenomenon is observed in the models D = 3 m, the displacement magnitude is increasing when the tunnel excavation is near the ground surface. The shallowest tunnel excavation can generate the maximum displacement (-200.2 mm) at 14 m depth. But for the deepest tunnel, the maximum value is -20.8 mm. The ratio is up to 10. For tunnel depth H = 14 m, 28 m, and 42 m, the curves are overlapping on both the left and right areas. Therefore, the influence area by tunnel excavation is in a valid range from -4.3D (D is the tunnel diameter.) to 4.3D, which is from -60 m to 60 m. As the tunnel overburden depth increases, the curves of $S_{vt}$ along the ballast surface become flat.

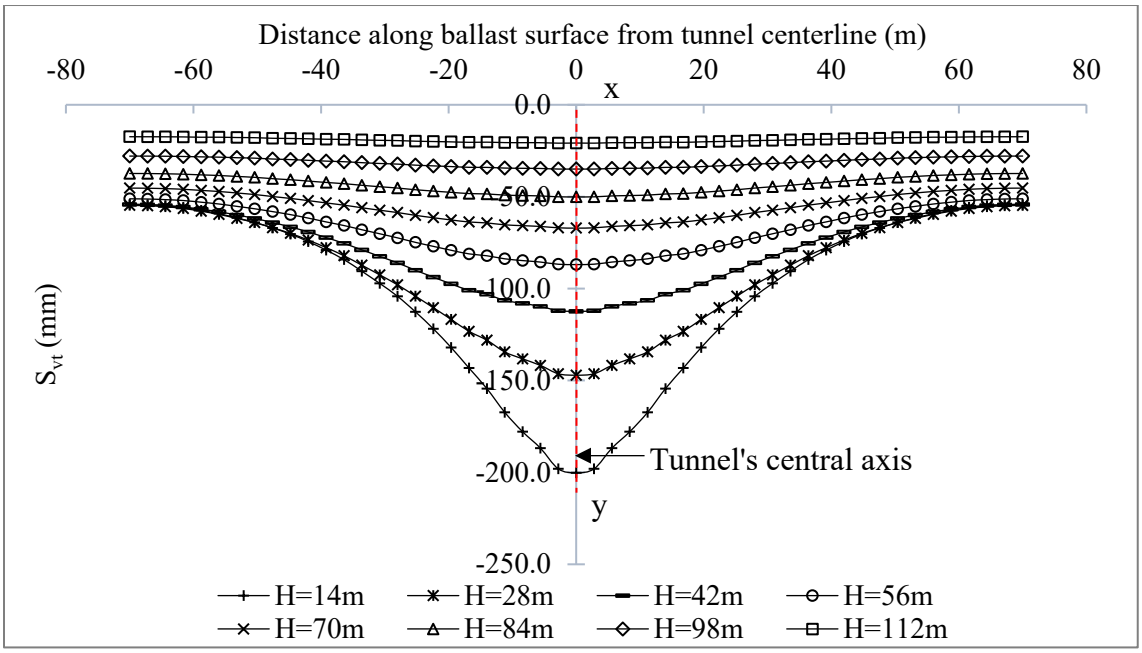


Figure 4.18. Displacement distribution along ballast surface, D = 14 m, $V_1$ = 0 km/h.

In Figure 4.19, the $S_{vt\text{-}max}$ difference between the curves decreases with increasing tunnel depth. The curves in Figure 4.20 are overlapped with each other. Furthermore, the magnitude of $S_{vt\text{-}max}$ for the same tunnel in different train loading models is varied. For example, the $S_{vt\text{-}max}$ for model (D = 14 m, H = 14 m, $V_1$ = 0 km/h) is 200.2 mm; it is 195.1 mm for model (D = 14 m, H = 14 m, $V_4$ = 120 km/h). There is a 2.6 % reduction in $S_{vt\text{-}max}$ between the two train loadings. It may prove that the magnitude of $S_{vt\text{-}max}$ for the same tunnel has a minor reduction, with the increasing train loading. It also means larger train loading can resist the upward movement induced by tunneling, but there is a maximum 2.6 % difference between $V_1$ = 0 km/h and $V_4$ = 120 km/h train loading on $S_{vt\text{-}max}$ for the same tunnel. In order to investigate the influence of train speeds on $S_{vt}$, the $S_{vt}$ along the ground surface from x = -70 m to x = 70 m for models of different diameter at different depths under train speed $V_1$ = 0 km/h are chosen as a reference data to compare with the models under other train speed conditions. The results are displayed in Table 4.3.

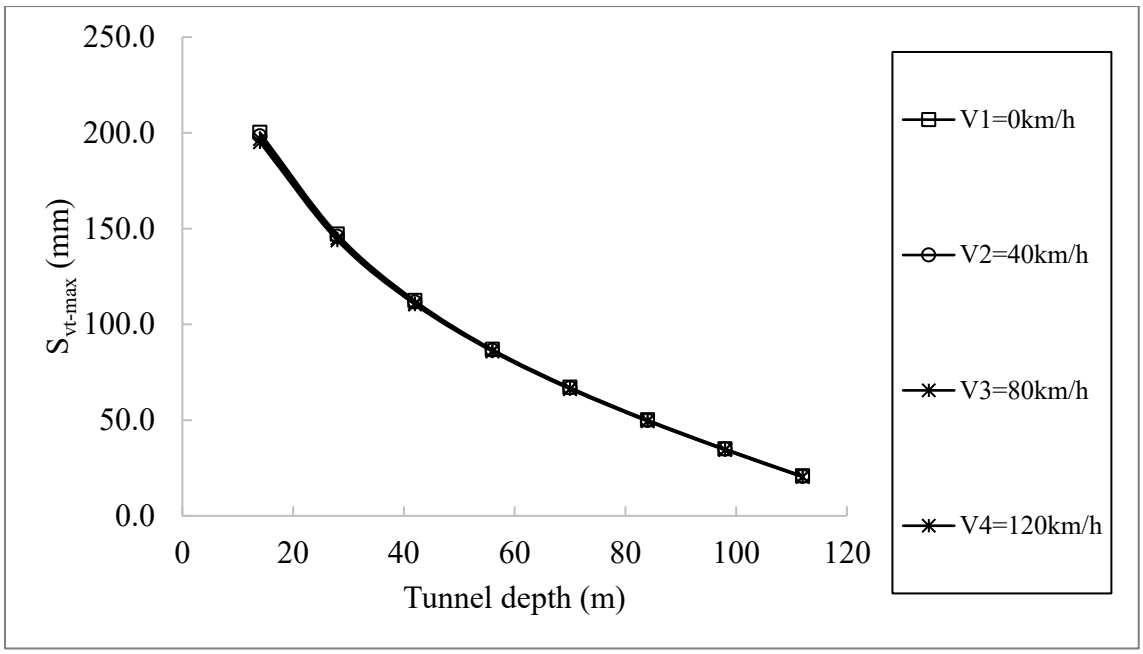


Figure 4.19. Tunnel depth (H) influence on $S_{vt\text{-}max}$, for four train speed conditions, D = 14 m.

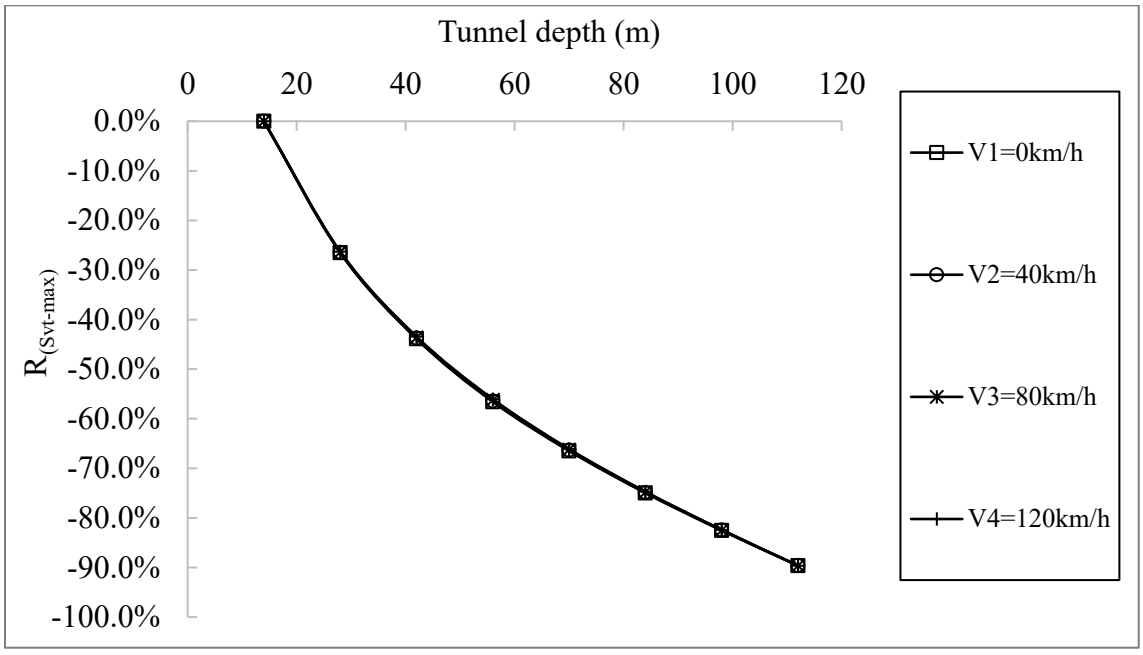


Figure 4.20. Tunnel depth (H) influence on $S_{vt\text{-}max}$ relative difference for four train speeds, D = 14 m.

Table 4.3 displays the average and maximum relative displacement difference of $S_{vt}$ between $V_1$ = 0 km/h and other train speed conditions along the ground surface. Corresponding to Table 4.3, both average and maximum relative difference increase gradually with the augment of train speed, except models H = 3 m under train speed $V_3$ = 80 km/h, and H = 3m, H = 6 m, H = 21 m, H = 24 m under train speed $V_4$ = 120 km/h of D = 3 m. These five models express a rapid growth of the maximum relative difference. In addition, Table 4.3 illustrates that the vertical displacement at train speed $V_2$ = 40 km/h have a range of average difference from 0.1 % to 0.8 % comparing with models at $V_1$ = 0 km/h; the maximum difference is from 0.3 % to 2.7 %. Similarly, models at train speed $V_3$ = 80 km/h have a range of average difference with $V_1$ = 0 km/h from 0.2 % to 3 %, and the maximum difference is from 0.6 % to 11.9 %; for models at train speed $V_4$ = 120 km/h, a range of average difference with $V_1$ = 0 km/h is from 0.4 % to 4.9 %, and the maximum difference is from 1.0 % to 14.6 %.

Table 4.3 Average and maximum relative difference of $S_{vt}$ along the ground surface (%)

| / | | Average relative difference (%) | | | | Maximum relative difference (%) | | | |
|---|---|---|---|---|---|---|---|---|---|
| | | V (km/h) | | | | | | | |
| D (m) | H/D | 0 | 40 | 80 | 120 | 0 | 40 | 80 | 120 |
| 3 | 1 | 0 | 0.4 | 3.0 | 4.7 | 0 | 1.7 | 11.9 | 14.6 |
| | 2 | 0 | 0.8 | 1.2 | 4.9 | 0 | 2.7 | 4.3 | 14.6 |
| | 3 | 0 | 0.7 | 1.3 | 2.5 | 0 | 1.9 | 4.6 | 8.1 |
| | 4 | 0 | 0.7 | 1.1 | 2.0 | 0 | 2.3 | 3.9 | 6.6 |
| | 5 | 0 | 0.5 | 1.3 | 2.1 | 0 | 1.6 | 4.5 | 6.5 |
| | 6 | 0 | 0.4 | 1.1 | 2.0 | 0 | 1.2 | 2.8 | 5.7 |
| | 7 | 0 | 0.5 | 1.1 | 4.9 | 0 | 1.6 | 3.4 | 13.4 |
| | 8 | 0 | 0.4 | 0.9 | 2.1 | 0 | 1.2 | 2.6 | 7.0 |
| 4 | 1 | 0 | 0.4 | 0.7 | 1.5 | 0 | 1.4 | 2.6 | 5.1 |
| | 2 | 0 | 0.3 | 0.7 | 1.4 | 0 | 1.3 | 3.0 | 5.3 |
| | 3 | 0 | 0.3 | 0.7 | 1.4 | 0 | 1.1 | 2.5 | 4.8 |
| | 4 | 0 | 0.3 | 0.7 | 1.4 | 0 | 1.1 | 1.9 | 4.8 |
| | 5 | 0 | 0.4 | 0.7 | 1.4 | 0 | 1.3 | 2.7 | 4.8 |
| | 6 | 0 | 0.3 | 0.7 | 1.4 | 0 | 1.0 | 2.1 | 4.5 |
| | 7 | 0 | 0.4 | 0.8 | 1.5 | 0 | 1.4 | 2.6 | 4.8 |
| | 8 | 0 | 0.4 | 0.7 | 1.2 | 0 | 1.1 | 2.1 | 4.7 |
| 5 | 1 | 0 | 0.2 | 0.4 | 0.8 | 0 | 0.8 | 1.3 | 2.5 |
| | 2 | 0 | 0.2 | 0.4 | 0.8 | 0 | 0.7 | 1.5 | 2.7 |
| | 3 | 0 | 0.2 | 0.4 | 0.8 | 0 | 0.6 | 1.3 | 2.4 |
| | 4 | 0 | 0.2 | 0.4 | 0.8 | 0 | 0.6 | 1.4 | 2.6 |
| | 5 | 0 | 0.2 | 0.4 | 0.8 | 0 | 0.7 | 1.3 | 2.5 |
| | 6 | 0 | 0.2 | 0.4 | 0.8 | 0 | 0.7 | 1.5 | 2.8 |
| | 7 | 0 | 0.2 | 0.4 | 0.8 | 0 | 0.7 | 1.3 | 2.7 |
| | 8 | 0 | 0.2 | 0.4 | 0.9 | 0 | 0.8 | 1.5 | 2.9 |
| 6 | 1 | 0 | 0.1 | 0.3 | 0.5 | 0 | 0.5 | 1.0 | 1.8 |
| | 2 | 0 | 0.2 | 0.4 | 0.6 | 0 | 0.5 | 1.0 | 1.6 |

Table 4.3 Average and maximum relative difference of $S_{vt}$ along the ground surface (%) – Continued

| / | | Average relative difference (%) | | | | Maximum relative difference (%) | | | |
|---|---|---|---|---|---|---|---|---|---|
| | | V (km/h) | | | | | | | |
| D (m) | H/D | 0 | 40 | 80 | 120 | 0 | 40 | 80 | 120 |
| | 3 | 0 | 0.2 | 0.3 | 0.6 | 0 | 0.5 | 1.0 | 1.9 |
| | 4 | 0 | 0.2 | 0.4 | 0.6 | 0 | 0.5 | 1.1 | 1.6 |
| | 5 | 0 | 0.1 | 0.3 | 0.6 | 0 | 0.4 | 0.9 | 1.8 |
| | 6 | 0 | 0.2 | 0.3 | 0.6 | 0 | 0.4 | 0.7 | 1.4 |
| | 7 | 0 | 0.2 | 0.3 | 0.6 | 0 | 0.4 | 0.7 | 1.4 |
| | 8 | 0 | 0.2 | 0.4 | 0.6 | 0 | 0.4 | 1.1 | 2.1 |
| 7 | 1 | 0 | 0.1 | 0.2 | 0.4 | 0 | 0.3 | 0.6 | 1.0 |
| | 2 | 0 | 0.2 | 0.3 | 0.5 | 0 | 0.4 | 0.8 | 1.3 |
| | 3 | 0 | 0.2 | 0.3 | 0.5 | 0 | 0.4 | 0.8 | 1.2 |
| | 4 | 0 | 0.2 | 0.3 | 0.6 | 0 | 0.4 | 0.7 | 1.5 |
| | 5 | 0 | 0.2 | 0.3 | 0.8 | 0 | 0.5 | 0.9 | 1.5 |
| | 6 | 0 | 0.2 | 0.3 | 0.5 | 0 | 0.4 | 0.7 | 1.3 |
| | 7 | 0 | 0.1 | 0.3 | 0.6 | 0 | 0.3 | 0.9 | 1.4 |
| | 8 | 0 | 0.2 | 0.3 | 0.7 | 0 | 0.3 | 0.7 | 1.3 |
| 8 | 1 | 0 | 0.1 | 0.3 | 0.4 | 0 | 0.4 | 0.8 | 1.3 |
| | 2 | 0 | 0.2 | 0.4 | 0.6 | 0 | 0.5 | 1.0 | 1.6 |
| | 3 | 0 | 0.2 | 0.4 | 0.8 | 0 | 0.5 | 0.9 | 1.8 |
| | 4 | 0 | 0.2 | 0.3 | 0.5 | 0 | 0.4 | 0.8 | 1.2 |
| | 5 | 0 | 0.2 | 0.4 | 0.6 | 0 | 0.4 | 0.8 | 1.3 |
| | 6 | 0 | 0.2 | 0.3 | 0.8 | 0 | 0.3 | 0.7 | 1.4 |
| | 7 | 0 | 0.2 | 0.3 | 0.6 | 0 | 0.4 | 0.8 | 1.3 |
| | 8 | 0 | 0.2 | 0.4 | 0.6 | 0 | 0.4 | 0.8 | 1.6 |
| 9 | 1 | 0 | 0.1 | 0.3 | 0.4 | 0 | 0.5 | 1.0 | 1.6 |
| | 2 | 0 | 0.2 | 0.4 | 0.6 | 0 | 0.6 | 1.3 | 1.8 |
| | 3 | 0 | 0.2 | 0.4 | 0.6 | 0 | 0.5 | 1.1 | 1.6 |
| | 4 | 0 | 0.2 | 0.4 | 0.6 | 0 | 0.4 | 0.9 | 1.4 |
| | 5 | 0 | 0.2 | 0.4 | 0.6 | 0 | 0.4 | 0.8 | 1.3 |
| | 6 | 0 | 0.2 | 0.4 | 0.6 | 0 | 0.4 | 0.7 | 1.2 |
| | 7 | 0 | 0.2 | 0.4 | 0.6 | 0 | 0.4 | 0.7 | 1.2 |
| | 8 | 0 | 0.2 | 0.4 | 0.6 | 0 | 0.4 | 0.8 | 1.3 |
| 10 | 1 | 0 | 0.2 | 0.4 | 0.5 | 0 | 0.7 | 1.4 | 2.0 |
| | 2 | 0 | 0.3 | 0.5 | 0.7 | 0 | 0.8 | 1.4 | 2.1 |
| | 3 | 0 | 0.2 | 0.5 | 0.7 | 0 | 0.6 | 1.2 | 1.8 |
| | 4 | 0 | 0.2 | 0.4 | 0.6 | 0 | 0.5 | 1.0 | 1.5 |
| | 5 | 0 | 0.2 | 0.4 | 0.6 | 0 | 0.5 | 0.9 | 1.4 |
| | 6 | 0 | 0.2 | 0.4 | 0.7 | 0 | 0.4 | 0.8 | 1.3 |
| | 7 | 0 | 0.3 | 0.5 | 0.7 | 0 | 0.5 | 0.8 | 1.3 |
| | 8 | 0 | 0.3 | 0.5 | 0.8 | 0 | 0.5 | 0.9 | 1.5 |

Table 4.3 Average and maximum relative difference of $S_{vt}$ along the ground surface (%) – Continued

| / | | Average relative difference (%) | | | | Maximum relative difference (%) | | | |
|---|---|---|---|---|---|---|---|---|---|
| | | V (km/h) | | | | | | | |
| D (m) | H/D | 0 | 40 | 80 | 120 | 0 | 40 | 80 | 120 |
| 11 | 1 | 0 | 0.2 | 0.4 | 0.6 | 0 | 0.8 | 1.6 | 2.3 |
| | 2 | 0 | 0.3 | 0.5 | 0.8 | 0 | 0.8 | 1.5 | 2.3 |
| | 3 | 0 | 0.3 | 0.5 | 0.8 | 0 | 0.6 | 1.2 | 1.9 |
| | 4 | 0 | 0.3 | 0.5 | 0.7 | 0 | 0.6 | 1.0 | 1.6 |
| | 5 | 0 | 0.3 | 0.5 | 0.8 | 0 | 0.5 | 0.9 | 1.7 |
| | 6 | 0 | 0.3 | 0.5 | 0.7 | 0 | 0.5 | 0.9 | 1.4 |
| | 7 | 0 | 0.3 | 0.6 | 0.9 | 0 | 0.5 | 0.9 | 1.5 |
| | 8 | 0 | 0.4 | 0.7 | 1.0 | 0 | 0.6 | 1.1 | 1.7 |
| 12 | 1 | 0 | 0.2 | 0.5 | 0.7 | 0 | 1.0 | 1.9 | 2.7 |
| | 2 | 0 | 0.3 | 0.6 | 0.9 | 0 | 0.9 | 1.7 | 2.5 |
| | 3 | 0 | 0.3 | 0.5 | 0.8 | 0 | 0.7 | 1.2 | 1.9 |
| | 4 | 0 | 0.3 | 0.5 | 0.7 | 0 | 0.6 | 1.0 | 1.6 |
| | 5 | 0 | 0.3 | 0.5 | 0.7 | 0 | 0.5 | 1.0 | 1.5 |
| | 6 | 0 | 0.3 | 0.6 | 0.8 | 0 | 0.5 | 1.0 | 1.4 |
| | 7 | 0 | 0.4 | 0.7 | 1.0 | 0 | 0.6 | 1.0 | 1.7 |
| | 8 | 0 | 0.5 | 0.9 | 1.3 | 0 | 0.7 | 1.2 | 2.0 |
| 13 | 1 | 0 | 0.3 | 0.5 | 0.8 | 0 | 1.1 | 2.1 | 2.9 |
| | 2 | 0 | 0.3 | 0.7 | 1.0 | 0 | 0.9 | 1.7 | 2.6 |
| | 3 | 0 | 0.3 | 0.6 | 0.8 | 0 | 0.7 | 1.3 | 2.0 |
| | 4 | 0 | 0.3 | 0.5 | 0.8 | 0 | 0.6 | 1.1 | 1.6 |
| | 5 | 0 | 0.3 | 0.6 | 0.8 | 0 | 0.5 | 1.0 | 1.5 |
| | 6 | 0 | 0.4 | 0.7 | 1.0 | 0 | 0.6 | 1.0 | 1.6 |
| | 7 | 0 | 0.4 | 0.8 | 1.2 | 0 | 0.6 | 1.2 | 1.8 |
| | 8 | 0 | 0.6 | 1.2 | 1.7 | 0 | 0.8 | 1.5 | 2.4 |
| 14 | 1 | 0 | 0.3 | 0.6 | 0.9 | 0 | 1.1 | 2.1 | 3.1 |
| | 2 | 0 | 0.4 | 0.7 | 1.0 | 0 | 0.9 | 1.7 | 2.6 |
| | 3 | 0 | 0.3 | 0.6 | 0.9 | 0 | 0.7 | 1.3 | 1.9 |
| | 4 | 0 | 0.2 | 0.5 | 0.7 | 0 | 0.5 | 1.0 | 1.6 |
| | 5 | 0 | 0.3 | 0.6 | 0.8 | 0 | 0.6 | 1.0 | 1.5 |
| | 6 | 0 | 0.4 | 0.7 | 1.0 | 0 | 0.6 | 1.0 | 1.6 |
| | 7 | 0 | 0.5 | 0.9 | 1.4 | 0 | 0.8 | 1.3 | 2.0 |
| | 8 | 0 | 0.8 | 1.6 | 2.4 | 0 | 1.0 | 2.0 | 3.1 |

As discussed in previous sections, the railway is simulated as a track in-use. The tunnel construction is the only variable. Therefore, the deformation of the ballast surface caused by tunnel construction is a crucial part to ensure whether the railway can operate safely.

### 4.3.3 Allowable Maximum Displacement to Ensure Railway Operation Safety

Zhang et al. (2014) provided that the allowable value in addition to railway embankment deformation by tunnel construction should be less than 10 mm. Also, Yang and Zhang (2015) state that the upheaval displacement of the ground surface should be controlled within 10 mm and the overall ground surface settlement should less than 30 mm. Subsequently, 10 mm is chosen as the subsidence control standard in this thesis. Thus, the allowable tunnel excavation induced by the maximum railway embankment displacement in the function of train speed $V_1$ = 0 km/h is displayed in Table 4.4. If the $S_{vt\text{-}max}$ is less than 10 mm, then the tunnel can be constructed while the railway line is in operation. Note that this criterion is only used for the condition, in which there is no existing ground reinforcement before the railway starts to be used; it also has no ground reinforcement before or during tunnel construction other than tunnel liner.

Table 4.4 $S_{vt\text{-}max}$ (mm) for allowable tunnel construction without reinforcement underneath railways, $V_1$ = 0 km/h

| D (m) | H (m) | $S_{vt\text{-}max}$ (mm) |
|---|---|---|
| 3 | 3 | 6.4 |
| | 6 | 5.6 |
| | 9 | 4.9 |
| | 12 | 4.5 |
| | 15 | 4.1 |
| | 18 | 3.8 |
| | 21 | 3.5 |
| | 24 | 3.3 |
| 4 | 16 | 10.0 |
| | 20 | 9.1 |
| | 24 | 8.3 |
| | 28 | 7.6 |
| | 32 | 7.0 |

Corresponding to Table 4.4, only 13 tunnels could be constructed without any ground reinforcement among all 96 tunnel designs considered in this thesis. It means, for most tunnel diameters and tunnel depths, the soft ground must take supports plus tunnel liner to maintain the ground surface stability. For tunnels having diameters less or equal to three meters, the tunnel can be safely constructed in the soft clay with properties set in this thesis. Furthermore, for the tunnels whose diameter is equal to four meters, the tunnel can be excavated when tunnel depth is equal to or greater than 16 m.

### 4.4 Scenario 3 - Influence of Tunnel Diameter (D) to the Vertical Surface Displacement

The tunnel depth-diameter ratio (H/D) decides the tunnel overburden depths for each diameter. Although tunnel depths for different diameters are varied, the H/D can be taken as a criterion to conduct the influence of tunnel diameter on the vertical surface displacement. Figure 4.21 illustrates the $S_{vt\text{-}max}$ from all tunnel diameters corresponding to tunnel depth to diameter ratio (H/D). Moreover, Table 4.5 shows that the relative difference of $S_{vt\text{-}max}$ with different D and H/D.

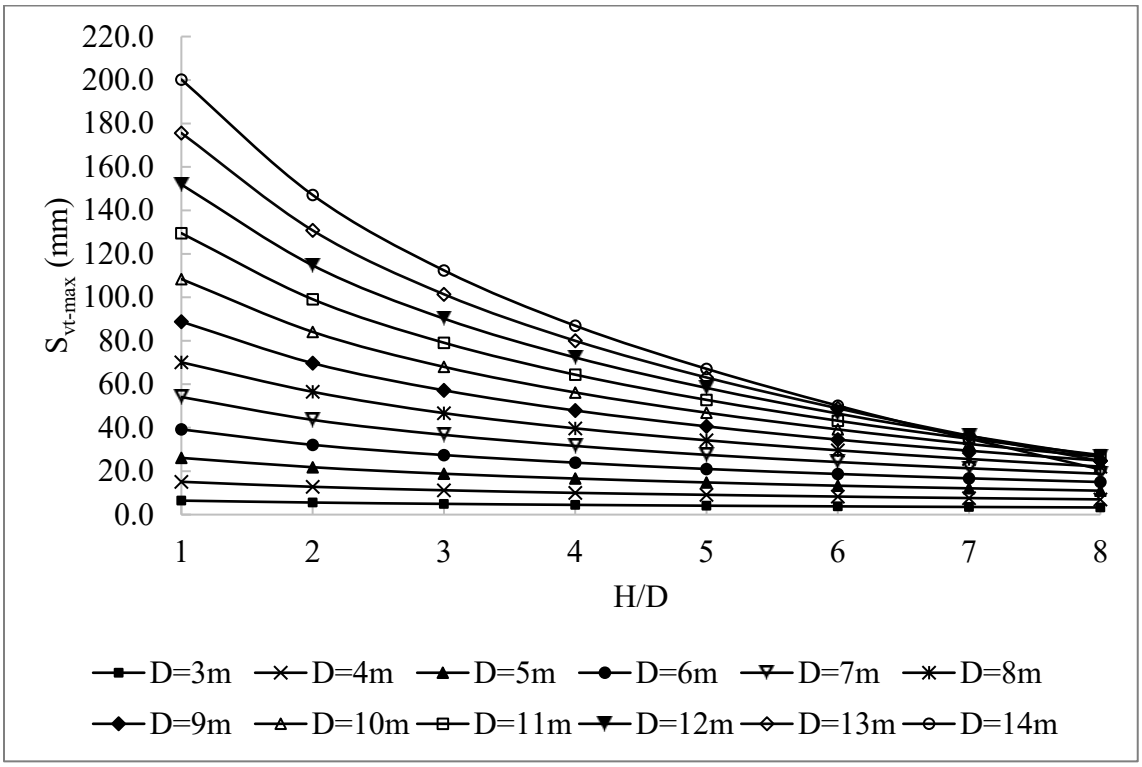


Figure 4.21. Maximum vertical displacement at the ballast surface, D = 3 m to D = 14 m.

With the increasing tunnel depth to diameter ratio, the difference of $S_{vt\text{-}max}$ gradually decreases as tunnel diameter increases. According to the data from Table 4.5, when tunneling diameter changes from 3 m to 4 m, the $S_{vt\text{-}max}$ increases more than 100 % at each H/D ratio. On the other hand, the $S_{vt\text{-}max}$ increments from tunnel D = 13 m to D = 14 m at H/D = 1 is only 0.14. It means that the one-meter increase of tunnel diameter for small and shallow tunnels affects ground surface displacement more than for large and shallow tunnels. To note that there are some negative values in Table 4.5. For instance, the tunnel diameter increasing from 12 m to 13 m at H/D = 8 ratio has an 8 % declination on $S_{vt\text{-}max}$. The reason is that the tunnel D = 13 m at a depth of H/D = 8 is closer to the lower boundary than D = 12 m at a depth of H/D = 8. In the RS2 model, the lower boundary is simulated as the foundation/bedrock rock, which has no movement.

Table 4.5 The relative difference of $S_{vt\text{-}max}$ changes when tunnel diameter is increased in 1m increments

| D change with 1 m increment (m) | | H/D=1 | H/D=2 | H/D=3 | H/D=4 | H/D=5 | H/D=6 | H/D=7 | H/D=8 |
|---|---|---|---|---|---|---|---|---|---|
| 3 | 4 | 135 % | 131 % | 127 % | 124 % | 122 % | 119 % | 116 % | 113 % |
| 4 | 5 | 73 % | 70 % | 68 % | 66 % | 63 % | 60 % | 59 % | 57 % |
| 5 | 6 | 50 % | 47 % | 46 % | 44 % | 42 % | 41 % | 38 % | 36 % |
| 6 | 7 | 38 % | 36 % | 34 % | 32 % | 31 % | 29 % | 28 % | 25 % |
| 7 | 8 | 30 % | 30 % | 27 % | 26 % | 24 % | 22 % | 20 % | 18 % |
| 8 | 9 | 27 % | 23 % | 22 % | 21 % | 19 % | 17 % | 15 % | 12 % |
| 9 | 10 | 22 % | 21 % | 19 % | 17 % | 16 % | 14 % | 11 % | 7 % |
| 10 | 11 | 19 % | 18 % | 16 % | 15 % | 13 % | 10 % | 7 % | 3 % |
| 11 | 12 | 17 % | 16 % | 14 % | 12 % | 10 % | 8 % | 4 % | -2 % |
| 12 | 13 | 16 % | 14 % | 12 % | 11 % | 8 % | 5 % | 0 % | -8 % |
| 13 | 14 | 14 % | 12 % | 11 % | 9 % | 6 % | 3 % | -4 % | -16 % |

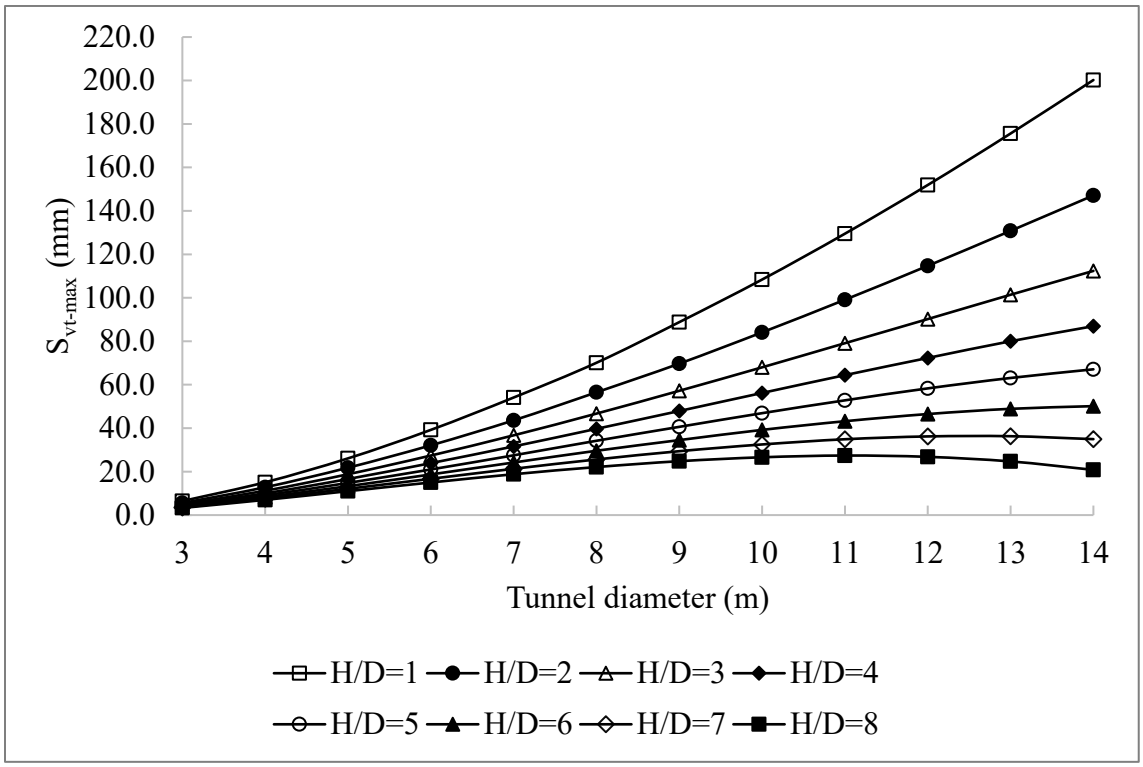


Figure 4.22. H/D ratio related to tunnel diameter influence on $S_{vt\text{-}max}$.

Table 4.6 The relative difference of $S_{vt\text{-}max}$ changes from tunnel D = 3 m to other tunnel diameters

| D (m) | $S_{vt\text{-}max}$ growth factors from D = 3 m to other D tunnel diameters | | | | | | | |
|---|---|---|---|---|---|---|---|---|
| | H/D = 1 | H/D = 2 | H/D = 3 | H/D = 4 | H/D = 5 | H/D = 6 | H/D = 7 | H/D = 8 |
| 3 | 0 | 0 | 0 | 0 | 0 | 0 | 0 | 0 |
| 4 | 1 | 1 | 1 | 1 | 1 | 1 | 1 | 1 |
| 5 | 3 | 3 | 3 | 3 | 3 | 3 | 2 | 2 |
| 6 | 5 | 5 | 5 | 4 | 4 | 4 | 4 | 4 |
| 7 | 7 | 7 | 6 | 6 | 6 | 5 | 5 | 5 |
| 8 | 10 | 9 | 8 | 8 | 7 | 7 | 6 | 6 |
| 9 | 13 | 12 | 11 | 10 | 9 | 8 | 7 | 7 |
| 10 | 16 | 14 | 13 | 12 | 10 | 9 | 8 | 7 |
| 11 | 19 | 17 | 15 | 13 | 12 | 10 | 9 | 7 |
| 12 | 23 | 20 | 17 | 15 | 13 | 11 | 9 | 7 |
| 13 | 26 | 23 | 20 | 17 | 14 | 12 | 9 | 7 |
| 14 | 30 | 26 | 22 | 18 | 15 | 12 | 9 | 5 |

From Figure 4.22 and Table 4.6, it can be observed that a large tunnel diameter generates more ground vertical displacement than a small tunnel. As discussed in Section 4.3.3, tunnels of D = 3 m at all eight depths are allowed to be constructed under the operating railway. The increments of $S_{vt\text{-}max}$ from tunnel D = 3 m to other tunnel diameters in Table 4.6 provides a clear statement of the influence of parameter D. For instance, at tunnel depth of H/D = 1, $S_{vt\text{-}max}$ of D = 14 m tunnel is 30 times larger than the $S_{vt\text{-}max}$ of D = 3 m.

## 4.5 Summary

In this chapter, three scenarios were established to distinguish the three conditions of ground deformation. The first scenario, Section 4.1, discussed the influence of train loadings at different train speeds on the ballast surface vertical displacement. The displacement increases as the train loadings increases. The maximum subsidence ($S_{vv\text{-}max}$) occurred at the middle wheel of the locomotive bogie. The magnitude of $S_{vv\text{-}max}$ had a linear relationship with train operation speed.

Tunnel excavation under an existing operating railway was the second scenario that was interpreted in Section 4.2. In total, 12 different tunnel diameters (from 3 m to 14 m) were used in the simulations. The models of tunnel D = 3m and D = 14 m were chosen as examples to display the simulation results. Models at other diameters follow similar trends, but with different magnitude; and these results are displayed in Appendix B. Vertical ballast surface displacements induced by tunnel excavation with train operation above were smaller than those only caused by train loadings. As an explanation, it was reasonable that tunnel excavation leads to the uplifting of ground due to initial stress theory, field stress setting and boundary conditions, which have been introduced in

Section 3.1.5. On the other hand, train operation was treated as a constant applied on the ballast surface; tunnel construction regards as a variable. Therefore, the $S_{vp}$ occurs on the base of $S_{vv}$; it results in that the values of $S_{vp}$ were smaller than $S_{vv}$.

The last scenario is to discuss the difference between the previous two scenarios. Tunnel excavation is the only variable between Scenario 1 and 2. It discusses the ground surface displacement induced by tunneling only. Tunnel diameter and tunnel depth are two crucial parameters affecting the vertical ballast surface displacement. With increasing tunnel depth, the tunnel excavation had less impact on the vertical ground surface deformation. Moreover, larger tunnel diameter tunnels generated larger deformation of the ballast surface. The standard of allowable railway embankment deformation was adopted to be 10 mm. Therefore, corresponding to Table 4.4, tunnel D = 3 m at depth 3 m, 6 m, 9 m, 12 m, 15 m, 18 m, 21 m 24 m, and tunnel D = 4 m at depth 16 m, 20 m, 24 m, 28 m, 32 m can be constructed while the trains were allowed to pass at a maximum speed of 120 km/h. Corresponding to the discussion in Section 4.3.2, both the average and maximum relative difference are in a limited range, which leads to a small vertical displacement change comparing with the models at train speed $V_1$ = 0 km/h. The allowable tunnel construction under different train speeds is the same.

# Chapter 5 Conclusion and Recommendations

This chapter summarizes the key findings and contributions of this research thesis. Since there were a number of assumptions made in this thesis, there are still some limitations that should be considered for a future study.

## 5.1 Thesis Summary

With the aim of investigating the influence of train speeds, tunnel diameters and depths on ground surface displacement, two-dimensional FEM models were developed in RS2. Before establishing the models, a mesh convergence study and model verifications were performed to validate the accuracy of FEM modeling. The results illustrated that the convergence occurs at 5476 mesh elements, corresponding to a 0 % displacement discrepancy, which means the number of mesh elements should be greater than 5476 for most models to obtain stabilized results. The model verifications were performed by comparing the RS2 simulation results with analytical methods from Jaeger and Cook (1976) and Salencon (1969). While, the train speed is selected to be 0 km/h, 40 km/h, 80 km/h and 120 km/h. According to the literature review in Chapter 2 and Section 3.1.2, train loadings were applied to the interface between ballast and sleepers (crossties), which represents the ground surface in the models. The railway embankment was constructed on natural ground, which was specified as silty clay. After applying train loadings, tunnels with different diameters at various depths were modeled.

All FEM models were generated as a function of the overburden ratio of H/D parameter, where H is the tunnel depth, and D is the tunnel diameter. The range of H/D is from 1 to 8, with increments of 1. The range of the tunnel diameters selected in this thesis was 3 m to 14 m with an increment of 1 m. Therefore, there are 96 models for each trainload condition, and 384 models in total. There are three scenarios that were considered in the parametric study of the influence parameters: train speed, tunnel diameter and depth. Scenario 1 studied the ground surface displacement caused solely by moving trains. Scenario 2 incorporated the effect of tunnel excavation in addition to moving trains; thus, the tunnel excavation is the only variable between Scenario 1 and 2. Scenario 3 only examined the influence of tunnel excavation on the ground surface displacement. In Scenario 2 and 3, the models of tunnel D = 3 m and D = 14 m were chosen as examples to display the simulation results, that states the situation of minimum and maximum tunnel diameter in this thesis.

## 5.2 Conclusion

The findings from the analysis of results can be summarized as follows:

- The ground surface vertical displacement ($S_{vv}$) increases as the train loading increases in the absence of tunneling. The maximum subsidence ($S_{vv\text{-}max}$) occurred at the middle wheel of the locomotive bogie. The relationship of $S_{vv\text{-}max}$ and operation train speed is linear.

- When the ground surface displacement ($S_{vp}$) is under the influence by both train loading and tunnel excavation, the displacement increases with the growth of train speed. The location of maximum displacement ($S_{vp\text{-}max}$) is alterative with different tunnel diameter.
- Shallow depth tunnels with low depth-diameter ratio (H/D) generate more significant ground surface displacement than deeper buried tunnels.
- Larger tunnel diameters generate more ground vertical displacement than smaller tunnels.
- Tunnels with 3 m diameter at any overburden depth or tunnels with 4 m diameter at the depth deeper than 16 m can be constructed beneath an existing railway within the subsidence control standard (10 mm) without additional measures.
- Corresponding to Table 4.5, the one-meter increase of tunnel diameter for a small shallow tunnel affects the ground surface displacement more than a large shallow tunnel, while the overburden ratio (H/D) remains the same.

## 5.3 Limitations

The most relevant parameters were considered in this study. However, there are still some factors that could be considered to more precisely simulate the actual train loading conditions. The railway track was assumed to be a straight line, thus curved tracks were not concerned in this thesis. The curved tracks can generate centrifugal forces on the rail, that can cause unequal forces on the two rails. Also, wheels, track, and the contact between them are assumed to be ideal in the simulation, that means the friction forces between the wheel and rail were neglected. Environmental factors, like temperature and wind, can also lead to other kinds of track forces; but they are not taken into account in the train loadings calculation. According to Indraratna et al. (2011), the friction between wheel and rail, the high rail temperature, the crosswind and the wheel flange-rail induced lateral force are the components of lateral track force, lead to a complex calculation of train loading, which is difficult to simulate in a two-dimensional model. High temperature can also affect the length of the rail, that can result in longitudinal track force. Consequently, the train loading calculation is simplified by only considering vertical loadings.

The natural ground is set to be silty clay, which is a homogenous soil mass in simulation. However, the soil ground profile can consist of multiple layers of soils under real conditions. In addition, ground water was not incorporated in the models. The advancing process of tunneling under the railway tracks is not simulated in this thesis. It can help to understand the displacement of the ground surface along the tunnel construction direction. But in this thesis, the disturbance of tunneling on the railway embankment is the main focus.

## 5.4 Future Work

Some suggestions and improvements for future work can be stated based on this thesis. Three-dimensional models are recommended to help simulate complex situations, which are closer to the realistic field construction. Moreover, ground water analysis should be considered since the soil behavior will be different between under drained conditions and undrained conditions. Also, the time dependent displacement behavior of the soil in the long-term could be considered. For train loading calculation, the environmental factors, practical track conditions (curved, uneven track) can be performed in simulation to model a more realistic situation.

# References


1. American Railway Engineering and Maintenance-of-Way Association (AREMA) (2010). *AREMA manual for railway engineering*, Landover, MD.
2. American Railway Engineering and Maintenance-of-Way Association (AREMA) (2012). *AREMA manual for railway engineering*, Landover, MD.
3. Bian, X., Hong, Z. S., and Ding, J. W. (2016). "Evaluating the effect of soil structure on the ground response during shield tunnelling in Shanghai soft clay." *Tunnelling and Underground Space Technology*, 58, 120-132.
4. Bobet, A. (2010). "Numerical methods in geomechanics." *The Arabian Journal for Science and Engineering*, 35(1B), 27-48.
5. Budhu, M. (2010). *Soil mechanics and foundations*, 3rd Ed., John Wiley & Sons Inc., Hoboken, NJ, USA.
6. Cao, J., and Wei, K., (2008). "Study on ground surface deformation induced by shield tunneling under existing railway in soft ground." *Gansu Science and Technology*, 24(4), 111-113. In Chinese.
7. Chakeri, H., and Ünver, B. (2014). "A new equation for estimating the maximum surface settlement above tunnels excavated in soft ground." *Environmental Earth Sciences*, 71(7), 3195-3210.
8. Chapman, D. N., Metje, N., and Stark, A. (2010). *Introduction to tunnel construction*. Spon Press, New York, NY, USA.
9. Clough, G. W., and Schmidt, B. (1981). *Design and performance of excavations and tunnels in soft clay*. Elsevier, San Francisco, USA.
10. Clough, R. W. (1960). "The finite element method in plane stress analysis." In *Proceedings of 2nd ASCE Conference on Electronic Computation*, Pittsburgh, PA, September 8 and 9, 1960.
11. Deane, A. P., and Bassett, R. H. (1995). "The Heathrow Express Trial Tunnel." In *Proceedings of the Institution of Civil Engineers* - Geotechnical Engineering, July 1995, 113(3), 144–156.
12. Desai, C. S, and Christian, J. T. (Eds.). (1977). *Numerical methods in geotechnical engineering*. McGraw-Hill Inc., USA.
13. Dick, S. M., Otter, D. E., and Connor, R. J. (2011). "Comparison of railcar and bridge design loadings for development of a railroad bridge fatigue loading." In *AREMA 2011 Annual Conference,* Minneapolis, MN, September 20, 2011.
14. Ercelebi, S. G., Copur, H., and Ocak, I. (2011). "Surface settlement predictions for Istanbul Metro tunnels excavated by EPB-TBM." *Environmental Earth Sciences*, 62(2), 357-365.
15. Esveld, C.(2001). *Modern railway track (Vol. 385)*. MRT-productions, Zaltbommel, The Netherlands.
16. Gong, Q. M., and Zhou, S. H. (2008). "Shield tunneling beneath existing railway line in soft ground." In *Geotechnical Aspects of Underground Construction in Soft Ground: Proceedings of the 6th International Symposium (IS-Shanghai 2008)* , CRC Press, London, UK, 381-384.

17. Gong, T., Yang, X., Qi, C., and Ding, D. (2012). "Numerical analysis of influence of large-diameter epb shield tunneling on ground deformation in Beijing area." In *Proceedings of 2nd International Conference on Electronic & Mechanical Engineering and Information Technology,* Atlantis Press*,* Paris, France, September 7, 2012, 864-869.
18. Huo, J., Wang, B., and Zhou, S. (2011). "Safety analysis of foundation reinforcement scheme for shield tunnel under-passing intercity railway." *China Railway Science*, 32(5), 71-77. In Chinese.
19. Ieronymaki, E. S., Whittle, A. J., and Sureda, D. S. (2017). "Interpretation of free-field ground movements caused by mechanized tunnel construction." *Journal of Geotechnical and Geoenvironmental Engineering*, 143(4), 04016114.
20. Indraratna, B., Salim, W., and Rujikiatkamjorn, C. (2011). *Advanced rail geotechnology–ballasted track*, CRC press, Leiden, Netherlands.
21. Jaeger, J.C. and Cook, N.G.W. (1976). *Fundamentals of rock mechanics*, 3rd Ed., Chapman and Hall, London, UK.
22. Jeffs, T., and Tew, G. P. (1991). *A review of track design procedures: sleepers and ballast, Vol. 2,* Railways of Australia BHP Research, Melbourne Laboratories, Melbourne, Australia.
23. Johansson, A. (2006). "Out-of-round railway wheels—assessment of wheel tread irregularities in train traffic." *Journal of Sound and Vibration*, 293(3), 795-806.
24. Karakus, M. (2007). "Appraising the methods accounting for 3D tunnelling effects in 2D plane strain FE analysis." *Tunnelling and Underground Space Technology*, 22(1), 47-56.
25. Karakus, M., and Fowell, R. J. (2005). "Back analysis for tunnelling induced ground movements and stress redistribution." *Tunnelling and Underground Space Technology*, 20(6), 514-524.
26. Knothe, S. (1957). "Observations of surface movements under influence of mining and their theoretical interpretation." In *Proceedings of the European Congress on Ground Movement*, Leeds, UK, April 9 to 12, 1957, 210-218.
27. Ledesma, A., and Romero, E. (1997). "Systematic back analysis in tunnel excavation problems as a monitoring technique." In *Proceedings of the International Conference on Soil Mechanics and Foundation Engineering-International Society for Soil Mechanics and Foundation Engineering* (Vol. 3), AA BALKEMA, Hamburg, Germany, September 6, 1997, 1425-1428.
28. Lee, K. M., and Rowe, R. K. (1990). "Finite element modelling of the three-dimensional ground deformations due to tunnelling in soft cohesive soils: Part I—Method of analysis." *Computers and Geotechnics*, 10(2), 87-109.
29. Lee, K. M., and Rowe, R. K. (1990). "Finite element modelling of the three-dimensional ground deformations due to tunnelling in soft cohesive soils: Part 2—results." *Computers and Geotechnics*, 10(2), 111-138.
30. Li, D., Hyslip, J. P., Sussmann, T. R., and Chrismer, S. M. (2016). *Railway geotechnics*, Taylor & Francis Group, London, UK.
31. Li, G. X. (2004). *Advanced soil mechanics*. Tsinghua University Press, Beijing, China. In Chinese.
32. Loganathan, N., and Poulos, H. G. (1998). "Analytical prediction for tunneling-induced ground movements in clays." *Journal of Geotechnical and Geoenvironmental Engineering*, 124(9), 846-856.

33. Lv, P.L., and Zhou, S.H. (2007). “Analysis on upper rail settlement in soft ground resulting from shield tunneling across main railway line.” *China Railway Science*, 28(2), 12-16. In Chinese.
34. Maidl, B., Thewes, M., and Maidl, U. (2014). *Handbook of tunnel engineering II. Basics and additional services for design and construction*, Willey, Ernst & Sohn, Berlin, Germany.
35. Mair, R. J. (2008). “Tunnelling and geotechnics: new horizons.” *Géotechnique*, 58(9), 695-736.
36. Mair, R. J., Taylor, R. N., and Bracegirdle, A. (1993). “Subsurface settlement profiles above tunnels in clays.” *Geotechnique*, 43(2), 315-320.
37. Ministry of Railway of the People’s Republic of China (2016). *Code for design of railway earth structure, TB10001-2016,* Beijing, China. In Chinese.
38. Munjiza, A. A. (2004). *The combined finite-discrete element method*, John Wiley & Sons, London, UK.
39. Hung, C. J., National Highway Institute (U.S.), Parsons, Brinckerhoff, Quade and Douglas. (2010). *Technical manual for design and construction of road tunnels--civil elements*, Department of Transportation, Federal Highway Administration, National Highway Institute, Washington, D.C., U.S.
40. Ocak, I. (2014). “A new approach for estimating the transverse surface settlement curve for twin tunnels in shallow and soft soils.” *Environmental Earth Sciences*, 72(7), 2357-2367.
41. O'Reilly, M. P., and New, B. M. (1982). “Settlements above tunnels in the United Kingdom-their magnitude and prediction.” *In: Proceedings of Tunneling’82 Symposium*, Institution of Mining and Metallurgy, Brighton, London, June 7 to 11, 1982, 173-181.
42. Owen, D. R. J., and Hinton, E. (1980). *Finite elements in plasticity*, Pineridge press, Swansea, UK.
43. Palmer, J. H. L., and Belshaw, D. J. (1980). “Deformations and pore pressures in the vicinity of a precast, segmented, concrete-lined tunnel in clay.” *Canadian Geotechnical Journal*, 17(2), 174-184.
44. Panet, M., and Guenot, A. (1982). “Analysis of convergence behind the face of a tunnel.” *In: Proceedings of International Symposium Tunnelling’82*, The Institution of Mining and Metallurgy, Brighton, London, June 7 to 11, 1982, 197–204.
45. Pavement Interactive (n.d.). “Elastic modulus.” *Pavement Interactive*. <https://www.pavementinteractive.org/reference-desk/design/design-parameters/elastic-modulus/> (Accessed Sept., 2019)
46. Peck, R.B. (1969). “Deep excavation and tunnelling in soft ground: state-of-the art report.” *In Proceedings of 7th International Conference on Soil Mechanics and Foundation Engineering,* Mexico, 225-290.
47. Phienwej, N. (1997). Ground movements in shield tunneling in Bangkok soils. *In Proceedings of 14th International Conference on Soil Mechanics and Foundation Engineering*, September 6 to 12, 1997, 3, 1469-1472.
48. Pietruszczak, S. (2010). *Fundamentals of plasticity in geomechanics*. CRC Press, Boca Raton, FL, USA.
49. Potts, D. M., and Zdravković, L. (1999). *Finite element analysis in geotechnical engineering: Theory (Vol. 1)*, Thomas Telford, London, UK.

50. Potts, D. M., and Zdravković, L., Addenbrooke, T. I., Higgins, K. G., & Kovačević, N. (2001). *Finite element analysis in geotechnical engineering: application (Vol. 2)*, Thomas Telford, London, UK.
51. Profillidis, V. A. (2014). *Railway management and engineering*, Ashgate Publishing Company, Burlington, VT, USA.
52. Ramasamy, N. (1992). "Soft ground tunneling in Bangkok subsoils," MEng thesis, Asian Inst. Of Technol., Bangkok, Thailand.
53. Rankin, W. J. (1988). "Ground movements resulting from urban tunnelling: predictions and effects." *Engineering Geology Special Publications*, Geological Society, London, 5(1), 79-92.
54. Rocscience Inc. (2019). "Convergence Creiteria." <https://www.rocscience.com/help/rs2/pdf_files/theory/Convergence_Criteria.pdf>
55. Rocscience Inc. (2019). "RS2 Stress Verification." <https://www.rocscience.com/help/rs2/pdf_files/verification/RS2_StressVerification_Part1.pdf>
56. Rocscience Inc. (2019). RS2 Excavation and Design support software, *Toronto, Canada*.
57. Rowe, R. K., Lo, K. Y., and Kack, G. J. (1983). "A method of estimating surface settlement above tunnels constructed in soft ground." *Canadian Geotechnical Journal*, 20(1), 11-22.
58. Sadeghi, J. (2012). "New advances in analysis and design of railway track system." *Reliability and Safety in Railway,* InTech Open, London, UK, 75-100.
59. Sadeghi, J., and Barati, P. (2010). "Evaluation of conventional methods in analysis and design of railway track system." *International Journal of Civil Engineering*, 8(1), 44-56.
60. Salencon, J. (1969), "Contraction quasi-statique d'une cavite´ a´ syme´trie sphe´rique ou cylindrique dans un milieu e´lastoplastique", *Annales Des Ports Et Chaussees*, 4, 231-236.
61. Selig, E. T., and Waters, J. M. (1994). *Track geotechnology and substructure management*, Thomas Telford, London, UK.
62. Shani, W., and TunnelTalk (2017). "Ground freezing TBM drive collapse in Germany." *TunnelTalk*, <https://www.tunneltalk.com/Germany-21Aug2017-Rastatt-TBM-rail-tunnel-collapse-brings-rail-traffic-to-a-halt.php> (Accessed Jul. 31, 2020)
63. Sun, Q. D., Indraratna, B., and Nimbalkar, S. (2015). "Deformation and degradation mechanisms of railway ballast under high frequency cyclic loading." *Journal of Geotechnical and Geoenvironmental Engineering*, 142(1), 04015056.
64. Swoboda, G. (1979). "Finite element analysis of the New Austrian Tunneling Method (NATM)." In *Proceedings of the 3rd International Conference on Numerical Methods in Geomechanics,* Aachen, April 2 to 6, 1979, 2, 581-586.
65. Swoboda, G., Marence, M., and Mader, I. (1994). "Finite element modelling of tunnel excavation". *International Journal of Engineering Modelling*, 6, 51-63.
66. UIC (International Union of Railways) (2006). *Loads to be considered in railway bridge design (Leaflet 776-1)*, 5th Eds., International Union of Railways, Paris, France.
67. Whittle, A. J., Hsieh, Y. M., Pinto, F., and Chatzigiannelis, Y. (2001). "Numerical and analytical modeling of ground deformations due to shallow tunneling in soft soils." In *First MIT Conference on Computational Fluid and Solid Mechanics*, Massachusetts Institute of Technology Cambridge, June 12 to 15, 2001, Cambridge, MA, USA, 546-549.

68. Xiao, L., and Zhang, Q. (2011). "3D numerical modeling of ground settlements caused by shield tunneling across multi-tracks of railway." *Journal of Tongji University. Natural Science*, 39(9), 1286-1291. In Chinese.
69. Xie, X., Yang, Y., and Ji, M. (2016). "Analysis of ground surface settlement induced by the construction of a large-diameter shield-driven tunnel in Shanghai, China." *Tunneling and Underground Space Technology*, 51, 120-132.
70. Xu, Y. J., Tao, L. J., Li, W. B., Fan, J. Y., and Wang, W. P. (2010). "A Numerical simulation study on the settlement laws of the high-speed railway's subgrade induced by the construction of twin shield tunnel." *Journal of Beijing University of Technology*, 36(12), 1618-1623. In Chinese.
71. Yang, H. T., and Zhang, H. J. (2015). "Grouting Scheme Optimization of Large Diameter Shield Tunneling Undercrossing the Building in the Soft Area." *Journal of Beijing University of Civil Engineering and Architecture*, 31(2), 29-33. In Chinese.
72. Yang, T. L, Li, X., Dong, J. K., and Li, Y. T. (2009). "Analysis of Ground Subsidence Caused by Shield Tunneling under Railway." *Mine Surveying*, (1), 12-14. In Chinese.
73. Zhang, H. B., Yin, Z. Z., and Zhu, J. G. (2005). "3D finite element simulation on deformation of soil mass during shield tunneling." *Chinese Journal of Rock Mechanics and Engineering*, 24(5), 755-760. In Chinese.
74. Zhang, H.J., Gong, Q., and Di, H. G. (2014). "Numerical analysis of shield tunnel driving underneath an existing railway and related reinforcement effects on subsidence control." In *ICPTT 2014: Creating Infrastructure for a Sustainable World,* the Committee on Sustainability of the American Society of Civil Engineers, California, USA, November 6 to 8, 2014, 828-835.
75. Zhang, T. W., Cui, Y. J., Lamas-Lopez, F., Calon, N., & D'Aguiar, S. C. (2016). "Modelling stress distribution in substructure of French conventional railway tracks." *Construction and Building Materials*, 116, 326-334.
76. Zhao, Y., and Qi, T. (2014). "Tunneling-induced settlement evaluation for new tunnel underneath existing tunnel." *In Proceedings of Geo-Shanghai 2014*, Shanghai, China, ASCE, Reston, VA, May 26 to 28, 2014, 143-154.
77. Zhou, J., Shi, X., Du, K., Qiu, X., Li, X., and Mitri, H. S. (2017). "Feasibility of random-forest approach for prediction of ground settlements induced by the construction of a shield-driven tunnel." *International Journal of Geomechanics*, 17(6), 04016129.
78. Zhou, S. M., and Chen, J. J. (2002). "Hydrofracture grouting in soft flowing mucky ground for a metro tunnel." *Chinese Journal of Geotechnical Engineering,* 24(2), 222-224. In Chinese.
79. Zhu, C., and Li, N. (2017). "Prediction and analysis of surface settlement due to shield tunneling for Xi'an Metro." *Canadian Geotechnical Journal*, 54(4), 529-546.

## Appendix A: Soil Properties

Table A-1 Physical and Mechanical Parameters of Soils (Xie et al. 2014)

| Name | h (m) | γ (kN/m$^3$) | $c$ (kPa) | $\varphi^\circ$ | $E$ (MPa) | $v$ |
|---|---|---|---|---|---|---|
| Muddy silty clay | 6.0 | 16.5 | 11 | 14.1 | 10 | 0.34 |
| Muddy clay | 6.0 | 17.4 | 11 | 11.7 | 10 | 0.34 |
| Sandy silt | 9.0 | 18.2 | 3 | 30.3 | 45 | 0.24 |
| Silty clay | 9.0 | 18.1 | 14 | 21.0 | 25 | 0.28 |
| Silty clay with thin silty sand interlayer | 16.0 | 18.4 | 22 | 15.6 | 22 | 0.28 |
| Fine silty sand | 38.0 | 19.5 | 2 | 31.1 | 60 | 0.2 |

Note: h is average thickness; γ is bulk unit weight; $c$ is cohesion; $\varphi$ is friction angle; $E$ is Young's modulus; $v$ is Poisson's ratio.

Table A-2 Physical and Mechanical Parameters of Soils (Chakeri and Ünver 2014)

| Name | h (m) | γ (kN/m$^3$) | $c$ (kPa) | $\varphi^\circ$ | $E$ (MPa) | $v$ | $K$ |
|---|---|---|---|---|---|---|---|
| Fill | 1.2 | 19.0 | 29 | 35 | 15 | 0.30 | 0.42 |
| Silt, clay | 8.0 | 19.0 | 40 | 27 | 30 | 0.35 | 0.55 |
| Silt with gravel, clay with gravel | 11.6 | 19.0 | 30 | 35 | 80 | 0.27 | 0.43 |
| Well graded silty gravel, silt with gravel | base | 19.0 | 20 | 38 | 100 | 0.27 | 0.38 |

Note: h is average thickness; γ is bulk unit weight; $c$ is cohesion; $\varphi$ is friction angle; $E$ is Young's modulus; $v$ is Poisson's ratio; $K$ is earth pressure coefficient.

Table A-3 Physical and Mechanical Parameters of Soils (Ercelebi et al. 2011)

| Name | h (m) | $N_{30}$ | $S_u$ (kPa) | $\varphi^\circ$ | $E$ (kPa) | $\gamma_n$ (kN/m$^3$) | $\gamma_{dry}$ (kN/m$^3$) | $PI$ (%) | Permeability (cm/s) |
|---|---|---|---|---|---|---|---|---|---|
| Fill | 2.5 | 10 | 13 | 20 | 8,000 | 19.8 | 13.8 | - | 1.0 |
| Very stiff clay | 4.0 | 20 | 85 | 9 | 51,000 | 18.2 | 12.7 | 33 | $1.0\times10^{-4}$ |
| Dense sand | 5.0 | 35 | 40 | 35 | 24,000 | 19.0 | 13.5 | - | 0.5 |
| Very dense sand | 3.0 | 64 | 50 | 35 | 30,000 | 19.5 | 15.0 | - | 0.25 |
| Hard clay | base | 45 | 150 | 12 | 90,000 | 18.6 | 14.0 | 45 | $1.0\times10^{-4}$ |

Note: $h$ is thickness; $N_{30}$ is standard penetration number; $S_U$ is undrained shear strength; $\varphi$ is internal friction angle; $E$ is Young's modulus estimated as $E = 600S_U$; $\gamma_n$ is natural unit weight; $\gamma_{dry}$ is dry unit weight; $PI$ is plasticity index.

Table A-4 Some general geotechnical properties of the study area (Ocak 2013)

| Name | $\gamma$ (kN/m$^3$) | $E$ (MPa) | $c$ (kPa) | $v$ | $\varphi^\circ$ | $W$ (%) | $K$ | SPT 30 |
|---|---|---|---|---|---|---|---|---|
| Fill | 18.0 | 5 | 1 | 0.30 | 10 | - | - | 10 |
| Sand | 18.3 | 25 | 1 | 0.25 | 35 | - | $10^{-5}$ to $10^{-4}$ | 40 |
| Very dense sand | 18.5 | 30 | 1 | 0.30 | 30 | 31 | $10^{-7}$ to $10^{-6}$ | 45 |
| Clay (Gungoren fr.) | 16.5 | 20 | 20 | 0.35 | 14 | - | $10^{-9}$ to $10^{-8}$ | 60 |
| Hard clay (Gungoren fr.) | 17.2 | 28 | 25 | 0.40 | 20 | 35 | $10^{-11}$ to $10^{-9}$ | 70 |

Note: $\gamma$ is bulk unit weight; $E$ is compression modulus; $c$ is cohesion; $\varphi$ is friction angle; $W$ is water content; $K$ is permeability; SPT 30 is standard penetration test.

Table A-5 Material properties of strata for New Jiuyanshan Tunnel (Zhao et al. 2014)

| Name | h (m) | $K$ (MPa) | $G$ (MPa) | $\rho$ (kg/m$^3$) | $\varphi^\circ$ | $c$ (kPa) |
|---|---|---|---|---|---|---|
| Medium sandy loess | 34.9 | 560 | 22 | 1,650 | 13 | 10 |
| Stiff sandy loess | 16.0 | 690 | 35 | 1,850 | 15 | 20 |
| Clayed loess | 34.0 | 1,200 | 48 | 1,950 | 18 | 50 |
| Weathered shale | 51.0 | 2,300 | 69 | 2,100 | 27 | 70 |
| Shale | 24.1 | 36,000 | 111 | 2,400 | 42 | 100 |

Note: h is average thickness; $K$ is bulk modulus; $G$ is shear modulus; $\rho$ is bulk density; $\varphi$ is friction angle; $c$ is cohesion.

Table A-6 Physical and mechanical parameters of soils and materials (Xiao and Zhang 2011)

| Name | $\rho(g/m^3)$ | $c\ (kPa)$ | $\varphi^\circ$ | E (MPa) | $v$ |
|---|---|---|---|---|---|
| Ballasted layer | 2.00 | - | - | 130 | 0.30 |
| Miscellaneous fill | 1.96 | 26 | 11.2 | 3.11 | 0.34 |
| Silty clay | 1.90 | 8 | 27.5 | 7.40 | 0.33 |
| Silt | 1.92 | 32 | 17.1 | 11.2 | 0.36 |
| Silty clay | 2.02 | 12 | 30.0 | 5.27 | 0.37 |
| Silty sand | 2.01 | 23 | 9.5 | 5.79 | 0.33 |
| Silty clay | 1.98 | 33 | 19.1 | 7.65 | 0.38 |
| Clay | 2.05 | 30 | 25 | 12.20 | 0.38 |
| Grouting layer | 2.10 | - | - | 2580 | 0.29 |
| Lining | 2.50 | - | - | 34500 | 0.29 |

Note: $\rho$ is bulk unit weight; $c$ is cohesion; $\varphi$ is friction angle; $E$ is Young's modulus; $v$ is Poisson's ratio.

Table A-7 Physical and mechanical parameters of soils (Zhang et al. 2005)

| Name | ω(%) | $\gamma\ (kN/m^3)$ | $c\ (kPa)$ | $\varphi^\circ$ | $a(MPa^{-1})$ | $LI$ | $e$ |
|---|---|---|---|---|---|---|---|
| Silty silt | 36.2 | 18.4 | 6.0 | 30.0 | 0.19 | 0.93 | 1.415 |
| Muddy clay | 52.5 | 16.9 | 14.0 | 9.0 | 0.79 | 1.28 | 1.468 |
| Silty clay | 36.7 | 17.7 | 14.0 | 20.5 | 0.50 | 1.27 | 1.060 |
| Sandy clay | 28.0 | 19.2 | 3.0 | 35.0 | 0.10 | - | 0.770 |
| Silt | 27.2 | 19.7 | 3.0 | 36.0 | 0.10 | - | 0.670 |

Note: ω is water content; γ is bulk unit weight; $c$ is cohesion; $a$ is coefficient of compressibility; $\varphi$ is friction angle; $LI$ is liquidity index; $e$ is void ratio.

Table A-8 Physical and mechanical parameters of soils (Cao and Wei 2008)

| Name | h (m) | $\gamma\ (kN/m^3)$ | $c\ (kPa)$ | $\varphi^\circ$ | $B\ (MPa)$ | $K_0$ | ω(%) | $e$ |
|---|---|---|---|---|---|---|---|---|
| Miscellaneous fill | 0.8 | - | - | - | - | - | - | - |
| Brown ~ yellow silty clay | 1.1 | 18.4 | 130 | 19.0 | 5.45 | 0.53 | 28.1 | 0.82 |
| Gray ~ yellow silty clay | 1.9 | 18.1 | 8.0 | 24.5 | 10.25 | 0.37 | 26.3 | 0.81 |
| Gray silty clay | 6.2 | 17.4 | 17.0 | 16.0 | 3.11 | 0.52 | 40.5 | 1.13 |
| Gray clay | 4.0 | 17.7 | 16.0 | 11.5 | 3.14 | 0.56 | 39.3 | 1.11 |
| Dark green silty clay | 3.8 | 18.3 | 18.0 | 13.5 | 5.41 | 0.51 | 41.5 | 1.13 |

Note: h is average thickness; γ is bulk unit weight; $c$ is cohesion; $\varphi$ is friction angle; $B$ is compression modulus (bulk modulus); $K$ is earth pressure coefficient (at rest); ω is water content; $e$ is void ratio.

Table A-9 Physical and mechanical parameters of soils (Huo et al. 2011)

| Name | ω (%) | γ (kN/m$^3$) | $c$ (kPa) | $\varphi^\circ$ | $B$ (MPa) | $e$ |
|---|---|---|---|---|---|---|
| Silty clay | 30.0 | 19.4 | 21.3 | 12.9 | 5.61 | 0.826 |
| Silty clay | 32.7 | 19.1 | 18.1 | 10.7 | 4.66 | 0.890 |
| Silt and silty sand | 27.0 | 19.2 | 8.7 | 27.6 | 12.02 | 0.818 |
| Silty clay | 32.1 | 19.0 | 17.4 | 14.4 | 5.38 | 0.880 |

Note: ω is water content; γ is bulk unit weight; $c$ is cohesion; $\varphi$ is friction angle; $B$ is compression modulus (bulk modulus); $e$ is void ratio.

Table A-10 Physical and Mechanical Parameters of Soils (Zhang et al. 2014)

| Name | h (m) | $\gamma$ (kN/m$^3$) | $c$ (kPa) | $\varphi^\circ$ | $B$ (MPa) | $K_0$ | $v$ |
|---|---|---|---|---|---|---|---|
| Miscellaneous fill | 2.1 | 17.9 | 9 | 24.5 | 7.47 | 0.46 | 0.32 |
| Brown ~ gray silty clay | 0.8 | 18.6 | 24 | 16 | 5.38 | 0.46 | 0.32 |
| Gray mucky silty clay | 1.8 | 17.7 | 15 | 11.5 | 3.48 | 0.47 | 0.33 |
| Gray sandy silty | 1.7 | 18.8 | 7 | 28 | 12.54 | 0.48 | 0.33 |
| Gray mucky silty clay | 3.6 | 17.5 | 13 | 11 | 2.99 | 0.49 | 0.33 |
| Gray mucky clay | 6 | 16.8 | 14 | 9 | 2.29 | 0.51 | 0.35 |
| Gray mucky clay | 3.8 | 17.1 | 15 | 10 | 2.67 | 0.5 | 0.35 |
| Gray silty clay | 5.8 | 17.8 | 17 | 13.5 | 4.32 | 0.46 | 0.35 |
| Gray silty clay | 1.4 | 17.8 | 10 | 24 | 4.85 | 0.45 | 0.35 |
| Dark green ~ straw yellow clay | - | 19.5 | 44 | 16 | 7.72 | 0.47 | 0.35 |

Note: h is average thickness; $\gamma$ is bulk unit weight; $c$ is cohesion; $\varphi$ is friction angle; $B$ is compression modulus (bulk modulus); $K_0$ is lateral earth pressure coefficient at rest; $v$ is Poisson's ratio.

## Appendix B: Displacement Distribution, $S_{vt\text{-}max}$, $R_{Svt\text{-}max}$ (%) for Models from D = 4 m to D = 13 m, Referring to Scenario 3

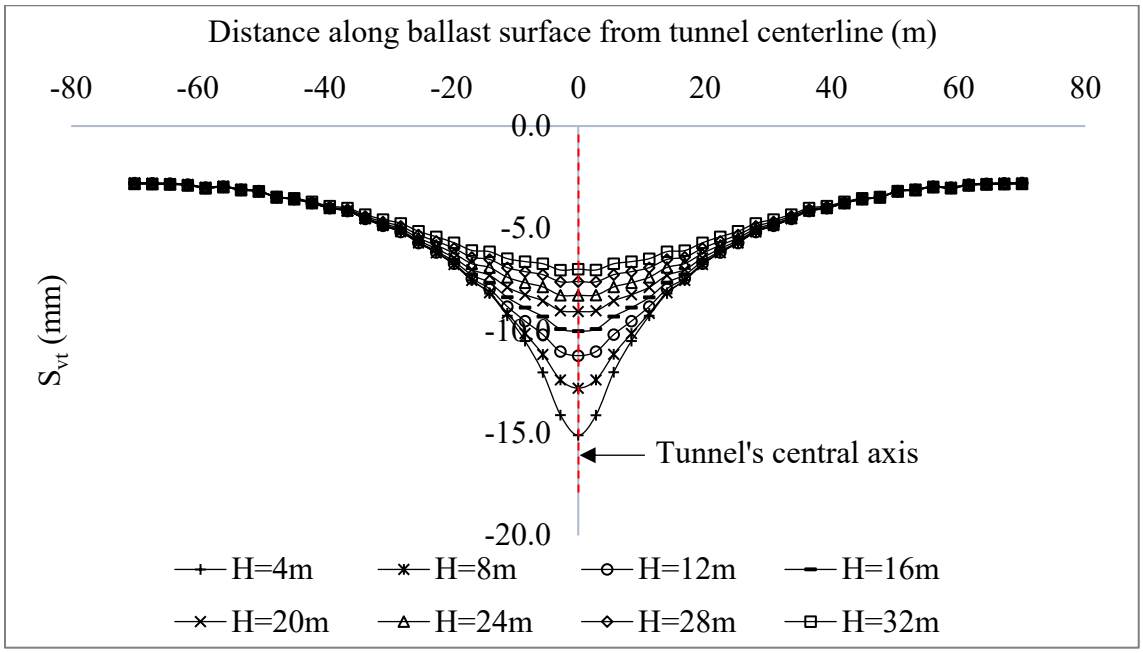


Figure B-1 Displacement distribution along ballast surface for model D = 4 m.

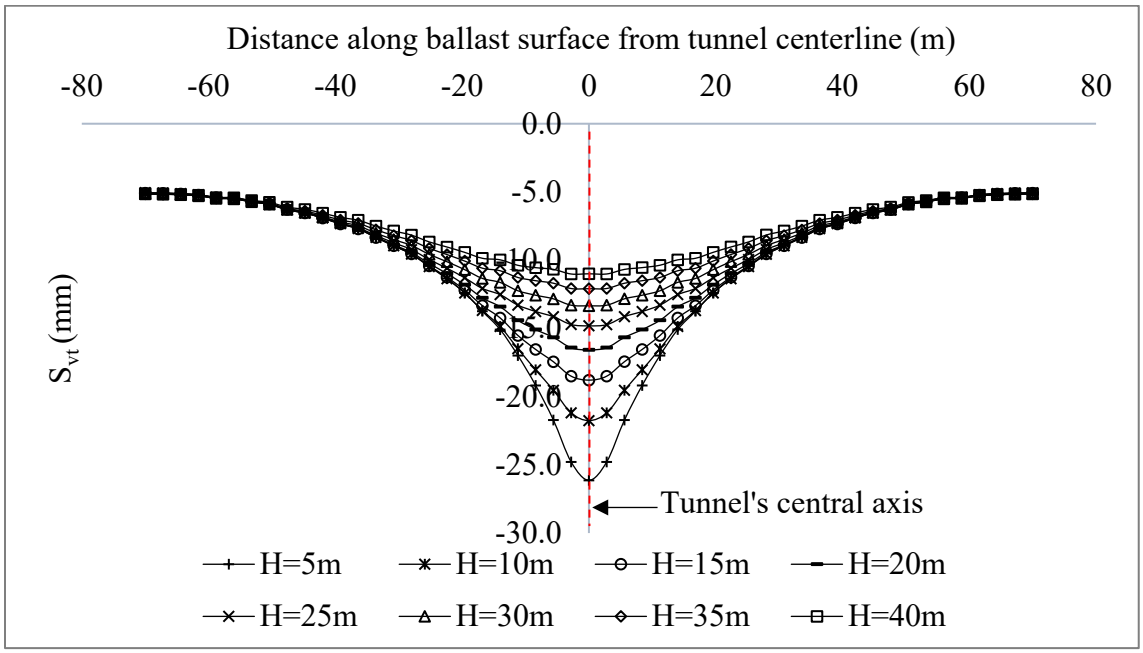


Figure B-2 Displacement distribution along ballast surface for model D = 5 m.

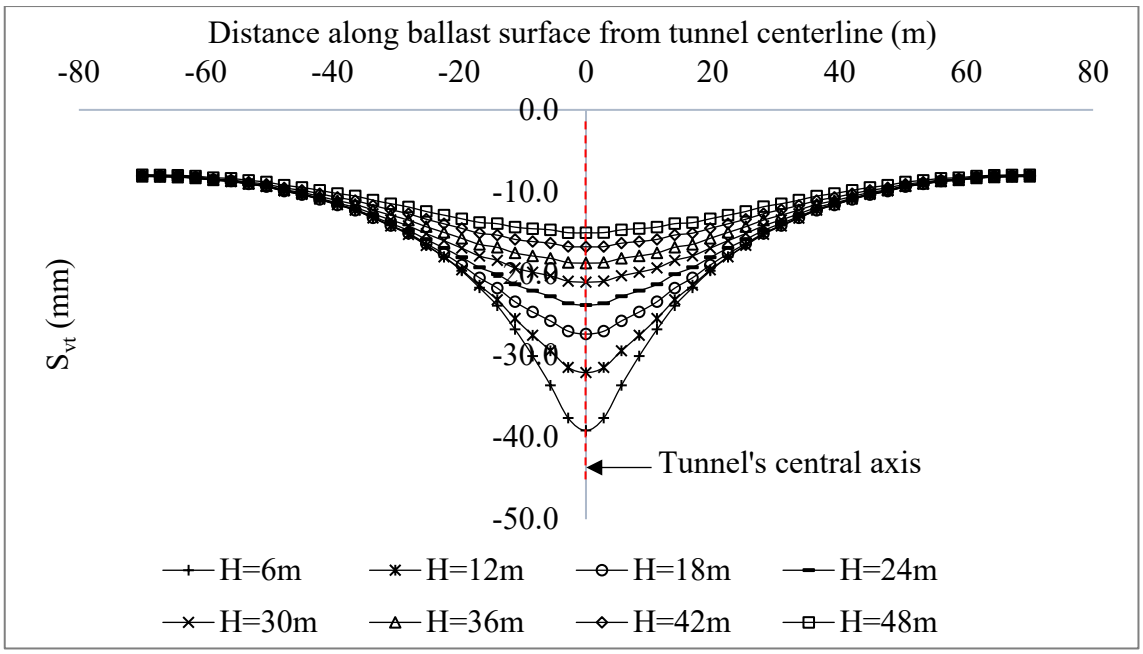


Figure B-3 Displacement distribution along ballast surface for model D = 6 m.

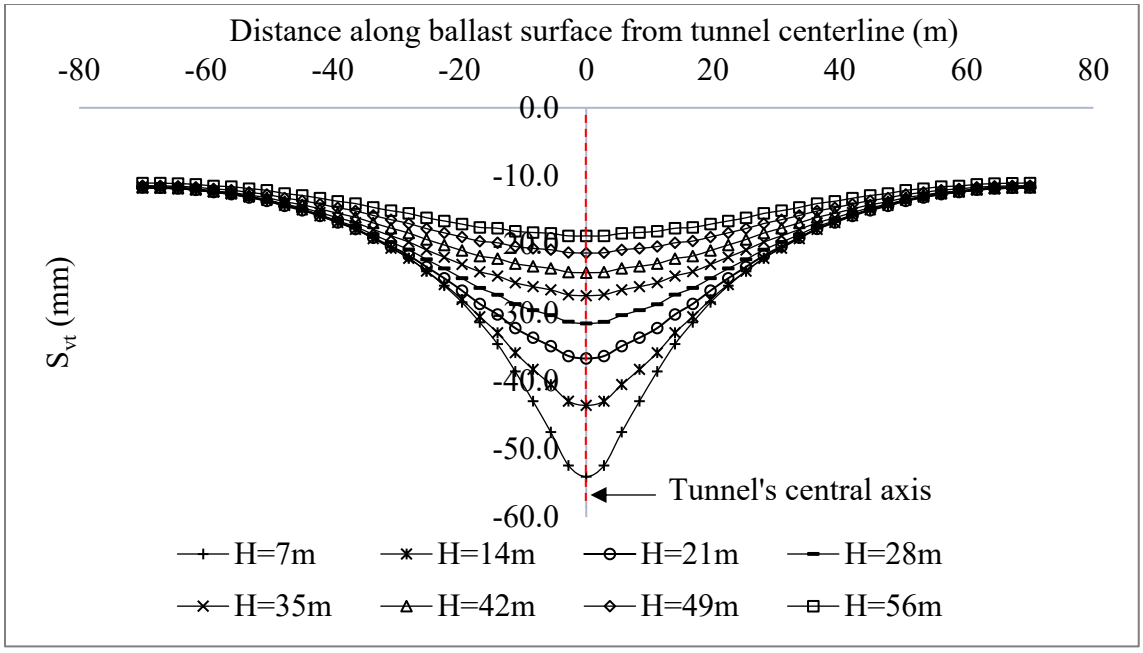


Figure B-4 Displacement distribution along ballast surface for model D = 7 m.

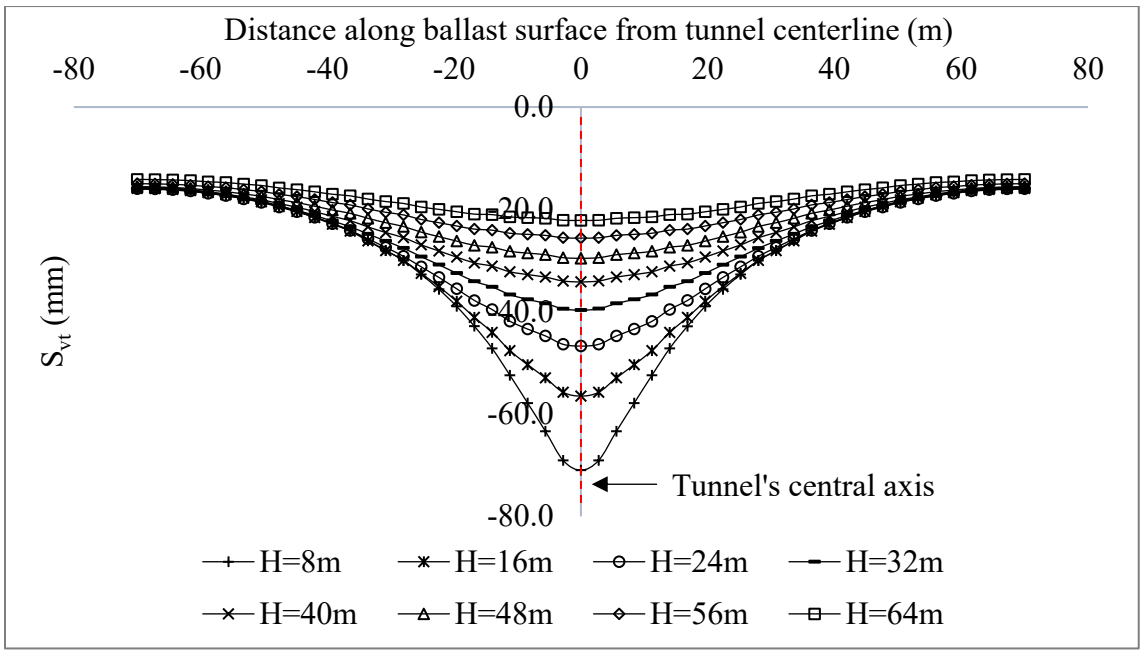


Figure B-5 Displacement distribution along ballast surface for model D = 8 m.

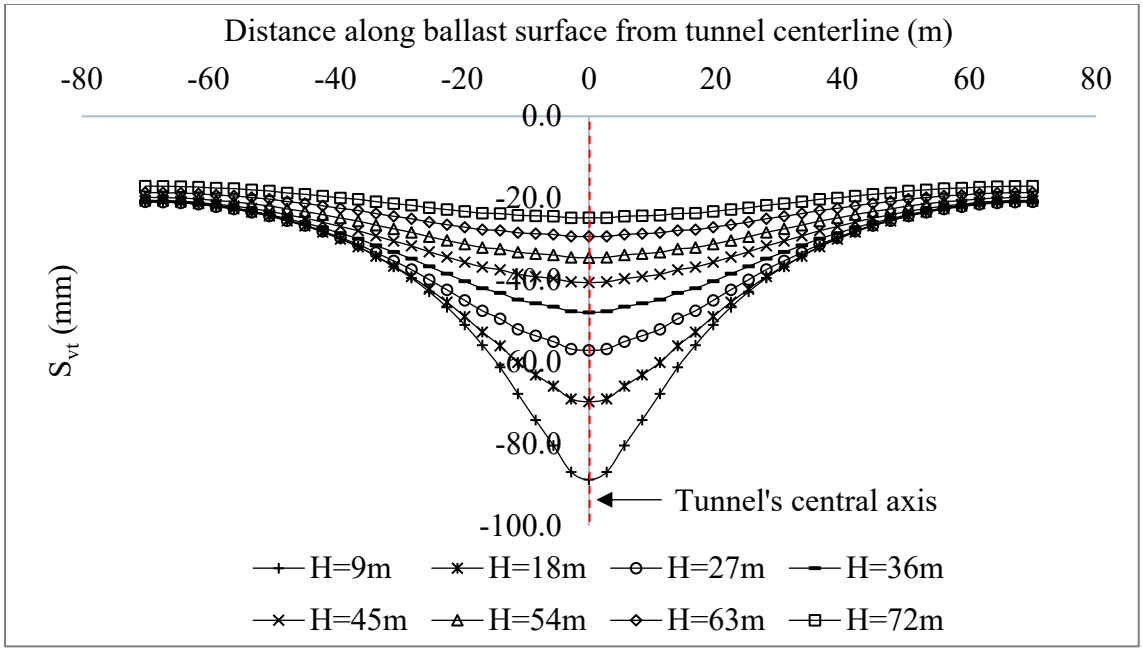


Figure B-6 Displacement distribution along ballast surface for model D = 9 m.

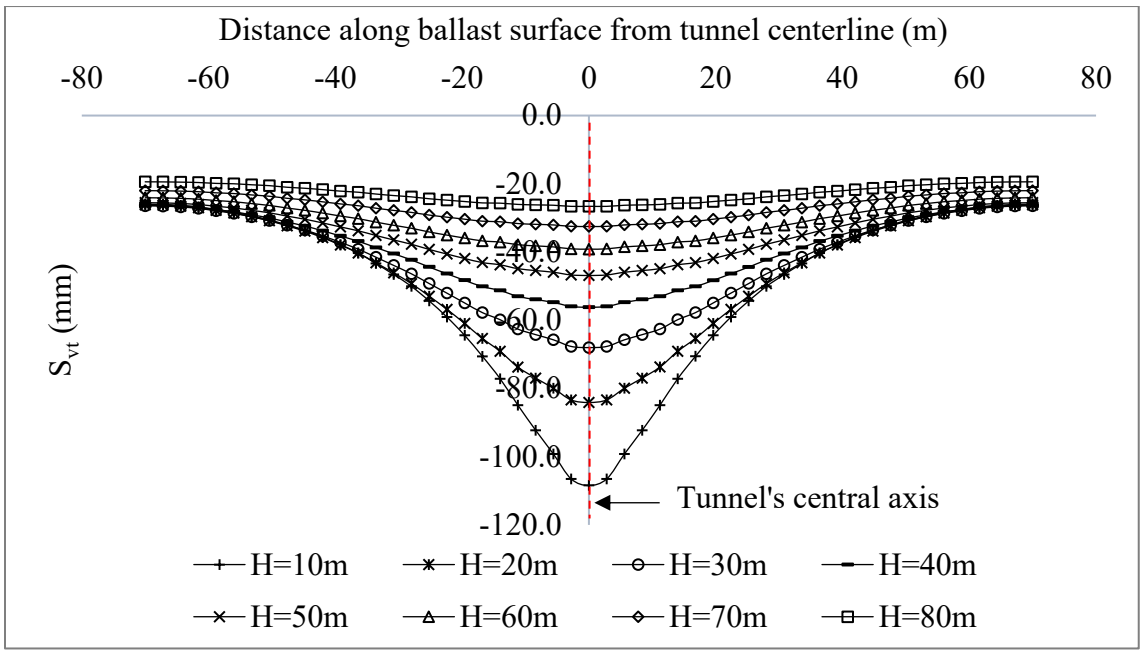


Figure B-7 Displacement distribution along ballast surface for model D = 10 m.

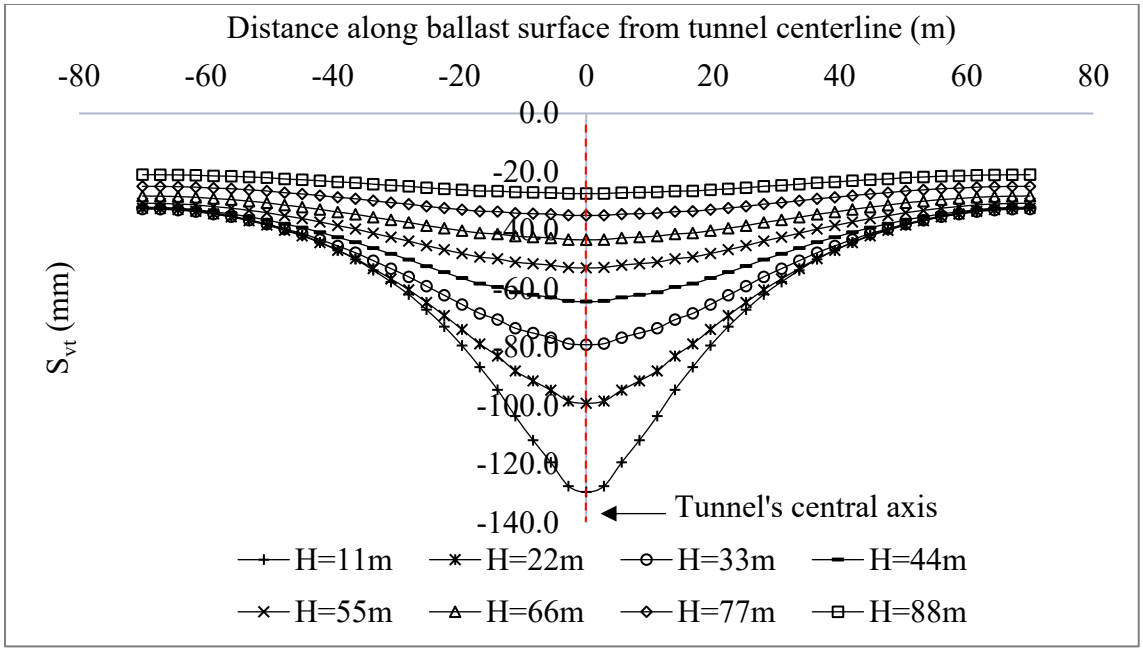


Figure B-8 Displacement distribution along ballast surface for model D = 11 m.

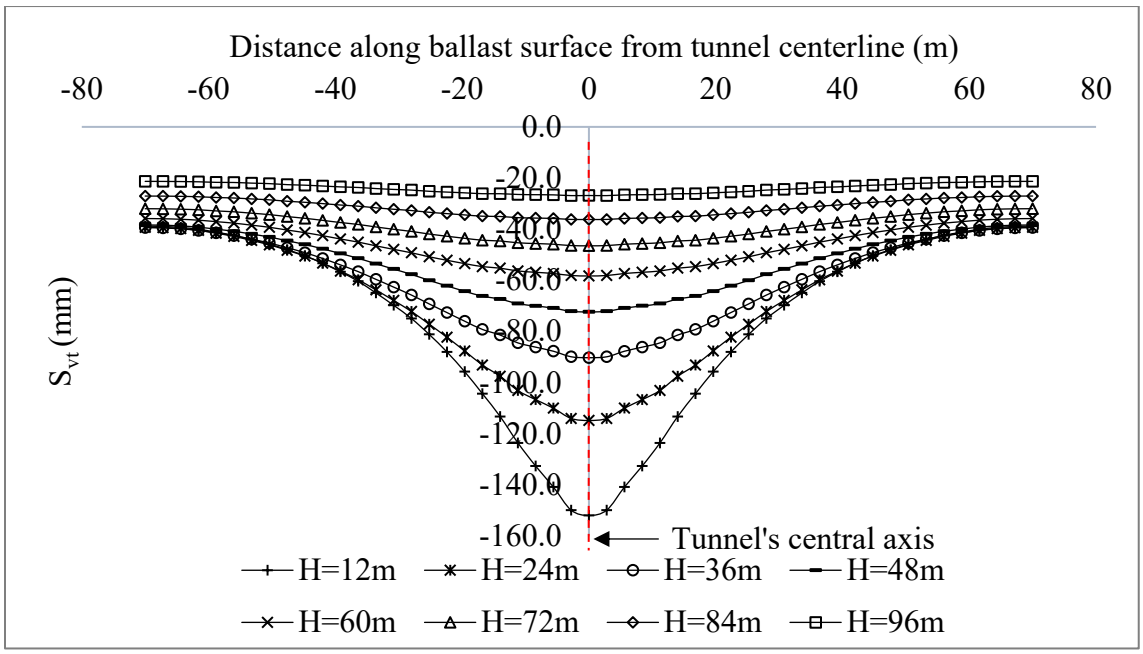


Figure B-9 Displacement distribution along ballast surface for model D = 12 m.

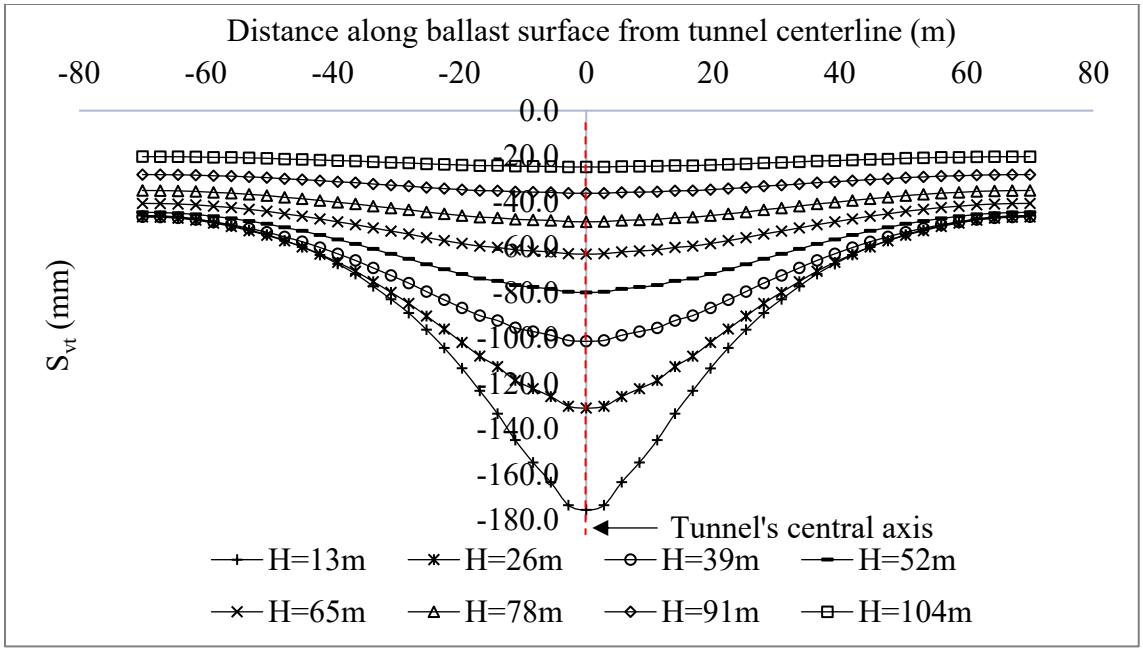


Figure B-10 Displacement distribution along ballast surface for model D = 13 m.

Table B-1 Summary of $S_{vt\text{-}max}$ induced by tunnel excavation only for tunnel diameter D = 4 m to D = 13 m; and $R_{Svt\text{-}max}$ (%) for each tunnel diameter

| D (m) | H (m) | $S_{vt\text{-}max}$ (mm) | $R_{Svt\text{-}max}$ (%) |
|---|---|---|---|
| 4 | 4 | 15.1 | 0.0 |
| | 8 | 12.8 | -15.2 |
| | 12 | 11.2 | -25.8 |
| | 16 | 10.0 | -33.8 |
| | 20 | 9.1 | -39.7 |
| | 24 | 8.3 | -45.0 |
| | 28 | 7.6 | -49.7 |
| | 32 | 7.0 | -53.6 |
| 5 | 5 | 26.1 | 0.0 |
| | 10 | 21.8 | -16.5 |
| | 15 | 18.8 | -28.0 |
| | 20 | 16.6 | -36.4 |
| | 25 | 14.8 | -43.3 |
| | 30 | 13.3 | -49.0 |
| | 35 | 12.1 | -53.6 |
| | 40 | 11.0 | -57.9 |
| 6 | 6 | 39.2 | 0.0 |
| | 12 | 32.1 | -18.1 |
| | 18 | 27.4 | -30.1 |
| | 24 | 23.9 | -39.0 |
| | 30 | 21.0 | -46.4 |
| | 36 | 18.7 | -52.3 |
| | 42 | 16.7 | -57.4 |
| | 48 | 15.0 | -64.7 |
| 7 | 7 | 54.1 | 0.0 |
| | 14 | 43.6 | -19.4 |
| | 21 | 36.7 | -32.2 |
| | 28 | 31.6 | -41.6 |
| | 35 | 27.5 | -49.2 |
| | 42 | 24.2 | -55.3 |
| | 49 | 21.3 | -60.6 |
| | 56 | 18.8 | -65.2 |
| 8 | 8 | 70.1 | 0.0 |
| | 16 | 56.5 | -19.4 |
| | 24 | 46.7 | -33.4 |
| | 32 | 39.7 | -43.4 |
| | 40 | 34.2 | -51.2 |
| | 48 | 29.6 | -57.8 |
| | 56 | 25.6 | -63.5 |

Table B-1 Summary of $S_{vt\text{-}max}$ induced by tunnel excavation only for tunnel diameter D = 4 m to D = 13 m; and $R_{Svt\text{-}max}$ (%) for each tunnel diameter – Continued

| D (m) | H (m) | $S_{vt\text{-}max}$ (mm) | $R_{Svt\text{-}max}$ (%) |
|---|---|---|---|
| | 64 | 22.1 | -68.5 |
| 9 | 9 | 88.8 | 0.0 |
| | 18 | 69.7 | -21.5 |
| | 27 | 57.2 | -35.6 |
| | 36 | 47.9 | -46.1 |
| | 45 | 40.6 | -54.3 |
| | 54 | 34.5 | -61.1 |
| | 63 | 29.4 | -66.9 |
| | 72 | 24.8 | -72.1 |
| 10 | 10 | 108.4 | 0.0 |
| | 20 | 84.1 | -22.4 |
| | 30 | 68.0 | -37.3 |
| | 40 | 56.2 | -48.2 |
| | 50 | 46.9 | -56.7 |
| | 60 | 39.2 | -63.8 |
| | 70 | 32.5 | -70.0 |
| | 80 | 26.6 | -75.5 |
| 11 | 11 | 129.5 | 0.0 |
| | 22 | 99.1 | -23.5 |
| | 33 | 79.1 | -38.9 |
| | 44 | 64.4 | -50.3 |
| | 55 | 52.8 | -59.2 |
| | 66 | 43.2 | -66.6 |
| | 77 | 34.9 | -73.1 |
| | 88 | 27.4 | -78.8 |
| 12 | 12 | 151.9 | 0.0 |
| | 24 | 114.7 | -24.5 |
| | 36 | 90.2 | -40.6 |
| | 48 | 72.3 | -52.4 |
| | 60 | 58.3 | -61.6 |
| | 72 | 46.5 | -69.4 |
| | 84 | 36.2 | -76.2 |
| | 96 | 26.8 | -82.4 |
| 13 | 13 | 175.6 | 0.0 |
| | 26 | 130.8 | -25.5 |
| | 39 | 101.4 | -42.3 |
| | 52 | 80.0 | -54.4 |
| | 65 | 63.1 | -64.1 |
| | 78 | 48.9 | -72.2 |

Table B-1 Summary of $S_{vt\text{-}max}$ induced by tunnel excavation only for tunnel diameter D = 4 m to D = 13 m; and $R_{Svt\text{-}max}$ (%) for each tunnel diameter – Continued

| D (m) | H (m) | $S_{vt\text{-}max}$ (mm) | $R_{Svt\text{-}max}$ (%) |
|---|---|---|---|
| | 91 | 36.3 | -79.3 |
| | 104 | 24.7 | -85.9 |

# Appendix C: Train Loadings Distribution in the Models

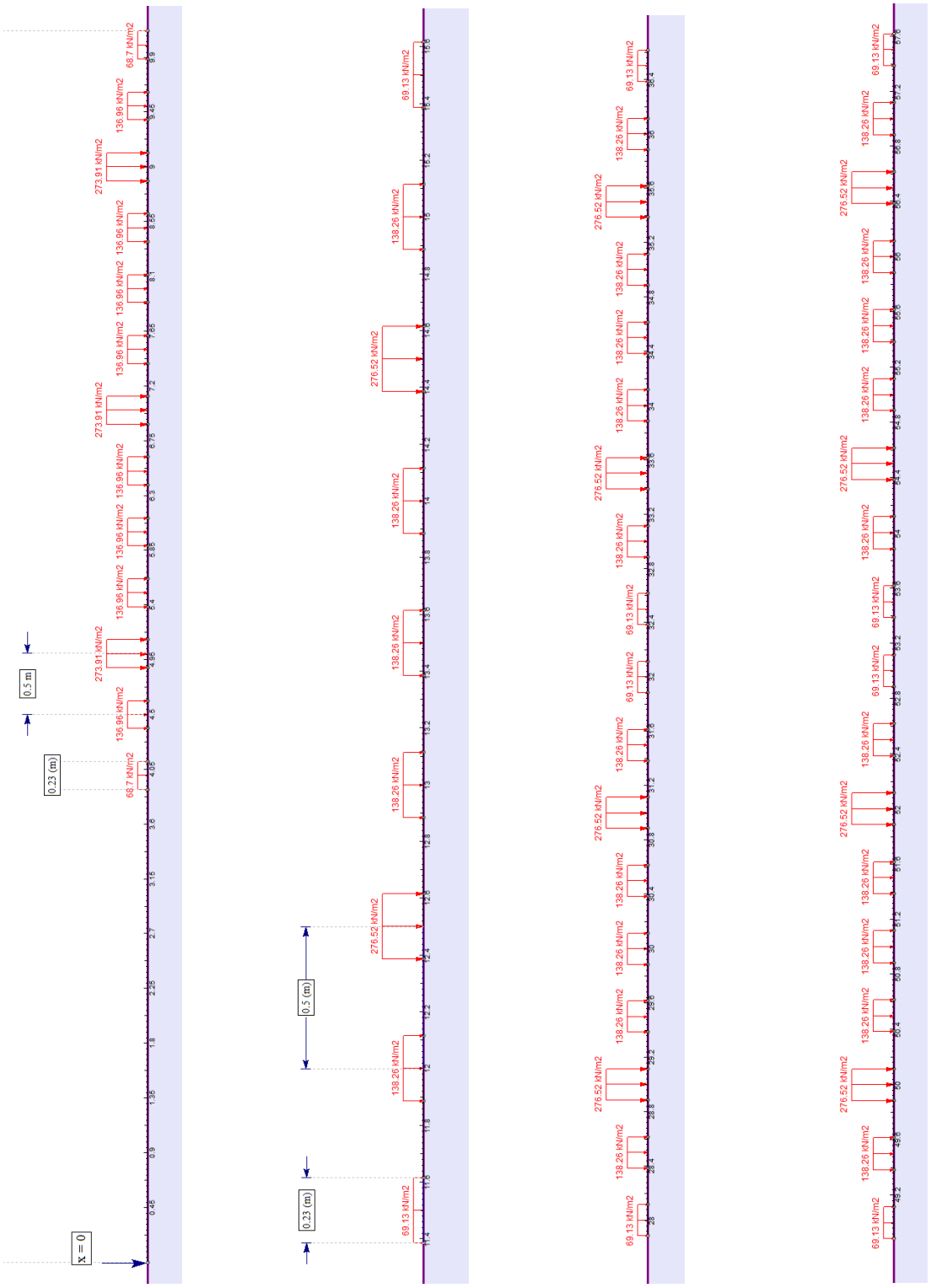


Figure C-1 Train loadings magnitude and distribution along x-axis ($V_1$ = 0 km/h).

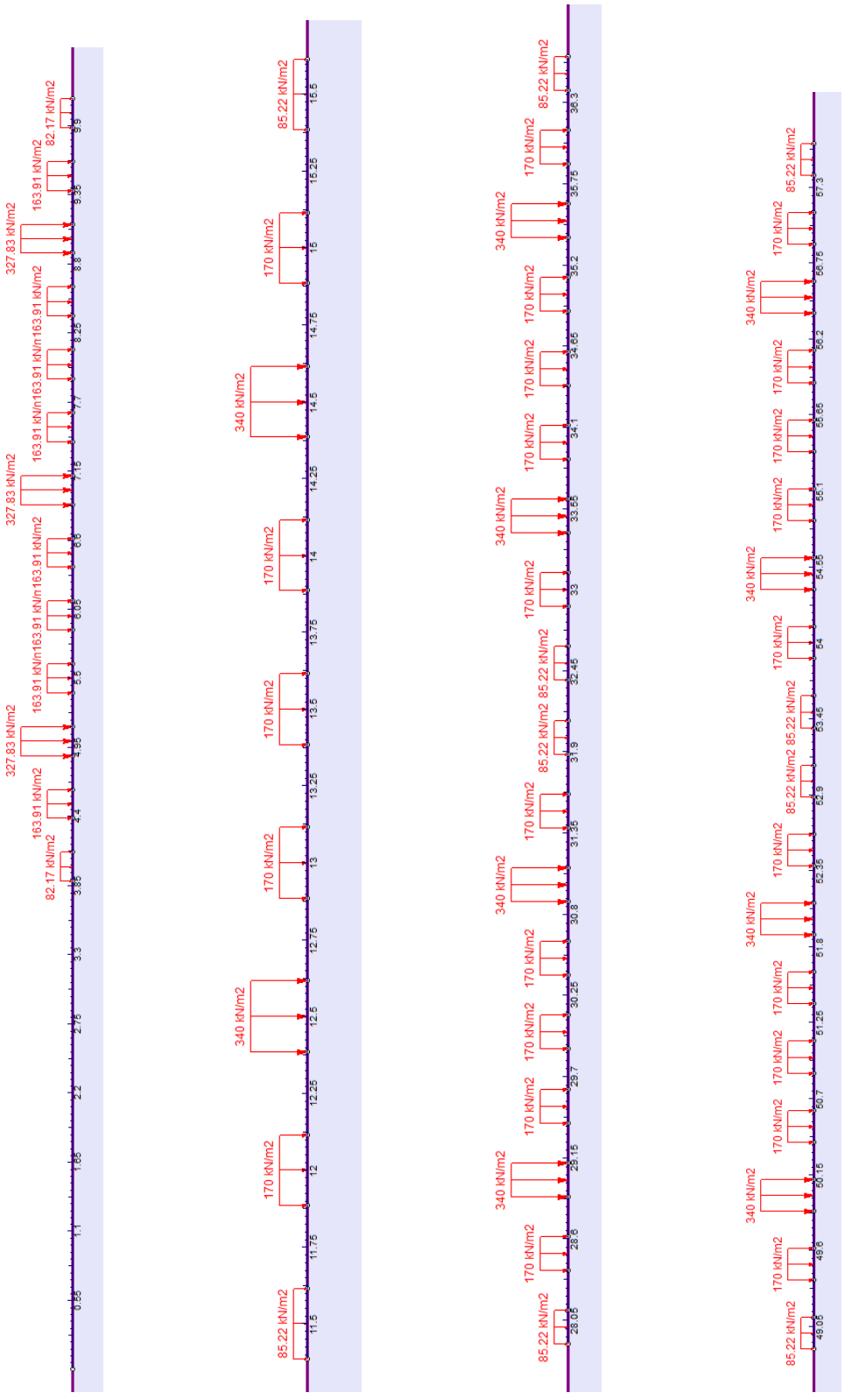

Figure C-2 Train loadings magnitude and distribution along x-axis ($V_2$ = 40 km/h).

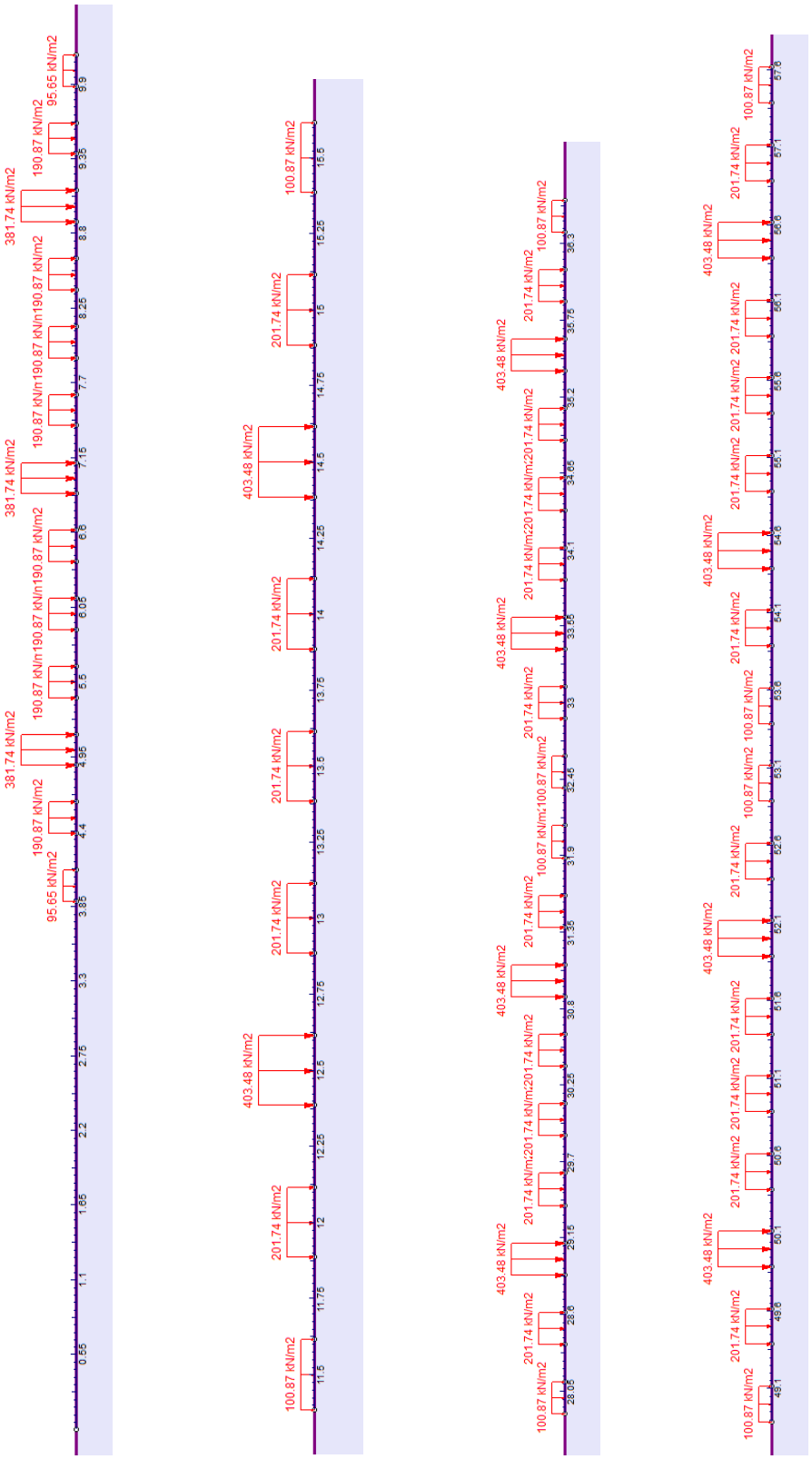


Figure C-3 Train loadings magnitude and distribution along x-axis ($V_3$ = 80 km/h).

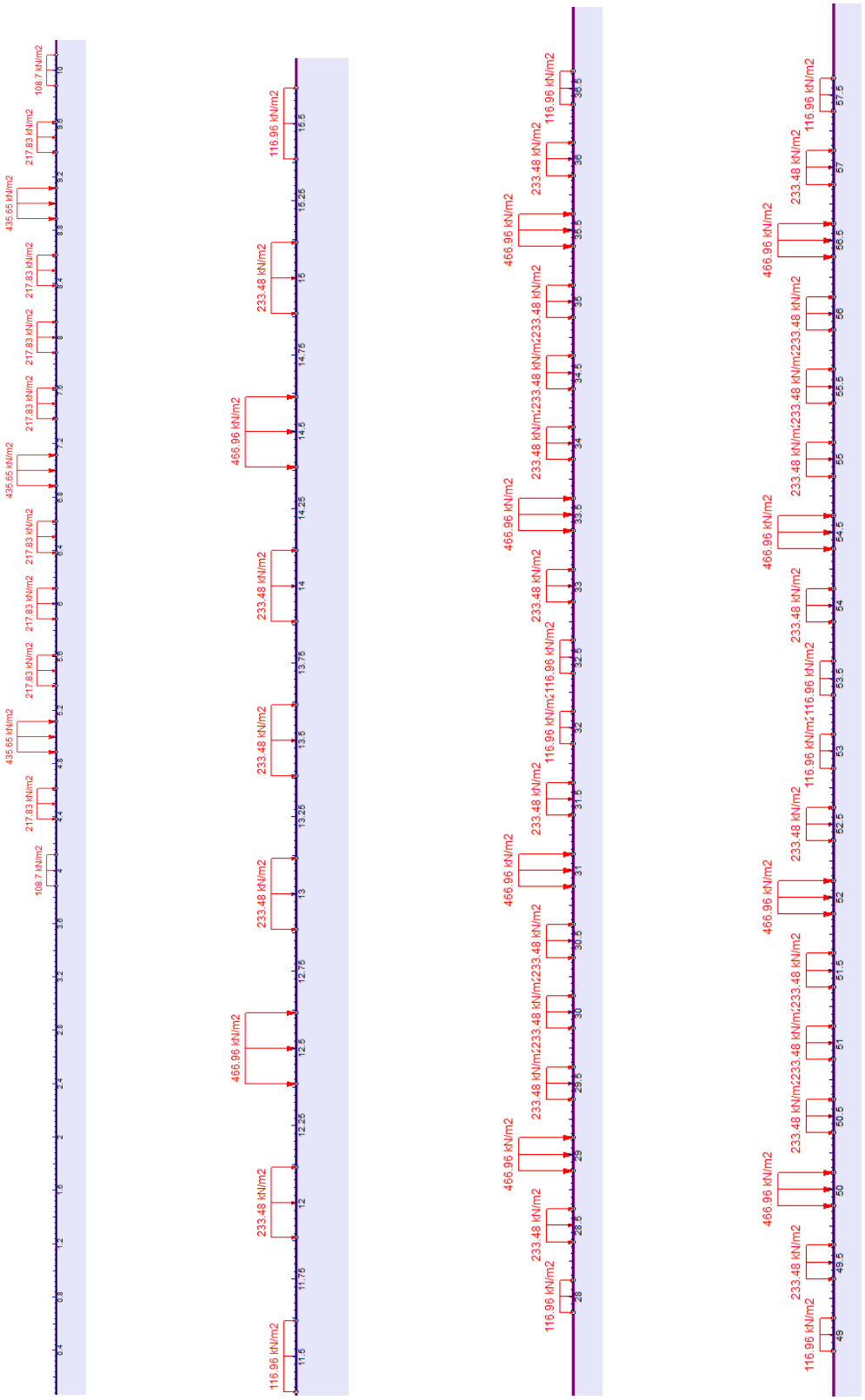

Figure C-4 Train loadings magnitude and distribution along x-axis ($V_4$ = 120 km/h).